APPNING: ANIMAL POPULATION IMAGING

EDITED BY: Michel Dojat, Jan G. Bjaalie and Emmanuel L. Barbier
PUBLISHED IN: Frontiers in Neuroinformatics

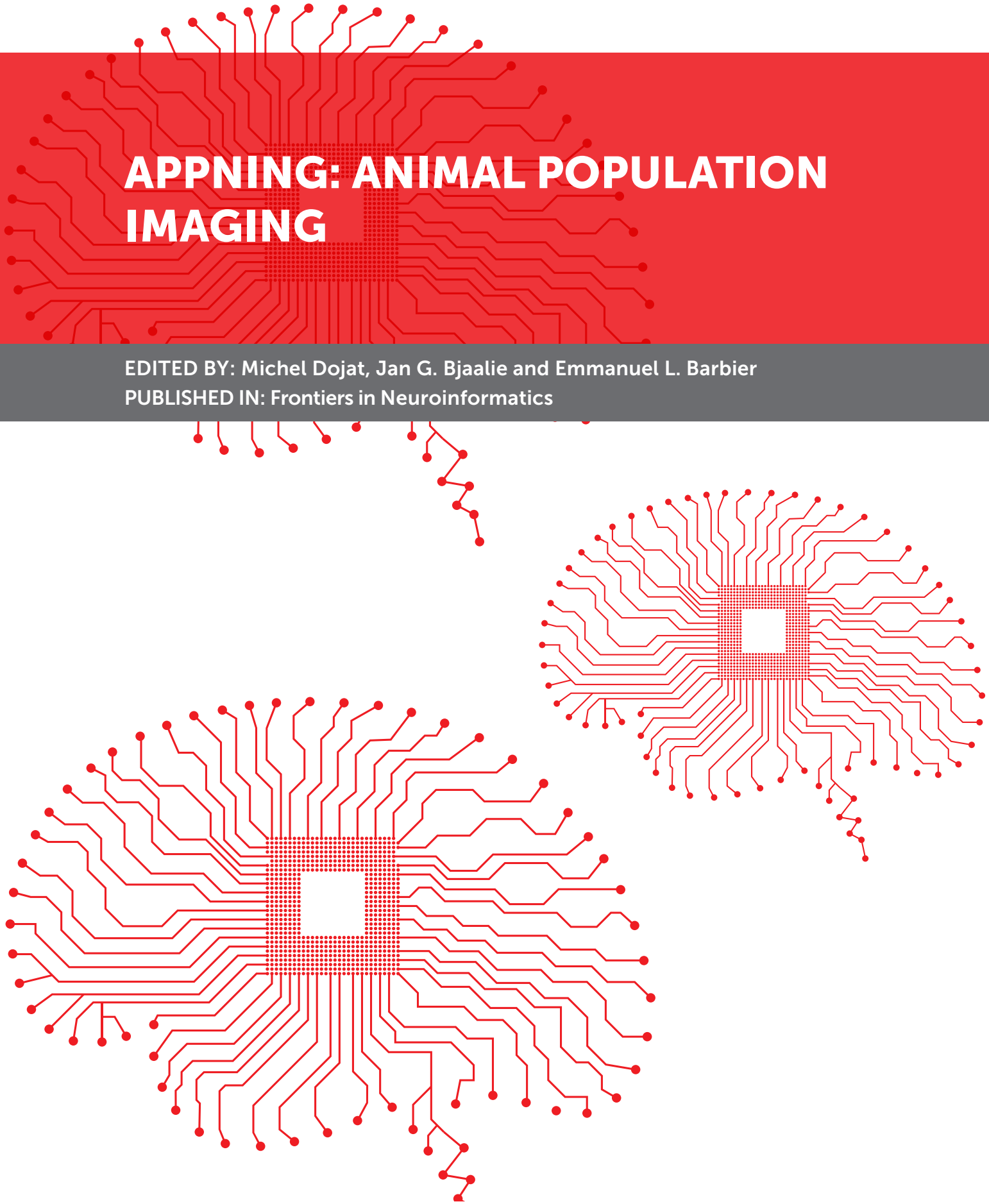

frontiers Research Topics

frontiers

ISSN 1664-8714
ISBN 978-2-88966-865-6
DOI 10.3389/978-2-88966-865-6

About Frontiers

Frontiers is more than just an open-access publisher of scholarly articles: it is a pioneering approach to the world of academia, radically improving the way scholarly research is managed. The grand vision of Frontiers is a world where all people have an equal opportunity to seek, share and generate knowledge. Frontiers provides immediate and permanent online open access to all its publications, but this alone is not enough to realize our grand goals.

Frontiers Journal Series

The Frontiers Journal Series is a multi-tier and interdisciplinary set of open-access, online journals, promising a paradigm shift from the current review, selection and dissemination processes in academic publishing. All Frontiers journals are driven by researchers for researchers; therefore, they constitute a service to the scholarly community. At the same time, the Frontiers Journal Series operates on a revolutionary invention, the tiered publishing system, initially addressing specific communities of scholars, and gradually climbing up to broader public understanding, thus serving the interests of the lay society, too.

Dedication to Quality

Each Frontiers article is a landmark of the highest quality, thanks to genuinely collaborative interactions between authors and review editors, who include some of the world's best academicians. Research must be certified by peers before entering a stream of knowledge that may eventually reach the public - and shape society; therefore, Frontiers only applies the most rigorous and unbiased reviews.
Frontiers revolutionizes research publishing by freely delivering the most outstanding research, evaluated with no bias from both the academic and social point of view. By applying the most advanced information technologies, Frontiers is catapulting scholarly publishing into a new generation.

What are Frontiers Research Topics?

Frontiers Research Topics are very popular trademarks of the Frontiers Journals Series: they are collections of at least ten articles, all centered on a particular subject. With their unique mix of varied contributions from Original Research to Review Articles, Frontiers Research Topics unify the most influential researchers, the latest key findings and historical advances in a hot research area! Find out more on how to host your own Frontiers Research Topic or contribute to one as an author by contacting the Frontiers Editorial Office: frontiersin.org/about/contact

APPNING: ANIMAL POPULATION IMAGING

Topic Editors:
Michel Dojat, Institut National de la Santé et de la Recherche Médicale (INSERM), France
Jan G. Bjaalie, University of Oslo, Norway
Emmanuel L. Barbier, Institut National de la Santé et de la Recherche Médicale (INSERM), France

Citation: Dojat, M., Bjaalie, J. G., Barbier, E. L., eds. (2021). APPNING: Animal Population Imaging. Lausanne: Frontiers Media SA.
doi: 10.3389/978-2-88966-865-6

Table of Contents

frontiers in Neuroinformatics

EDITORIAL
published: 13 May 2021
doi: 10.3389/fninf.2021.676603

Editorial: APPNING: Animal Population Imaging

Michel Dojat[1]*, *Jan G. Bjaalie*[2] *and Emmanuel L. Barbier*[1]

[1] University Grenoble Alpes, Inserm U1216, Grenoble Institut Neurosciences, Grenoble, France, [2] Department of Molecular Medicine, Institute of Basic Medical Sciences, University of Oslo, Oslo, Norway

Keywords: data sharing, open science, neuroimaging, brain, neuroscience

Editorial on the Research Topic

APPNING: Animal Population Imaging

This editorial review of the Research Topic Appning describes several solutions to support the sharing of animal imaging data and processing tools. Appning promotes the federation of multiple sources of information, processing tools and shows how this contributes to the diffusion of knowledge distributed in various preclinical imaging centers.

ANIMAL DATA SHARING

Some large data repositories (e.g., for brain studies, The MJ Fox Parkinson's database or the Human Connectome project) and specific architectures (e.g., COINS, LONI) are now available for human population imaging. The animal imaging community has also growing requirements for multicenter studies, for example to allow the comparison of academic results as in brain connectivity studies (Grandjean et al., 2020) or to characterize the effects of drugs (Bruns et al., 2015). To share preclinical imaging data and data analysis pipelines, only few tools are available that take into account the specificities of animal studies (Liu et al., 2020; Messinger et al., 2020), and few studies aim at standardization of acquisition and post-processing techniques.

Kain et al. describe a solution, *Small Animal Shanoir* (*SAS*), for the management of imaging data and metadata. *SAS* is a preclinical extension of a cloud-based solution dedicated to the management of human brain imaging repositories, Shanoir (Barillot et al., 2016). The main feature of this working solution is to rely on a core ontology, OntoNeurolog, which allows for the federation of different local databases via the mapping of their corresponding data models to the ontology, and facilitates its extension, for instance for managing preclinical studies. Additionally, to reinforce its extensibility capacity, *SAS* is designed as a set of independent micro-services. Then, a specific micro-service, *Dicomifier*, is dedicated to the transformation to Nifti format, widely used by several neuroimaging pipelines, of raw files in Bruker format, Bruker being a manufacturer of preclinical MR scanners, or of Dicom files. Associated data acquisition parameters are kept under a json file associated to each Nifti file stored in SAS. The web-oriented architecture allows for querying and retrieving stored images and processing pipelines. A data transfer module can interface the data management system to computing platforms for pipelines execution and the storage of image processing results. Specific authentication mechanisms allow for the fine control of data access, from an access restricted to a specific user's community to a publicly access for promoting open science. *SAS* was used for the project described by Deruelle et al. in this Research Topic.

Mandino et al. review the efforts done by the animal MRI community toward the standardization of data acquisition and analysis procedures in the context of whole brain functional

Edited and reviewed by:
Sean L. Hill,
Centre for Addiction and Mental Health, Canada

***Correspondence:**
Michel Dojat
michel.dojat@inserm.fr

Received: *05 March 2021*
Accepted: *09 April 2021*
Published: *13 May 2021*

Citation:
Dojat M, Bjaalie JG and Barbier EL (2021) Editorial: APPNING: Animal Population Imaging. Front. Neuroinform. 15:676603. doi: 10.3389/fninf.2021.676603

MRI; a key aspect for animal population imaging via multi-center studies. Based on their 868 research papers analysis, they showed that animal studies (mainly on rats and Sprague Dawley strain, in general carried out on 10 subjects at 7T and 9.4T) were underpowered and the false-positive rate incorrectly controlled, similarly to human studies (Button et al., 2013; Eklund et al., 2016). Several sources of variations among studies, from animal preparation and anesthesia to the use of *ad-hoc* pipelines or/and *ad-hoc* templates, hamper the comparison of published results. The authors propose guidelines to improve data sharing and reproducibility. They emphasize the importance of raw datasets sharing for data re-analysis with other processing pipelines allowing results comparison between studies, the adoption of standard templates for the reporting of results (e.g., coordinates of activation clusters) similarly to human neuroimaging studies (Fox et al., 2014), and the availability of open-source validated pipelines to unify data processing.

PIPELINES COMPOSITION AND PIPELINE SHARING

As shown by Mandino et al. in their review of the small animal literature, a source of difficulty for comparing results in animal studies is the absence of a core of validated solutions for data processing and analysis, similarly to what is available for human neuroimaging. Four papers address this point. To facilitate the sharing of raw MR brain imaging data, Ioanas et al. present a tool to transform files in a proprietary format (Bruker files) to Bids format that has been proposed for human neuroimaging studies (Gorgolewski et al., 2016). The workflow is implemented as a function, *bru2bids*, written in Python. In the same vein, Celestine et al. propose the Python package *Samba-MRI* to preprocess, register to templates, perform functional analysis, and perfusion measures from raw MR brain imaging datasets. It reuses several neuroimaging python libraries (e.g., Nipype, Nibabel or Nilearn) and incorporates additional features for group-wise registration or inter-modality registration. The code is available via the open GitHub platform. One can mention here the recent work of Brossard et al. (2020) who introduce a package to design pipelines and obtain multiparametric MRI maps that was extensively evaluated at the preclinical level. The papers from Groeneboom et al. and Yates et al. propose software for analyzing histological rodent brain images. Indeed, the recent *in vitro* imaging systems provide large collections of high-resolution images that raise specific computational problems for memory management and time execution. The former, *Nutil*, allows to automatize image processing and analysis of 2D brain histological sections. Standard image transformations are proposed to the user and their execution has been optimized to deal with large datasets. *Nutil* can be used independently or conjointly with the *Quint* workflow. *Quint* is a suite of tools that allows for the quantification and the spatial analysis of selected features in series of histological section images of rodent brain within a known atlas space. It combines several pre-existing tools for pre-processing, registration to 3D reference atlas (mouse and rat) and object segmentation, for the quantification of specific parameters in regions defined by the atlas. The *Quint* suite allows the user to perform in a convenient way, a quantitative analysis at different levels of granularity on large imaging datasets.

APPLICATIONS OF EXISTING DATA SHARING AND DATA ANALYSIS SOLUTIONS

MR imaging is a non-invasive versatile technique that allows to assess to various anatomical, functional or physiological parameters. Then, the T1 and T2 relaxation times are tissue and region-dependent parameters that may reflect structural alterations and may be used as biomarkers for various pathologies. The goal of Deruelle et al. was to define maps of T1 and T2 values for specific rat brain regions. To serve as reference, such maps should be defined based on a sufficient number of healthy animals reflecting inter-individual variability. They designed a multi-center study which included two data provider centers and three image processing pipeline provider centers. They used the SAS architecture (Kain et al.) and showed first, that MR data from 40 rats acquired in two centers could be successfully combined; second, that a good reproducibility could be obtained when using different processing solutions. Their study demonstrates the feasibility of a multi-center animal study if an appropriate architecture for data management and pipelines composition and execution is available. Raw data and reference T1 and T2 relaxometry maps, as well as processing pipelines are freely available via SAS.

Badea et al. use genetically modified mouse models to relate genotype with brain aging trajectory for Alzheimer's disease. They use diffusion tensor imaging to compare structural connectomes, and region volumes for two gene modified mouse groups associated with genetic risk for Alzheimer disease. Additionally, behavioral tests provide information about learning and memory function deficits. They show that behavioral and imaging markers allow to identify vulnerable brain networks induced by the genetic risk factor. Their findings contribute to a better understanding of the physio-pathological mechanisms triggering the onset of the Alzheimer's disease. All generated datasets generated are available to the scientific community and may be pooled with new data to reinforce the robustness of the findings.

Interestingly, all the papers of the RT Appning concern the investigation of the rodent brain with both *in vivo*, MR imaging, and *in vitro*, histological imaging. Indeed, neuroimaging is the domain for which scientists have developed to date several solutions for sharing data and process large data repositories. This is certainly due to the impressive quantity of neuroimaging studies performed in the recent years, generating large-scale databases. This is also stimulated by publications showing the poor replicability and reproducibility of the results obtained (Carp, 2012;

Button et al., 2013; Nichols et al., 2017; Poldrack et al., 2017). Because these caveats are not restricted to brain studies, but concern many areas of life science (Ioannidis, 2005), new solutions for dealing with other organs and species will for sure emerge.

AUTHOR CONTRIBUTIONS

MD wrote the first draft of the manuscript. All authors contributed to manuscript revision, read, and approved the submitted version.

REFERENCES

Barillot, C., Bannier, E., Commowick, O., Corouge, I., Baire, A., Fakhfakh, I., et al. (2016). Shanoir: applying the software as a service distribution model to manage brain imaging research repositories. *Front. ICT* 3:25. doi: 10.3389/fict.2016.00025

Brossard, C., Montigon, O., Boux, F., Delphin, A., Christen, T., Barbier, E. L., et al. (2020). MP3: medical software for processing multi-parametric images pipelines. *Front. Neuroinform.* 14:594799. doi: 10.3389/fninf.2020.594799

Bruns, A., Mueggler, T., Künnecke, B., Risterucci, C., Prinssen, E. P., Wettstein, J. G., et al. (2015). "Domain gauges": a reference system for multivariate profiling of brain fMRI activation patterns induced by psychoactive drugs in rats. *Neuroimage* 112, 70–85. doi: 10.1016/j.neuroimage.2015.02.032

Button, K. S., Ioannidis, J. P., Mokrysz, C., Nosek, B. A., Flint, J., Robinson, E. S., et al. (2013). Power failure: why small sample size undermines the reliability of neuroscience. *Nat. Rev. Neurosci.* 14, 365–376. doi: 10.1038/nrn3475

Carp, J. (2012). The secret lives of experiments: methods reporting in the fMRI literature. *Neuroimage* 63, 289–300. doi: 10.1016/j.neuroimage.2012.07.004

Eklund, A., Nichols, T. E., and Knutsson, H. (2016). Cluster failure: why fMRI inferences for spatial extent have inflated false-positive rates. *Proc. Natl. Acad. Sci. U.S.A.* 113, 7900–7905. doi: 10.1073/pnas.1602413113

Fox, P. T., Lancaster, J. L., Laird, A. R., and Eickhoff, S. B. (2014). Meta-analysis in human neuroimaging: computational modeling of large-scale databases. *Annu. Rev. Neurosci.* 37, 409–434. doi: 10.1146/annurev-neuro-062012-170320

Gorgolewski, K. J., Auer, T., Calhoun, V. D., Craddock, R. C., Das, S., Duff, E. P., et al. (2016). The brain imaging data structure, a format for organizing and describing outputs of neuroimaging experiments. *Sci. Data* 3:160044. doi: 10.1038/sdata.2016.44

Grandjean, J., Canella, C., Anckaerts, C., Ayranci, G., Bougacha, S., Bienert, T., et al. (2020). Common functional networks in the mouse brain revealed by multi-centre resting-state fMRI analysis. *Neuroimage* 205:116278. doi: 10.1016/j.neuroimage.2019.116278

Ioannidis, J. P. (2005). Why most published research findings are false. *PLoS Med.* 2:e124. doi: 10.1371/journal.pmed.0020124

Liu, Y., Perez, P. D., Ma, Z., Ma, Z., Dopfel, D., Cramer, S., et al. (2020). An open database of resting-state fMRI in awake rats. *Neuroimage* 220:117094. doi: 10.1016/j.neuroimage.2020.117094

Messinger, A., Sirmpilatze, N., Heuer, K., Loh, K. K., Mars, R. B., Sein, J., et al. (2020). A collaborative resource platform for non-human primate neuroimaging. *Neuroimage* 226:117519. doi: 10.1016/j.neuroimage.2020.117519

Nichols, T. E., Das, S., Eickhoff, S. B., Evans, A. C., Glatard, T., Hanke, M., et al. (2017). Best practices in data analysis and sharing in neuroimaging using MRI. *Nat. Neurosci.* 20, 299–303. doi: 10.1038/nn.4500

Poldrack, R. A., Baker, C. I., Durnez, J., Gorgolewski, K. J., Matthews, P. M., Munafò, M. R., et al. (2017). Scanning the horizon: towards transparent and reproducible neuroimaging research. *Nat. Rev. Neurosci.* 18, 115–126. doi: 10.1038/nrn.2016.167

Conflict of Interest: The authors declare that the research was conducted in the absence of any commercial or financial relationships that could be construed as a potential conflict of interest.

frontiers in Neuroinformatics

METHODS
published: 03 December 2019
doi: 10.3389/fninf.2019.00075

QUINT: Workflow for Quantification and Spatial Analysis of Features in Histological Images From Rodent Brain

Sharon C. Yates[1], Nicolaas E. Groeneboom[1], Christopher Coello[1], Stefan F. Lichtenthaler[2,3,4], Peer-Hendrik Kuhn[5], Hans-Ulrich Demuth[6], Maike Hartlage-Rübsamen[7], Steffen Roßner[7], Trygve Leergaard[1], Anna Kreshuk[8], Maja A. Puchades[1] and Jan G. Bjaalie[1]**

[1]Neural Systems Laboratory, Institute of Basic Medical Sciences, University of Oslo, Oslo, Norway, [2]German Center for Neurodegenerative Diseases (DZNE), Munich, Germany, [3]Neuroproteomics, School of Medicine, Klinikum rechts der Isar, and Institute for Advanced Study, Technical University of Munich, Munich, Germany, [4]Munich Cluster for Systems Neurology (SyNergy), Munich, Germany, [5]Institute of Pathology, Technical University of Munich, Munich, Germany, [6]Department of Molecular Drug Design and Target Validation Fraunhofer Institute for Cell Therapy and Immunology, Halle (Saale), Leipzig, Germany, [7]Paul Flechsig Institute for Brain Research, University of Leipzig, Leipzig, Germany, [8]European Molecular Biology Laboratory, Heidelberg, Germany

OPEN ACCESS

Edited by:
Arjen van Ooyen, Vrije Universiteit Amsterdam, Netherlands

Reviewed by:
Amy Bernard, Allen Institute for Brain Science, United States
Joanes Grandjean, Radboud University Nijmegen Medical Centre, Netherlands

***Correspondence:**
Maja A. Puchades
m.a.puchades@medisin.uio.no
Jan G. Bjaalie
j.g.bjaalie@medisin.uio.no

Received: *11 February 2019*
Accepted: *15 November 2019*
Published: *03 December 2019*

Citation:
Yates SC, Groeneboom NE, Coello C, Lichtenthaler SF, Kuhn P-H, Demuth H-U, Hartlage-Rübsamen M, Roßner S, Leergaard T, Kreshuk A, Puchades MA and Bjaalie JG (2019) QUINT: Workflow for Quantification and Spatial Analysis of Features in Histological Images From Rodent Brain. Front. Neuroinform. 13:75. doi: 10.3389/fninf.2019.00075

Transgenic animal models are invaluable research tools for elucidating the pathways and mechanisms involved in the development of neurodegenerative diseases. Mechanistic clues can be revealed by applying labelling techniques such as immunohistochemistry or *in situ* hybridisation to brain tissue sections. Precision in both assigning anatomical location to the sections and quantifying labelled features is crucial for output validity, with a stereological approach or image-based feature extraction typically used. However, both approaches are restricted by the need to manually delineate anatomical regions. To circumvent this limitation, we present the QUINT workflow for quantification and spatial analysis of labelling in series of rodent brain section images based on available 3D reference atlases. The workflow is semi-automated, combining three open source software that can be operated without scripting knowledge, making it accessible to most researchers. As an example, a brain region-specific quantification of amyloid plaques across whole transgenic Tg2576 mouse brain series, immunohistochemically labelled for three amyloid-related antigens is demonstrated. First, the whole brain image series were registered to the Allen Mouse Brain Atlas to produce customised atlas maps adapted to match the cutting plan and proportions of the sections (*QuickNII* software). Second, the labelling was segmented from the original images by the Random Forest Algorithm for supervised classification (*ilastik* software). Finally, the segmented images and atlas maps were used to generate plaque quantifications for each region in the reference atlas (*Nutil software*). The method yielded comparable results to manual delineations and to the output of a stereological method. While the use case demonstrates the QUINT workflow

for quantification of amyloid plaques only, the workflow is suited to all mouse or rat brain series with labelling that is visually distinct from the background, for example for the quantification of cells or labelled proteins.

Keywords: rodent brain analysis, Alzheimer's disease, quantification, workflow, APP—amyloid precursor protein, beta-amyloid

INTRODUCTION

Transgenic rodent models are useful tools in the study of neurodegenerative disorders, providing clues to the origins and mechanisms of the protein aggregates that accumulate and harm neurons and synapses in these conditions (Dawson et al., 2018). A common study approach is to section the brains and apply immunohistochemical or other histological techniques to reveal features that can be explored by microscopy. Qualitative assessments of such features can reveal vulnerable brain regions, while understanding the connectivity of affected regions may provide insight into disease mechanisms (Thal et al., 2002; Hurtado et al., 2010). The ability to accurately assign anatomical location to the data is of crucial importance to the validity of the conclusions drawn, and is a limiting factor in these studies. Present resources for assigning anatomical location to whole brain rodent data are not easily applicable to 2D histological series, especially if cutting angles deviate even marginally from the coronal, sagittal or horizontal planes. Even with diligent sectioning, small deviations of a few degrees are common. Our recent registration tool, *QuickNII*, allows users to perform that correction (Puchades et al., 2019). For users with coding expertise, other tools for registration of image series to reference atlases are also available (Kopec et al., 2011; Fürth et al., 2018; Xiong et al., 2018). Furthermore, combining datasets from different sources or comparison of data from different animal models is difficult unless the data are linked to the same atlas reference system (Simmons and Swanson, 2009; Kim et al., 2017; Bjerke et al., 2018).

The gold standard for quantification of features in 2D image series is stereological analysis applied to anatomical regions that have been manually delineated by an expert in the field (Schmitz and Hof, 2005). However, in practical terms, this method is difficult to apply optimally due to a shortage of anatomical expertise, the significant numbers of sections for analysis, and limited availability of time. Large scale projects and multi-centre collaborations would benefit from the automation of both the extraction and spatial analysis steps. The introduction of the machine learning concept has opened up possibilities for semi-automated extraction of features based on supervised machine learning algorithms (Berg et al., 2019). Furthermore, the new generation of three-dimensional digital brain atlases developed for murine brains (Lein et al., 2007; Hawrylycz et al., 2011; Oh et al., 2014; Papp et al., 2014; Kjonigsen et al., 2015) serve as spatial frameworks for data sharing and integration (Boline et al., 2008; Zaslavsky et al., 2014), while also providing possibilities for automation of spatial analysis.

To this end, we have developed the QUINT workflow based on image analysis using a series of neuroinformatic tools. The workflow entails three steps. In the first step, images are registered to a 3D reference atlas. This step utilises a three-dimensional brain atlasing tool, *QuickNII* (Puchades et al., 2019) that supports arbitrary cutting angles, and is used to generate atlas maps that are customised specifically to match each section. In the second step, segmentation of distinct features such as labelled cells or aggregates is performed with *ilastik*. The *ilastik* software benefits from a supervised machine learning approach (Berg et al., 2019) allowing a combination of many parameters for segmentation as is demonstrated in the use cases here. However, the workflow is compatible with segmentations produced by other means, such as *NIH ImageJ* (Schneider et al., 2012), or with another image analysis tool provided that it supports segmented image export. As illustrated by Pallast et al. (2019), different types of features may require different segmentation tools. In the third step, the *Nutil* software draws on the atlas maps and segmentations to quantify segmented objects in relation to the delineated brain regions contained in the atlas. *Nutil* also extracts the xyz position of the segmented objects for viewing in reference atlas space. As an example, we present the quantification of human amyloid precursor protein (hAPP) and β-amyloid deposits across a whole mouse brain series immunohistochemically labelled For the human APP N-Terminus (rat monoclonal antibody; Höfling et al., 2016), Aβ (4G8 mouse monoclonal antibody) and pyro-glutamate modified Aβ [pE-Aβ; J8 mouse monoclonal antibody (Hartlage-Rübsamen et al., 2018)]. The results are validated by comparing the workflow output with ground truth data manually segmented with the *NIH ImageJ* tool (Schneider et al., 2012), and by comparing to stereological counts with the MBF Bioscience *Stereo Investigator* Area Fraction Fractionator probe. A second example is shared to demonstrate the use of the workflow for quantification of another type of labelling (parvalbumin positive cells in an Allen Mouse Brain series).

MATERIALS AND METHODS

The workflow for serial brain section image analysis comprises several parts (**Figure 1**): namely, image pre-processing (*Nutil* using the *Transform feature*); registration of images to a reference atlas (*QuickNII*); segmentation of labelled features (*ilastik*); and quantification of features per atlas region (*Nutil* using the *Quantifier feature*).

Use Case Material: Animal, Immunohistochemical Labelling and Image Acquisition

An 18-month-old male Tg2576 mouse (Hsiao et al., 1996) mimicking the amyloid pathology of Alzheimer's disease

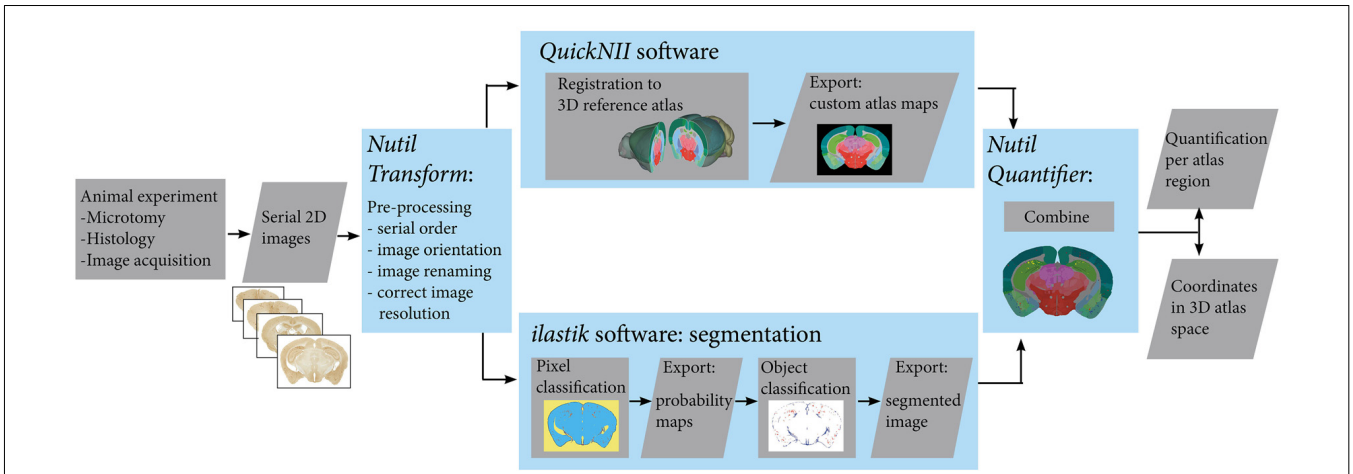

FIGURE 1 | Workflow for automated quantification and spatial analysis. Diagram showing key steps of the workflow (blue frames). After sectioning and labelling, brain sections are digitalised. Serial section images are pre-processed, and then registered to a 3-D reference atlas space using the *QuickNII* tool. The same images are segmented using the *ilastik* tool. Exported custom atlas maps and segmented images are then combined in the *Nutil* tool in order to extract quantification of objects in atlas brain regions as well as 3D coordinates of the objects.

supplied the material for the first use case (plaque quantification). This study was carried out in accordance with the principles of the Basel Declaration and recommendations of the ARRIVE guidelines, National Centre for the Replacement, Refinement and Reduction of Animals in Research, UK. The protocol used was approved by the responsible authority Landesdirektion Sachsen, Germany, license number T28/16. The mouse was sacrificed by CO_2 inhalation and the brain was fixed using the transcardial perfusion fixation method. First, the brain was perfused with 30 mL of PBS, followed by 30 mL of 4% paraformaldehyde (PFA) solution and post-fixed at 4°C overnight. The brain was cryoprotected by immersion in 30% sucrose for 3 days and sectioned using a freezing microtome in 30 µm thick coronal sections. Every 4th section (60 sections) was used for immunolabelling of hAPP using the species-specific monoclonal rat antibody 1D1 (dilution 1:2; Höfling et al., 2016). Neighbouring sections with the same sampling frequency were labelled with the 4G8 antibody detecting pan-Aβ (BioLegend RRID:AB_2734548, 1:8,000) and with the J8 antibody detecting pE-Aβ (1:2,000; Hartlage-Rübsamen et al., 2018). After incubation with biotinylated secondary antibodies (1:1,000; Dianova; Hamburg, Germany) in TBS with 2% bovine serum albumin for 60 min at room temperature, the ABC method was applied, which comprised incubation with complexed streptavidin–horseradish peroxidase (1:1,000; Sigma; Deisenhofen, Germany). Incubations were separated by washing steps (3-times, 5 min). Binding of peroxidase was visualised by incubation with 4 mg 3,3′-diaminobenzidine and 2.5 µl H_2O_2 per 5 ml Tris buffer (0.05 M; pH 7.6) for 1–2 min. Stained brain sections were extensively washed and mounted onto microscope slides. All brain sections were scanned using a Zeiss Axioscan Z1 slide scanner running Zeiss Zen Software (Carl Zeiss MicroImaging, Jena, Germany) with a 20× objective. Images were exported in Tagged Information File Format (TIFF). The background in the raw images was adjusted within the Zen software in order to optimise the signal to noise ratio, with the same parameters for all images, thereby allowing comparative results. The resolution of the exported Tiff images was constant within each series (0.284 µm/pixel for the antibody 1D1 and 0.265 µm/pixel for the antibodies 4G8 and J8).

Use Case: Allen Mouse Brain Series

To demonstrate quantification of another type of labelling, the QUINT workflow was applied to parvalbumin positive cells in an image series exported from the Allen Mouse Brain Atlas Data Portal. The image series encompassed 20 sagittal mouse brain sections from the left hemisphere labelled for parvalbumin by *in situ* hybridisation, available at http://mouse.brain-map.org/experiment/show/75457579 (© 2004 Allen Institute for Brain Science. Allen Mouse Brain Atlas. Available from: mouse.brain-map.org). All the analysis parameters and workflow output files for this dataset are published on the human brain project (HBP) Platform (DOI: 10.25493/6DYS-M3W; Yates and Puchades, 2019), and so are not described here in full.

Image Pre-processing Steps: Nutil Transform

The *Transform* feature in the *Nutil* software enables image rotation, renaming, resizing and mirroring and was used to prepare the image series for *QuickNII* alignment and *ilastik* segmentation. Several sets of images were prepared as the input size requirements for the *QuickNII* and *ilastik* software differ. For *QuickNII*, the input requirements are described in Puchades et al. (2019). For *ilastik* the resizing was performed in order to enable efficient processing and to comply with the pixel scale restriction of the features imposed by the *ilastik* software. To clarify, the pixel classification algorithm relies on input from manual user annotations of training images, and

the features–intensity, edge and/or texture–of the image pixels. The features at different scales are computed as filters with pre-smoothing by a Gaussian with a sigma ranging from 0.3 to 10. For each pixel, the algorithm thus considers the values of the filters in a small sphere around the pixel (the maximal sphere radius is approximately 35 pixels) in the annotated regions, on a scale of 0.3 to 10 pixels. This means that the pixel features must fall within a maximum 10 × 10 pixel window for detection (for example, a repeating textural pattern). The resize factor was selected with reference to this maximum pixel scale to bring the labelled objects within the detection range for all the features, hence achieving a better segmentation (see the *ilastik* manual for more information). In practise, a test run was performed with *ilastik* on images of different sizes to find the optimal resolution for segmentation, with a final resize factor of 0.1 selected for the pE-Aβ series, and a factor of 0.05 for the hAPP and pan-Aβ series.

The *Nutil software* is shared through the HBP[1] and is available for download at NITRC[2] with an extensive user manual. See also Github[3].

Alignment of Sections to Atlas Space With QuickNII

The three image series (hAPP, pan-Aβ and pE-Aβ) were aligned to reference atlas space with the *QuickNII* atlasing tool (**Figure 2**; Puchades et al., 2019). This open access software allows assignment of spatial location to serial brain section images. The reference atlases available in the tool are the Waxholm Space Rat Atlas for rat data (Papp et al., 2014; Kjonigsen et al., 2015) and the Allen Mouse Brain Atlas for mouse data (© 2004 Allen Institute for Brain Science. Allen Mouse Brain Atlas. Available from: http://download.alleninstitute.org/informatics-archive/current-release/mouse_ccf/annotation/ccf_2015/) (Lein et al., 2007; Oh et al., 2014).

Within *QuickNII*, the volumetric brain reference atlases are used to generate customised atlas maps that match the spatial orientation and proportions of the experimental sections. In the software, the location is defined by superimposing the reference atlas onto the section images in a process termed "anchoring." In "anchoring" the cutting angle of the reference atlas is adjusted to match the plane of the sections, with the position of each section identified prior to a manual adaptation of each atlas image to match the section images using affine transformations. Anchoring of a series of, e.g., 100 sections from an animal, typically takes 2–6 h, depending on the quality of the sections in the series (distorted sections are more difficult to anchor).

The *QuickNII* software is available at NITRC[4] through the HBP[1].

Image Segmentation With *Ilastik*

The *ilastik* software was used to segment the downscaled section images for immunohistochemically labelled plaques (60 images per series: hAPP, Aβ and pE-Aβ; Berg et al., 2019; version 1.2.2. post2 for Windows, 64-bit). The segmentation was performed in two steps. First using Pixel Classification to differentiate the immunoreactivity from the background, followed by Object Classification to differentiate the specific immunoreactivity from labelled artefacts (**Figure 3**). For each image series, only 10% of the images were used to train the classifiers, which were then applied to the whole series in a batch mode, saving considerable time compared to an individual segmentation approach (segmentation of a whole image series takes a few hours depending on the size and number of images).

Ilastik Pixel Classification Workflow

The Pixel Classifiers were trained with the training images selected for each series (approximately every 6th section per series). All the available features (texture, edge, and intensity) and feature scales (0.3–10 pixels) were included in the classification algorithms. In the training phase, annotations were placed on the first training image, a few pixels at a time, with inspection of the predictions with each annotation. To refine the classifier and increase its applicability to the whole series, each training image was annotated in turn until the predictions were of a good standard across all the training images. The trained classifier was then applied to the series in the batch mode, with probability maps exported for the whole series.

Ilastik Object Classification Workflow

The object classifier differentiates objects based on features such as size and shape, and was applied to the output of the pixel classification to remove artefacts that could not be removed by pixel classification alone (for example, the elongated immunoreactivity around the edges of sections as opposed to the typically circular plaques). The training approach was the same as for the pixel classification, with the same subset of training images used. The probability maps were thresholded at a probability of 0.4 for all the series, with the object size filters set to 8–10,00,000 pixels for the hAPP and pE-Aβ series, and 4–10,00,000 pixels for the pan-Aβ series (the pan-Aβ labelled objects were smaller than the hAPP and pE-Aβ objects). All the object features in the *ilastik* software, except the location features, were included in the classifier (find more information on this in the *ilastik* user manual). The trained classifier was applied to the whole series in the batch mode, with the object prediction maps exported in PNG format. *NIH imageJ* was then used to apply colours to the predictions maps with the glasbey lookup table, and the coloured versions used as input for *Nutil Quantifier*.

Quantification of Labelling in the Different Brain Regions With Nutil Quantifier

Once the section images were segmented (*ilastik*) and registered to the relevant reference atlas (*QuickNII*), *Nutil*—a software application developed in-house—was used to extract quantitative data about the labelling in each region in the reference atlas (*Quantifier* feature).

Nutil is a stand-alone application that allows for object classification from arbitrary image input files. The code for

[1]www.humanbrainproject.eu
[2]https://www.nitrc.org/projects/nutil/
[3]https://github.com/leuat/nutil
[4]https://www.nitrc.org/projects/quicknii/

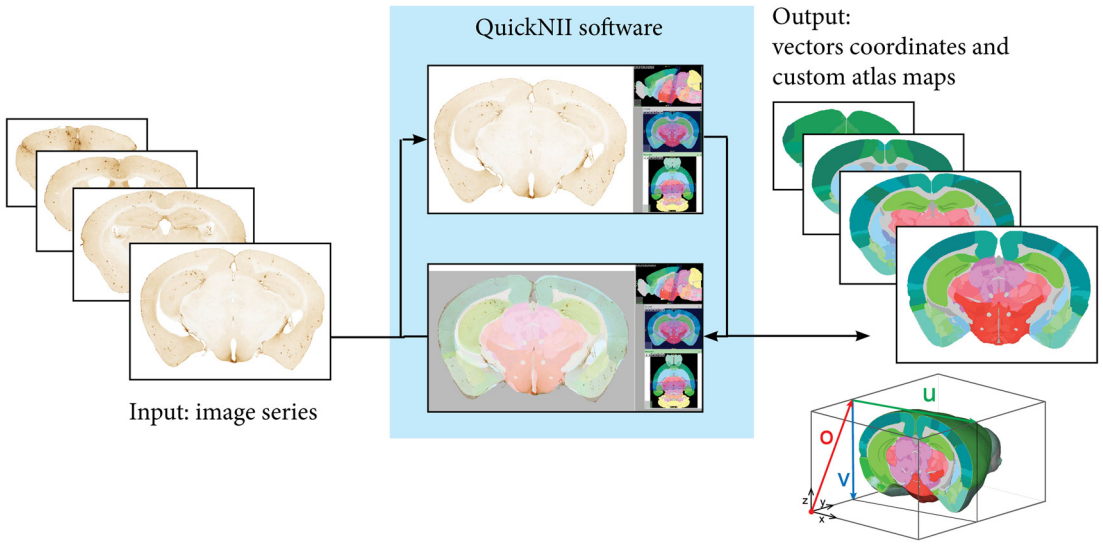

FIGURE 2 | Registration to reference atlas by *QuickNII*. Following initial preprocessing steps where the sequence and orientation of the serial images is validated and a configuration file generated, images are imported to *QuickNII* together with a 3-D reference atlas of the mouse brain. In *QuickNII*, an atlas overlay image which is interactively manipulated to generate an image with position, scale, and orientation (rotation and tilt) that best matches the selected experimental images (DV: +13; ML: −4). *QuickNII* automatically propagates information about position, scale, and tilt to the entire series. By iterative anchoring of selected key sections, the user can optimize the automatically propagated parameters. The rotation and position of the overlay atlas image is validated and if needed adjusted by the user. Output from *QuickNII* is a series of custom atlas plates matching each anchored experimental image, and an XML file describing a set of vectors (o, u, and v) that define the position of each image relative to the technical origin of the reference atlas used.

Quantifier uses a standard recursive pixel filling algorithm in order to scan for and separate individual objects in a 2D segmented image. This means that for each pixel that is not classified as a background pixel, the algorithm checks whether there are neighbouring pixels that are also not part of the background. If so, *Nutil* applies the same algorithm to these neighbours, and repeats the process until all surrounding pixels are background only. The cluster of collected pixels is considered to be an object, which is added to a global list of objects before being assigned a label ID that is matched with the corresponding reference atlas. This is performed by selecting the top left pixel from each identified object and using this position as a lookup in the reference atlas image files. In addition, the statistical properties of each cluster are calculated and stored (position, width, height, area, size, et cetera). When the entire batch process has completed, reports are produced, which are based on user inputs such as individual colour assignment for different label IDs, areas to exclude, areas to merge, et cetera. Finally, a set of report files are generated, in addition to customised atlas images superimposed with colour-coded (and labelled) objects.

Nutil is available for download at NITRC with an extensive user manual[5]. See also Github[6]. The *Nutil Quantifier* feature is fast to run, taking seconds to minutes on a desktop computer depending on the size and number of images for analysis.

[5]https://www.nitrc.org/projects/nutil/
[6]https://github.com/leuat/nutil

Validation of the Image Segmentation

In order to validate the segmentations produced with the *ilastik* software, their area outputs as determined with *Nutil Quantifier* were compared to ground truth measurements obtained by manual delineation of plaques for five sections (s14, s54, s94, s134 and s174), and to stereological measurements on 30 sections (s6, s14, s22, s30, s38, s40, s54, s62, s70, s78, s86, s94, s120, s110, s118, s126, s134, s142, s150, s158, s166, s174, s182, s190, s198, s206, s214, s222, s230, s238). The comparisons were performed on section images that were immunohistochemically labelled for hAPP (1D1 antibody) and restricted to clearly visible plaques (we excluded neuronal hAPP labelling). For both the 5 and 30 section subsets, the sections were regularly spaced and spanned the full volume of the brain. The subsets represented 8% and 50% of the full hAPP series, respectively. The section images that were used to train the classifiers (training images) were not selected for the validation.

The ground truth area measurements were obtained for five of the sections by manual delineation of the hAPP immunoreactive plaques by an expert in the field, with the *NIH ImageJ* tool (Analyse function) on images at 5% of the original size. Immunolabelled plaques were delineated for individual objects at the pixel level. For each image, the surface area occupied by plaques was calculated with reference to the resize factor and the pixel length in the original image.

Stereological analysis of hAPP immunoreactivity was performed with the Area Fraction Fractionator probe in the *MBF Stereo Investigator* software (version 2017.02.2; MBF Bioscience,

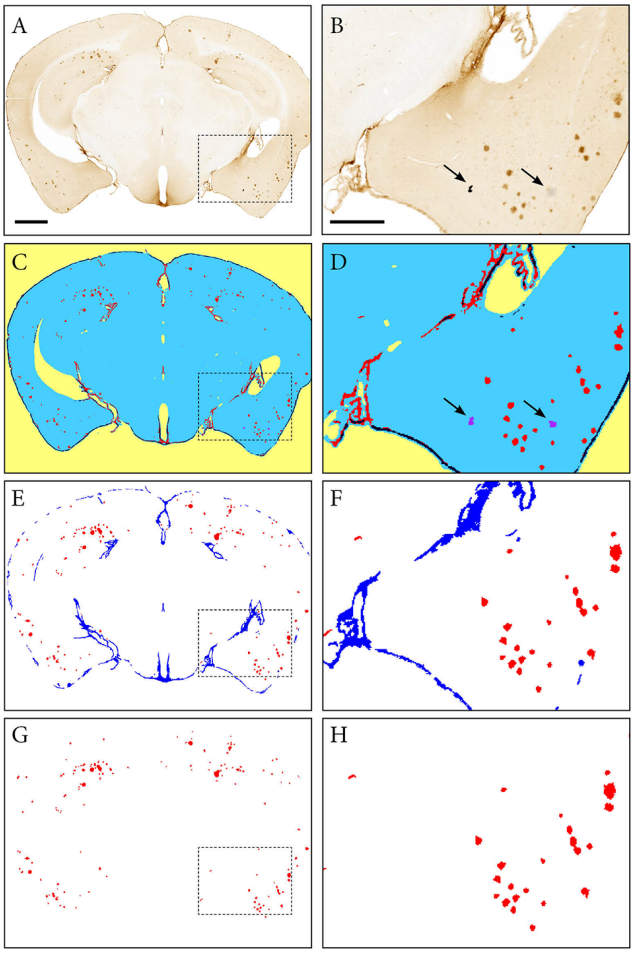

FIGURE 3 | Segmentation of images with the *ilastik* software. An image of a Tg2576 mouse brain section, immunohistochemically labelled for pan-Aβ (4G8), processed with the pixel and object classification workflows in the *ilastik* software (version 1.2.2. post2). Panels **(A,C,E,G)** show the whole image, with **(B,D,F,H)** representing the area identified in the dashed box. **(C,D)** show the output of the pixel classification workflow, with images segmented into five classes based on differences in intensity, edge and texture (red: specific immunohistochemical labelling, blue: unlabelled tissue, purple: artefacts, black: non-specific labelling, yellow: background). The pixel classification workflow is able to differentiate labelling and artefacts such as marks on the coverslip and debris (see arrows). Panels **(E,F)** show the output of the object classification workflow: the probability maps derived from the pixel classification workflow were thresholded at 0.4 for the channel representing the labelling, and classified into two classes based on object-level features such as size and shape (red: β-amyloid plaques, blue: non-specific labelling). Panels **(G,H)** show the object classification output with the blue channel removed to visualize the β-amyloid plaques only. Images **(A,C,E,G)** are displayed at the same magnification with the scale bar representing 1 mm. The scale bar for figures **(B,D,F,H)** represents 500 μm.

Chicago, IL, USA) with a sampling grid of 300 μm × 300 μm, a counting frame of 200 μm × 200 μm, and a 20 μm point spacing. The settings were selected with reference to the literature (Tucker et al., 2008; Liu et al., 2017; Wagner et al., 2017). Points within the section contours that overlapped the hAPP immunoreactive plaques were marked as positive; with all remaining points marked as negative. hAPP plaque load was calculated by the software with respect to the magnification. The 30 section subset included the five sections for which ground truth measurements were available, allowing comparison of three methods for the five section subset.

Validation of the Atlas Delineations

To validate the atlas delineations derived from the *QuickNII* software, we compared the plaque loads for five sections in three anatomical brain regions delineated by two alternative methods. The comparisons were performed on section images that were immunohistochemically labelled for hAPP (1D1 antibody) and restricted to clearly visible plaques (we excluded neuronal hAPP labelling). For the first delineation method, five section images were segmented to extract labelled plaques with the *ilastik* method. The segmentations were then visualised on top of the original images, and the cortex, olfactory region and hippocampus manually delineated with the *NIH ImageJ* tool with guidance from the Franklin and Paxinos mouse brain atlas version 3 (Franklin and Paxinos, 2008). The *Analyse* function in *NIH ImageJ* was used to quantify hAPP plaques in the delineated regions for each brain section. Brain region-specific hAPP load was calculated by dividing the area occupied by hAPP labelling within the selected brain region by the total area occupied by the brain region. For the second method, the same five segmentations were processed with the QUINT workflow with the delineations derived from the *QuickNII* atlas maps. The hAPP loads were extracted for the cortex, olfactory region and hippocampus for the five sections from the output reports.

RESULTS

Workflow Description

We present the QUINT workflow for quantification and spatial analysis of features in large series of labelled mouse or rat brain sections (**Figure 1**). The different steps are indicated below:

1. Image pre-processing (change the contrast, resolution, file type) with the *Transform* feature in the *Nutil* software
2. Registration of sections to reference atlas space using the *QuickNII software* to generate atlas maps adapted to the orientation of the images
3. Segmentation of the labelling with the *ilastik* image analysis software using two classifiers
4. Data analysis with the *Quantifier* feature in the *Nutil* software (combines the segmentation results with input from the atlas maps to give a list of individual plaque features, region level features and whole brain features, enabling quantitative regional analysis).

The procedures used in all steps (*a to d*) are detailed in the "Materials and Methods" section. Image pre-processing: (a) is necessary in order to produce copies of the images that are suitable for each tool in the workflow. The registration of the sections; (b) to the Allen Mouse Brain Atlas (© 2004 Allen Institute for Brain Science. Allen Mouse Brain Atlas, Available from: http://download.alleninstitute.org/informatics-archive/current-release/mouse_ccf/annotation/ccf_2015/;

Lein et al., 2007; Oh et al., 2014) is performed with the *QuickNII* tool (Puchades et al., 2019). Briefly, as illustrated in **Figure 2**, image series are uploaded to the software and visualised with reference atlas overlays that have adjustable transparency. A few sections with highly distinguishable landmarks are selected for adjusting the dorso-ventral and the medio-lateral angles of the atlas in order to match the cutting angles of the brain sections. Once these sections are registered to the atlas, the software automatically propagates the spatial information to the rest of the image series. After a rapid overview of the registration results and eventual minor positional adjustments, atlas maps corresponding to each image are exported. These atlas maps are used for the region-based analysis of the labelled features.

The next step (c) consists of segmentation of the labelled features present in the brain sections (**Figures 3A,B**). In the first *ilastik* step, a subset of the image series is used to train the classifier with the pixel classification workflow (**Figures 3C,D**). The user defines classes based on intensity, edge and texture and annotates a few example pixels of each class. The second *ilastik* step, object classification, is used for the removal of artefacts (**Figures 3E,F**). The resulting segmentations identify the plaques in a colour with a unique RGB colour code (**Figures 3G,H**).

In the last step (d), the *Quantifier* feature in *Nutil* enables quantitative regional analysis of labelling based on the segmentations and corresponding atlas maps. The software is simple to run, requiring no specialist computing or programming knowledge. The user specifies the path to the input and output directories in a simple Microsoft Excel template titled *Quantifier* (the input directories should contain the segmentations and the atlas maps), in addition to entering analysis parameters. The necessary input parameters are the pixel scale (area represented by one pixel in the segmentations), and the minimum and maximum object size cut-offs. The template is then uploaded to the *Nutil* software, which drawn on the information in the template to perform the analysis. The output files are automatically saved to the specified output directory and consist of quantitative reports with variables such as number of objects and surface area of objects per region. Text files listing the xyz coordinates of each segmented pixel in reference atlas space are also generated for viewing with the *Meshview* atlas viewer (provided *via* the MediaWiki link at https://www.nitrc.org/projects/meshview). *Nutil* also generates customised atlas images with the segmented objects superimposed providing an overview of the objects per atlas region.

Validation of Object Segmentation

As accurate segmentation of the labelled objects is important for a valid quantitative result, we decided to compare our results with three different methods. The segmentations generated with *ilastik* were compared to manual delineation of labelled objects by an expert in the field (five sections), and to measurements obtained with a stereological method (30 sections). The hAPP labelled series was selected for the validation. The *ilastik* segmentations gave hAPP load estimates that were similar to the stereological estimates, and that represented the outputs from manual object delineations for the five sections for which manual object delineations were available (error of *ilastik* estimates relative to manual object delineations: mean −0.06% with a SD of 0.09%; error of stereological estimate relative to manual object delineations: mean −0.05% with a SD of 0.11%; see **Figure 4A**).

For the 30 sections, the mean error of the hAPP loads from the *ilastik* method relative to the stereological method was 2.79×10^{-3}% with a SD of 0.16% (see **Figure 4B**). To summarise, this means that for this image series, the *ilastik* method allows the user to establish the plaque load (restricted to hAPP labelled plaques) with 95% confidence to within an error of ±0.32%. As described in the results, the plaque load variations detected from section to section and between brain regions were of a much greater magnitude than this error, indicating that the *ilastik* method is suitable for detecting these differences.

Validation of Anatomical Delineations From QuickNII

In a separate study, to validate the accuracy of the atlas delineations from *QuickNII*, we compared the hAPP loads from the QUINT workflow to loads calculated based on manual delineations of three brain regions for five sections (cortex, olfactory region and hippocampus; **Figure 5**). The *QuickNII* delineations gave hAPP loads that were representative of the loads from the manual delineations for all the sections and brain regions that were investigated (**Figures 5E–G**). Overall, the QUINT workflow slightly underestimated the hAPP loads relative to the manual method for all the explored brain regions (deviation of the workflow derived cortical hAPP load from the manual method: mean of −0.11% with SD of 0.07%; deviation of workflow derived olfactory hAPP load from manual method: mean of −0.21% with SD of 0.23%; mean and SD are not provided for the hippocampus as only two sections contained this region).

Use Case Analysis

The QUINT workflow was used to analyse and compare three consecutive series labelled for hAPP (1D1), pan-Aβ (4G8) and pE-Aβ (J8) in one Tg2576 mouse model for Alzheimer's disease. Each series were composed of approximately 60 sections extending from the olfactory lobes to the cerebrum (the cerebellum was not included). All three series were registered to the Allen Mouse Brain Atlas (© 2004 Allen Institute for Brain Science. Allen Mouse Brain Atlas, Available from: http://download.alleninstitute.org/informatics-archive/current-release/mouse_ccf/annotation/ccf_2015/) using *QuickNII*. The section images can be viewed with custom atlas overlays adjusted for angle deviations (**Supplementary Data Sheet 1**).

Labelled plaques were segmented and quantified using the QUINT workflow as represented in **Figures 6**, **7**. Plaques were found mainly in the olfactory regions (1.5–2.5%), the neocortex (1–1.5%), the hippocampal region (1–1.5%) and white matter tracts (0.5%; **Figure 6G**). The plaque burden was lower in the striatum, thalamic regions and midbrain (less than 0.5%). All Aβ and APP species co-localised in the

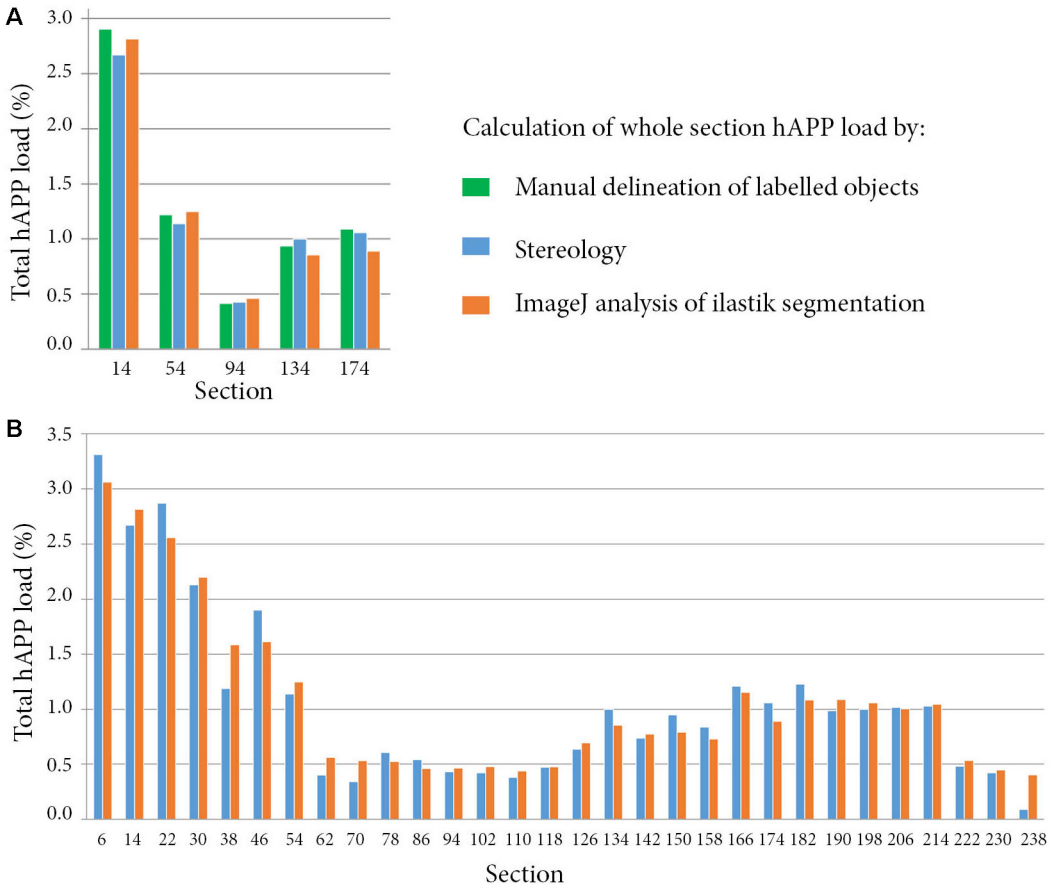

FIGURE 4 | Comparison of whole section human amyloid precursor protein (hAPP) load outputs from three alternative quantitative methods. For all the methods, the whole section hAPP load was calculated by dividing the area occupied by hAPP labelling by the total section area. Calculations were restricted to plaques that were immuno-labelled with the hAPP antibody (1D1). Panel **(A)** compares hAPP load outputs from three alternative methods for five sections. The methods include expert manual delineation of hAPP labelled objects (green), stereological estimate with the area fraction fractionator probe (blue), and quantification with NIH *ImageJ* based on the *ilastik* segmentations (orange). Panel **(B)** compares hAPP load outputs from the stereological method and from the segmentations for thirty whole brain sections that were regularly spaced and spanned the full volume of the brain.

same regions, with small differences, as seen in **Figures 6A–C**. The customised atlas images superimposed with colour-coded objects are found in the **Supplementary Material**. The size of plaques and their distribution in the whole series is illustrated in **Figure 8**. The pE-Aβ positive plaques were more numerous but much smaller in size than plaques labelled for hAPP or pan-Aβ labelled with 4G8 (**Figure 7**). As we were interested to detect subregion expression differences in the hippocampus, we refined the analysis to smaller brain regions. As demonstrated in **Figure 7**, the subiculum showed more hAPP and pan-Aβ labelling than the entorhinal cortex (EC), the cornu ammonis (CA) region of the hippocampus and the dentate gyrus (DG), whereas the subregion with highest pE-Aβ labelling was the EC.

Our workflow is demonstrated here on brain section images from one animal only, with analysis restricted to hAPP and Aβ plaques. However, the QUINT workflow can also be applied to other types of labelling like cell somas, as demonstrated by the quantification and spatial analysis of parvalbumin positive cells from an Allen mouse brain *in situ* hybridisation experiment shared through the HBP platform: DOI: 10.25493/6DYS-M3W (Yates and Puchades, 2019).

DISCUSSION

In this report, we present a new workflow for analysis of labelling in brain-wide image series. The QUINT workflow builds on newly developed tools and resources for brain atlasing and segmentation, and consists of three main steps. In the first step, *QuickNII* (Puchades et al., 2019) is used to generate customised atlas maps corresponding to experimental brain sections for mice, using the Allen Mouse Brain Atlas (© 2004 Allen Institute for Brain Science. Allen Mouse Brain Atlas, Available from: http://download.alleninstitute.org/informatics-archive/current-release/mouse_ccf/; Lein et al., 2007; Oh et al., 2014), and for rats using the Waxholm rat brain atlas version 2.0 (Papp et al., 2014; Kjonigsen et al., 2015). In the second step, the machine learning-based image analysis tool, *ilastik*, is used

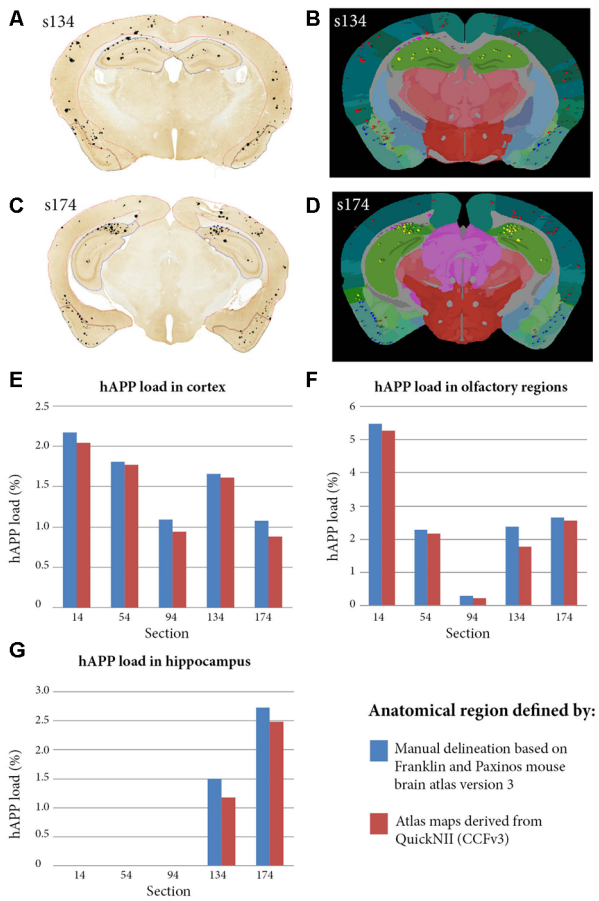

FIGURE 5 | Comparison of hAPP load outputs in three anatomical brain regions defined by two alternative anatomical delineation methods. Brain region-specific hAPP load was calculated by dividing the area occupied by hAPP labelling within the selected brain region, by the total area occupied by the brain region. The calculations were restricted to plaques that were immuno-labelled with the hAPP antibody (1D1). For the first method, five brain section images were segmented with *ilastik* and visualised on top of the sections to allow manual delineation of brain regions. The cortex, olfactory region and hippocampus were delineated with *NIH ImageJ* with guidance from the Franklin and Paxinos mouse brain atlas version 3 (panels **A,C** show the cortex, olfactory region and hippocampus delineated in red, blue and yellow in section s134 and s174 respectively). The analyse function in NIH *Image J* was used to quantify hAPP load in the delineated regions. For the second method, the five segmentations were processed with the QUINT workflow with input from the *QuickNII* derived atlas maps (panels **B,D** show examples for s134 and s174 respectively). hAPP loads were extracted for the cortex, olfactory region and hippocampus from the output reports. Panels **(E–G)** compare hAPP loads in the cortex, olfactory regions and hippocampus respectively for the five sections, with the loads calculated by the two alternative methods described.

to segment the objects of interest from the immunolabelled images. In the final step, *Nutil* is used to combine the customised atlas maps and segmented images and to extract and quantify objects in each parcellated brain region for each section and for the whole image series. The tools allow users to perform analyses at different levels, and to customise the granularity of such analyses. Furthermore, *Nutil* supports the extraction of spatial coordinates for each segmented object for viewing in the MeshView brain atlas viewer (AMBA version 3 2015, available at www.nitrc.org/projects/meshview *via* the MediaWiki link). The QUINT workflow is also compatible with segmentations generated with other image analysis software, so users are not restricted to using *ilastik* for segmentation.

As a proof of concept, and to further characterise the amyloid expression in the Tg2576 Alzheimer mouse model, the workflow was applied to three series labelled with antibodies against the hAPP N-terminus (1D1), pan-Aβ (4G8) and pE-Aβ (J8). Our results show a plaque load of 1–3% depending on the brain region, and are in accordance with other studies (Schilling et al., 2008; Liu et al., 2017). When analysing the plaque load in more detailed brain regions, we were able to detect subregional differences. This was particularly true of the hippocampal regions where we detected the highest load for hAPP and pan-Aβ in the subiculum, compared to pE-Aβ that had more prominent labelling in the entorhinal cortex. This subregional difference could be of relevance to the pathophysiology and may be related to the expression of the enzyme that catalyses pE-Aβ formation (Hartlage-Rübsamen et al., 2009). Studies indicate that this protein might influence or even seed the aggregation of other amyloid peptide species (Schilling et al., 2006; Schlenzig et al., 2009; Nussbaum et al., 2012), and so it is interesting to observe its localisation from a mechanistic point of view. Our workflow allows comparison of the expression of different proteins across brain regions for any region defined in the Allen Mouse Brain Atlas, potentially highlighting associations that would otherwise remain undetected.

We conducted a validation study of the workflow in two parts, with the first exploring how well the outputs from the *ilastik* segmentations corresponded to outputs from two alternative quantitative methods. The alternative methods included manual delineation of labelled objects, which was performed on five sections that were regularly spaced thoughout the whole brain, and a stereological method that was applied to thirty sections (half of the full dataset).

For all the sections, the segmentations gave plaque load estimates that were similar to the outputs from the other two methods, with the *ilastik* method establishing the plaque load with 95% confidence to within an error of ±0.32% of the stereological output. In other words, the *ilastik* method was as good at detecting the absolute plaque load per section as the stereological method in this mouse. The absolute error rate could be reduced further by introducing a manual adjustment step to remove false-positive labelling from the segmentations. However, even without this manual adjustment, the method is sensitive enough to detect the significant differences in plaque expression that are seen between different sections. A known challenge for the stereological evaluation was the sparse distribution of the plaques throughout the brain, and the concentration of the plaques in the frontal regions, which could at least partially account for the discrepancy between the stereological outputs and the outputs from the manual object delineations. As suggested by Boyce and Gundersen (Boyce and Gundersen, 2018), the classic fractionator approaches that rely on systematic random sampling are highly inefficient and

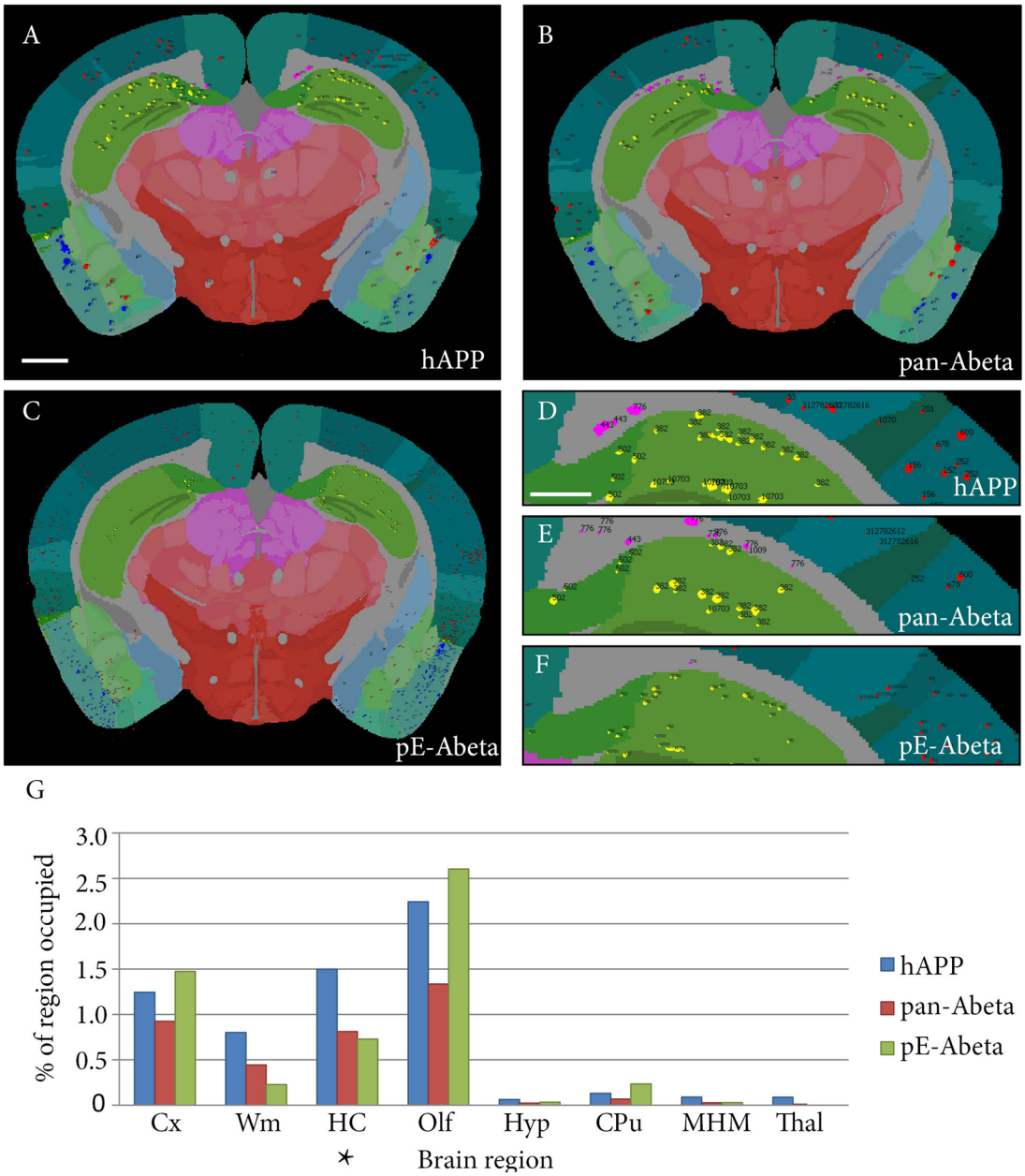

FIGURE 6 | Whole brain comparative analysis of three series labelled for hAPP, pE-Aβ and pan-Aβ in a Tg 2576 Mouse. Examples of Nutil image output (segmentations superimposed on the atlas maps) for the hAPP **(A,D)**, pan-Aβ **(B,E)** and pE-Aβ series **(C,F)**. The segmented object colours represent their anatomical location: isocortex (red); hippocampus (yellow); white matter tracts (pink); olfactory regions (blue); caudate putamen (CPu; black). Panel **(G)** shows the comparative quantification results for the whole brain for the three series (the blue, red and green bars represent hAPP, pan-Aβ and pE-Aβ labelling respectively). The abbreviations in the graph represent the following brain regions: isocortex (Cx); white matter tracts (Wm); hippocampal region (HC); olfactory regions (Olf); hypothalamus (Hyp); CPu; midbrain, hind brain and medulla (MHM); thalamus (Thal). Images **(A–C)** are displayed at the same magnification with the scale bar representing 1 mm. The scale bar for figures **(D–F)** represents 500 μm. The asterisk in panel **(G)** indicates the region represented in **Figure 7**.

impractical for sparse labelling. However, by increasing the sampling frequency in our stereological analysis, we obtained results very close to the manual delineation of objects.

As demonstrated there are clear advantages to a segmentation based workflow. However, segmentation also introduces some limiting factors. One limitation is that it imposes restrictions on the resolution of the images that can be used as input. In the examples shown here, we segment relatively large objects (plaques) and therefore had the option to downscale the raw images to speed up the analysis, while still achieving good quantification of labelling (*ilastik* has an upper image size limit). However, when segmenting smaller protein aggregates, such as

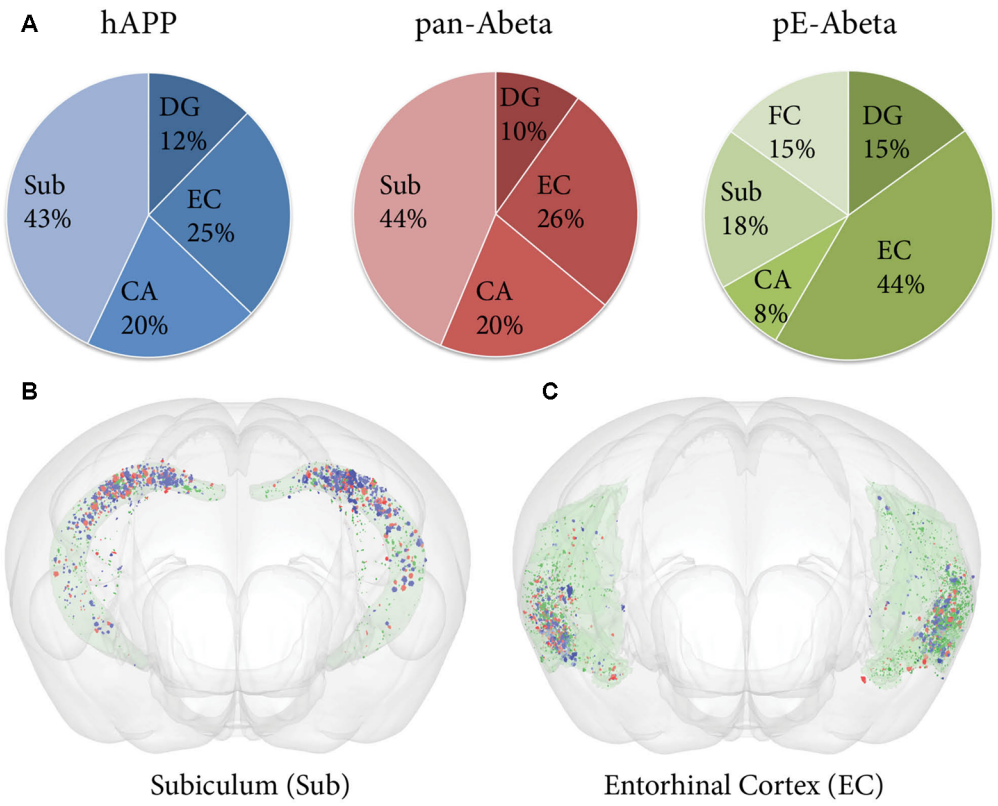

FIGURE 7 | Comparative analysis of hAPP, pE-Aβ and pan-Aβ labelling in the hippocampus of a Tg 2576 mouse. **(A)** The pie charts show the percentage of the total labelling of hAPP (blue chart), pan-Aβ (red chart) and pE-Aβ (green chart) in the hippocampus expressed in the subiculum (Sub), dentate gyrus (DG), entorhinal cortex (EC), cornu ammonis (CA) and fasciola cinereum (FC; **B,C**). The expression differences are visualised for the subiculum and the EC with the MeshView atlas viewer (the regions are shown in pale green with the Nutil output from the three series covisualised, with objects labelled for hAPP, pan-Aβ and pE-Aβ in blue, red and dark green respectively). Both the pie charts and the brain images reveal spatial expression differences for the three markers in the hippocampus.

nuclear Huntingtin (not shown), downsizing is not an option. In this case, the images would first have to be split into high resolution tiles, in order to perform the segmentation, and then retiled prior to analysis. Furthermore, as explained in the methods part, the size of the object (number of pixels) has an impact on the segmentation quality as there are restrictions on the pixel scales of the features that can be included in the *ilastik* algorithm (scale up to 10 pixels for intensity, edge and texture in the *ilastik* version used here). A test run with some representative images of different sizes is therefore recommended to determine the optimal image resolution for segmentation. Alternatively, another software or analysis approach could be used to generate the segmentations. The workflow is compatible with segmentations from other image analysis software as long as they comply with the *Nutil* input requirement (segmentations must be 24-bit colour images in PNG format). Users are therefore not restricted to *ilastik* for segmentation.

In the second part of the validation study, we tested the accuracy of region-based quantification by comparing the plaque load outputs from the QUINT workflow to loads determined by atlas delineations that were manually applied for three regions (cortex, olfactory region and hippocampus) on five sections. We demonstrate that the QUINT workflow is able to detect the regional expression differences seen at this level of granularity for this image series. In this particular case, we found that the workflow slightly underestimated the real plaque load. Closer inspection of the *QuickNII* atlas maps for the selected sections showed that the anatomical location of a minority of the plaques were incorrectly assigned. For example, some of the hippocampal plaques were incorrectly assigned to the corpus callosum. Indeed, the accuracy of the workflow for region-based quantification is entirely dependent on the accuracy of overlap between the experimental section and the corresponding atlas map. Currently, we have to adapt the image registration of the *QuickNII* tool from a global fit (whole slide) to a more local fit when we want to analyse specific regions of the brain more precisely (this is particularly relevant for the analysis of smaller regions). However, this limitation would be circumvented if *QuickNII* supported non-linear registration of the image sections to the atlas, and this is planned for implementation in a future release.

One of the main advantages of the QUINT workflow for quantification is that it uses a reference atlas to delineate the regions, allowing studies on brain regions that are not usually explored. As most stereological studies require the experimenter to manually delineate the region of analysis, some regions with

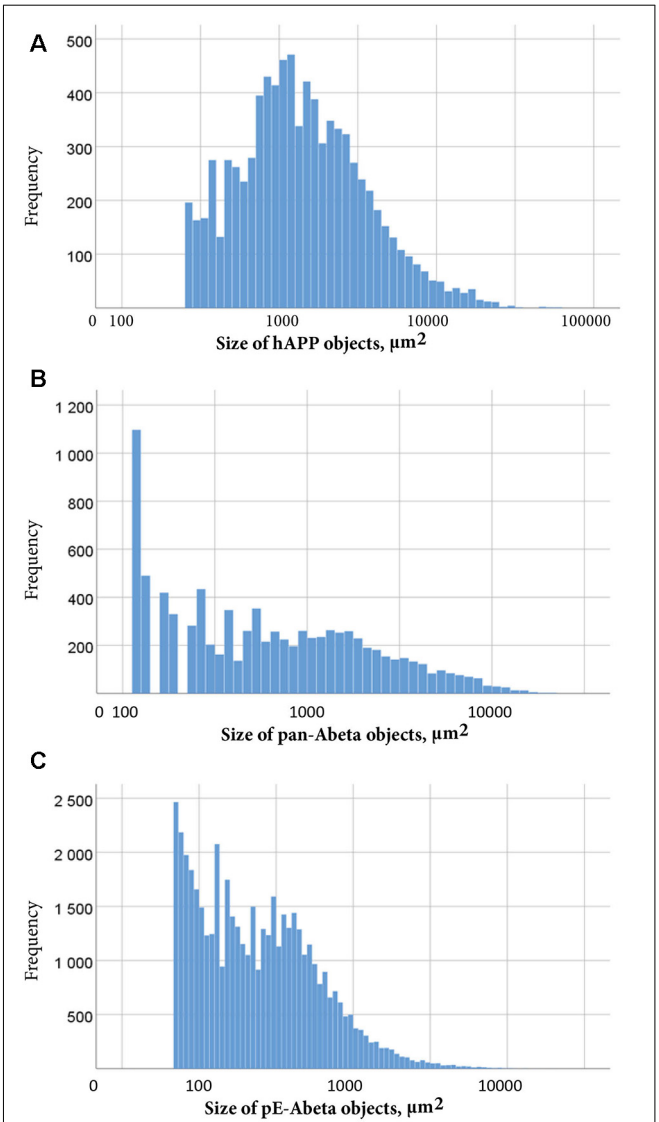

FIGURE 8 | Size distribution of objects labelled for hAPP **(A)**, pan-Aβ **(B)** and pE-Aβ **(C)** in a whole T2576 mouse brain series. Object size in μm^2 is represented on the x-axis on a common logarithmic scale with frequency on the y-axis. To remove false positive objects, minimum object size cut-offs of 258 μm^2, 112 μm^2 and 56 μm^2 were applied to the hAPP **(A)**, pan-Aβ **(B)** and pE-Aβ **(C)** series, respectively.

very few visible landmarks (i.e., thalamus or olfactory bulb) are typically not included in these studies. More importantly, as rodent reference atlas delineations are improved and extended, scientists will be able to conduct even more targeted studies enabling detailed mapping of subregional expression differences. By registering many datasets to the same reference atlas, the data are made more comparable and interoperable (Bjerke et al., 2018), increasing the likelihood for reuse. Importantly, our method relies on histological sections, without a need for block-face images.

The whole workflow is rapid, user-friendly and does not necessitate coding aptitudes as is often the case for similar image analysis software (Vandenberghe et al., 2016; Fürth et al., 2018; Xiong et al., 2018). The optimal dataset for the workflow would include images of undistorted whole brain tissue sections spanning the full volume and with clearly distinguishable features. We do not recommend the workflow for sections with major tissue distortions as no correction in QuickNII can compensate for this. Sections representing only one hemisphere will also lead to higher uncertainty, as it is not possible to determine the mediolateral cutting angle without assessing the appearance of landmarks in both the right and left hemisphere. This is also true for incomplete sections in which major parts of the brain are missing. There are, however, other types of limitations that the workflow can overcome. For example, non-specific labelling can be filtered out with the Object Classification workflow, and sections with tissue distortions may benefit from a local anchoring approach. Introducing corrections for limitations of these kinds may, however, increase the processing time or marginally increase the error rate.

The workflow is intended to enable more efficient and comprehensive analysis than is currently possible with traditional tools, but does not compensate for a lack of anatomical or biological expertise on the part of the researcher. Both the output of the segmentation and registration steps should be validated by visual inspection prior to quantification, and interpretations must be made in light of limitations. A complete analysis of a set of images such as those analysed here (approximately 60 images of sections of average quality) takes less than 24 h. The atlas registration can be done in 2–3 h, with the segmentation taking from 1 to 2 h depending on the image size, and the analysis with *Nutil* being very quick (less than 30 min). In conclusion, we believe that this workflow will enable large scale studies and the integration of results from many studies in different laboratories.

DATA AVAILABILITY STATEMENT

The datasets generated for this study are available on request to the corresponding author.

ETHICS STATEMENT

All experiments were performed according to ethical guidelines (License number T28/16 of the Landesdirektion Sachsen, Germany).

AUTHOR CONTRIBUTIONS

SY performed *ilastik* and *Nutil* analyses, performed the validation studies, contributed to the development of the *Nutil* software and contributed to writing the article. NG created the *Nutil* software, contributed to the writing of the technical parts of the article and to the design of the validation studies. CC contributed to the development of workflows and validation studies. SL, P-HK, H-UD, MH-R and SR provided animal tissue and antibodies used in the use-case, and contributed to writing the article. TL contributed to the development of workflows and to writing the article. AK contributed with *ilastik* software support. MP conceived the study, supervised the analysis and

the development of software tools, performed file pre-processing and *QuickNII* registrations and coordinated the writing of the article. JB conceived the study, supervised development of software tools, contributed with infrastructure, and contributed to writing of the article. All the authors reviewed and approved the manuscript.

FUNDING

This work was supported by the Norwegian research council within the European Union Joint Program for Neurodegenerative Disease (JPND) Research Project CrossSeeds Grant 247995 (to JB). The tools development received support from the European Union's Horizon 2020 Framework Programme for Research and Innovation under the Specific Grant Agreement No. 720270 (HBP SGA1) and Specific Grant Agreement No. 785907 (HBP SGA2; to JB). This work was supported by the Deutsche Forschungsgemeinschaft (German Research Foundation) within the framework of the Munich Cluster for Systems Neurology (EXC 2145 SyNergy project ID 390857198; to SL). Aspects of this work were supported by the German Federal Department of Education, Science, and Technology, Bundesministerium für Bildung und Forschung (BMBF; grant #01ED1501B to SR) within the European Union Joint Program for Neurodegenerative Disease (JPND) Research, Project CrossSeeds, and by the Alzheimer Forschungsinitiative e.V. (AFI #16004) to SR. Aspects of this work were supported by the German Federal Department of Education, Science, and Technology, BMBF (grant #01ED1501A to H-UD) within the European Union Joint Program for Neurodegenerative Disease (JPND) Research, Project CrossSeeds.

ACKNOWLEDGMENTS

We thank Gergely Csucs and Dominik Kutra for expert technical assistance. We also thank Martin Øvsthus, Heidi Kleven and Camilla Blixhavn for assistance with *QuickNII* registrations. Histological section images were acquired at the Norbrain Slidescanning Facility at the Institute of Basic Medical Sciences, University of Oslo. We thank Hong Qu for assistance with the scanning of the images.

SUPPORTING INFORMATION

A folder containing the customised atlas maps can be found online. The **Supplementary File S1**, contains a Table with overview of the different software as well as links to a viewer for raw data inspection.

SUPPLEMENTARY MATERIAL

The Supplementary Material for this article can be found online at: https://www.frontiersin.org/article/10.3389/fninf.2019.00075/full#supplementary-material.

REFERENCES

Berg, S., Kutra, D., Kroeger, T., Straehle, C. N., Kausler, B. X., Haubold, C., et al. (2019). ilastik:interactive machine learning for (bio) image analysis. *Nat. Methods* doi: 10.1038/s41592-019-0582-9

Bjerke, I. E., Ovsthus, M., Papp, E. A., Yates, S. C., Silvestri, L., Fiorilli, J., et al. (2018). Data integration through brain atlasing: human brain project tools and strategies. *Eur. Psychiatry* 50, 70–76. doi: 10.1016/j.eurpsy.2018.02.004

Boline, J., Lee, E. F., and Toga, A. W. (2008). Digital atlases as a framework for data sharing. *Front. Neurosci.* 2, 100–106. doi: 10.3389/neuro.01.012.2008

Boyce, R. W., and Gundersen, H. J. G. (2018). The automatic proportionator estimator is highly efficient for estimation of total number of sparse cell populations. *Front. Neuroanat.* 12:19. doi: 10.3389/fnana.2018.00019

Dawson, T. M., Golde, T. E., and Lagier-Tourenne, C. (2018). Animal models of neurodegenerative diseases. *Nat. Neurosci.* 21, 1370–1379. doi: 10.1038/s41593-018-0236-8

Franklin, K. B. J., and Paxinos, G. (2008). *The Mouse Brain in Stereotaxic Coordinates.* Amsterdam, London: Elsevier.

Fürth, D., Vaissière, T., Tzortzi, O., Xuan, Y., Martin, A., Lazaridis, I., et al. (2018). An interactive framework for whole-brain maps at cellular resolution. *Nat. Neurosci.* 21, 139–149. doi: 10.1038/s41593-017-0027-7

Hartlage-Rübsamen, M., Bluhm, A., Piechotta, A., Linnert, M., Rahfeld, J. U., Demuth, H. U., et al. (2018). Immunohistochemical evidence from APP-transgenic mice for glutaminyl cyclase as drug target to diminish pE-aβ formation. *Molecules* 23:E924. doi: 10.3390/molecules23040924

Hartlage-Rübsamen, M., Staffa, K., Waniek, A., Wermann, M., Hoffmann, T., Cynis, H., et al. (2009). Developmental expression and subcellular localization of glutaminyl cyclase in mouse brain. *Int. J. Dev. Neurosci.* 27, 825–835. doi: 10.1016/j.ijdevneu.2009.08.007

Hawrylycz, M., Baldock, R. A., Burger, A., Hashikawa, T., Johnson, G. A., Martone, M., et al. (2011). Digital atlasing and standardization in the mouse brain. *PLoS Comput. Biol.* 7:e1001065. doi: 10.1371/journal.pcbi.1001065

Höfling, C., Morawski, M., Zeitschel, U., Zanier, E. R., Moschke, K., Serdaroglu, A., et al. (2016). Differential transgene expression patterns in Alzheimer mouse models revealed by novel human amyloid precursor protein-specific antibodies. *Aging Cell* 15, 953–963. doi: 10.1111/acel.12508

Hsiao, K., Chapman, P., Nilsen, S., Eckman, C., Harigaya, Y., Younkin, S., et al. (1996). Correlative memory deficits, Aβ elevation and amyloid plaques in transgenic mice. *Science* 274, 99–102. doi: 10.1126/science.274.5284.99

Hurtado, D. E., Molina-Porcel, L., Iba, M., Aboagye, A. K., Paul, S. M., Trojanowski, J. Q., et al. (2010). Aβ accelerates the spatiotemporal progression of tau pathology and augments tau amyloidosis in an Alzheimer mouse model. *Am. J. Pathol.* 177, 1977–1988. doi: 10.2353/ajpath.2010.100346

Kim, Y., Yang, G. R., Pradhan, K., Venkataraju, K. U., Bota, M., Garcia Del Molino, L. C., et al. (2017). Brain-wide maps reveal stereotyped cell-type-based cortical architecture and subcortical sexual dimorphism. *Cell* 171, 456.e422–469.e422. doi: 10.1016/j.cell.2017.09.020

Kjonigsen, L. J., Lillehaug, S., Bjaalie, J. G., Witter, M. P., and Leergaard, T. B. (2015). Waxholm space atlas of the rat brain hippocampal region: three-dimensional delineations based on magnetic resonance and diffusion tensor imaging. *Neuroimage* 108, 441–449. doi: 10.1016/j.neuroimage.2014.12.080

Kopec, C. D., Bowers, A. C., Pai, S., and Brody, C. D. (2011). Semi-automated atlas-based analysis of brain histological sections. *J. Neurosci. Methods* 196, 12–19. doi: 10.1016/j.jneumeth.2010.12.007

Lein, E. S., Hawrylycz, M. J., Ao, N., Ayres, M., Bensinger, A., Bernard, A., et al. (2007). Genome-wide atlas of gene expression in the adult mouse brain. *Nature* 445, 168–176. doi: 10.1038/nature05453

Liu, P., Reichl, J. H., Rao, E. R., McNellis, B. M., Huang, E. S., Hemmy, L. S., et al. (2017). Quantitative comparison of dense-core amyloid plaque accumulation in amyloid-β protein precursor transgenic mice. *J. Alzheimers Dis.* 56, 743–761. doi: 10.3233/JAD-161027

Nussbaum, J. M., Schilling, S., Cynis, H., Silva, A., Swanson, E., Wangsanut, T., et al. (2012). Prion-like behaviour and tau-dependent cytotoxicity of pyroglutamylated amyloid-β. *Nature* 485, 651–655. doi: 10.1038/nature 11060

Oh, S. W., Harris, J. A., Ng, L., Winslow, B., Cain, N., Mihalas, S., et al. (2014). A mesoscale connectome of the mouse brain. *Nature* 508, 207–214. doi: 10.1038/nature13186.

Pallast, N., Wieters, F., Fink, G. R., and Aswendt, M. (2019). Atlas-based imaging data analysis tool for quantitative mouse brain histology (AIDAhisto). *J. Neurosci. Methods* 326:108394. doi: 10.1016/j.jneumeth.2019.108394

Papp, E. A., Leergaard, T. B., Calabrese, E., Johnson, G. A., and Bjaalie, J. G. (2014). Waxholm space atlas of the Sprague–Dawley rat brain. *Neuroimage* 97, 374–386. doi: 10.1016/j.neuroimage.2014.04.001

Puchades, M. A., Csucs, G., Ledergerber, D., Leergaard, T. B., and Bjaalie, J. G. (2019). Spatial registration of serial microscopic brain images to three-dimensional reference atlases with the *QuickNII* tool. *PLoS One* 14:e0216796. doi: 10.1371/journal.pone.0216796

Schilling, S., Lauber, T., Schaupp, M., Manhart, S., Scheel, E., Bohm, G., et al. (2006). On the seeding and oligomerization of pGlu-amyloid peptides (*in vitro*). *Biochemistry* 45, 12393–12399. doi: 10.1021/bi0612667

Schilling, S., Zeitschel, U., Hoffmann, T., Heiser, U., Francke, M., Kehlen, A., et al. (2008). Glutaminyl cyclase inhibition attenuates pyroglutamate Aβ and Alzheimer's disease-like pathology. *Nat. Med.* 14, 1106–1111. doi: 10.1038/nm. 1872

Schlenzig, D., Manhart, S., Cinar, Y., Kleinschmidt, M., Hause, G., Willbold, D., et al. (2009). Pyroglutamate formation influences solubility and amyloidogenicity of amyloid peptides. *Biochemistry* 48, 7072–7078. doi: 10.1021/bi900818a

Schmitz, C., and Hof, P. R. (2005). Design-based stereology in neuroscience. *Neuroscience* 130, 813–831. doi: 10.1016/j.neuroscience.2004. 08.050

Schneider, C. A., Rasband, W. S., and Eliceiri, K. W. (2012). NIH Image to ImageJ: 25 years of image analysis. *Nat. Methods* 9, 671–675. doi: 10.1038/ nmeth.2089

Simmons, D. M., and Swanson, L. W. (2009). Comparing histological data from different brains: sources of error and strategies for minimizing them. *Brain Res. Rev.* 60, 349–367. doi: 10.1016/j.brainresrev.2009.02.002

Thal, D. R., Rub, U., Orantes, M., and Braak, H. (2002). Phases of Aβ-deposition in the human brain and its relevance for the development of AD. *Neurology* 58, 1791–1800. doi: 10.1212/wnl.58.12.1791

Tucker, S. M., Borchelt, D. R., and Troncoso, J. C. (2008). Limited clearance of pre-existing amyloid plaques after intracerebral injection of Aβ antibodies in two mouse models of Alzheimer disease. *J. Neuropathol. Exp. Neurol.* 67, 30–40. doi: 10.1097/nen.0b013e31815f38d2

Vandenberghe, M. E., Herard, A. S., Souedet, N., Sadouni, E., Santin, M. D., Briet, D., et al. (2016). High-throughput 3D whole-brain quantitative histopathology in rodents. *Sci. Rep.* 6:20958. doi: 10.1038/srep20958

Wagner, L. K., Gilling, K. E., Schormann, E., Kloetzel, P. M., Heppner, F. L., Kruger, E., et al. (2017). Immunoproteasome deficiency alters microglial cytokine response and improves cognitive deficits in Alzheimer's disease-like APPPS1 mice. *Acta Neuropathol. Commun.* 5:52. doi: 10.1186/s40478-017-0453-5

Xiong, J., Ren, J., Luo, L., and Horowitz, M. (2018). Mapping histological slice sequences to the allen mouse brain atlas without 3D reconstruction. *Front. Neuroinform.* 12:93. doi: 10.3389/fninf.2018.00093

Yates, S. C., and Puchades, M. A. (2019). Extraction of parvalbumin positive cells from an Allen mouse brain *in situ* hybridisation experiment [Data set]. *Hum. Brain Proj. Neuroinformatics Platform* doi: 10.25493/6DYS-M3W

Zaslavsky, I., Baldock, R. A., and Boline, J. (2014). Cyberinfrastructure for the digital brain: spatial standards for integrating rodent brain atlases. *Front. Neuroinform.* 8:74. doi: 10.3389/fninf.2014.00074

Conflict of Interest: The authors declare that the research was conducted in the absence of any commercial or financial relationships that could be construed as a potential conflict of interest.

frontiers in Neuroinformatics

ORIGINAL RESEARCH
published: 10 December 2019
doi: 10.3389/fninf.2019.00072

Identifying Vulnerable Brain Networks in Mouse Models of Genetic Risk Factors for Late Onset Alzheimer's Disease

Alexandra Badea[1,2,3†], Wenlin Wu[4†], Jordan Shuff[5], Michele Wang[6], Robert J. Anderson[1], Yi Qi[1], G. Allan Johnson[1], Joan G. Wilson[2], Serge Koudoro[7], Eleftherios Garyfallidis[7], Carol A. Colton[2‡] and David B. Dunson[8‡]*

[1] Department of Radiology, Duke University, Durham, NC, United States, [2] Department of Neurology, Duke University School of Medicine, Durham, NC, United States, [3] Brain Imaging and Analysis Center, Duke University, Durham, NC, United States, [4] Pratt School of Engineering, Duke University, Durham, NC, United States, [5] Department of Biomedical Engineering, University of Delaware, Newark, NJ, United States, [6] Department of Psychology and Neuroscience, Trinity College of Arts & Sciences, Duke University, Durham, NC, United States, [7] School of Informatics, Computing, and Engineering, Indiana University Bloomington, Bloomington, IN, United States, [8] Department of Statistical Science, Trinity College of Arts & Sciences, Duke University, Durham, NC, United States

OPEN ACCESS

Edited by:
Emmanuel L. Barbier, Institut National de la Santé et de la Recherche Médicale (INSERM), France

Reviewed by:
Marc Dhenain, Centre National de la Recherche Scientifique (CNRS), France
Chung-Chuan Lo, National Tsing Hua University, Taiwan

***Correspondence:**
Alexandra Badea
alexandra.badea@duke.edu

† These authors have contributed equally to this work

‡ These authors share senior authorship

Received: *05 July 2019*
Accepted: *13 November 2019*
Published: *10 December 2019*

Citation:
Badea A, Wu W, Shuff J, Wang M, Anderson RJ, Qi Y, Johnson GA, Wilson JG, Koudoro S, Garyfallidis E, Colton CA and Dunson DB (2019) Identifying Vulnerable Brain Networks in Mouse Models of Genetic Risk Factors for Late Onset Alzheimer's Disease. Front. Neuroinform. 13:72. doi: 10.3389/fninf.2019.00072

The major genetic risk for late onset Alzheimer's disease has been associated with the presence of APOE4 alleles. However, the impact of different APOE alleles on the brain aging trajectory, and how they interact with the brain local environment in a sex specific manner is not entirely clear. We sought to identify vulnerable brain circuits in novel mouse models with homozygous targeted replacement of the mouse ApoE gene with either human APOE3 or APOE4 gene alleles. These genes are expressed in mice that also model the human immune response to age and disease-associated challenges by expressing the human NOS2 gene in place of the mouse mNos2 gene. These mice had impaired learning and memory when assessed with the Morris water maze (MWM) and novel object recognition (NOR) tests. *Ex vivo* MRI-DTI analyses revealed global and local atrophy, and areas of reduced fractional anisotropy (FA). Using tensor network principal component analyses for structural connectomes, we inferred the pairwise connections which best separate APOE4 from APOE3 carriers. These involved primarily interhemispheric connections among regions of olfactory areas, the hippocampus, and the cerebellum. Our results also suggest that pairwise connections may be subdivided and clustered spatially to reveal local changes on a finer scale. These analyses revealed not just genotype, but also sex specific differences. Identifying vulnerable networks may provide targets for interventions, and a means to stratify patients.

Keywords: mouse model, Alzheimer's disease, neurodegeneration, magnetic resonance imaging, tractography, tract based analysis, morphometric, diffusion tensor (DT) MRI

INTRODUCTION

The multifactorial nature of Alzheimer's disease AD has led to multiple hypotheses for disease onset and progression (Devanand et al., 2007), yet its etiology is not known. While pathological biomarkers have been well defined, cross-disciplinary approaches are critical to integrate knowledge on the spatiotemporal evolution of AD. Additionally, sensitive tools that permit early detection and monitoring changes are critical to enable useful interventions. Analyses of Aβ plaques and tau tangles are considered to provide the "classical" biomarkers of AD. But Aβ plaques and tau tangles are accompanied by neuronal dystrophy and loss (Serrano-Pozo et al., 2011). For the small percentage of individuals with the mutated forms of these proteins, the onset and progression of these biomarkers are clearly dependent on the genetic mutations. However, most individuals afflicted with AD have a late onset form of AD (LOAD). There is a long asymptomatic period that often precedes the overt phases, and during this time other processes besides those centered directly on Aβ plaque formation may be activated to cause neurodegenerative diseases. These processes may involve microglia, astrocytes, and the vasculature (De Strooper and Karran, 2016). In particular, for LOAD, there is a pressing need to better understand the role of non-classical risk factors in AD including age, sex, and genes, and how they interact to modulate the brain response to stressors (Sala Frigerio et al., 2019).

One of the best known genetic risk factors for LOAD is conferred by the APOE4 genotype (Schellenberg, 1995; Huynh et al., 2017). The APOE4/4 genotype is associated with a 30–55% risk of developing mild cognitive impairment (MCI) or AD by age 85, compared to a 10–15% risk for the APOE 3/3 genotype. Still, the precise cause for increased risk, or resilience conferred by the different APOE alleles, and the mechanisms mediating these relationships are poorly understood. While these risk factors may influence the brain levels of Aβ and hyperphosphorylated tau, it is likely that their underlying mechanisms contributing to AD onset, progression and overall pathology will vary. Besides being recognized as a major genetic risk for AD, the presence of APOE4 has been linked to other neurodegenerative diseases. These include age related macular degeneration, age related hearing loss, dementia with Lewy bodies and Parkinson's disease. APOE4 provides increased susceptibility to neuromuscular conditions including diabetic neuropathy and immunodeficiency viral neuropathy (Bedlack et al., 2000; Pankratz et al., 2006). Moreover, APOE4 is as a risk factor for cardiovascular disease, and stroke (Tudorache et al., 2017; Femminella et al., 2018; Belloy et al., 2019). Due to its complex, not yet completely understood role, we have examined in this work primarily phenotypes relevant to AD.

MRI can provide such phenotypes, e.g., early regional atrophy (Jack et al., 1999), and quantitative biomarkers that can be analyzed as networks (Torok et al., 2018). This is important because network connectivity integrates microstructural effects e.g., neurodegeneration of gray and white matter, or toxicity associated with Aß presence. We hypothesize that network approaches are sensitive to subtle changes arising from the interplay of several factors. While each effect may be small, the summed effect due to individual biomarkers may be significant. Here, we will generate a framework for integrating biomarkers using multimodal approaches (Wiesmann et al., 2016), thereby allowing us to better predict their pathological significance.

To help understand the mechanisms through which APOE genes and their products differentially modulate the brain milieu and circuits to switch from healthy to pathological aging, we use novel mouse models for the APOE4 associated genetic risk. We analyze behavioral and imaging markers including structural connectomics based on high resolution diffusion weighted imaging (DWI) to help understand the underpinnings of network vulnerability in aging and AD (Fischer et al., 2015).

The animal models are homozygous targeted replacement mice, expressing instead of the mouse protein the human APOE3 and APOE4 isoforms. To model the human immune response to age and disease associated challenges these double-transgenic mice only express human NOS2 gene products. This modification enables nitric oxide (NO) production and immune activity regulated by NO to better mimic the human response. Our study includes 12 months old male and female APOE3HN (APOE3/3 + human NOS2 on a mouse $Nos2^{-/-}$ background), and APOE4HN (APOE3/3 + human NOS2 on a mouse $Nos2^{-/-}$ background). Mice were characterized with a behavioral battery for memory function, and with MRI to determine selective vulnerability using regional atrophy and DTI parameters. To these tests we added connectopathy biomarkers extracted using novel statistical approaches that map brain circuits associated with selective vulnerability or resilience conferred by APOE genotypes. While limited in sample size, our study revealed sex specific differences were also present in the networks associated with genotype differences. Our efforts will help identify potential targets for interventions, and future efforts to build models that explain the influence of APOE genotypes on age, sex, and AD associated circuit vulnerability.

MATERIALS AND METHODS

Animals

Using mouse models, we sought to identify vulnerable brain circuits associated with memory dysfunction typical of pathological aging, and with the highest known genetic risk for LOAD - the presence of APOE4 genotype relative to APOE3 genotype. To better model the APOE4 associated risk in humans with AD we have used mouse models named huAPO3/HN and huAPOE4/HN. In these mice, the human NOS2 gene replaced the mouse Nos2 gene ($HuNOS2^{+/+}/mNos2^{-/-}$; abbreviated HN). More similar to humans, $HuNOS2^{+/+}/mNos2^{-/-}$ mice show unique redox characteristics compared to mice expressing either mNos2, or mNos2 knockouts. To "add-in" the impact of APOE genotype on generation and expression of AD-like pathology, these novel mouse strains co-express HuAPOE3 or HuAPOE4 but on the HuNOS2 background described above. The total number of mice used was 10 APOE3HN mice (4 females, 6 males), and 14 APOE4HN mice (7 males and 7 females), aged to 12 months.

Behavior Testing

The Morris Water Maze

Mice were handled for 5 days prior to the beginning of behavioral testing for the purpose of habituation to the researchers performing the tests. Morris water maze (MWM) was conducted for 5 days, followed by a novel object recognition (NOR) test (2 days).

The MWM tests a mouse's spatial memory and learning based on their preference for standing on solid ground, as opposed to swimming. Mice are placed in a quadrant of a pool with directional cues and are expected to find a clear platform underneath the water, on which they may stand. Because of their aversion to swimming and the consistent placement of the platform, mice are expected to learn that the platform is located in the same position relative to directional cues and locate it more and more quickly over time. We assessed learning by measuring the amount of time a mouse swam, the distance it swam in the pool, and the percent of the swim time, and swim distance in the target quadrant in which the platform is located (termed target swim time and target swim distance, respectively). The MWM apparatus was a circular pool with 122 cm diameter, and behavior was tracked using with a ceiling-mounted Logitech camera, and analyzed with the video analysis software ANY-maze (Stoelting, Wood Dale, IL, United States). Black mice were allowed to swim in transparent water and were expected to find a glass platform (similar indices of refraction do not allow for easy visibility) located in the south west (SW) quadrant of the pool. Mice were trained for 5 days undergoing four trials each day. For each trial, mice were placed in one quadrant of the maze and had to swim to a 10 cm wide circular platform submerged 1.5 centimeters below the surface of the water (not visible). Each trial consisted of placing the mouse into the water at one of four different starting positions, one in each quadrant and allowing them to swim freely for 1 min. The time needed for the mice to find the hidden platform was recorded as well as the swim path length. If they were unable to locate the platform within the allotted time, they were guided to the platform and allowed to remain there for 10 s. Probe trials were conducted on days 3 and 5, 1 h after the last training trial. During the probe trial the submerged platform was removed and mice were given 1 min to swim in the pool. The amount of time spent in the previous location of the target zone was recorded.

Novel Object Recognition

The NOR test assesses a mouse's memory through exploration. Mice traditionally spend more time exploring novel stimuli, so when they are faced with a stimulus that is novel and one that is familiar, they are expected to remember the familiar object and spend more time exploring and engaging with the more novel object. The day before testing, mice were placed in a 40 cm square open field arena for 5 min to habituate them to the apparatus and the test room. 24 h after habituation, mice were acclimated in the test room for 1 h before beginning trials. Mice first completed an acquisition trial, in which they were placed in the apparatus with two identical objects for 5 min. After a 90 min retention period, mice were then placed in the arena again for 5 min with two dissimilar objects - one that is familiar, and one that is novel. 24 h later, the mice were placed in the arena again for 5 min with a pair of dissimilar objects - one that is the original familiar object, and one that is novel. After each trial, the mouse was returned to its cage. Between trials, the apparatus was cleaned with ethanol solution to eliminate animal clues. The amount of time spent exploring the novel object and the amount of time spent exploring both objects were measured. From this we calculated a recognition index as the time exploring novel object/(time exploring novel object + time exploring familiar object) × 100%. The location preference was similarly calculated, but for two identical objects.

Statistical analyses for behavior tasks was done in JMP (SAS, Cary, NC, United States)[1]. Analysis for multiple measurements acquired in the same animal over time was performed by repeated measures two-way ANOVA using linear mixed models fixed effects for genotype and time and random effects for animals. Tukey HSD was used for *post hoc* corrections. 2-group comparisons used a two-tailed *t*-test, while comparisons between three or more trials were done using a one-way ANOVA. $P < 0.05$ was considered significant.

Imaging

Brain specimens were imaged on a 9.4 T, 8.9 cm vertical bore Oxford magnet, with shielded coils, providing gradients up to 2000 mT/m (Resonance Research, Inc., Billerica, MA, United States), and controlled by an Agilent Direct Drive Console (Agilent Technologies, Santa Clara, CA, United States). In house made solenoid coils (13 mm diameter) were used to image brain specimens within the skull, in order to avoid tissue damage and distortions. To prepare actively stained brain specimens the animals were anesthetized to a surgical plane and perfused through the left cardiac ventricle, with outflow from the right atrium. Saline (0.9%) was used to flush out the blood, at a rate of 8 ml/min, for ∼5 min. For fixation we used a 10% solution of neutral buffered formalin phosphate containing 10% (50 mM) Gadoteridol (ProHance, Bracco Diagnostics Inc., Monroe Township, NJ, United States), at a rate of 8 ml/min for ∼5 min. Gadoteridol reduced the spin lattice relaxation time (T1) of tissue to ∼100 ms. Mouse heads were stored in 10% formalin for 12 h, then transferred to a 0.01 M solution of phosphate buffered saline (PBS) containing 0.5% (2.5 mM) Gadoteridol, at 4°C for ∼30 days to rehydrate the tissue. Extraneous tissue around the cranium was removed prior to imaging, and specimens were placed in MRI-compatible tubes, immersed in perfluoropolyether (Galden Pro, Solvay, NJ, United States) for susceptibility matching.

We used a diffusion weighted MR imaging to derive microstructural and connectivity information. Our protocol used compressed sensing DWI with an acceleration factor of 4, allowing for efficient sampling and reconstruction in a high performance computing cluster environment (Anderson et al., 2018b; Wang et al., 2018). The DWI protocol used 46 diffusion weighted acquisitions, interwoven with 5 non-diffusion-weighted scans, and the following parameters: TE 12 ms, TR 90 ms, BW 125 kHz, $b \approx 4000$ s/mm^2, diffusion pulse width 4 ms, separation

[1]https://www.jmp.com

6 ms, amplitude 130.67 G/cm. Images were acquired over a 22 × 11 × 11 mm field of view, with a matrix 368 × 184 × 184, over 14 h, and reconstructed at 55 μm isotropic resolution.

Image and Network Analysis

Images were processed using a high-performance computing pipeline (Anderson et al., 2017, 2018a,b), to perform diffeomorphic mapping of a symmetric mouse brain atlas, containing 332 regions, based originally of the one presented in Calabrese et al. (2015). To perform these processes we employed at the core of our pipeline advanced normalization tools (Avants et al., 2008, 2011). Each brain was thus segmented in 332 regions. Regional and voxel wise analyses were conducted as in Badea et al. (2019). The Statistical Parametric Mapping SPM toolbox, version 12 (Friston et al., 1994) was used with cluster false discovery rate correction.

We have implemented code for tract based analyses[2]. The tracts connecting pairs of atlas regions (Anderson et al., 2018a) were used to build connectomes based on a constant solid angle (Q-Ball method) method implemented in DIPY (Garyfallidis et al., 2014). We used a relative peak ratio of 0.5, separation angle 25°, and 4 parallel compute threads. We used local tracking with 1 seed per voxel in the whole brain mask, and 0.5 step size. We saved 10% of the 3,000,000 tracks, in trk files of ∼1.5 GB, and their computations required about 20 min/brain using an iMac Pro with 3 GHz Intel Xeon W, 10 cores, with 128 GB memory. Tracts were visualized using DIPY.

Tracts from individual brains were clustered based on a Euclidian distance metric minimization (Garyfallidis et al., 2012), then registered (Garyfallidis et al., 2015, 2018) to a reference brain, before being once more clustered in the space for each specific population (APOE3HN, and APOE4HN).

We hypothesized that genotype and sex modulates network properties, and that we can identify vulnerable circuits relevant to AD. Subnetwork changes were derived using a recently proposed method (Zhang et al., 2019), called tensor network PCA or TNPCA, which is a semi-symmetric tensor generalization of PCA. In short, this works with a tensor network $X \in \mathbb{R}^{P\,x\,P\,x\,N}$, given by the concatenation of the adjacency matrices $Ai \in \mathbb{R}^{P\,x\,P}$ for $i = 1, \ldots N$, where P is the number of nodes (atlas regions), and N is the number of subjects. Zhang et al. (2019) estimated a CP model for the semi-symmetric tensors ($X \in \mathbb{R}^{I1\,x\,I2 \ldots I..N}$) by solving:

$$\min_{dk,\ vk,\ uk,} \left|\left| X - \sum_{k=1}^{K} d_k v_k \circ v_k \circ u_k \right|\right|_2^2$$

subject to

$$u_k^T u_k = 1,\ v_k^T v_k = 1,\ v_k^T v_j = 0,\ j < k$$

[2]https://github.com/portokalh/wuconnectomes

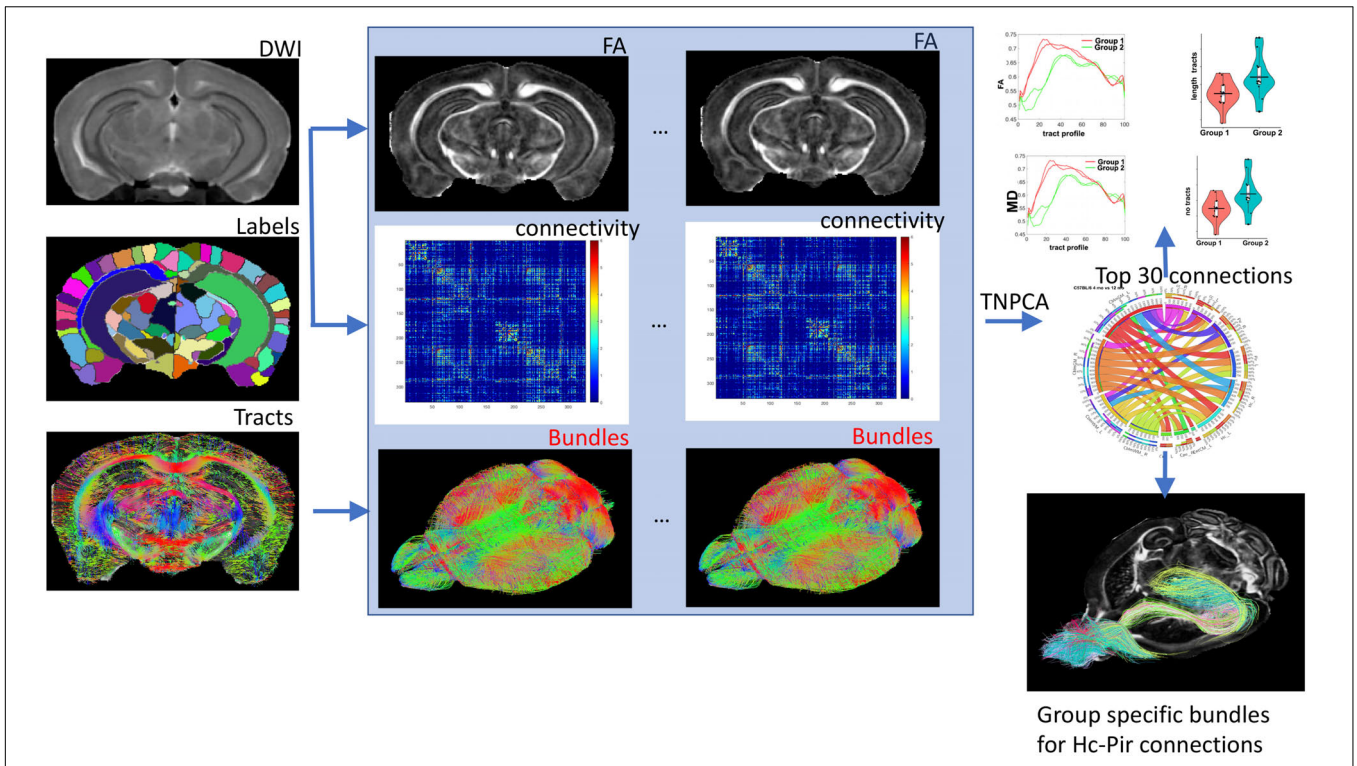

FIGURE 1 | The main elements of our flowchart for characterizing differences between mouse models based on connectivity included image reconstructions and coregistration of individual DWI acquisitions, brain parcelation in 332 regions, and connectome reconstruction based on a constant solid angle method. TNPCA was used to derive subgraphs discriminating two genotypes and the resulting selected pairwise connections between nodes were analyzed for tract length and FA differences. The hippocampus-piriform connections are shown as an example. Hc: hippocampus; Pir: piriform cortex.

where v_k are P sized vectors, constrained to have orthogonal columns, u_k are N sized vectors, and d_k are CP scaling parameters. In our context u_k denotes the subject mode, and $v_k^T v_k$ the network mode.

The subject modes provides a low dimensional embedding of the connectome for each subject, and can be associated with traits (genotype/phenotypes). The weighted sum of network modes $d_k \circ v_k \circ u_k$ provides a principal brain network which captures the most variation across the population. Thus $\{v_k \circ v_k\}$ can be seen as basis networks, $u_{k(i)}$ are the normalized coefficients for each subject i, and d_k are the scaling factors. We are interested in how the connectome varies across levels of the trait, and for discrete cases such as the genotype, the problem can be approached using linear discriminant analysis, while for continuous cases the problem can be approached using canonical correlation. We used 15 principal components identified from TNPCA, and the projection weights from a Fisher linear discriminant to estimate the top 30 pairwise connections, discriminating amongst our groups/genotypes. These were further analyzed for differences in bundles length and fractional anisotropy (FA). The overall process is detailed in **Figure 1**.

We used Quick bundles (Garyfallidis et al., 2012) for a more spatially refined analysis based spatial clustering with a distance of 2 mm, and focused on the top 6 subbundles, for comparing along the tract properties between genotypes and sexes. Bundle statistics were evaluated using R[3].

RESULTS

We have phenotyped a novel mouse model of genetic risk for LOAD using behavior, regional and voxel based MRI analyses, and network connectopathies based on a recently published dimensionality reduction method called tensor network factorization. Regional and voxel based analyses pointed to overlapping sets of regions affected by atrophy and with lower FA indicative of different microstructural properties. Our results indicated that even though qualitative differences between representative animals of the two groups were subtle, we could separate population groups by genotype based on the lower dimensional representation relying on the tensor network

[3]www.r-project.org

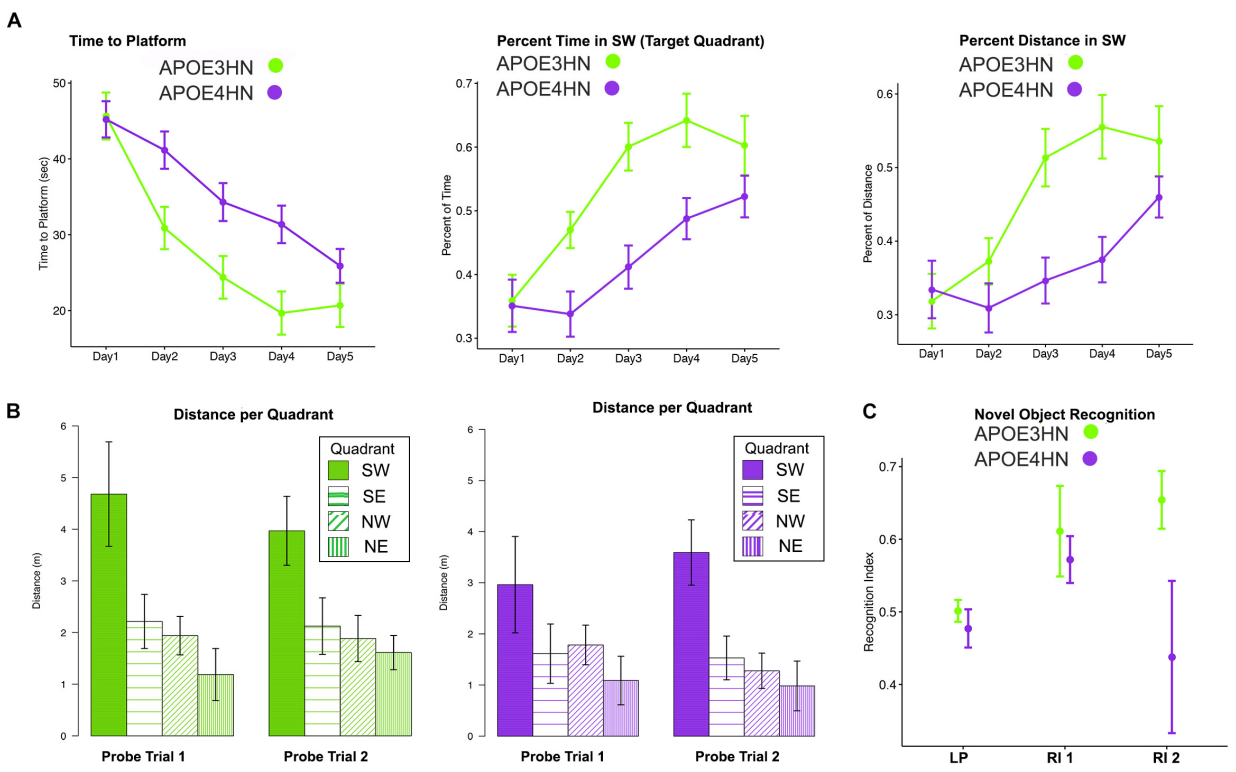

FIGURE 2 | Main repeated measured ANOVA (RMANOVA) results for the memory testing based on acquisition performance and probe trial results (mean ± SEM) in the Morris Water Maze indicate that both APOE3HN and APOE4HN mice learn but there is a significant effect of genotype for both swim time and swim distance. As swim time and distance to hidden platform decreased, the percentage of time spent and distance swam in the target quadrant increased **(A)**. The probe trials indicated that both genotypes had a preference for the SW target quadrant, but APOE3HN mice spent more time swimming in the SW quadrant than APOE4HN mice in the first probe trial **(B)**. E = northeast, NW = northwest, SE = southeast, SW = southwest (target quadrant). N = 11 APOE3HN, N = 14 APOE4HN mice. **(C)** A novel object recognition test revealed that animals had equal location preferences (LP), and object recognition indices (RI) 90 min later, however, after 24 h APOE4HN mice had lower recognition indices relative to APOE3HN mice (t = –2.28, p = 0.04). N = 10 APOE3HN, N = 6 APOE4HN mice (some APOE4HN were not be tested to preserve the matched ages for MRI). Data show mean values, and standard error bars.

TABLE 1 | Volume atrophy was observed at the level of the whole brain (mm^3) in APOE4HN mice relative to APOE3HN mice, and in select regions (volumes are reported for one hemisphere, as % of total brain volume).

Structure	APOE4HN (mean ± SD)	APOE3HN (mean ± SD)	pFDR	CI[1]	CI[2]	*t*	Cohen *d*	Diff (%)
Temporal_association _cortex (%)	0.243 ± 0.028	0.274 ± 0.023	2.67E-02	−0.054	−0.009	−2.93	−1.21	−11.53
Cingulate_cortex _area_25 (%)	0.037 ± 0.002	0.042 ± 0.002	2.68E-04	−0.007	−0.003	−5.64	−2.34	−11.50
Cingulate_cortex _area_32 (%)	0.175 ± 0.011	0.195 ± 0.02	1.31E-02	−0.034	−0.008	−3.32	−1.37	−10.68
Cingulate_cortex _area_29b	0.032 ± 0.003	0.035 ± 0.003	1.48E-02	−0.006	−0.001	−3.26	−1.35	−10.46
Ventral_intermediate _entorhinal_cortex	0.096 ± 0.006	0.107 ± 0.003	3.20E-04	−0.015	−0.007	−5.51	−2.28	−10.30
Accumbens	0.434 ± 0.011	0.475 ± 0.011	2.43E-06	−0.051	−0.032	−9.04	−3.74	−8.67
Cingulate_cortex_area _24b_prime	0.054 ± 0.003	0.058 ± 0.004	1.61E-02	−0.008	−0.002	−3.22	−1.33	−7.91
Secondary_visual_cortex _mediomedial_area	0.192 ± 0.009	0.206 ± 0.016	3.26E-02	−0.024	−0.004	−2.82	−1.17	−6.85
Amygdalopiriform _transition_area	0.026 ± 0.002	0.028 ± 0.001	3.05E-02	−0.003	−0.001	−2.86	−1.18	−6.83
Primary_visual_cortex _monocular_area	0.409 ± 0.015	0.437 ± 0.032	2.38E-02	−0.049	−0.009	−3.01	−1.25	−6.60
Cingulate_cortex _area_29c	0.181 ± 0.008	0.193 ± 0.008	7.49E-03	−0.019	−0.005	−3.64	−1.51	−6.35
Dorsal_tenia_tecta	0.056 ± 0.003	0.059 ± 0.003	1.38E-02	−0.006	−0.001	−3.29	−1.36	−6.03
Cerebellar_cortex	4.553 ± 0.157	4.805 ± 0.205	1.10E-02	−0.405	−0.100	−3.43	−1.42	−5.25
Pontine_nucleus	0.126 ± 0.004	0.132 ± 0.006	4.00E-02	−0.010	−0.001	−2.71	−1.12	−4.35
Basal lateral amygdala	0.139 ± 0.005	0.145 ± 0.004	2.29E-02	−0.011	−0.002	−3.04	−1.26	−4.35
Middle_cerebellar _peduncle	0.159 ± 0.006	0.167 ± 0.005	1.79E-02	−0.012	−0.002	−3.17	−1.31	−4.31
Cingulate_cortex_area_30	0.294 ± 0.011	0.307 ± 0.009	1.90E-02	−0.022	−0.004	−3.14	−1.30	−4.24
Piriform_cortex	5.422 ± 0.077	5.554 ± 0.155	3.62E-02	−0.231	−0.033	−2.76	−1.14	−2.37
TotalBrain (mm^3)	488.64 ± 11.21	522.44 ± 17.52	2.30E-04	−45.94	−21.66	−5.77	−2.39	−6.47

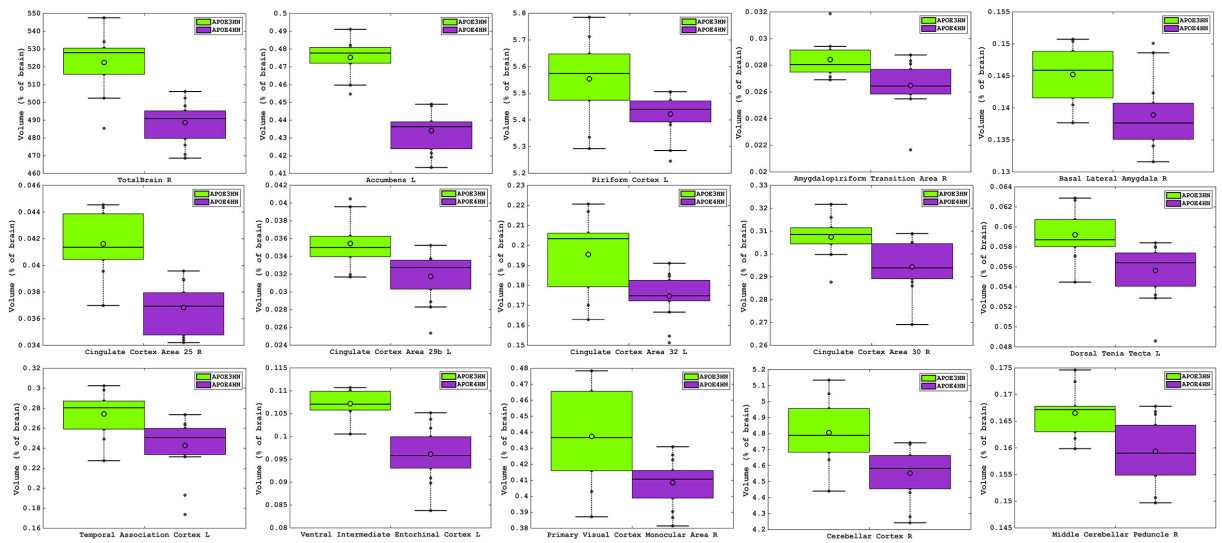

FIGURE 3 | Volume atrophy was detected in regions spanning from the rostral to the caudal aspects of the brain, and ranged from 10% for the temporal association cortex, entorhinal and cingulate cortex, down to 2% for the piriform cortex. The visual cortex, accumbens and amygdalo-piriform transition areas were ∼7% smaller and the cerebellum was ∼5% smaller in APOE4HN mice, FDR = 5%.

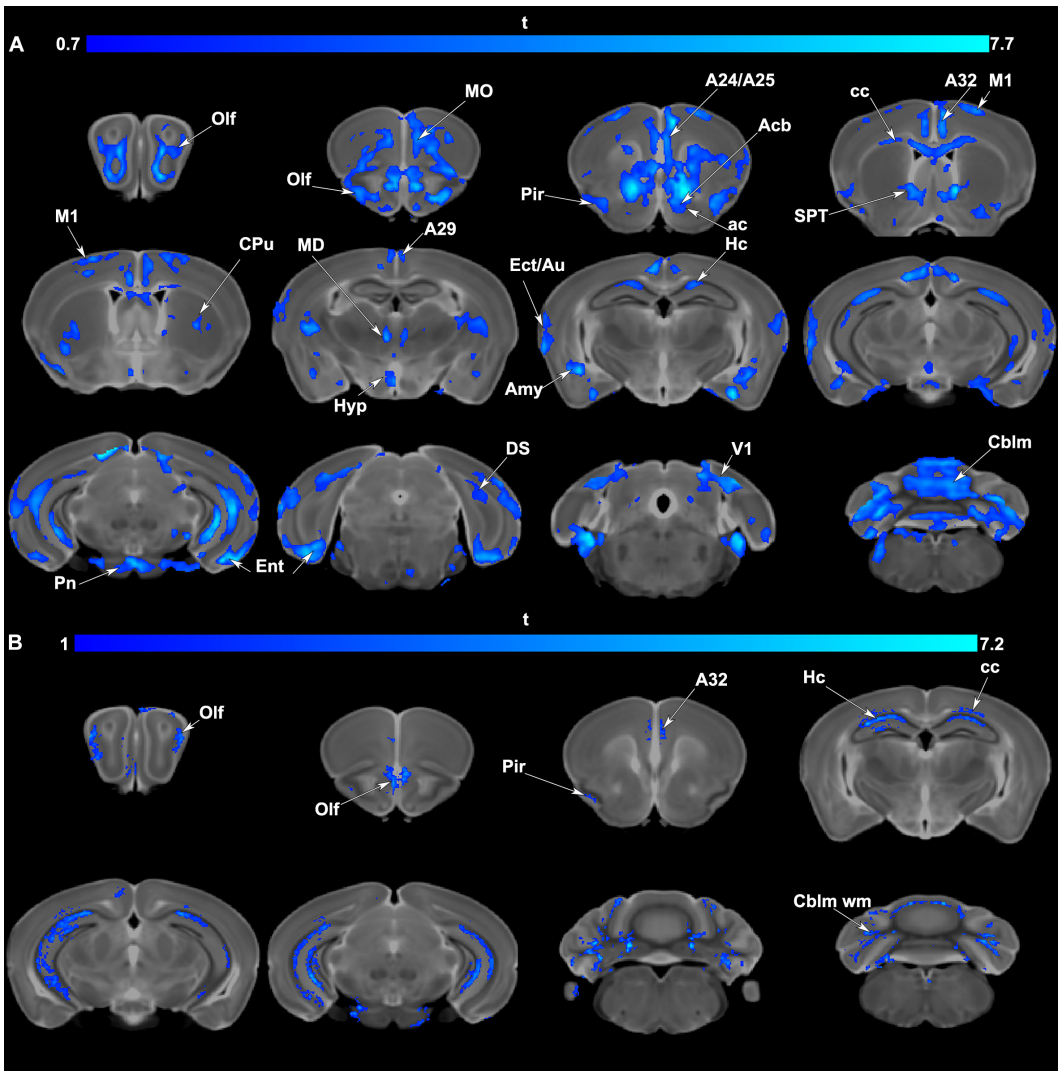

FIGURE 4 | (A) Voxel based analyses indicated that volume atrophy occurred in vulnerable regions comprising olfactory/piriform (Olf, Pir) cingulate (A24,25,29, 32), sensory (Ect: ectorhinal, Au: auditory, V1: primary visual cortex) and motor cortex (M1), and the entorhinal cortex (Ent). Deeper gray matter regions with atrophy in APOE4 carriers included the accumbens (Acb), caudate putamen (CPu), hippocampal formation (Hc, subiculum: DS), amygdala (Amy), as well thalamic nuclei (mediodorsal: MD) and the cerebellum (Cblm) and pontine nuclei (Pn). Among white matter tracts the anterior commissure (ac), and corpus callosum (cc) also had areas of atrophy. Results are presented as t maps, FDR cluster-corrected for multiple comparisons, using an initial cluster forming threshold of 0.05 significance, and the whole brain as a mask (blue color). **(B)** Voxel based analyses indicative of fractional anisotropy (FA) reductions suggested vulnerable brain networks. These included the olfactory (Olf) and in particular the piriform cortex (Pir), cingulate cortex (A32), hippocampus (Hc), and the white matter of the corpus callosum (cc) and cerebellum (Cblm wm). Results are presented as t maps, FDR cluster-corrected for multiple comparisons, using initial cluster forming threshold of 0.05 significance, and the whole brain as a mask (blue color). The DWI minimum deformation average template serves as the background.

decomposition. Our results identified subgraphs of connected vulnerable regions, and these included areas known to be involved in memory function (e.g., hippocampus), as well as in sensory motor functions (e.g., olfactory areas, and cerebellum).

Learning and Memory Deficits

Since memory is expected to be deficient in animal models of AD, we tested both spatial and NOR memory in 14 APOE4HN and 11 APOE3HN animals (one died before being imaged). Spatial memory was examined through acquisition and probe trials in the MWM (**Figures 2A,B**). Swim time (and distance) to the hidden platform got shorter with time for both groups. Repeated measures ANOVA (RMANOVA) detected a significant effect of day $F(4,92) = 26.1$, $p < 0.001$ (**Figure 2A**), and genotype [$F(1,23) = 6.3$, $p < 0.02$], while the interaction term of day by genotype was $F(4,92) = 2.0$, $p < 0.09$. For swim distance there was a significant main effect of day $F(4,83.8) = 34.4$, $p < 0.0001$, and a significant day × genotype interaction with $F(4,83.8) = 3.6$, $p < 0.01$. Within genotypes there was a significant difference after Tukey HSD tests for swim distance for APOE3HN mice between days 1 and 2 ($t = 3.5$, $p < 0.02$); 1 and 3 ($t = 6.3$, $p < 0.0001$); 1 and 4 ($t = 7.3$, $p < 0.0001$); 1 and 5 ($t = 8.5$, $p < 0.0001$); 2 and 4 ($t = 4$,

TABLE 2 | The top connections for the subnetworks differentiating between APOE3HN and APOE4HN connectomes.

	Connection	Load		Connection	Load
1	Hippocampus_right—cerebellar_cortex_left	92.49	16	Cerebellar_cortex_right—corpus_callosum_left	73.48
2	Cerebellar_white_matter_left—cerebellar_cortex_left	−91.78	17	Cerebellar_cortex_right—cerebellar_white_matter_left	−73.3
3	Piriform_cortex_right—cerebellar_cortex_left	91.36	18	Cerebellar_cortex_left—piriform_cortex_left	72.87
4	Cerebellar_cortex_right—hippocampus_right	89.09	19	Cerebellar_white_matter_left—hippocampus_left	69.75
5	Cerebellar_cortex_right—piriform_cortex_left	89.04	20	Corpus_callosum_right—cerebellar_cortex_right	67.61
6	Cerebellar_white_matter_right—cerebellar_cortex_right	−84.69	21	Corpus_callosum_right—cerebellar_white_matter_left	67.04
7	Cerebellar_white_matter_right—hippocampus_left	82.28	22	Gigantocellular_reticular_nucleus_right—piriform_cortex_left	−64.24
8	Cerebellar_cortex_right—piriform_cortex_right	80.79	23	Gigantocellular_reticular_nucleus_left—piriform_cortex_left	−63.63
9	Hippocampus_right—piriform_cortex_left	−80.58	24	Cerebellar_cortex_left—hippocampus_left	61.36
10	Cerebellar_white_matter_right—piriform_cortex_left	79.61	25	Cerebellar_white_matter_right—corpus_callosum_left	61.18
11	Piriform_cortex_right—cerebellar_white_matter_left	78.76	26	Cerebellar_cortex_right—striatum_left	61.04
12	Piriform_cortex_right—hippocampus_left	−77.31	27	Cerebellar_white_matter_left—piriform_cortex_left	60.3
13	Cerebellar_cortex_right—hippocampus_left	76.73	28	Cerebellar_white_matter_right—piriform_cortex_right	60.19
14	Corpus_callosum_right—cerebellar_cortex_left	76.46	29	Striatum_right—cerebellar_cortex_left	59.53
15	Cerebellar_white_matter_right—cerebellar_cortex_left	−74.67	30	Corpus_callosum_left—cerebellar_cortex_left	58.95

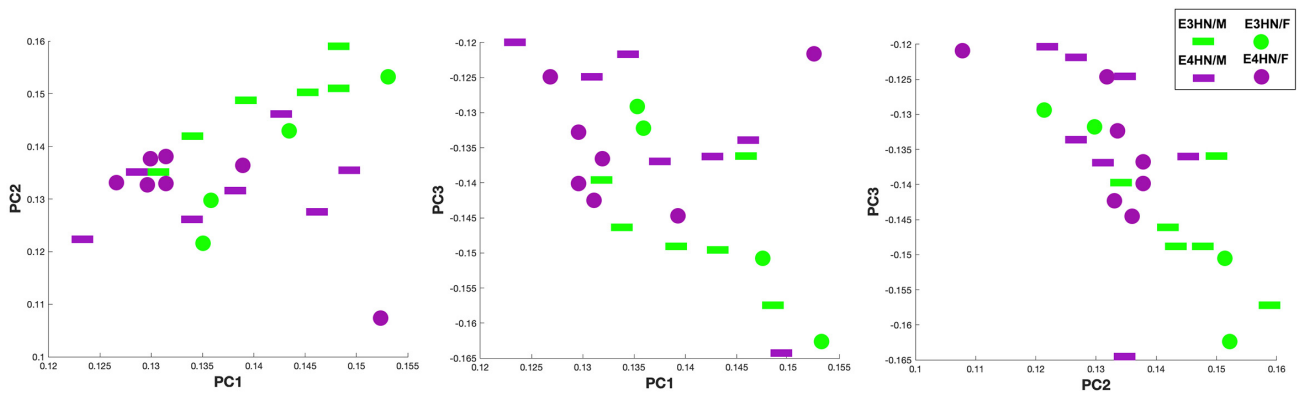

FIGURE 5 | Scatter plot of the top three principal components for the connectome TNPCA analysis. The two genotypes are shown in green: APOE3HN, and purple: APOE4HN. Sex information is also indicated, although sex was not used as a predictor (female: disk, male: bar).

$p < 0.006$); 2 and 5 (5.2, $p < 0.0001$). For genotype APOE4HN these differences were significant between days 1 and 4 ($t = 3.8$, $p < 0.01$); 1 and 5 ($t = 5.8$, $p < 0.0001$); 2 and 4 ($t = 3.8$, $p < 0.01$); 2 and 5 ($t = 5.7$, $p < 0.0001$); 3 and 5 ($t = 3.3$, $p < 0.04$). No differences were noted between days 4 and 5.

We have measured the percent time spent in the target quadrant during learning trials and found a significant effect of day [$F(4,92) = 14.3$, $p < 0.0001$] and genotype [$F(1,23) = 15.8$, $p < 0.0006$], with a possible interaction term ($p < 0.1$). At day 3 the difference between genotypes was largest ($t = 3.5$, $p = 0.02$). For the percent distance swam in the target quadrant during the learning trials we found a significant main effect for day [$F(4,83.7) = 13.8$, $p < 0.0001$], for genotype [$F(1,21.7) = 15.7$, $p < 0.0007$] and a significant interaction [$F(4,83.7) = 3.6$, $p < 0.01$]. The differences with genotype were significant for days 3 ($t = 3.6$, $p < 0.02$); and persisted for day 4 ($t = 3.9$, $p < 0.008$). Differences subsided by day 5.

The first probe trial was performed on the third day and indicated a significant effect of quadrant only ($p < 0.0001$). APOE3HN mice had a significant preference for the SW quadrant relative to the SE ($t = 3.9$, $p = 0.006$), NE ($t = 5.3$, $p < 0.0001$), NW ($t = 4.1$, $p = 0.003$), but not for SE. APOE4HN mice preferred the target SW quadrant over SE ($t = 4$, $p = 0.004$) and NE quadrants ($t = 4.3$, $p = 0.001$), but only reached a trend for NW (2.8, $p = 0.1$).

The first probe distance swam in the target quadrant provided a more sensitive marker for the memory deficits, showing significant genotype ($p < 0.003$), and quadrant effects ($p < 0.0001$). Genotypes had significant differences, with APOE3HN mice swimming longer in the SW than APOE4HN mice ($t = 3.74$, $p = 0.008$). APOE3HN preferred the SW relative to NE ($t = 6.9$, $p < 0.0001$), NW ($t = 5.4$, $p < 0.0001$), SE ($t = 4.9$, $p = 0.0002$). APOE4HN also preferred the SW over NE ($t = 4.2$, $p = 0.002$), and differences reached a trend relative to SE ($t = 3$, $p = 0.07$), but they made no distinction relative to NW.

The second probe swim times performed on the fifth day also showed an effect of the quadrant ($p < 0.0001$), but not for genotype. APOE3HN mice preferred the SW to NE ($t = 3.8$, $p < 0.006$), NW ($t = 4.3$, $p = 0.03$), SE (4.3, $p = 0.06$). APOE4HN

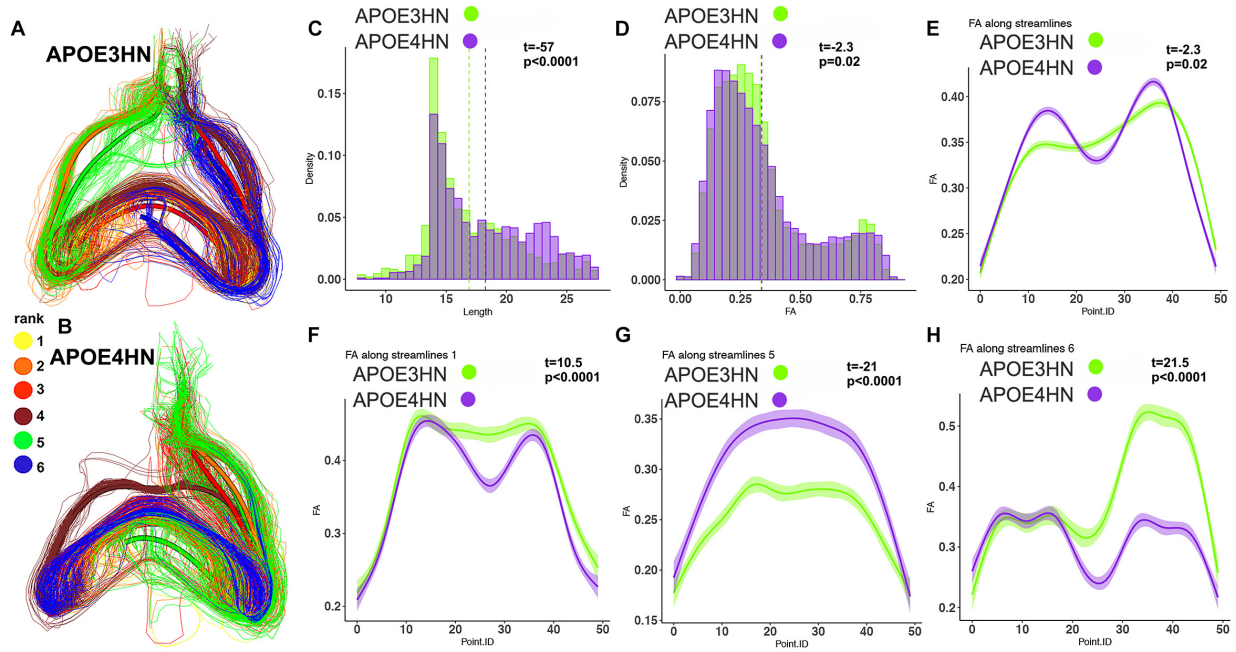

FIGURE 6 | The piriform cortex-hippocampal interhemispheric connections through the top 6 bundles were ranked according to size (yellow for the first and largest bundle, orange for the second, red for the third, brown for the fourth, green for the fifth, blue for the sixth. The interhemispheric connections appeared stronger in the APOE3HN mice relative to APOE4HN mice **(A)** and **(B)**, according to the size based ranking for the major sub-bundles. This indicated different connectivity patterns for the two genotypes. Differences in fiber length distributions between the two genotypes are shown in **(C)**, and in FA distributions in **(D)** using histogram densities. These indicate a slight shift toward longer length **(C)**, but lower FA values in APOE4HN mice, which may suggest dismyelination **(D)**. After establishing spatial correspondence through an affine bundle centroid registration, we detected that differences along the bundle containing all connections between the piriform cortex and hippocampus were not uniform **(E)**. We identified the top 3 sub-bundles accounting for the largest difference between the genotypes **(F–H)**. FA appeared in general lower for APE4HN mice in sections of two of these subbundles **(F,H)**, but higher in one subbundle **(G)**.

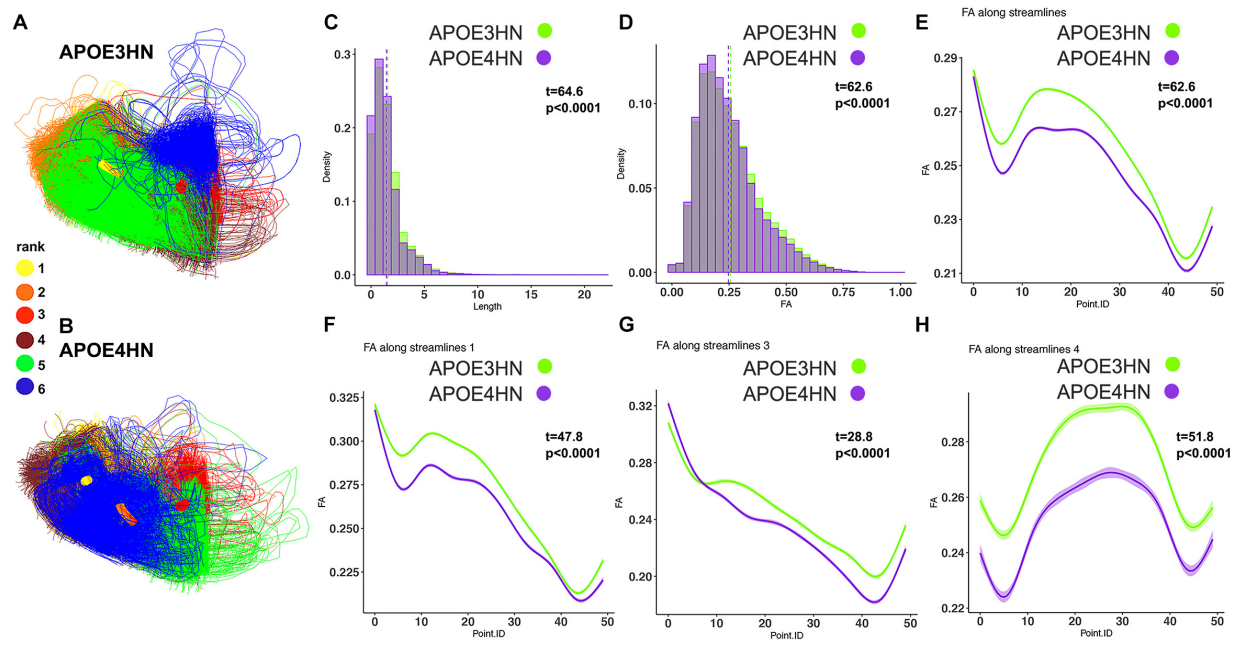

FIGURE 7 | The 2nd ranked connection discriminating between the genotypes involved intrahemispheric cerebellar connections between white and gray matter. APOE4HN **(B)** showed consistent deficiencies relative to APOE3HN **(A)** carriers in fiber length and FA distributions **(C,D)**. These differences were evident in whole bundle **(E)** and subbundle analyses **(F–H)**.

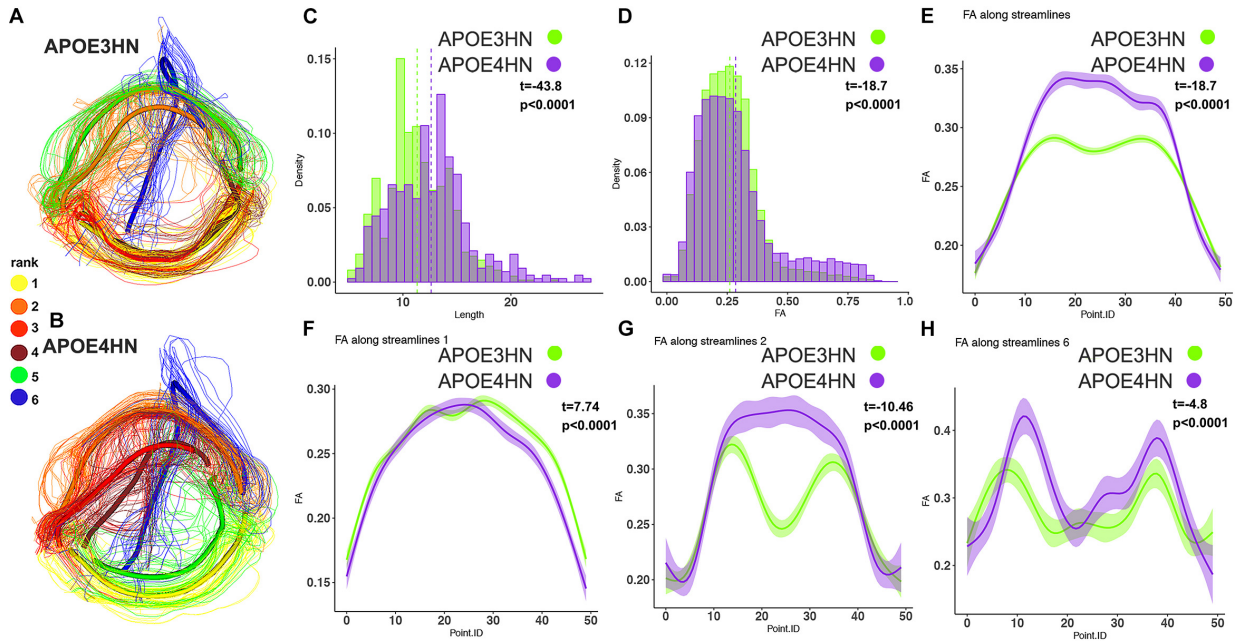

FIGURE 8 | The interhemispheric hippocampal cerebellar connections showed significant differences between APOE3HN **(A)** and APOE4HN **(B)** mice in length **(C)** and FA **(D,E)**. The top three subbundles with significant differences between genotypes showed lower FA for APOE4HN mice relative to APOE3HN in the largest subbundle **(F)**, but higher FA for the 2nd and 6th spatially matched subbundles **(G,H)**, and also higher variability for the APOE4HN genotype.

mice also preferred the SW to the NE ($t = 3.8$, $p < 0.0001$), NW ($t = 4.8$, $p < 0.002$), SE ($p = 3.1$, $p = 0.05$).

The second probe swim distance showed a significant effect of quadrant ($p < 0.004$), and genotype ($p < 0.0001$). Between genotypes the swim distance in SW was not significantly different. APOE3HN mice swan longer distance in the SW relative to NE ($t = 5.9$, $p < 0.0001$), NW ($t = 5.2$, $p = 0.0001$), SE (4.6, $p = 0.0004$). APOE4HN mice also preferred the SW to the NE ($t = 6.3$, $p < 0.0001$), NW ($t = 5.6$, $p < 0.0001$), SE ($p = 5$, $p = 0.0001$) (**Figure 2C**).

During the NOR APOE4HN and APOE3HN mice showed no location preference for the sites of the two objects presented. The immediate recognition index was not different between genotypes. After 90 min, however, APOE4HN mice showed more similar preferences for the familiar and novel objects (RI = 0.44 ± 0.07 (SE), CI = [0.28. 0.60]) relative to APOE3HN mice (0.65 ± 0.06 (SE), CI = [0,53 0.78]). This indicated that APOE4HN mice did not remember the familiar object used during the acquisition trial. APOE3HN mice had a higher recognition index compared to APOE4HN mice at 24 h after the initial trial ($t = 2.3$, $p = 0.04$)].

Volume Loss

The total brain volume for APOE4HN mice was 6% smaller relative to APOE3HN controls. An ROI (region of interest) analysis for the 332 brain parcelation revealed significant atrophy occurred for regions shown in **Table 1** and **Figure 3**.

The largest volume loss in APOE4HN mice relative to the APOE3HN controls was in the range of ∼10% and occurred for the cingulate cortex (areas 25, 29b, and 32), the ventral intermediate entorhinal cortex and the temporal association cortex. The accumbens, amygdalo-piriform transition area, and secondary visual cortex were 7% or smaller in APOE4HN mice relative to APOE3HN mice. Finally, the cerebellar cortex, middle cerebellar peduncle and pontine nuclei were ∼4% smaller, while the piriform cortex was 2% smaller.

Microstructural Integrity

Regional analyses for FA did not survive multiple comparison correction, but there was a trend for the medial lemniscus to have higher FA in APOE4HN carriers (p corrected = 0.1). The cerebral peduncle had a 6% lower FA in APOE4HN mice (p corrected = 0.1). Similarly, the axial diffusivity differences did not survive the multiple correction, and the longitudinal fasciculus of pons in APOE4HN mice had a 4% lower axial diffusivity (p uncorrected = 0.02), and the cerebellar white matter had 6% larger radial diffusivity (p uncorrected = 0.02).

Voxel Based Analyses

Voxel based analyses indicated significant volume (**Figure 4A**) and FA (**Figure 4B**) reductions occurred in APOE4 carriers relative to APOE3 carriers. Areas of atrophy included the olfactory cortices, hippocampus, subiculum, cingulate cortex, amygdala and entorhinal cortex, as well as the cerebellum. Sensory motor cortex areas also suffered atrophy. Areas with FA reductions were less extensive than those with volume atrophy and were noted in the olfactory/piriform and cingulate cortices, hippocampus and cerebellum.

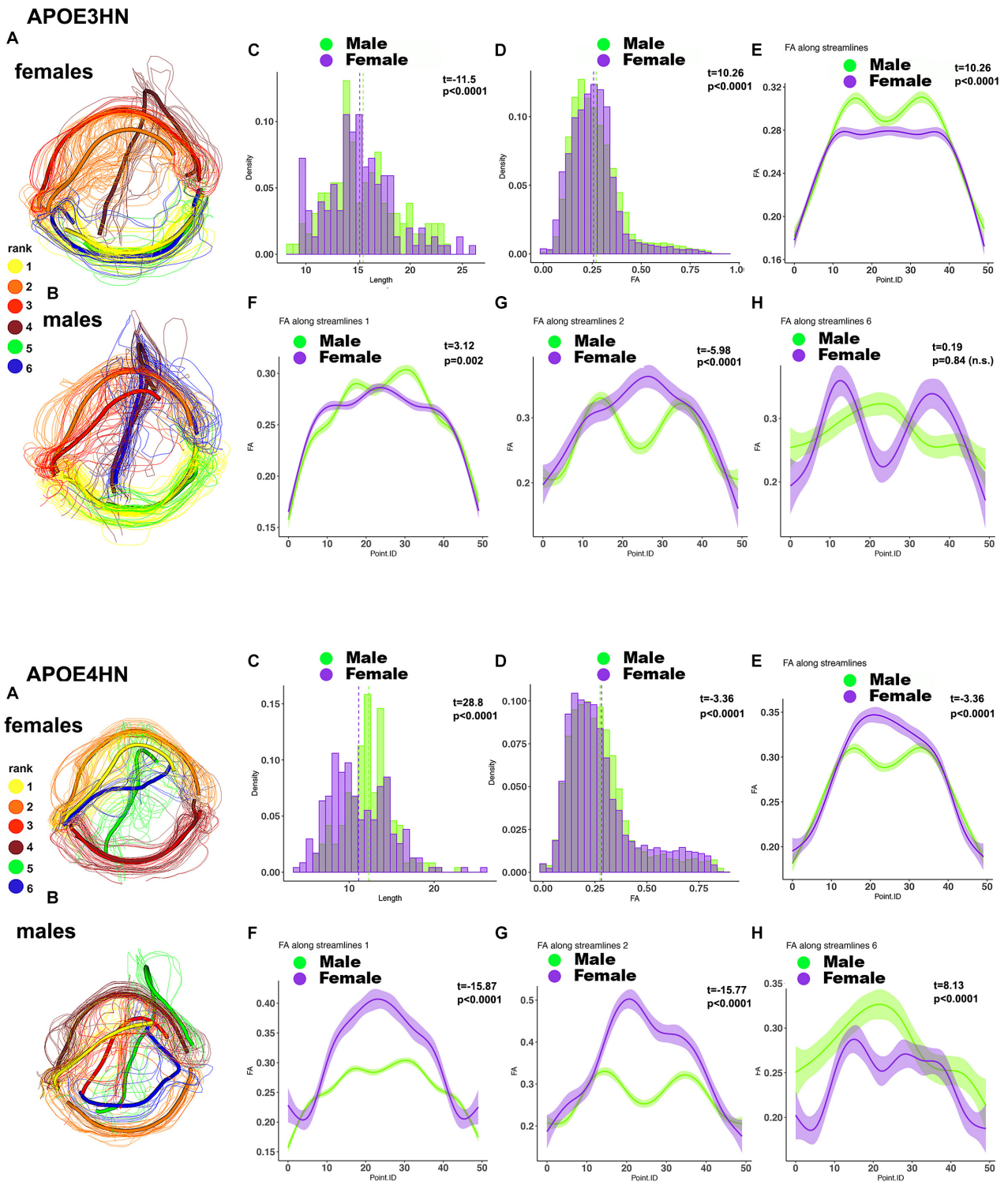

FIGURE 9 | Within genotype, between sex (**A**: female; **B**: male) analyses for the hippocampal-cerebellar interhemispheric connections. APOE3HN females had longer connections compared to males and the opposite was true for APOE4HN mice **(C)**. Differences in FA over the whole set of streamlines **(D)** were subtler in terms of effect sizes, but clearly evident in our along the bundle analysis. APOE3HN males had overall higher FA values than females, and the opposite was true for APOE4HN mice **(E)**. The top subbundles with significant genotype differences **(F)** had also higher FA for APOE3HN males compared to females (bundle 1), while APOE4HN females had higher FA compared to males. The 2nd ranked bundle showed higher FA in females compared to males of both genotypes, with a more accentuated difference for APOE4HN mice **(H)**. The 3rd ranked subbundle did not show sex differences for APOE3HN mice, while APOE4HN males showed higher FA compared to females of the same genotype.

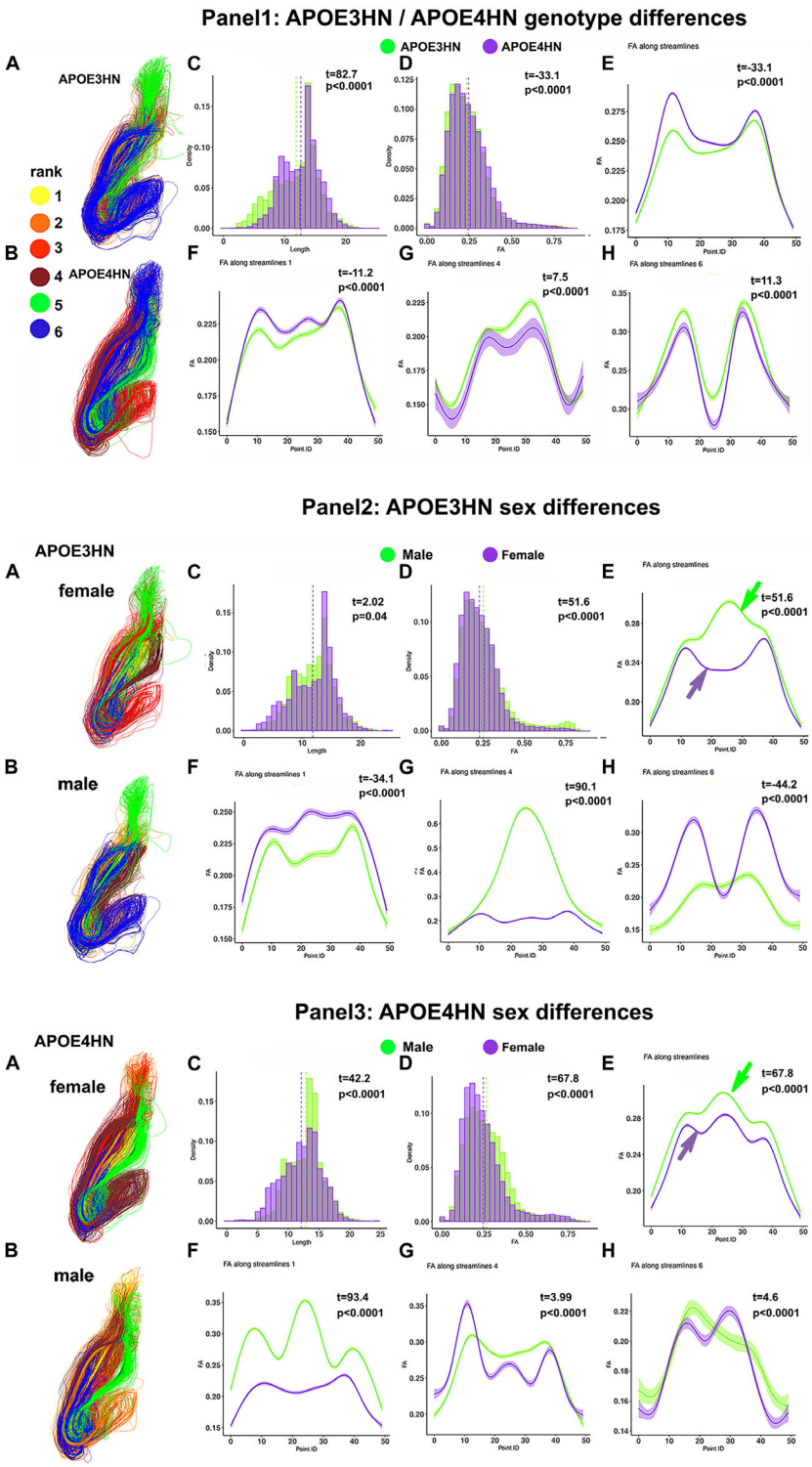

FIGURE 10 | Intrahemispheric connections between the hippocampus and piriform cortex. The first panel compares the two genotypes; the second panel compares the two sexes, within the APOE3HN genotype; the third panel compare the two sexes, within the APOE4HN genotype. Fiber length and FA distributions are shown in **Panels 1–3, C,D**. Qualitatively males of the two genotypes presented more similar, consistent bundle FA shapes, while females showed more variability between the genotypes **(panels 2E,3E)**. Overall, females had lower FA along the entire bundle set in both APOE3HN **(panel 2E)** and APOE4HN mice **(panel 3E)**. Interestingly, APOE3HN females had larger FA than males for the largest subbundle **(panel 2F)**. However, FA was lower along the same subbundle in APOE4HN females relative to males of the same genotype **(panel 3F)**, and differences were larger relative to those between males and females of APOE3HN genotype. These patterns varied by subbundle, and spatially, along the bundles.

Connectopathies

The tensor network analysis revealed the top connected subnetwork (**Table 2**) differentiating the two genotypes. The top 30 resulting connected subnetworks included predominantly interhemispheric connections, and 7 distinct anatomical regions: the hippocampus, piriform cortex, cerebellum (white matter and gray matter), the caudate putamen/striatum, gigantoreticular nucleus and the corpus callosum. Intrahemispheric connections pointed to a role for the cerebellum. The three most frequent major structures included the piriform cortex, the hippocampus, and the cerebellum.

Figure 5 shows the scatter plot for the top three principal components, which explained 61% percent of the variation, while the top 15 explained 91% of the variation between genotypes. We selected examined the same graphs to identify whether sex differences were also apparent within genotypes, but these differences were less clear in our small sample.

We selected examples among the top ranked connections, featuring the most frequent regions. We observed that the interhemispheric connectivity between the hippocampus and piriform cortex (ranked 9) was stronger in APOE3HN mice relative to APOE4HN mice, as illustrated qualitatively in **Figures 6A,B** showing the top 6 largest bundles, ranked according to their size. **Figures 6C–E** compare the distributions of fiber length, FA, and FA along the whole bundle set for the two genotypes. **Figures 6F–H** compare the FA distribution along spatially matched subbundles between genotypes, indicating that FA is non-uniform along the bundles.

The second ranked connection pertained to the intracerebellar connectivity, and APOE4HN mice had consistently shorter connections, and lower FA along the bundles; both when analyzing the connectivity of the two nodes, as well as along the significant sub bundles (**Figure 7**).

The third example shows the interhemispheric connection between the hippocampus and cerebellum (**Figure 8**), which was the top ranked connection discriminating between genotypes. Distinct bundles showed larger FA in APOE4HN (overall, and in subbundles 2 and 6), while the largest subbundle (1) showed higher FA for the first portion of the bundle but lower FA for the second half.

A further analysis of the hippocampal-cerebellar interhemispheric connections revealed within genotype, between sex differences in the length and FA distributions in both APOE3HN, and APOE4HN mice, as well as in the spatially characteristic patterns along the bundles (**Figure 9**). Sex based differences based on fiber length were smaller in APOE3HN mice, compared to those observed in APOE4HN models. The males appeared to have higher FA along the whole bundle relative to the females in APOE3HN mice, but the opposite was seen in APOE4HN mice. The spatial distribution of these effects was not uniform throughout the brain or along subbundles. This illustrates that sex specific differences may be harder to detect in the absence of detailed bundle analytics performed in spatially aligned bundles.

We have examined the intrahemispheric connections between the hippocampus and piriform cortex (**Figure 10**), and observed larger variability within the APOE4HN genotype relative to APOE3HN, as indicated by the width of the confidence intervals (particularly in panel 1G). Qualitatively males of the two genotypes presented more similar/or consistent bundle FA shapes, and females showed more variability in the FA curve shape between the genotypes (panel 2E, and 3E, arrows). Overall, females had lower FA along the entire bundle set in both APOE3HN (panel 2E) and APOE4HN mice (panel 3E). However, we observed lower FA values along the largest subbundle in APOE4HN females relative to males of the same genotype (panel 3F), and larger differences relative to those between males and females of APOE3HN genotype (where females had larger FA overall). We noted a spatially varying pattern of FA changes along bundles, possibly denoting different myelination, or microenvironment properties.

Together, differences in behavioral responses, morphometry, FA and connectivity denote that APOE4HN and APOE3HN mice may use different strategies for learning and memory; and that an association of multiple factors probably contributed to the observed behavioral impairment. We have found that the bundle analysis may confer increased sensitivity to genotype and sex differences, by investigating changes beyond the level of associating the connectivity between two regions with a single entry in the connectome matrix. Our along the bundle analyses revealed rather than a uniform effect, a spatially varying pattern of FA changes along bundles, possibly denoting increased sensitivity to local connectivity, myelination, or microenvironment properties.

DISCUSSION

There is a rapid growth in the number of people affected by Alzheimer's disease, yet we do not know its etiology or have effective treatments. To examine factors which contribute to the switch from normal to pathological aging we focused on the APOE polymorphic alleles. The causes for increased risk, or conversely resilience, conferred by the major APOE alleles are not known. The APOE4/4 genotype is the main genetic risk for late onset Alzheimer's disease (AD), and is associated with a 30–55% risk of developing mild cognitive impairment or AD by age 85, compared to 10–15% for the APOE3/3 genotype.

To help understand the mechanisms through which APOE genes and their products differentially modulate the brain and its circuits, we implemented a multi-disciplinary approach using homozygous targeted replacement APOE3 and APOE4 mice expressing the major human APOE isoforms, under the control of the mouse endogenous ApoE promoter. To model the human immune response to aging we used double-transgenic mice that express human NOS2 gene products. This modification enables NO production and immune activity regulated by NO to better mimic the human response. Mice were characterized with a cognitive behavioral battery for memory alterations typical of AD, and with MRI to determine selective vulnerability of associated brain networks. Our imaging measures were based on volume and DWI; and our analyses of brain connections provided insight into networks properties.

We aimed to reveal how APOE genotypes differentially confer vulnerability or resilience to select brain circuits during aging, and for different sexes. Identification of vulnerable networks may help understand the etiology of neurodegenerative disease, and facilitate targeted interventions. Monitoring such changes with sensitive biomarkers may help stratify patients, and assess response to therapies.

Our behavioral tests determined that APOE4HN mice have deficits in the learning and memory function as tested in the MWM during learning trials and during the first probe tests at 3 days, but not at 5 days. The NOR also indicated deficits as the recognition index was lower when tested at 24 h, but not 90 min after the initial objects presentations. These deficits in long term memory for APOE4HN mice suggest perturbations in brain networks involved in memory function.

APOE4HN had 6% smaller brains when compared to age matched APOE3HN controls, and the regions accounting for these differences included the entorhinal and temporal association cortex, the cingulate cortex and amygdala (McGaugh et al., 1996), suggesting alterations in emotional memory in addition to the demonstrated spatial and object recognition memory effects we have measured. Interestingly, the amygdalopiriform transition area, and the accumbens were also smaller in APOE4HN mice. Sensory and motor areas such as the olfactory areas/the piriform cortex, the visual and motor cortex areas, and the cerebellum and its connections also suffered atrophy. These regional changes point to spatially extensive network alterations in APOE4HN mice. Voxel based analyses confirmed these findings and added information due to increased sensitivity to smaller clusters of atrophy in the primary motor cortex, striatum, septum, subiculum, and the mediodorsal thalamic nuclei. We found changes in the volume of the pons and cerebellum, which have been traditionally thought to be involved only in late stages of AD, but have also been shown in age related tauopathy, independently of Aβ presence (Josephs et al., 2017). Fractional anisotropy and connectivity also helped distinguish APOE4 from APOE3 carriers. Interestingly, hyper functional connectivity (Wang et al., 2017) in MCI APOE4 carriers may suggest a compensatory role for the cerebellum at early stages. When present, cerebellar pathology has been associated with increased rates of cognitive dysfunction (Liang and Carlson, 2019), and to be predictive of conversion from MCI to AD. Moreover, in cases of accelerated neurodegeneration, such as chronic traumatic encephalopathy (CTE) following repeated traumatic brain injury (TBI), the cerebellum appears to be one of the most vulnerable brain regions and exhibiting pathology early on (Liang and Carlson, 2019).

This is in contrast with the traditional view associating the cerebellum exclusively with motor coordination and learning, but supported by more recent studies, which have revealed a role for the cerebellum in cognitive functions such as attention, language, working memory, emotion, and in visuospatial navigation (Timmann and Daum, 2007; Baillieux et al., 2008; Timmann et al., 2010). Viral tracer studies have recently demonstrated previously unknown connections between the cerebellum and hippocampus – in particular a polysynaptic circuit from the cerebellar fastigial nucleus with a thalamic relay in the LDDM/LDVL and VL, which in turn synapses on the subiculum, retrosplenial cortex, and rhinal cortex, which all project to the hippocampus (Bohne et al., 2019). These connections are indicative of a role in spatial navigation. Our studies support that APOE4 carriers have differences in such pathways connecting the cerebellum with the hippocampus and also with the piriform cortex, and these differences co-exist with alterations in spatial learning and memory, as well as remote memory for object recognition. Our study suggests that more attention needs to be given to understanding the role of the cerebellum in neurodegenerative diseases, and associated cognitive deficits.

White matter tracts with reduced volume included the corpus callosum, anterior commissure and the middle cerebellar peduncles. FA reductions, commonly seen as indicators of altered microstructural integrity in white matter tracts, were found mostly in the corpus callosum and the cerebellar white matter. In addition hippocampal projection pathways had lower FA, and we noted FA reductions in CA1 areas, where from projections connect to the subiculum and the entorhinal cortex, but also to the basolateral amygdala (BLA), which sends projections to the medial frontal cortex, and the accumbens (also the bed nucleus of stria terminalis, and central amygdaloid nucleus) (Mandyam, 2013).

The complexity of these relationships and the extent of the networks involved demands the development of integrative methods followed by dimensionality reduction strategies. Here we have used a recently developed method (Zhang et al., 2019) for assembling structural connectomes into tensor networks, and mapping those into a reduced dimensional space to identify significant subnetworks associated with traits. This relies on a generalization of principal component analysis. In our case the top 15 principal components explained 91% of the variance. The tensor network principal component analysis helped reveal the top 30 connections, including seven unique structures that best distinguished amongst our two genotypes. A significant portion of these connections were interhemispheric. We found that the pairwise connectivity between two nodes, most often used in standard connectometry studies contain rich information that can be further exploited to reveal genotype and sex differences. The histogram based analyses for tract length and FA were supplemented by bundle specific analyses on spatially clustered sub-bundles, and illustrated different wiring patterns and properties in APOE4HN and APOE3HN, as well as between sexes within each genotype. We paid particular attention to the interhemispheric connections between the hippocampus and piriform cortex, the cerebellum and hippocampus, and the intrahemispheric cerebellar connections. Prompted by the frequency of appearance for the piriform cortex and hippocampus in the top list of connections we also examined the properties of their intrahemispheric connections (**Figure 10**), and these confirmed the male associated differences between genotypes, while showing a stronger tendency for lower FA along these projections for APOE4HN mice.

The main limitations of this study come from the small sample size, and the fact that we pooled our bundles for statistical analysis rather than stratifying them by animal. We argue this provides a first step approach to study differences with genotypes

in animal cohorts which provide virtually genetically identical replicates. Also, formalin fixation may affect tissue properties and cause shrinkage, and we have tried to control these factors by preserving the same interval between animal sacrifice and imaging. Further studies should include more replicates of each sex to infer sex specific interactions between vulnerable networks and APOE alleles.

We note that APOE-HN mice do not express mutated APP leading to prevalent amyloid pathology, therefore our study could not address the mechanism of interaction between the various APOE alleles and Aß. However, the literature suggests that APOE4 exerts an effect on the pathogenesis on AD through Aß and also Aß independent pathways (Huang, 2010). While the deposition of Aβ is apoE isoform-specific, it is not clear whether and how they influence the accumulation and progression of tau pathology (Balu et al., 2019). APOE isoforms also affect neuroinflammation, vascular function, metabolism, synaptic plasticity, and transcription regulation (Liao et al., 2017). In addition to the human APOE alleles, our mouse models have a murine NO synthase 2 knockout background ($mNos2^{-/-}$) (Colton et al., 2006, 2014). In place of the mouse Nos2 gene these express a functional human NOS2 gene (Vitek et al., 2006). These modifications lead to reduced immune-activated *NOS2* expression and *iNOS* production compared to wild type rodents. This allows to model the human innate immune response, in particular with respect to the redox microenvironment, and NO production (Hoos et al., 2014). Mouse models on this genetic background expressing APP mutations present multiple AD like phenotypes (Wilcock et al., 2008; Colton et al., 2014; Kan et al., 2015; Badea et al., 2016). Here we assessed the differential effects of the interaction of the humanized NOS background with APOE3 and APOE4 alleles.

Our current study cannot rule out developmental effects in our mice, however, human studies point to APOE4 associated differences in asymptomatic and young carriers (Reiter et al., 2012; Piers, 2018), which may change in time (Koelewijn et al., 2019). Further studies should explore in more detail the relation between behavioral, imaging, and connectome markers.

Our findings parallel other investigations in the study of connectivity alterations associated with APOE status in human carriers and mouse models (Heise et al., 2014; Wiesmann et al., 2016; Luo et al., 2017; Korthauer et al., 2018). These studies support the presence of alterations in both functional and structural connectomes, and report separately such biomarkers. They generally point to a role for the hippocampus and its connection, and vascular function through perfusion changes, which changes may affect cognition. The importance of multimodal approaches (Wiesmann et al., 2016) and developing a framework for integrating such biomarkers has long been recognized (Madden et al., 2009), and connectomes present such an opportunity.

We argue that unique entries in a connectome contain rich information which can be further exploited at finer scales, and perhaps using different modalities. In our analyses we found significant differences in the size based ranking of the subbundles, indicating different wiring patterns in mice with different APOE alleles, and perhaps compensatory mechanisms – which are not evident at the level of whole bundle/pairwise connectivity analysis. The high resolution imaging allowed us to infer subdivisions of the bundles, based on spatial geometric relationships, and these remain to be validated using complementary methods. APOE4HN mice had consistently lower FA along the cerebellar connections, while the patterns for the interhemispheric hippocampal-cerebellar and hippocampal-piriform connections varied by subbundles, and position along the bundle, with lower FA for the largest subbundle in APOE4 carriers, but higher FAs were also observed. We observed frequently higher variability in APOE4HN mice, and in APOE4HN females compared to males. An examination of sex based differences in the hippocampal cerebellar connections indicated more consistency between the males of APOE4HN and APOE3HN genotypes, with females showing more differences with genotype in the FA curve shape (**Figure 9E**), and females of the same genotype showing more variability (**Figures 9E–G**). We note that the connections we analyzed run also through gray matter, rather than just white matter. Thus the associated FA values may be affected by aging and pathology, which led to increased FA values in gray matter.

We identified changes in volume and FA in areas which have been associated with amyloid deposition in AD patients, such as the entorhinal cortex, hippocampus, cingulate cortex and amygdala. However, our animal models do not have APP mutations predisposing them to abundant amyloid deposition, which suggests that the regions we have identified may be part of a vulnerable brain network prone to the development, propagation and deposition of misfolded proteins, proteinopathies, or involved in other pathological processes as well. While some of the significant differences in the connectome identified decreased FA along the tracts connecting these regions, the reverse was also noted. Such findings have also been reported in human APOE4 carriers, particularly at younger ages, and the effects are not uniform throughout the brain. We believe that FA may show different patterns, not only between genotypes or sexes, but even along bundles and these differences can be due to changes in the local brain microenvironment, toxicity, or myelination. Compensatory mechanisms can also play a role. In **Figure 6** we note that the subbundle 5 passes largely through gray matter, so we may observe changes due to gliosis in the vicinity of such bundles.

We also found changes in the striatum gigantocellular reticular nuclei, cerebellum and cortical motor related regions. These results support the role of APOE4 (Serrano-Pozo et al., 2011) as a risk factor for Parkinson's disease (Pankratz et al., 2006), where alpha synuclein may also be preferentially deposited in the CA2–CA3 regions of the hippocampus, insula, amygdala and cingulate cortex (Harding and Halliday, 2001; Bertrand et al., 2004). This points to shared mechanisms and vulnerable networks across neurodegenerative conditions such as AD and PD. Approximately 25% of AD patients develop PD, and 50% of PD patients develop AD after 65 years of age (Hansen et al., 1990). Moreover, 70% of LOAD patients display α-synuclein-positive LB-like inclusions in the amygdala and limbic structures (Trojanowski et al., 1998; Hamilton, 2000).

Identifying differences between these vulnerable networks, based on multivariate biomarkers may help stratify patients, as e.g., dementia with Lewy bodies can be distinguished from Parkinson's disease dementia based on the presence of Aβ deposits in the striatum (Duda et al., 2002) and hippocampus (Masliah et al., 1993).

We have shown that behavioral and imaging markers corroborate to help identify vulnerable networks in novel mouse models of pathological aging, relying on the genetic risk factor conferred by APOE4 alleles. We have also tried to gain insight into the rich information behind one single entry in a connectome. Imaging and DWI based connectomics provided multiple sensitive biomarkers to monitor the integrity of these networks or their failure in aging and disease. We hope that future work will address the mechanism underlying the switch from normal to pathological aging, and will help monitor the effects of interventions.

DATA AVAILABILITY STATEMENT

All datasets generated for this study are included in the article/supplementary material.

ETHICS STATEMENT

The animal study was reviewed and approved by Duke IACUC.

AUTHOR CONTRIBUTIONS

AB, WW, CC, and DD designed the research. AB, WW, MW, RA, YQ, JS, and JW performed the research and analyzed the data. AB, WW, SK, and EG contributed new analytical tools. GJ founding director of CIVM, helped build and maintain the imaging resources at CIVM. AB, CC, WW, JS, and DD wrote the manuscript.

FUNDING

This work was supported by the National Institutes of Health through K01 AG041211, R01 AG045422, R56 AG051765, R56 AG 057895, R01AG057895, R01 MH118927, and R01 AG066184. We are grateful for NSF support through the REU initiative at Duke (Award 1659615). Imaging was performed at the Center for *In Vivo* Microscopy (CIVM), supported through P41 EB015897.

ACKNOWLEDGMENTS

We thank all CIVM-ers for their efforts to build and maintain this imaging resource, and a collaborative learning environment. We also thank Dr. Zhengwu Zhang and Dr. Richard O'Brien for helpful discussions.

REFERENCES

Anderson, R. J., Cook, J. J., Delpratt, N., Nouls, J. C., Gu, B., McNamara, J. O., et al. (2018a). Small animal multivariate brain analysis (SAMBA) – a high throughput pipeline with a validation framework. *Neuroinformatics* 17, 451–472.

Anderson, R. J., Wang, N., Cook, J. J., Cofer, G. P., Dibb, R., Johnson, G. A., et al. (2018b). A high performance computing cluster implementation of compressed sensing reconstruction for MR histology. *Proc. Intl. Soc. Mag. Reson. Med.* 26.

Anderson, R. J., Cook, J. J., Delpratt, N. A., Nouls, J. C., Gu, B., McNamara, J. O., et al. (2017). Small Animal multivariate brain analysis (SAMBA): a high throughput pipeline with a validation framework. *arXiv[preprint]*

Avants, B. B., Epstein, C. L., Grossman, M., and Gee, J. C. (2008). Symmetric diffeomorphic image registration with cross-correlation: evaluating automated labeling of elderly and neurodegenerative brain. *Med. Image Anal.* 12, 26–41. doi: 10.1016/j.media.2007.06.004

Avants, B. B., Tustison, N. J., Song, G., Cook, P. A., Klein, A., and Gee, J. C. (2011). A reproducible evaluation of ANTs similarity metric performance in brain image registration. *Neuroimage* 54, 2033–2044. doi: 10.1016/j.neuroimage.2010.09.025

Badea, A., Delpratt, N. A., Anderson, R. J., Dibb, R., Qi, Y., Wei, H., et al. (2019). Multivariate MR biomarkers better predict cognitive dysfunction in mouse models of Alzheimer's disease. *Magn. Reson. Imaging* 60, 52–67. doi: 10.1016/j.mri.2019.03.022

Badea, A., Kane, L., Anderson, R. J., Qi, Y., Foster, M., Cofer, G. P., et al. (2016). The fornix provides multiple biomarkers to characterize circuit disruption in a mouse model of Alzheimer's disease. *Neuroimage* 142, 498–511. doi: 10.1016/j.neuroimage.2016.08.014

Baillieux, H., De Smet, H. J., Paquier, P. F., De Deyn, P. P., and Marien, P. (2008). Cerebellar neurocognition: insights into the bottom of the brain. *Clin. Neurol. Neurosurg.* 110, 763–773. doi: 10.1016/j.clineuro.2008.05.013

Balu, D., Karstens, A. J., Loukenas, E., Maldonado Weng, J., York, J. M., Valencia-Olvera, A. C., et al. (2019). The role of APOE in transgenic mouse models of AD. *Neurosci. Lett.* 707:134285. doi: 10.1016/j.neulet.2019.134285

Bedlack, R. S., Strittmatter, W. J., and Morgenlander, J. C. (2000). Apolipoprotein E and neuromuscular disease: a critical review of the literature. *Arch. Neurol.* 57, 1561–1565.

Belloy, M. E., Napolioni, V., and Greicius, M. D. (2019). A quarter century of APOE and Alzheimer's disease: progress to date and the path forward. *Neuron* 101, 820–838. doi: 10.1016/j.neuron.2019.01.056

Bertrand, E., Lechowicz, W., Szpak, G. M., Lewandowska, E., Dymecki, J., and Wierzba-Bobrowicz, T. (2004). Limbic neuropathology in idiopathic Parkinson's disease with concomitant dementia. *Folia Neuropathol.* 42, 141–150.

Bohne, P., Schwarz, M. K., Herlitze, S., and Mark, M. D. (2019). A new projection from the deep cerebellar nuclei to the hippocampus via the Ventrolateral and Laterodorsal Thalamus in mice. *Front. Neural Circ.* 13:51. doi: 10.3389/fncir.2019.00051

Calabrese, E., Badea, A., Cofer, G., Qi, Y., and Johnson, G. A. (2015). A diffusion mri tractography connectome of the mouse brain and comparison with neuronal tracer data. *Cereb. Cortex* 25, 4628–4637. doi: 10.1093/cercor/bhv121

Colton, C. A., Vitek, M. P., Wink, D. A., Xu, Q., Cantillana, V., Previti, M. L., et al. (2006). NO synthase 2 (NOS2) deletion promotes multiple pathologies in a mouse model of Alzheimer's disease. *Proc. Natl. Acad. Sci. U.S.A.* 103, 12867–12872. doi: 10.1073/pnas.0601075103

Colton, C. A., Wilson, J. G., Everhart, A., Wilcock, D. M., Puolivali, J., Heikkinen, T., et al. (2014). mNos2 deletion and human NOS2 replacement in Alzheimer disease models. *J. Neuropathol. Exp. Neurol.* 73, 752–769. doi: 10.1097/NEN.0000000000000094

De Strooper, B., and Karran, E. (2016). The cellular phase of Alzheimer's disease. *Cell* 164, 603–615.

Devanand, D. P., Pradhaban, G., Liu, X., Khandji, A., De Santi, S., Segal, S., et al. (2007). Hippocampal and entorhinal atrophy in mild cognitive impairment: prediction of Alzheimer disease. *Neurology* 68, 828–836. doi: 10.1212/01.wnl.0000256697.20968.d7

Duda, J. E., Giasson, B. I., Mabon, M. E., Lee, V. M., and Trojanowski, J. Q. (2002). Novel antibodies to synuclein show abundant striatal pathology in Lewy body diseases. *Ann. Neurol.* 52, 205–210. doi: 10.1002/ana.10279

Femminella, G. D., Taylor-Davies, G., Scott, J., and Edison, P. (2018). Do cardiometabolic risk factors influence amyloid, tau, and neuronal function in APOE4 carriers and non-carriers in Alzheimer's disease trajectory? *J. Alzheimer's Dis.* 64, 981–993. doi: 10.3233/JAD-180365

Fischer, F. U., Wolf, D., Scheurich, A., and Fellgiebel, A. (2015). Altered whole-brain white matter networks in preclinical Alzheimer's disease. *Neuroimage Clin.* 8, 660–666. doi: 10.1016/j.nicl.2015.06.007

Friston, K. J., Worsley, K. J., Frackowiak, R. S., Mazziotta, J. C., and Evans, A. C. (1994). Assessing the significance of focal activations using their spatial extent. *Hum. Brain Mapp.* 1, 210–220. doi: 10.1002/hbm.460010306

Garyfallidis, E., Brett, M., Amirbekian, B., Rokem, A., van der Walt, S., Descoteaux, M., et al. (2014). Dipy, a library for the analysis of diffusion MRI data. *Front. Neuroinform.* 8:8. doi: 10.3389/fninf.2014.00008

Garyfallidis, E., Brett, M., Correia, M. M., Williams, G. B., and Nimmo-Smith, I. (2012). QuickBundles, a method for tractography simplification. *Front. Neurosci.* 6:175. doi: 10.3389/fnins.2012.00175

Garyfallidis, E., Cote, M. A., Rheault, F., Sidhu, J., Hau, J., Petit, L., et al. (2018). Recognition of white matter bundles using local and global streamline-based registration and clustering. *Neuroimage* 170, 283–295. doi: 10.1016/j.neuroimage.2017.07.015

Garyfallidis, E., Ocegueda, O., Wassermann, D., and Descoteaux, M. (2015). Robust and efficient linear registration of white-matter fascicles in the space of streamlines. *Neuroimage* 117, 124–140. doi: 10.1016/j.neuroimage.2015.05.016

Hamilton, R. L. (2000). Lewy bodies in Alzheimer's disease: a neuropathological review of 145 cases using alpha-synuclein immunohistochemistry. *Brain Pathol.* 10, 378–384. doi: 10.1111/j.1750-3639.2000.tb00269.x

Hansen, L., Salmon, D., Galasko, D., Masliah, E., Katzman, R., DeTeresa, R., et al. (1990). The Lewy body variant of Alzheimer's disease: a clinical and pathologic entity. *Neurology* 40, 1–8.

Harding, A. J., and Halliday, G. M. (2001). Cortical lewy body pathology in the diagnosis of dementia. *Acta Neuropathol.* 102, 355–363.

Heise, V., Filippini, N., Trachtenberg, A. J., Suri, S., Ebmeier, K. P., and Mackay, C. E. (2014). Apolipoprotein E genotype, gender and age modulate connectivity of the hippocampus in healthy adults. *Neuroimage* 98, 23–30. doi: 10.1016/j.neuroimage.2014.04.081

Hoos, M. D., Vitek, M. P., Ridnour, L. A., Wilson, J., Jansen, M., Everhart, A., et al. (2014). The impact of human and mouse differences in NOS2 gene expression on the brain's redox and immune environment. *Mol. Neurodegener.* 9:50. doi: 10.1186/1750-1326-9-50

Huang, Y. (2010). Aβ-independent roles of apolipoprotein E4 in the pathogenesis of Alzheimer's disease. *Trends Mol. Med.* 16, 287–294. doi: 10.1016/j.molmed.2010.04.004

Huynh, T. V., Davis, A. A., Ulrich, J. D., and Holtzman, D. M. (2017). Apolipoprotein E and Alzheimer's disease: the influence of apolipoprotein E on amyloid-beta and other amyloidogenic proteins. *J. Lipid Res.* 58, 824–836. doi: 10.1194/jlr.R075481

Jack, CR Jr, Petersen, R. C., Xu, Y. C., O'Brien, P. C., Smith, G. E., Ivnik, R. J., et al. (1999). Prediction of AD with MRI-based hippocampal volume in mild cognitive impairment. *Neurology* 52, 1397–1403.

Josephs, K. A., Murray, M. E., Tosakulwong, N., Whitwell, J. L., Knopman, D. S., Machulda, M. M., et al. (2017). Tau aggregation influences cognition and hippocampal atrophy in the absence of beta-amyloid: a clinico-imaging-pathological study of primary age-related tauopathy (PART). *Acta Neuropathol.* 133, 705–715. doi: 10.1007/s00401-017-1681-2

Kan, M. J., Lee, J. E., Wilson, J. G., Everhart, A. L., Brown, C. M., Hoofnagle, A. N., et al. (2015). Arginine deprivation and immune suppression in a mouse model of Alzheimer's disease. *J. Neurosci.* 35, 5969–5982. doi: 10.1523/JNEUROSCI.4668-14.2015

Koelewijn, L., Lancaster, T. M., Linden, D., Dima, D. C., Routley, B. C., Magazzini, L., et al. (2019). Oscillatory hyperactivity and hyperconnectivity in young APOE-varepsilon4 carriers and hypoconnectivity in Alzheimer's disease. *eLife* 8:e36011. doi: 10.7554/eLife.36011

Korthauer, L. E., Zhan, L., Ajilore, O., Leow, A., and Driscoll, I. (2018). Disrupted topology of the resting state structural connectome in middle-aged APOE ε4 carriers. *Neuroimage* 178, 295–305. doi: 10.1016/j.neuroimage.2018.05.052

Liang, K. J., and Carlson, E. S. (2019). Resistance, vulnerability and resilience: a review of the cognitive cerebellum in aging and neurodegenerative diseases. *Neurobiol. Learn. Mem.* doi: 10.1016/j.nlm.2019.01.004 [Epub ahead of print].

Liao, F., Yoon, H., and Kim, J. (2017). Apolipoprotein E metabolism and functions in brain and its role in Alzheimer's disease. *Curr. Opin. Lipidol.* 28, 60–67. doi: 10.1097/MOL.0000000000000383

Luo, X., Qiu, T., Jia, Y., Huang, P., Xu, X., Yu, X., et al. (2017). Intrinsic functional connectivity alterations in cognitively intact elderly APOE ε4 carriers measured by eigenvector centrality mapping are related to cognition and CSF biomarkers: a preliminary study. *Brain Imaging Behav.* 11, 1290–1301. doi: 10.1007/s11682-016-9600-z

Madden, D. J., Bennett, I. J., and Song, A. W. (2009). Cerebral white matter integrity and cognitive aging: contributions from diffusion tensor imaging. *Neuropsychol. Rev.* 19, 415–435. doi: 10.1007/s11065-009-9113-2

Mandyam, C. D. (2013). The interplay between the hippocampus and amygdala in regulating aberrant hippocampal neurogenesis during protracted abstinence from alcohol dependence. *Front. Psychiatry* 4:61. doi: 10.3389/fpsyt.2013.00061

Masliah, E., Mallory, M., DeTeresa, R., Alford, M., and Hansen, L. (1993). Differing patterns of aberrant neuronal sprouting in Alzheimer's disease with and without Lewy bodies. *Brain Res.* 617, 258–266. doi: 10.1016/0006-8993(93)91093-8

McGaugh, J. L., Cahill, L., and Roozendaal, B. (1996). Involvement of the amygdala in memory storage: interaction with other brain systems. *Proc. Natl. Acad. Sci. U.S.A.* 93, 13508–13514. doi: 10.1073/pnas.93.24.13508

Pankratz, N., Byder, L., Halter, C., Rudolph, A., Shults, C. W., Conneally, P. M., et al. (2006). Presence of an APOE4 allele results in significantly earlier onset of Parkinson's disease and a higher risk with dementia. *Mov. Disord.* 21, 45–49. doi: 10.1002/mds.20663

Piers, R. J. (2018). Structural brain volume differences between cognitively intact ApoE4 carriers and non-carriers across the lifespan. *Neural. Regen. Res.* 13, 1309–1312. doi: 10.4103/1673-5374.235408

Reiter, K., Alpert, K. I., Cobia, D. J., Kwasny, M. J., Morris, J. C., Csernansky, J. C., et al. (2012). Cognitively normal individuals with AD parents may be at risk for developing aging-related cortical thinning patterns characteristic of AD. *Neuroimage* 61, 525–532. doi: 10.1016/j.neuroimage.2012.03.083

Sala Frigerio, C., Wolfs, L., Fattorelli, N., Thrupp, N., Voytyuk, I., Schmidt, I., et al. (2019). The major risk factors for Alzheimer's disease: age, sex, and genes modulate the microglia response to abeta plaques. *Cell Rep.* 27, 1293.e6–1306.e6. doi: 10.1016/j.celrep.2019.03.099

Schellenberg, G. D. (1995). Genetic dissection of Alzheimer disease, a heterogeneous disorder. *Proc. Natl. Acad. Sci. U.S.A.* 92, 8552–8559. doi: 10.1073/pnas.92.19.8552

Serrano-Pozo, A., Frosch, M. P., Masliah, E., and Hyman, B. T. (2011). Neuropathological alterations in Alzheimer disease. *Cold Spring Harb. Perspect. Med.* 1:a006189. doi: 10.1101/cshperspect.a006189

Timmann, D., and Daum, I. (2007). Cerebellar contributions to cognitive functions: a progress report after two decades of research. *Cerebellum* 6, 159–162. doi: 10.1080/14734220701496448

Timmann, D., Drepper, J., Frings, M., Maschke, M., Richter, S., Gerwig, M., et al. (2010). The human cerebellum contributes to motor, emotional and cognitive associative learning. A Review. *Cortex* 46, 845–857. doi: 10.1016/j.cortex.2009.06.009

Torok, J., Maia, P. D., Powell, F., Pandya, S., Raj, A., Alzheimer's Disease, et al. (2018). A method for inferring regional origins of neurodegeneration. *Brain* 141, 863–876. doi: 10.1093/brain/awx371

Trojanowski, J. Q., Goedert, M., Iwatsubo, T., and Lee, V. M. (1998). Fatal attractions: abnormal protein aggregation and neuron death in Parkinson's disease and Lewy body dementia. *Cell Death Differ.* 5, 832–837. doi: 10.1038/sj.cdd.4400432

Tudorache, I. F., Trusca, V. G., and Gafencu, A. V. (2017). Apolipoprotein E – a multifunctional protein with implications in various pathologies as a result of its structural features. *Comput. Struct. Biotechnol. J.* 15, 359–365. doi: 10.1016/j.csbj.2017.05.003

Vitek, M. P., Brown, C., Xu, Q., Dawson, H., Mitsuda, N., and Colton, C. A. (2006). Characterization of NO and cytokine production in immune-activated microglia and peritoneal macrophages derived from a mouse model expressing the human NOS2 gene on a mouse NOS2 knockout background. *Antioxid. Redox. Signal.* 8, 893–901. doi: 10.1089/ars.2006.8.893

Wang, N., Anderson, R. J., Badea, A., Cofer, G., Dibb, R., Qi, Y., et al. (2018). Whole mouse brain structural connectomics using magnetic resonance histology. *Brain Struct. Funct.* 223, 4323–4335. doi: 10.1007/s00429-018-1750-x

Wang, Z., Dai, Z., Shu, H., Liao, X., Yue, C., Liu, D., et al. (2017). APOE Genotype effects on intrinsic brain network connectivity in patients with amnestic mild cognitive impairment. *Sci. Rep.* 7:397. doi: 10.1038/s41598-017-00432-0

Wiesmann, M., Zerbi, V., Jansen, D., Haast, R., Lutjohann, D., Broersen, L. M., et al. (2016). A dietary treatment improves cerebral blood flow and brain connectivity in aging apoE4 mice. *Neural. Plast.* 2016:6846721. doi: 10.1155/2016/6846721

Wilcock, D. M., Lewis, M. R., Van Nostrand, W. E., Davis, J., Previti, M. L., Gharkholonarehe, N., et al. (2008). Progression of amyloid pathology to Alzheimer's disease pathology in an amyloid precursor protein transgenic mouse model by removal of nitric oxide synthase 2. *J. Neurosci.* 28, 1537–1545. doi: 10.1523/jneurosci.5066-07.2008

Zhang, Z., Allen, G. I., Zhu, H., and Dunson, D. (2019). Tensor network factorizations: relationships between brain structural connectomes and traits. *Neuroimage* 197, 330–343. doi: 10.1016/j.neuroimage.2019.04.027

Conflict of Interest: The authors declare that the research was conducted in the absence of any commercial or financial relationships that could be construed as a potential conflict of interest.

frontiers in Neuroinformatics

REVIEW
published: 22 January 2020
doi: 10.3389/fninf.2019.00078

Animal Functional Magnetic Resonance Imaging: Trends and Path Toward Standardization

*Francesca Mandino[1,2], Domenic H. Cerri[3], Clement M. Garin[4,5], Milou Straathof[6], Geralda A. F. van Tilborg[6], M. Mallar Chakravarty[7,8], Marc Dhenain[4,5], Rick M. Dijkhuizen[6], Alessandro Gozzi[9], Andreas Hess[10], Shella D. Keilholz[11], Jason P. Lerch[12,13], Yen-Yu Ian Shih[3] and Joanes Grandjean[1,14]**

[1] Singapore Bioimaging Consortium, Agency for Science, Technology and Research, Singapore, Singapore, [2] Faculty of Biology, Medicine and Health, The University of Manchester, Manchester, United Kingdom, [3] Center for Animal MRI, Department of Neurology, Biomedical Research Imaging Center, The University of North Carolina at Chapel Hill, Chapel Hill, NC, United States, [4] Direction de la Recherche Fondamentale, MIRCen, Institut de Biologie François Jacob, Commissariat à l'Énergie Atomique et aux Énergies Alternatives, Fontenay-aux-Roses, France, [5] Neurodegenerative Diseases Laboratory, Centre National de la Recherche Scientifique, UMR 9199, Université Paris-Sud, Université Paris-Saclay, Fontenay-aux-Roses, France, [6] Biomedical MR Imaging and Spectroscopy Group, Center for Image Sciences, University Medical Center Utrecht, Utrecht University, Utrecht, Netherlands, [7] Department of Psychiatry, Douglas Mental Health University Institute, McGill University, Montreal, QC, Canada, [8] Department of Biological and Biomedical Engineering, Douglas Mental Health University Institute, McGill University, Montreal, QC, Canada, [9] Functional Neuroimaging Laboratory, Istituto Italiano di Tecnologia, Centre for Neuroscience and Cognitive Systems @ UNITN, Rovereto, Italy, [10] Institute of Experimental and Clinical Pharmacology and Toxicology, Friedrich–Alexander University Erlangen–Nürnberg, Erlangen, Germany, [11] Department of Biomedical Engineering, Georgia Tech, Emory University, Atlanta, GA, United States, [12] Hospital for Sick Children, Department of Medical Biophysics, University of Toronto, Toronto, ON, Canada, [13] Wellcome Centre for Integrative NeuroImaging, University of Oxford, Oxford, United Kingdom, [14] Department of Radiology and Nuclear Medicine, Donders Institute for Brain, Cognition, and Behaviour, Donders Institute, Radboud University Medical Center, Nijmegen, Netherlands

OPEN ACCESS

Edited by:
Jan G. Bjaalie,
University of Oslo, Norway

Reviewed by:
Jiaojian Wang,
University of Pennsylvania, United States
Noam Shemesh,
Champalimaud Foundation, Portugal
Abraham Z. Snyder,
Washington University in St. Louis, United States

***Correspondence:**
Joanes Grandjean
Joanes.Grandjean@radboudumc.nl

Received: 29 May 2019
Accepted: 19 December 2019
Published: 22 January 2020

Citation:
Mandino F, Cerri DH, Garin CM, Straathof M, van Tilborg GAF, Chakravarty MM, Dhenain M, Dijkhuizen RM, Gozzi A, Hess A, Keilholz SD, Lerch JP, Shih Y-YI and Grandjean J (2020) Animal Functional Magnetic Resonance Imaging: Trends and Path Toward Standardization. Front. Neuroinform. 13:78. doi: 10.3389/fninf.2019.00078

Animal whole-brain functional magnetic resonance imaging (fMRI) provides a non-invasive window into brain activity. A collection of associated methods aims to replicate observations made in humans and to identify the mechanisms underlying the distributed neuronal activity in the healthy and disordered brain. Animal fMRI studies have developed rapidly over the past years, fueled by the development of resting-state fMRI connectivity and genetically encoded neuromodulatory tools. Yet, comparisons between sites remain hampered by lack of standardization. Recently, we highlighted that mouse resting-state functional connectivity converges across centers, although large discrepancies in sensitivity and specificity remained. Here, we explore past and present trends within the animal fMRI community and highlight critical aspects in study design, data acquisition, and post-processing operations, that may affect the results and influence the comparability between studies. We also suggest practices aimed to promote the adoption of standards within the community and improve between-lab reproducibility. The implementation of standardized animal neuroimaging protocols will facilitate animal population imaging efforts as well as meta-analysis and replication studies, the gold standards in evidence-based science.

Keywords: resting-state, rodent, non-human primate, optogenetics, DREADD

INTRODUCTION

A detailed understanding of the mammalian brain structure and function is one of the greatest challenges of modern neuroscience. Approaching the complexity of the organ and the levels of organization of neuronal circuits across several orders of magnitudes, both spatially and temporally, requires the collective scientific efforts from multiple teams across several disciplines. Neuroimaging, especially by means of magnetic resonance imaging (MRI), is playing a preponderant role in mapping the human and animal brain, due to its non-invasiveness, excellent soft-tissue contrast, and multiple readouts. The human neuroimaging research has accelerated over the past decade, fueled by numerous discoveries about brain structure and function and its relation to disorders. In turn, this has led to population imaging efforts aimed to describe variations in brain structure and function, and their relation to behavioral traits, genetic polymorphisms, and pathology. For instance, since its original description in 1995 (Biswal et al., 1995), resting-state functional connectivity (RS-FC) has been at the center of numerous population imaging initiatives, such as the 1,000 Functional Connectomes Project (Biswal et al., 2010), the WU-Minn Human Connectome Project (Van Essen and Ugurbil, 2012; Van Essen et al., 2013), and the UK Biobank (Miller et al., 2016). In addition to providing an important baseline of healthy cohorts, these initiatives are complemented with population imaging dedicated to specific psychiatric and neurological disorders, such as the Alzheimer's Disease Neuroimaging Initiative (Petersen et al., 2010; Weiner et al., 2012), the Autism Brain Imaging Data Exchange (Di Martino et al., 2014), or Attention-Deficit Hyperactivity Disorder (HD-200 Consortium, 2012). Collectively, these resources have significantly advanced our understanding of neuro- and psychopathologies, as well as providing an understanding of disorder spectrums at a population level.

In contrast to the above, functional neuroimaging studies in animals have remained mostly confined to single centers, often relying on lab-specific acquisition and processing protocols. There has been little pressure toward standardization within the community, and results from different centers have remained inherently difficult to compare, due to discrepancies related to animal housing and preparation, recording hardware, and analysis methodologies. It is now emerging that these preparation divergences are at the stem of a number of dissensions within the animal functional neuroimaging community, such as the nature of unilateral vs. bilateral resting-state networks (RSN) in mice (Jonckers et al., 2011; Grandjean et al., 2014; Mechling et al., 2014; Sforazzini et al., 2014), the bilateral BOLD response to non-noxious paw electrical stimulation in mice (Bosshard et al., 2010; Schroeter et al., 2014; Shim et al., 2018), the indirect artifacts emerging in optogenetics fMRI (ofMRI) through either heating or vascular photoactivation (Christie et al., 2013; Rungta et al., 2017; Schmid et al., 2017), or the spatial extent of distributed networks of translational relevance, such as the rodent "default mode network" (DMN) reviewed in Gozzi and Schwarz (2016). Only recently did efforts emerge to combine and compare structural and/or functional MRI from multiple centers in monkeys (Milham et al., 2018) and in mice (**Figure 1**; Grandjean et al., 2019a). These initial studies provide solid grounds for the development of replication studies, meta-analyses, and multi-center consortia, the gold standards in evidence-based science.

Presently, we aim to describe the current trends in the field and to examine how these impact the results and their comparability with the rest of the literature. While recommendations to enhance reproducibility exists for human neuroimaging (Poldrack et al., 2008), a large number of acquisition and data processing aspects remain specific to animal imaging. We systematically assessed the animal fMRI literature for data acquisition and analysis procedures to provide an overview of the collective directions taken within the animal imaging community. We then reviewed the major considerations taking place in the study design, and how these impact results and their interpretability. Finally, we use this information to provide a road map toward the adoption of standards that will enable animal population studies to inform on the functional mammalian brain.

METHODS

We searched the Pubmed database[1] on February 11, 2019 for the terms "functional magnetic resonance imaging," "functional MRI," or "fMRI" within the abstract or title, excluding studies in human and reviews, from 1990 onward, using the following command. *"Search ((fMRI[Title/Abstract]) OR functional MRI[Title/Abstract]) OR functional magnetic resonance imaging[Title/Abstract] Sort by: Best Match Filters: Abstract; Publication date from 1990/01/01 to 2019/12/31; Other Animals."* The query returned 2279 entries. The title and abstract from these were manually screened to exclude studies that did not contain primary research using MRI to assess brain function in animals. In total, 868 research article were considered relevant and could be readily accessed. We recorded the type of study: resting-state or paradigm free RS-FC recordings, pharmacological-evoked, opto-/chemogenetic neuromodulation, deep-brain stimulation (DBS), or stimulus-evoked (including blocks- or events-related designs with sensory stimulation, gas challenge, etc.). We recorded animals species, including strain, gender (male, female, both, N/A), number of animals used, animal preparation (awake, anesthetized free-breathing, anesthetized ventilated), anesthetic used for maintenance during fMRI, field strength, fMRI sequence and contrast, pre-processing softwares, and noted if the datasets were made available by the authors or in online repositories. The resulting table is made available in the **Supplementary Material**.

RESULTS AND DISCUSSION

Experimental Design

Animal fMRI presents the opportunity for new and creative directions in study design, but care must be taken to ensure that experimental changes in the fMRI signal are sufficiently robust

[1] https://www.ncbi.nlm.nih.gov/pubmed/

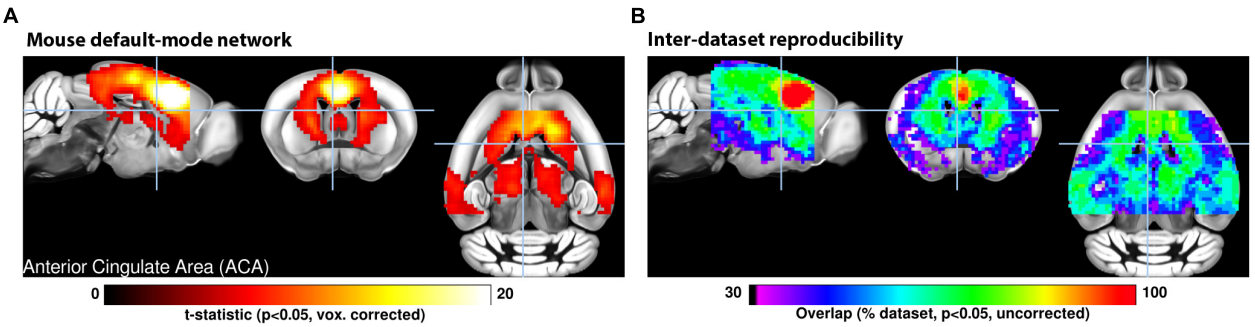

FIGURE 1 | (A) A seed-based analysis of the anterior cingulate area in 98 resting-state fMRI scans reveals the topological distribution of the mouse default-mode network. The regions co-activating with the seed include the dorsal striatum, dorsal thalamus, retrosplenial, and posterior parietal areas. **(B)** The reproducibility of the default-mode network was assessed in 17 independent datasets consisting of 15 scans each. Overlapping one-sample *t*-test maps are summarized in a color-coded overlay. 12/17 datasets present converging topological features, the remaining five failed to present evidence of distal connectivity relative to the seed. Adapted with permission from Grandjean et al. (2019a).

for detection and that results are not contaminated by procedural artifacts. Here we highlight evidence supporting standards and reporting strategies to optimize data quality, interpretation, and reproducibility for several common animal fMRI paradigms.

Stimulus-Evoked fMRI

In animal studies, stimulus-evoked fMRI usually refers to externally applied stimuli during fMRI (e.g., electrical forepaw stimulation), but many principles of study design can be applied to internally delivered stimuli as well, such as with deep-brain stimulation (DBS) and optogenetics. Stimuli can be applied in a block or event-related design. The former alternates between regular stimulation and no-stimulation conditions, while the latter uses brief stimuli presented at varying intervals (Amaro and Barker, 2006). Block designs are best suited to test frequency-related responses and enhance detection power, while event-related designs are best for determining accurate response-time courses and/or frequency-independent functional connectivity (Amaro and Barker, 2006; Van der Linden et al., 2007; Maus and van Breukelen, 2013; Allen et al., 2015; Schlegel et al., 2015; Soares et al., 2016).

Stimulus frequency has a large influence on stimulus-evoked fMRI results. In general, higher frequencies will increase the stimulus input per unit time, thus potentially boosting signal and ability to detect evoked responses (Amaro and Barker, 2006; Kim et al., 2010; Maus and van Breukelen, 2013), but excessive electrical or optical stimulation can cause tissue damage (Kiyatkin, 2007; Lai et al., 2015; Acker et al., 2016; Cogan et al., 2016), heating and related artifacts (Zeuthen, 1978; Kiyatkin, 2007; Cardin et al., 2010; Christie et al., 2013; Lai et al., 2015; Stujenske et al., 2015; Acker et al., 2016), and non-specific effects (Tuor et al., 2002; Christie et al., 2013; Schroeter et al., 2014; Shih et al., 2014; Schlegel et al., 2015; Rungta et al., 2017). Stimuli may also change basic physiology and therefore alter the fMRI response (Tuor et al., 2002; Ray et al., 2011; Tsubota et al., 2012; Li et al., 2013; Schroeter et al., 2014; Shih et al., 2014; Reimann C. et al., 2018), thereby occluding signal from the stimulus itself. These findings highlight the importance of carefully monitoring physiology (see below) and establishing frequency-response curves for the stimuli of choice.

Functional Connectivity MRI

Animal fMRI data acquired in the absence of stimulation or modulation, RS-FC, is commonly used to probe synchronization of spontaneously fluctuating signals between combinations of anatomically, functionally, or procedurally defined brain regions (Lowe et al., 2000; Lu et al., 2007; Zhao et al., 2008; van Meer et al., 2010, 2012; Lu and Stein, 2014; Pan et al., 2015; Guadagno et al., 2018; Grandjean et al., 2019a). The use of RS-FC in animal models has rapidly increased over the past decade (**Figure 2**). To collect the most robust and interpretable RS-FC data, a few principles have been proposed. Recent evidence suggests that brain network components exhibit non-stationary properties (Hutchison et al., 2013a; Keilholz et al., 2013; Liu and Duyn, 2013; Liang et al., 2015a; Pan et al., 2015; Gutierrez-Barragan et al., 2018), therefore repetition time should be sufficiently short (e.g., 1 s) to properly sampled the fluctuations and to detect these changes, and scan length should produce enough frames (a minimum of about 300) to account for a large number of temporal clusters (Majeed et al., 2011; Hutchison et al., 2013b; Jonckers et al., 2015). Critical aspects for such analyses are detailed in a later section. Furthermore, if brain modulation/stimulation is included, additional time should be added during the transition periods to and from resting-state to allow for stable connectivity, and subsequent resting periods following each manipulation should be grouped separately to account for potential neuroadaptations (Pawela et al., 2008; Zhao et al., 2008; Jonckers et al., 2015; Albaugh et al., 2016; Chan et al., 2017; Decot et al., 2017; Chen et al., 2018). Importantly, due to the nature of the signal fluctuations on which RS-FC relies, special care must be ensured with regard to physiology and anesthesia to ensure maximal detection. The effects of animal preparations are further discussed below.

Optogenetics

Many recent stimulus-evoked animal fMRI studies take advantage of the readily MR-compatible optogenetics toolkit

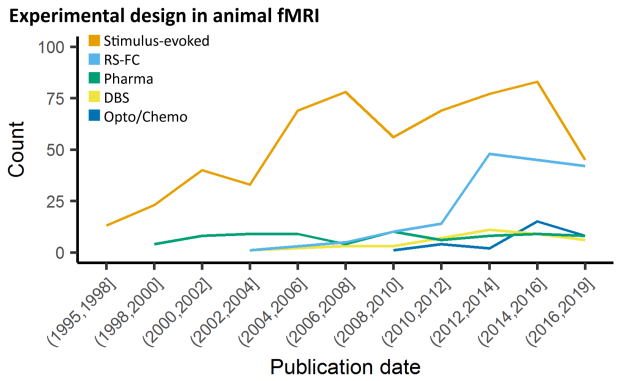

FIGURE 2 | Study design in animal fMRI over time. Stimulus-evoked fMRI (events or blocks related) remain the major component within animal literature. From 2006 and 2010, resting-state fMRI and opto-/chemogenetic fMRI, respectively, have represented an increasing proportion of the animal fMRI studies.

(**Figure 2**; Desai et al., 2011; Abe et al., 2012; Scott and Murphy, 2012; Kahn et al., 2013; Iordanova et al., 2015; Lemieux et al., 2015; Liang et al., 2015b; Takata et al., 2015; Weitz et al., 2015; Albaugh et al., 2016; Chai et al., 2016; Ryali et al., 2016; Yu et al., 2016; Hinz et al., 2017; Lohani et al., 2017; Albers et al., 2018; Brocka et al., 2018; Choe et al., 2018; Leong et al., 2018; Grandjean et al., 2019b). Optogenetics allows for robust stimulation of specific cellular and/or anatomical populations (Zhang et al., 2010; Fenno et al., 2011; Boyden, 2015; Deisseroth, 2015; Griessner et al., 2018), but despite these advantages this relatively new technique adds layers of complexity over DBS, thereby requiring more rigorous methodology and additional controls.

The light-activated channels/pumps expressed in optogenetics, also known as "opsins," provide a great deal of experimental flexibility (Fenno et al., 2011; Deisseroth, 2015; Guru et al., 2015). There are several opsins to choose from for optical excitation of cells, including the commonly used ChR2 (Nagel et al., 2003; Boyden et al., 2005; Zhang et al., 2006; Atasoy et al., 2008; Cardin et al., 2010) variants activated by penetrating red-shifted light (Zhang et al., 2008; Lin et al., 2013; Klapoetke et al., 2014) and ultra-fast variants capable of frequencies up to 200 Hz (Lin et al., 2009; Gunaydin et al., 2010; Hight et al., 2015). If stable excitation over even longer periods is required in fMRI, issues with a continuous light application can be avoided by using step-function opsins which are temporarily activated by a single pulse of light (Berndt et al., 2009; Ferenczi et al., 2016). Notably, there are also several opsins for cellular inhibition (Zhang et al., 2007; Berndt et al., 2014; Chuong et al., 2014), but their application for fMRI is limited as they require longer periods of illumination prone to heat-related artifacts, and anesthetized or sedated animals have low baseline levels of activity (Lahti et al., 1999; Brevard et al., 2003; Sicard et al., 2003).

Injection of viral constructs or expression of foreign genes can potentially change brain function (Liu et al., 1999; Klein et al., 2006; Zimmermann et al., 2008; Lin, 2011; Miyashita et al., 2013), and light can induce heating and related MRI artifacts, tissue damage, and non-specific effects (Elias et al., 1987; Christie et al., 2013; Stujenske et al., 2015; Schmid et al., 2016; Rungta et al., 2017) thus it is critical to characterize opsin expression and activation of the light source with light delivery to empty-vector (e.g., EYFP) controls. It follows that histological confirmation of fiber placement and construct co-localization with targeted promoters is required (Bernstein and Boyden, 2011; Witten et al., 2011; Madisen et al., 2012; Zeng and Madisen, 2012; Allen et al., 2015; Gompf et al., 2015; Lin et al., 2016; Decot et al., 2017). In addition, given the spatial nature of fMRI, the reporting of single-point measurements of light power should be avoided in favor of irradiance (mW/mm^2; Aravanis et al., 2007; Huber et al., 2008; Kahn et al., 2011; Yizhar et al., 2011; Schmid et al., 2017). Finally, light stimulation at frequencies at or below 20 Hz can produce a visual response by activating the visual-related network, requiring light masking or careful control comparison to view experimental effects (Ferenczi et al., 2016; Lin et al., 2016; Decot et al., 2017; Schmid et al., 2017).

Chemogenetics

Chemogenetics, initially termed "pharmacogenetics," utilizes pharmacologically inert ligands to stimulate genetically encoded designer receptors, with the aim to produce drug-like sustained activation or inhibition of specific neuronal populations. Initial attempts to combine this approach with fMRI have involved the regional re-expression of pharmacologically targetable endogenous G-coupled protein receptors (e.g., Htr1a, Gozzi et al., 2012). The recent development of a modular set of evolved G protein-coupled receptors, termed Designer Receptors Exclusively Activated by Designer Drugs (DREADDs) has greatly expanded the capabilities of this approach (Armbruster et al., 2007; Alexander et al., 2009; Lee et al., 2014; English and Roth, 2015; Roth, 2016; Sciolino et al., 2016; Smith et al., 2016; Zhu et al., 2016; Aldrin-Kirk et al., 2018). Like optogenetics, chemogenetics is readily MRI compatible (Giorgi et al., 2017; Roelofs et al., 2017; Chen et al., 2018; Griessner et al., 2018; Markicevic et al., 2018). Despite its potential, there is, however, an ongoing debate about the specificity of chemogenetics ligands both in neurobehavioral studies (MacLaren et al., 2016; Gomez et al., 2017; Mahler and Aston-Jones, 2018; Manvich et al., 2018) and in chemo-fMRI applications (Giorgi et al., 2017), thereby requiring rigorous methodology to control for potential off-target effects.

Both hM3Dq and hM4Di DREADDs are classically activated with infusion of the effector clozapine-N-oxide (CNO) (Armbruster et al., 2007; Alexander et al., 2009; Roth, 2016; Smith et al., 2016; Giorgi et al., 2017; Markicevic et al., 2018), but new evidence suggests that CNO does not cross the blood-brain barrier and instead is back-metabolized *in vivo* into its precursor, clozapine (Gomez et al., 2017; Mahler and Aston-Jones, 2018; Manvich et al., 2018). Importantly, unlike CNO, clozapine is a psychoactive drug, that possesses an affinity for many endogenous receptors. As a result, the use of high CNO doses may result in a plethora of undesirable off-target effects (Ashby and Wang, 1996; Selent et al., 2008; MacLaren et al., 2016; Roth, 2016), including unspecific fMRI response (Giorgi et al., 2017). Overall, it is apparent that chemogenetics effects

cannot be interpreted without proper non-DREADD expressing controls. Specifically, the effect of effector administration should be compared between DREADD expressing, and non-DREADD expressing animals and/or hemispheres. Finally, as with optogenetics, validation of DREADD expression and co-localization with target promoters is essential for data interpretation (Farrell et al., 2013; Smith et al., 2016; Giorgi et al., 2017; Gomez et al., 2017; Roelofs et al., 2017; Aldrin-Kirk et al., 2018; Chen et al., 2018; Markicevic et al., 2018).

Pharmacological fMRI

Modulating the brain with pharmacological agents during animal fMRI has a wide variety of traditional applications such as studying the global effects of compounds and their target neurotransmitter systems (Mueggler et al., 2001; Shah et al., 2004; Ferrari et al., 2012; Razoux et al., 2013; van der Marel et al., 2013; Jonckers et al., 2015). This approach does not require surgical methods, and is apt for identifying global or regional changes in function associated with new or existing drug therapies for neurotransmitter-related brain disorders (Leslie and James, 2000; Martin and Sibson, 2008; Canese et al., 2011; Bifone and Gozzi, 2012; Klomp et al., 2012; Minzenberg, 2012; Medhi et al., 2014), or to map the effect of exogenously administered neuromodulators. In addition, pharmacological challenges can be used to probe how targets and neurotransmitter systems modulate BOLD responses evoked by other stimuli or pharmacological agents (Marota et al., 2000; Hess et al., 2007; Schwarz et al., 2007; Knabl et al., 2008; Rauch et al., 2008; Shih et al., 2012a; Squillace et al., 2014; Shah et al., 2016; Decot et al., 2017; Bruinsma et al., 2018; Griessner et al., 2018). However, functional imaging with pharmacological agents may not be ideal for dynamic or repetitive studies as effects are dependent on diffusion and receptor kinetics (Steward et al., 2005; Ferris et al., 2006; Mandeville et al., 2013; Bruinsma et al., 2018), and subject to receptor desensitization and downregulation (Chen et al., 1999; Arey, 2014; Berg and Clarke, 2018); which in some instances may be species-specific (Knabl et al., 2008).

It is important to consider dose-response effects and the pharmacokinetics of each drug used in the experimental design. Ideally several doses of drug, and sufficiently long time series should be included in order to interpret the results according to dose-response and absorption/elimination functions (Leslie and James, 2000; Marota et al., 2000; Mueggler et al., 2001; Steward et al., 2005; Ferris et al., 2006; Rauch et al., 2008; Jenkins, 2012; Minzenberg, 2012; Jonckers et al., 2015; Shah et al., 2015; Bruinsma et al., 2018). Indeed, many pharmacological agents have known systemic effects which can influence animal physiology and the BOLD signal (Shah et al., 2004; Wang et al., 2006; Martin and Sibson, 2008; Ferrari et al., 2012; Klomp et al., 2012), and some drugs have direct effects on the vascular endothelium in the brain, which could alter properties of the hemodynamic response (Luo et al., 2003; Gozzi et al., 2007; Shih et al., 2012b). It is imperative to closely control and monitor animal physiology, and use appropriate doses in order to control for unwanted side effects. Importantly, vehicle controls are necessary for any pharmacological fMRI study, as increased blood flow/volume and increased blood pressure from systemic infusions can alter the MRI signal (Kalisch et al., 2001; Tuor et al., 2002; Gozzi et al., 2007; Reimann H. M. et al., 2018).

Species, Sample Size, and Gender Distribution

We assessed studies performed using animals, i.e., all species except homo sapiens. The rat and specifically the Sprague–Dawley strain was the most common species and strain used in fMRI studies, representing 55% of the total studies considered presently (**Figures 3A,B**). Non-human primate (NHP) studies were second and mostly relied on the macaques (23%). Studies involving medium-sized domestic mammals (cats, dogs, sheeps, pigs, and rabbits) presented 9% of the total literature considered. Studies on males (54%) had a higher incidence than studies in females (14%). A sizable number of studies (22%) omitted to specify the gender. This gender bias reflects a greater trend found throughout neuroscience and other biomedical disciplines (Beery and Zucker, 2011) and should require a greater consideration within the animal neuroimaging community. Finally, the total number of animals was assessed within the studies considered. It should be noted that this was done irrespective of the number of groups. There, we found that nearly half the studies were carried out on ten or fewer subjects (**Figure 3C**). This was particularly marked in studies with NHP (Percentiles 25, 50, 75 = [2, 3, 5]). While sample size depends on the goals of each study and appropriate power calculation, it remains unclear how group sizes were determined in most of these studies. The small group sizes reported here are consistent with general trends in neuroscience toward underpowered studies. Button et al. (2013) estimated that the median power level in neuroscience was at 21%. Hence these trends need to be carefully taken into consideration in the initial stages of study design so that the required animals are used to their full potential.

The wide range of experimental animals available for research offers unique opportunities to study evolutionary trends on distributed neuronal networks. To date, however, interspecies comparisons have remained a difficult task. fMRI has provided numerous descriptions of the network organization in mammals. Specifically, RSNs have been mainly studied in mammals to develop translational models of human diseases and to understand the mechanisms underlying their functional alterations. RSNs' organization has been described in numerous mammalian species (usually under anesthesia) including rodents (Hutchison et al., 2010; Jonckers et al., 2011; Sforazzini et al., 2014; Grandjean et al., 2017b), ferrets (Zhou et al., 2016), rabbits (Schroeder et al., 2016), dogs (Kyathanahally et al., 2015), prairie vole (Ortiz et al., 2018), and NHP (Vincent et al., 2007; Hutchison et al., 2010; Mantini et al., 2011; Belcher et al., 2013). Particularly active at rest, one of the most widely investigated networks is the DMN (Raichle, 2015; Buckner and DiNicola, 2019). This network comprises distributed polymodal cortices that are thought to be involved in memory consolidation and higher cognitive functions. Homologs of the human DMN (Raichle et al., 2001) have been identified in a variety of species including NHP (Vincent et al., 2007; Mantini et al., 2011), rats (Lu et al., 2012), mice (Sforazzini et al., 2014; Stafford et al., 2014) and

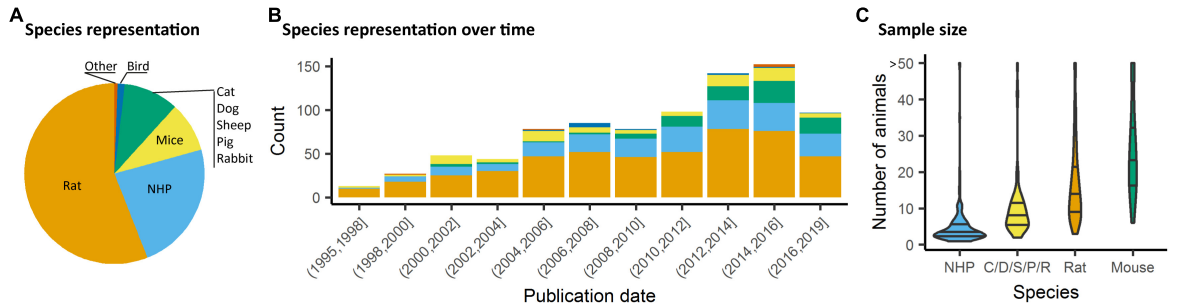

FIGURE 3 | Species distribution and sample size. **(A)** Animal representation in the documented studies. **(B)** Animal species occurrence in the literature over time. Rats and non-human primate (NHP) represent the major species used, however, since 2008, mice have been used in a growing proportion of animal fMRI studies. **(C)** Number of animals used per fMRI study irrespective of number of groups or classes. NHP studies are carried out with fewer animals (Percentiles$_{25,50,75}$ = [2, 3, 5]), whereas studies involving mice involved larger number of animals (Percentiles$_{25,50,75}$ = [17, 24, 34]).

rabbits (Schroeder et al., 2016). The hypothesis of two separated DMNs (anterior and a posterior) has been evoked in dogs (Kyathanahally et al., 2015) and ferrets (Zhou et al., 2016).

The description of each species' functional architectures has been based on a variety of acquisitions, analyses, and anesthesia or awake protocols. This lack of interspecies standardization is often justified by the variety of brain sizes, different response to anesthesia, and anatomical organizations observed within mammals. Throughout evolution, brain regions could have duplicated, fused, reorganized or expanded (Hutchison and Everling, 2012). A few studies have compared the connectivity between different species and with similar approaches. Using ICA, Jonckers et al. found that the extracted components, i.e., functional network regions, were more unilateral in mice compared to rats (Jonckers et al., 2011), however, this effect failed to be replicated in numerous follow-up studies in mice (e.g., Grandjean et al., 2014; Sforazzini et al., 2014). In mouse lemur primates and humans, the cortical large-scale networks repertoire presents important similarities but the regional organization into networks highlighted compositional and structural divergences (Garin et al., 2019). Strong interhemispheric functional connectivity (FC) between homotopic regions has been consistently observed in humans and primates suggesting a phylogenetically preserved mammalian characteristic (Hutchison and Everling, 2012). However, lateralized networks (i.e., fronto-parietal resting-state network) remain a phenomenon which has only been demonstrated in humans. According to the few comparative studies on mammals functional organization, humans seem to display the strongest variety of functional networks. The complexity and diversity of the animal behaviors are probably related to this large repertoire of networks. This complexity is also reflected by the white matter fiber tracts network (Nadkarni et al., 2018). Moreover, direct evidence is in favor of a close relationship between the structural and functional organization in humans (Damoiseaux and Greicius, 2009), in primates (Miranda-Dominguez et al., 2014) and in mice (Stafford et al., 2014; Grandjean et al., 2017b). However, a recent systematic review showed that structure-function correlations in mammalian brains depend on the connectivity measures, which differ across methods and scales (Straathof et al., 2019). The structure-function correspondence observed in multiple species is an important step in favor of the neural origin underlying the BOLD signal and provides a key to understanding neural network development through the evolution of complex brain structure.

Other universal properties of the brain topology have also emerged recently with graph analysis. One of them is the small-world feature which maximizes the efficiency of information transferred within a network. This network property has been found in multiple species including humans (Bullmore and Sporns, 2009), NHP (Barttfeld et al., 2015; Garin et al., 2019), rodents (Mechling et al., 2014), and ferrets (Zhou et al., 2016). Moreover, graph-based approaches have clearly revealed a modular nature of human (Sporns and Betzel, 2016), and rodent (Liska et al., 2015) rsfMRI networks, along with evidence of strongly functionally interconnected polymodal areas, exhibiting hub-like properties (Buckner et al., 2009; Liska et al., 2015). Concerning highly connected regions in human, macaque and mouse lemur, the posterior cingulate cortex was found to be critical in these three species with its major functional hubs located in the DMN (Garin et al., 2019). Interestingly, these areas seem to be instead shifted anteriorly in rodents, in which the anterior cingulate and prefrontal areas exhibit robust hub-like properties (Liska et al., 2015; Gozzi and Schwarz, 2016; Garin et al., 2019). This finding is consistent with rodent species lacking an evolutionary homolog of the primate posterior cingulate cortex (Vogt and Paxinos, 2014). Determining the fine-grained topology and contribution of regions critical for network organization and stability across species and evolution could highlight functional patterns that are especially relevant for network stability. Despite the lack of consensus concerning a standardized methodology in mammals fMRI, cross-species studies could provide essential clues toward a better understanding of brain physiology and evolution.

Animal Preparation and Anesthesia

Animal Preparation Impact on Motion and Stress

Functional MRI traditionally relies on temporal changes in hemodynamic parameters, e.g., blood oxygenation level-dependent contrast (BOLD), cerebral blood volume (CBV),

or cerebral blood flow (CBF). Functional MRI signals inform on neuronal activity through the evaluation of hemodynamic response i.e., the adaptability of local capillaries to deliver oxygen to active neurons at a greater rate than to inactive neurons. BOLD signal, the most commonly used fMRI parameter, is dependent on the relative levels of oxyhemoglobin and deoxyhemoglobin (oxygenated or deoxygenated blood), which is modulated by local blood volumes and flow. In addition, fMRI acquisitions are highly sensitive to subject movement, specifically at tissue boundaries. In humans, several studies showed that small head motions can produce spurious but spatially structured patterns which drastically impacts RS-FC (Power et al., 2014).

In animals, as well, it is critical to control for head motion. As animals are non-compliant species, the most widely used method to control for head stability is to anesthetize the animals and to stabilize the head with bite bar and ear bars (78%, **Figure 4A**). However, training for awake restraint techniques has been developed in rodents and primates (22%, **Figure 4A**). These procedures may include acclimation in a scanner environment with an increase of the exposure periods of time. Atraumatic devices such as cylindrical head-holder or flat ear bars can be used to fix the head (Liang et al., 2011). Moreover, head fixes attached to the skull with dental cement provide alternatives that do not require lengthy animal training (Yoshida et al., 2016). In primates, individualized plastic helmets have been constructed based on 3D anatomical images for better stabilization of the head (Belcher et al., 2013). The quality of the mechanical set-up to fix the head is critical: according to Kalthoff et al. (2011), even with carefully fixed heads, motion remains the main source of noise in rat fMRI at 11.75T and it contributes to 30% of the non-neuronal signal variance (60% being attributed to residual noise). This residual motion is related to respiration that represents 5% of the total variance of RS-FC signal (Kalthoff et al., 2011). It can be minimized by artificially ventilating and paralyzing the animal, a process that results in excellent control of the motion artifacts (Ferrari et al., 2012). Beyond motion, either spontaneous or related to ventilation, cardiac motion induces low-frequency BOLD fluctuations and is another source of noise for fMRI signal interpretation (Murphy et al., 2013). In some instances, cardiac responses can eclipse the neuronal response, especially in response to potentially stressful stimuli (Schroeter et al., 2014). Hence decisions to mitigate these strong confounding sources and variations between laboratories remain a major obstacle toward the standardization in animal imaging protocols, decisively more so than in human corresponding experiments.

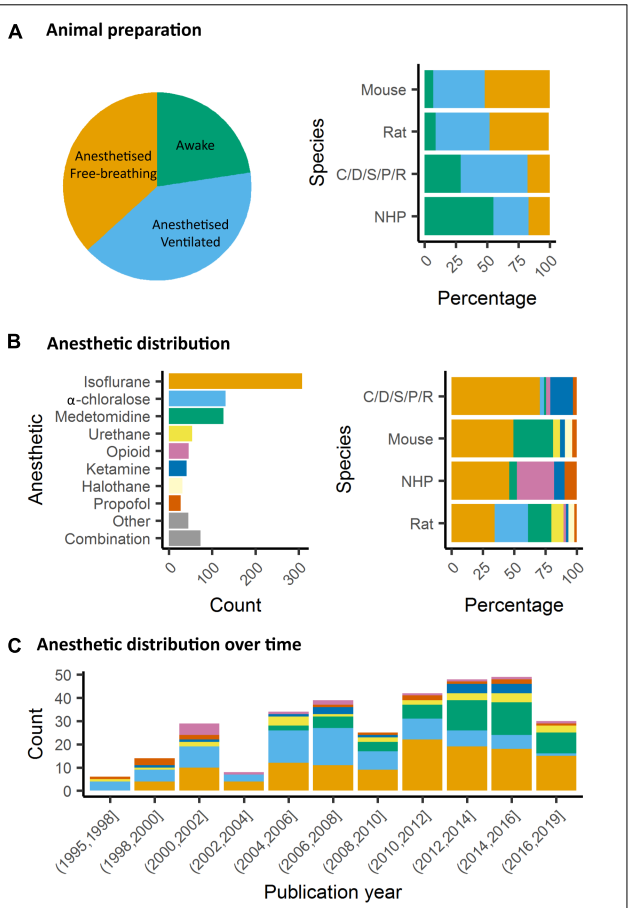

FIGURE 4 | Animal preparation and anesthesia trends. **(A)** Animal fMRI relies mainly on anesthesia to help restrain animals. NHP remain the major species acclimated to awake fMRI. **(B)** Isoflurane is the principal anesthetic used for maintenance during fMRI recordings. However, the distribution of other agents change with species. **(C)** Medetomidine is growing to become the second most used agent behind isoflurane.

Impact of Anesthesia on Animal Physiology

The global BOLD signal is modulated by heart rate, arterial CO_2 concentration, and temperature. Different anesthetics modulate various targets in the brain and have different impact on peripheral receptors acting on respiratory or cardiac regulation. Thus, they have different impact on BOLD signal and other hemodynamic readouts. For example, mechanically ventilated rats, for which arterial blood gases ($PaCO_2$, PaO_2) and pH were maintained constant, showed decreased T2* contrast between veins and parenchyma when anesthetized with isoflurane 2% as compared to medetomidine or ketamine/xylazine. This was explained by increased CBF and vasodilatation in animals under isoflurane (Ciobanu et al., 2012). The use of mechanical ventilation has the advantage of avoiding hypercapnia (increased paCO2) which has an impact on fMRI reproducibility (Biswal et al., 1997; Ramos-Cabrer et al., 2005). Hypercapnia also leads to vasodilation and increased CBF (Xu et al., 2011). The modulation of CBF could explain the decrease of the BOLD response specificity to neuronal activity induced by stimuli (Uhrig et al., 2018). Interestingly, Uhrig et al. showed different impacts of various anesthetics on blood oxygenation in different brain regions. For example, ketamine leads to higher oxygenation in the cortex as compared to the thalamus while the opposite occurs for propofol (Uhrig et al., 2014). This variability may affect the ability to detect networks connecting these regions. The impact of anesthesia on other physiological parameters, such as body temperature and peripheral cardiovascular activity can modulate the quality of the measured functional connectivity. Both these parameters represent strong benefits to be registered and kept stable to assure normal physiological conditions during

the acquisition. The body temperature is usually controlled with a heating cradle, pad or any additional heating system, leading to stable reported temperatures. In light of the above, controlling for the temperature, the $paCO_2$ and the movement parameters remains essential in assuring the animal stability and the quality of the data. Finally, anesthesia can tightly impact CBF autoregulation in response to peripheral blood pressure changes (Gozzi et al., 2007). Peripheral blood pressure recordings, and the presence of autoregulation, are parameters of critical importance for studies of neuromodulation using drugs, optogenetics and/or chemogenetics-fMRI (e.g., Giorgi et al., 2017), as well as in the case of somatosensory stimulation (Schroeter et al., 2014). This is because transmitter-induced peripherally evoked blood pressure changes, in the absence of physiological CBF autoregulation, can give rise to seemingly regionalized fMRI responses (Gozzi et al., 2007; Reimann H. M. et al., 2018). Future research is required to understand to which extent commonly used anesthetic regimens in rodents do preserve CBF autoregulation. While technically challenging, and invasive, blood pressure recordings can be carried out via femoral arterial cannulation (Ferrari et al., 2015), hence making it possible to understand whether peripheral cardiovascular response and central fMRI activity are temporally correlated.

Several anesthetics are used for animal studies (**Figure 4B**). They have been classified into several classes according to their targets: $GABA_A$ receptors, NMDA receptors, two-pore-domain K+ channels, and other modes of actions. $GABA_A$ receptors are the most widely used targets for anesthetics. They are chloride channels that hyperpolarize neurons, making them less excitable and thus inhibiting the possibility of an action potential. Widely used anesthetics as isoflurane, propofol and barbiturates are $GABA_A$ receptors agonists (Franks, 2008; Garcia et al., 2010). Each drug within this category displays a subtly unique pharmacological characteristic. For example, isoflurane and sevoflurane have opposite metabolic activities on cerebral blood flow and glucose consumption in various brain regions (Lenz et al., 1998). α-chloralose is widely used in the context of BOLD fMRI because it provides robust metabolic and hemodynamic responses to functional stimulation and is also expected to act on $GABA_A$ receptors (Garrett and Gan, 1998). NMDA receptors are other widely used targets. The use of antagonists for these receptors, such as ketamine, is supposed to block excitatory synaptic activity probably leading to anesthesia. This latter may be related to the fact that ketamine binds preferentially to the NMDA receptors on GABAergic interneurons. Ketamine, however, leads to a "dissociative anesthesia" during which the perception of pain is dissociated from the perception of noxious stimuli. Besides, it has psychotomimetic effects at low concentrations, leading to auditory and visual hallucinations (Franks, 2008). Ketamine and other NMDAr antagonists increase regional brain activity and cerebral blood volume, mainly in the anterior cingulate, the thalamus, the putamen, and the frontal cortex (Långsjö et al., 2003; Gozzi et al., 2008; Bonhomme et al., 2012). Two-pore-domain K+ channels are targeted by volatile anesthetics (isoflurane, halothane, nitrous oxide) which have different affinities for subfamilies (TREK-1 or TASK) of these receptors (Patel et al., 1999). These channels modulate the potassium conductance that contributes to the resting membrane potential in neurons. Their opening, therefore, facilitates a hyperpolarizing current, which reduces neuronal excitability and anesthetizes. Among other targets, α2-adrenergic receptor agonists are targeted by xylazine, medetomidine, dexmedetomidine (Sinclair, 2003). The activity of these drugs is related to their action on receptors located in the locus coeruleus and its projections. At this level, they reduce the release of norepinephrine, a neurotransmitter that is necessary for arousal. The anesthesia induced by these compounds resembles the state of non-REM sleep, i.e., the first four of the five stages of the sleep cycle (Franks, 2008).

Impact of Anesthetics on Neuronal Network Organization in Rodents

In rodents, isoflurane and medetomidine are currently the most commonly used anesthetics (**Figures 4B,C**). Importantly, isoflurane is almost systematically used for anesthesia induction, specifically in rodents. Variations in the induction time may lead to a lasting effect on brain function, even though anesthesia is switched to another agent (Magnuson et al., 2014). In addition to their different mechanisms of action ($GABA_A$ receptors agonist for isoflurane and α2 adrenergic receptor agonists for medetomidine), they have opposite vaso-properties (vasodilatation for isoflurane and vasoconstriction for medetomidine) which could impact neurovascular coupling differently. In rodents, isoflurane seems to preserve the interhemispheric and cortico-cortical FC but only at low doses (∼1%) (Wang et al., 2011; Grandjean et al., 2014; Uhrig et al., 2014; Bukhari et al., 2017). Medium to high doses induce burst-suppression effects which are reflected in an increase in the global signal (Liu et al., 2011, 2013; Grandjean et al., 2014). Medetomidine seems to present opposite effects such as a cortico-cortical disruption and a pronounced striatal FC (Grandjean et al., 2014; Bukhari et al., 2017; Paasonen et al., 2018). The effect of isoflurane and medetomidine and other anesthetics on the thalamo-cortical FC is still debated. Several studies suggested that a combination of isoflurane and medetomidine (med/iso) at low doses is the best compromise (**Table 1**, med/iso) to preserve FC and to recapitulate network properties of the awake state (Grandjean et al., 2014). However, this combination appears to inhibit thalamo-frontal cortical connectivity, when compared to connectomic estimates of the mouse connectome (Grandjean et al., 2017b). A number of studies in control and transgenic mouse models have been carried out with low doses of halothane (Sforazzini et al., 2014; Liska et al., 2015, 2018; Bertero et al., 2018; Gutierrez-Barragan et al., 2018; Pagani et al., 2019). This inhalational anesthetic produces stable and long-lasting RS-FC correlation recapitulating patterns of connectivity observed with med/iso combination (Grandjean et al., 2017b), with the advantage of robustly preserving thalamo-frontal connectivity, an effect that makes it especially apt for the investigation of prefrontal circuitry and the rodent default mode network (Bertero et al., 2018). However, the hepatotoxic properties of this compound have led its banning in most countries, preventing widespread use of this anesthetic regimen. Other anesthetics used in rodents (propofol, urethane, α-chloralose) are presented in

TABLE 1 | Anesthetics effects on the functional connectivity in rodents.

Anesthetics	Doses	Comparison	Effects	Studies	Species
Isoflurane	1%	vs. the awake state	Preserve interhemispheric FC	Jonckers et al. (2014)	Mice
		vs. anesthetics	Cortical and thalamo-cortical FC preserved but disruption of striatal FC	Grandjean et al. (2014)	
			Cortico-cortical FC preserved but disruption of thalamo-cortical FC	Bukhari et al. (2017)	
	1–2%	Increasing doses	Disruption of interhemispheric FC with increasing doses	Bukhari et al. (2018)	
	1.3%	vs. the awake state	Cortico-cortical and striatal FC increase	Paasonen et al. (2018)	Rats
Medetomidine	0.1 mg/kg	vs. anesthetics	Disruption of thalamo-cortical FC but pronounced striatal FC	Grandjean et al. (2014)	Mice
			Thalamo-cortical FC preserved but disruption cortico-cortical FC	Bukhari et al. (2017)	Mice
		vs. the awake state	Cortico-cortical FC decreased	Paasonen et al. (2018)	Rats
Med/iso	0.05 mg/kg; 0.5%	vs. anesthetics	Preserved FC	Grandjean et al. (2014)	Mice
				Bukhari et al. (2017)	
	0.06 mg/kg; 0.5%	vs. the awake state	Thalamo-cortical and intra-subcortical FC decrease	Paasonen et al. (2018)	Rats
Urethane	2.5 g/kg	vs. the awake state	Disruption of interhemispheric FC	Jonckers et al. (2014)	Mice
	1.5 g/kg	vs. anesthetics	Cortical and thalamo-cortical FC preserved but disruption of striatal FC	Grandjean et al. (2014)	
	1.25 g/kg	vs. the awake state	Replication of the awake state	Paasonen et al. (2018)	Rats
α-chloralose	120 mg/kg	vs. the awake state	Disruption of interhemispheric FC	Jonckers et al. (2014)	Mice
	60 mg/kg	vs. the awake state	Cortico-cortical FC suppression	Paasonen et al. (2018)	Rats

Review of five studies between 2014 and 2018.

Table 1. They are not further discussed here as they showed ambiguous effects on RS-FC and are no longer recommended. Notably, RSNs in mice were shown to converge in a multi-center comparison (**Figure 1**; Grandjean et al., 2019a), irrespective of anesthesia regimen, indicating to some extent that network properties are retained between different conditions.

Impact of Anesthetics on Neuronal Network Organization in Primates

In primates, isoflurane is the most used anesthetic (Vincent et al., 2007; Hutchison et al., 2013b; Miranda-Dominguez et al., 2014; Grayson et al., 2016). As in rodents, lower dose and shorter anesthesia duration are associated with an increased ability to detect RS-FC (**Table 2**; Barttfeld et al., 2015; Uhrig et al., 2018). Also, one should keep in mind that a direct comparison of the impact of anesthetics on cerebral networks is difficult because anesthesia depth also modulates networks and can lead to misinterpretation of the results.

Data Acquisition

Contrary to human fMRI, which is carried mostly at 1.5T, 3T, and in rarer cases at 7T, animal fMRI is carried at a variety of field strengths, with 7T and 9.4T being the most frequently encountered field strength (26 and 25% respectively, **Figure 5A**). The availability of ultra-high field strength small-bore systems in rodents further increase this range, with fMRI being recorded as high as 15.2T (Jung et al., 2019). While fewer animal MRI system vendors exist compared to human systems, this apparent similarity is compounded with a greater range of coil designs, including home-made coils or cryogenic coils (Baltes et al., 2011), which provide an additional source of variation among the animal studies. Whilst these factors are determined by the center where the acquisitions are performed, even greater variability comes in in the form of sequence parameters and the resulting contrasts across the different studies. This is exemplified in a report by Grandjean et al. which indicated cortical signal-to-noise ratios ranging from 20 to 400 in mice fMRI acquired at different centers (Grandjean et al., 2019a).

Neuronal activity induces vasodilation in surrounding capillaries and arterioles, which may propagate further up- and downstream toward arteries and draining veins. The resulting increase in CBF and CBV and blood oxygenation forms the basis of imaging strategies for fMRI. The most commonly used fMRI method is based on the BOLD contrast (Ogawa et al., 1990). BOLD contrast results from the paramagnetic properties of deoxyhemoglobin, which causes magnetic susceptibility effects inside blood vessels as well as in their surrounding tissue that can be detected with T2- or T2*-weighted sequences (Norris, 2006; Kim and Ogawa, 2012). Deoxyhemoglobin concentration increases dramatically from the arterial (<5%) to the venous side (∼40%) of the vascular tree due to the extraction of oxygen in the capillaries (Vovenko and Sokolova, 1998), which makes BOLD imaging particularly sensitive to capillaries, venules and veins. In healthy brain tissue, the neuronal activity typically induces an increase in CBF with resultant increased oxygen delivery that exceeds the decrease in oxygen due to capillary oxygen extraction. As a result, deoxyhemoglobin concentration in the capillaries and veins decreases, giving rise to a positive BOLD response in T2- or T2*-weighted images.

The most frequently used BOLD-weighted fMRI sequence in rodents is T2*-weighted gradient echo (GE) echo planar imaging (EPI) (**Figure 5B**). GE-EPI provides a relatively high contrast-to-noise ratio (CNR), which increases with field strength. At field strengths $\geq$ 7T, the intravascular contribution to the GE BOLD signal is negligible and signal changes scale almost linearly with echo time (TE) (Yacoub et al., 2003; Han et al., 2019). For optimal BOLD CNR, TE is typically set equal to the average

TABLE 2 | Anesthetics effects on the functional connectivity in primates.

Anesthetics	Doses	Comparison	Effects	Studies	Species
Isoflurane	1–2.75%	Increasing doses	Disruption of interhemispheric FC after 1.5%	Hutchison et al. (2014)	*Macaca fascicularis*
	0.89–1.19%	Duration effect	Reduction of the DMN FC with a prolonged administration	Li and Zhang (2018)	*Macaca mulatta*
Ketamine	20 mg/kg	vs. the awake state	Preservation of positive FC but average positive FC reduced	Uhrig et al. (2018)	*Macaca mulatta*
Sevoflurane	2.2–4.4 vol%	vs. the awake state	Average positive FC reduced	Uhrig et al. (2018)	*Macaca mulatta*

Review of five studies between 2014 and 2018.

gray matter tissue T2* value (for an overview of brain tissue T2 and T2* values we refer to Uludağ et al. (2009) and Han et al. (2019). The disadvantage of using GE-EPI for rodent fMRI, however, is its sensitivity to susceptibility artifacts, which are most prominent near air cavities such as the ear canals and around the olfactory bulb, particularly at long TE and high field strength. Furthermore, GE-EPI is highly sensitive to large veins (Uludağ et al., 2009), which makes this sequence spatially non-specific as neurovascular coupling occurs at the level of the capillaries. This has been clearly demonstrated by fMRI studies in rats subjected to electrical stimulation of the forepaws, where the highest GE-EPI BOLD response is observed in the outer layer of the somatosensory cortex where pial vessels are located (Mandeville and Marota, 1999; Han et al., 2019), while neuronal activation mostly occurs in deeper cortical layers. The relative contribution of capillaries to the BOLD signal increases with field strength but remains dominated by the macrovasculature even at 15.2T (Han et al., 2019).

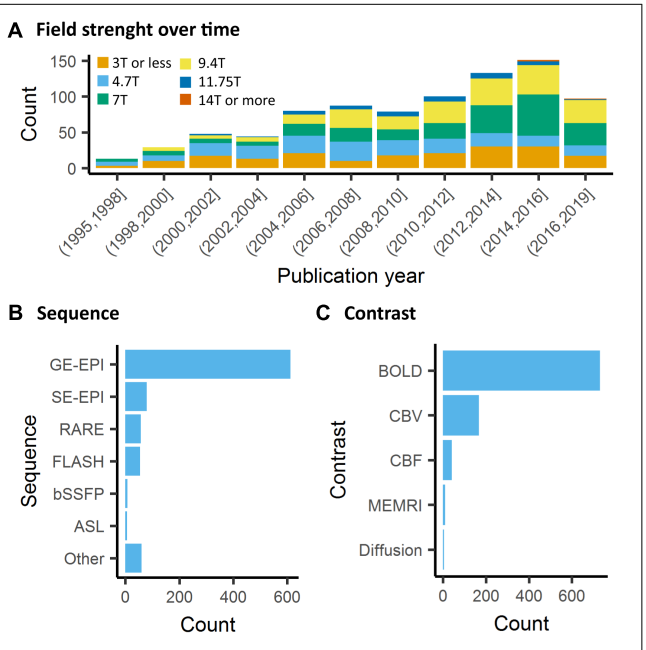

FIGURE 5 | Data acquisition. **(A)** There is a general trend toward higher strength of the main magnetic field in animal fMRI over time. In the past decade, the majority of studies were performed on 7T and 9.4T systems. **(B)** The acquisitions relied mainly on gradient echo EPI for the acquisition, while older studies either used FLASH or RARE sequences. **(C)** BOLD is the most commonly used contrast in animal studies. The availability of iron nanoparticles in animal studies explains the relative high incidence of CBV contrasts.

Spatial specificity for neuronal activity can be increased by using spin-echo (SE) EPI for BOLD fMRI (Norris, 2012; Han et al., 2019). SE BOLD is particularly sensitive to small vessels, as signal around large vessels is largely refocused by the 180° pulse. The relative contribution of the microvasculature increases with field strength and TE, and may be further increased by introducing diffusion gradients that reduce the remaining intravascular contribution from large vessels (Kim and Ogawa, 2012). To maintain spatial specificity, EPI train length should be reduced to a minimum to avoid introducing T2* effects (Goense and Logothetis, 2006). In the absence of intravascular contributions to the SE BOLD signal, CNR increases almost linearly with TE, achieving the best contrast when TE equals gray matter tissue T2. SE-EPI images show reduced sensitivity to susceptibility artifacts compared to GE-EPI. However, SE-EPI also comes with lower BOLD CNR, and longer acquisition times.

Since BOLD contrast depends on the TE of the sequence, multi-echo GE sequences have been proposed for BOLD fMRI data acquisition. In multi-echo EPI (ME-EPI), one excitation pulse is followed by acquisition at multiple TEs (Speck and Hennig, 1998). Short TE results in high signal intensity, minimal signal dropout but low CNR, whereas longer TE results in lower signal intensities, more signal dropout but higher CNR. The multi-echo approach has two main applications. First, images acquired at different TE can be combined to optimize the BOLD contrast per region (Posse et al., 1999; Poser et al., 2006), since T2* varies across the brain (Hagberg et al., 2002; Peters et al., 2007). Second, identifying TE-dependent and TE-independent signals can help to separate BOLD T2* signal fluctuations and noise (Kundu et al., 2012). The shortened T2* at high field strength, often used for preclinical imaging, provides less time for image acquisition at additional TEs and limits the time between adjacent TEs. Still, ME-EPI at three different TEs without acceleration is feasible for fMRI in rodents at 9.4T and 11.7T, with a TR of 1.5–3 s and acceptable spatial resolution (Kundu et al., 2014; Grandjean et al., 2017a,b).

Beside EPI, the balanced steady-state free precession (bSSFP) sequence enables acquiring BOLD-like contrast images at short TE (=TR/2), making these images relatively insensitive to signal dropouts and artifacts often seen in GE-EPI. The origin of the bSSFP contrast is, however, complex since it does not only depend on T1 and T2 but also on the flip angle, repetition time and off-resonance values (Miller, 2012). Functional MRI using bSSFP sequences can be performed in the so-called transition-band or the pass-band (Miller, 2012). Functional transition-band

bSSFP is sensitive to alterations in voxel off-resonances induced by changes in deoxyhemoglobin concentration. At short TE it provides T2-weighted contrast (Scheffler et al., 2001), whereas at long TE the image contrast is mainly T2*-weighted (Miller et al., 2007). Larger signal increases in response to neuronal activation have been measured compared to GE-EPI (Scheffler et al., 2001; Miller et al., 2006). However, transition-band SSFP is also sensitive to field inhomogeneities due to its sensitivity to off-resonances, making whole-brain coverage from anterior to posterior difficult to achieve (Miller, 2012). Furthermore, it is sensitive to physiological and time-varying noise (Miller, 2012). Pass-band bSSFP has been more widely used for fMRI (Miller and Jezzard, 2008; Scheffler and Ehses, 2016). Similar to transition-band bSSFP, its contrast origin shifts from BOLD T2 effects at short TE to BOLD T2* effects at long TE. However, the pass-band SSFP sequence is less sensitive to field inhomogeneities, and sensitivity to physiological noise can be lower than with GE-EPI (Miller et al., 2007). At short TE, an additional advantage is the suppression of BOLD sensitivity in large draining veins, making the sequence more selective to microvasculature contribution compared to GE-EPI (Báez-Yánez et al., 2017). However, bSSFP sequences have lower BOLD CNR than conventional GE-EPI at short TE (Miller et al., 2007; Zhong et al., 2007), and at long TE, banding-artifacts appear due to field inhomogeneities and macrovascular contributions increase. Consequently, the use of this sequence has so far remained marginal (**Figure 5B**).

Although BOLD contrast is mostly used for fMRI, alternative methods that directly measure CBV or CBF, are available (**Figure 5C**). CBV can be measured with the use of exogenous iron oxide-based contrast agents (Mandeville et al., 1998; Chen et al., 2001). Iron oxide nanoparticles used for CBV contrast exhibit strong r2 and r2* relaxivity, do not cross the intact blood-brain barrier, and have a long blood circulation half-life in the order of hours (Chen et al., 2001). Intravenous administration of nanoparticulate iron oxide introduces magnetic susceptibility effects within the vasculature and its surrounding tissue, which, at sufficiently high dose, are much larger than the effects of deoxyhemoglobin. As a result, intravascular T2*-weighted signal becomes negligible, while the extravascular T2*-weighted signal becomes highly sensitive to changes in CBV (Mandeville, 2012). An increase in CBV, as induced by neuronal activation, increases magnetic susceptibility within the imaging voxel, giving rise to negative CBV-dependent contrast in T2*-weighted images. CBV-dependent contrast is independent of field strength and most optimal when iron oxide injection causes a drop of 40–60% in signal intensity with respect to baseline (Mandeville, 2012). Since baseline signal intensity is strongly dependent on TE, contrast dose should be adjusted to the TE as well. A relatively high dose of contrast agent allows the use of short TE with the advantage of a reduction in susceptibility artifacts (Mandeville et al., 2004). The most commonly used imaging sequence for CBV contrast is GE-EPI, which, in contrast to BOLD GE-EPI, is particularly sensitive to changes in small vessels (arterioles, capillaries and venules). This, which is due to the strong magnetic susceptibility effects of the iron oxide, causes the extravascular signal from tissue surrounding large vessels to be largely eliminated. CBV-weighted fMRI is therefore considered more spatially specific to neuronal activity than GE BOLD fMRI. This has been clearly demonstrated in rats subjected to electrical forepaw, in which a spatial shift in the maximum contrast-to-noise ratio was observed from the cortical surface with GE BOLD fMRI to deeper layers of the somatosensory cortex with GE CBV-weighted fMRI (Mandeville and Marota, 1999; Keilholz et al., 2006). SE-EPI is typically not used for CBV-weighted fMRI as CNR is lower than with GE-EPI, and CBV changes in small vessels are underestimated (Mandeville et al., 2007).

Cerebral blood flow can be measured non-invasively with Arterial Spin Labelling (ASL), which uses radiofrequency pulse(s) to magnetically label the blood water in major arteries by inverting the longitudinal magnetization (Williams et al., 1992). After a waiting period, the labeled blood water exchanges with brain tissue water, leading to T1 shortening in the imaging plane. Subtracting a second scan without labeling results in an image with only the signal from the labeled inflowing spins. There are two main types of ASL: continuous ASL (cASL) and pulsed ASL (pASL) (Borogovac and Asllani, 2012). cASL sequences include a long labeling pulse and provide high signal-to-noise ratio but low labeling efficiency. In comparison, pASL involves short inversion pulses with high labeling efficiency but low signal-to-noise ratio. A practical advantage of pASL is that short inversion pulses are more easily implemented in ASL protocols. To combine the higher labeling efficiency of pASL and higher sensitivity of cASL, pseudo-continuous ASL (pCASL) was developed (Silva and Kim, 1999; Wu et al., 2007; Dai et al., 2008; Borogovac and Asllani, 2012), and further optimized with multi-phase image acquisitions to tackle rodent-related difficulties with variations in labeling efficiency across different vessels to prevent erroneous calculation of CBF (Larkin et al., 2018). Since EPI is the main read-out for ASL, the presence of a BOLD effect should be taken into account in ASL-based fMRI studies (Lu et al., 2006). Compared to BOLD fMRI, ASL-based fMRI provides about one-third of the contrast-to-noise ratio (Lu et al., 2003), has low temporal resolution and is more challenging to implement (Detre and Wang, 2002). On the other hand, ASL provides stable noise levels – enabling measurement of slow variations in brain function (Aguirre et al., 2002; Wang et al., 2003) – shows less intersubject variability (Tjandra et al., 2005), and is more sensitive to arterioles and microvasculature than to large draining veins (Silva et al., 1999; Tjandra et al., 2005).

By far the majority of rodent fMRI studies are executed with one of the abovementioned fMRI approaches that are based on the hemodynamic response to neuronal activation. Alternative fMRI methods aimed at more specific detection of neuronal responses have been developed, such as manganese-enhanced fMRI (Lin and Koretsky, 1997) and diffusion-weighted fMRI (Tsurugizawa et al., 2013) but these approaches have been hampered by non-uniform or limited sensitivity, low temporal resolution and uncertainties about the underlying mechanisms (Rudrapatna et al., 2012; Silva, 2012). Correspondingly, the application of these methods has so far remained marginal (**Figure 5C**). Recent developments in diffusion-weighted fMRI in rodents are likely to give rise to a renewed interest in the method (Abe et al., 2017; Nunes et al., 2019).

Data Analysis

Pre-processing

Image pre- and post-processing are an integral part of every fMRI study. Pre-processing refers to a number of steps to correct for artifacts and normalize data, e.g., motion correction, temporal filtering and co-registration to a reference template. A number of dedicated software packages are designed, usually for human studies, to carry out these functions. With differences in the precision and performance of the various tools available, e.g., motion correction (Morgan et al., 2007) or registration (Klein et al., 2009), the user selection of tools within data analysis is a non-negligible source of bias and variability between studies. Interestingly, an analysis in human fMRI revealed that 223 unique analysis pipelines were used to process data in 241 studies, implying that nearly every study is carried out with an individualized pipeline (Carp, 2012). Efforts to develop unified open-source pre-processing pipelines for human fMRI, e.g., fMRIPrep (Esteban et al., 2019), have yet to reach widespread adoption. In animals, we observed that a large number of studies relied on custom made pre-processing functions (26%, **Figure 6A**). SPM was the most common software package used for the analysis (27%). The preponderance of custom made software, as well as the combination of functions from several software suits in animal fMRI research, may be explained by the fact that specific functions were designed for the human brain. The pervasive use of *ad hoc* pipelines, encouraged by the lack of dedicated animal pipelines, is a major obstacle to results comparisons between centers.

Templates and Atlas Selection

Registration of fMRI results to a common reference space is an integral part of the pre-processing and enables unbiased group-level statistical analysis at a voxel-wise level. In human neuroimaging, standard space and coordinate systems are routinely used to report results in both figures and tables. In animals, we found that the vast majority of the studies did not register fMRI data to standard space (64%) while 24% relied on *ad hoc* templates. While this step ensures optimal registration due to similar image contrast, resolution, and orientation, this adds extra challenges in comparing across studies. Contrary to the ubiquitous Montreal Neurological Institute reference space in human (Mazziotta et al., 2001), animal templates have failed to reach a consensus yet, despite efforts to implement standards such as the Waxholm space (Johnson et al., 2010). This is exemplified by the various templates used in animal studies. In rats, five studies relied on (Schweinhardt et al., 2003), nine used (Schwarz et al., 2006), five used (Valdés-Hernández et al., 2011), and two used (Nie et al., 2013). In NHP, ten studies were normalized to Van Essen et al. (2012), ten used (Saleem and Logothetis, 2012), six used (McLaren et al., 2009), and six normalized to Rohlfing et al. (2012). In mice, seven studies were normalized to Janke and Ullmann (2015), four studies used (Lein et al., 2007), and two used (Dorr et al., 2008). More importantly, none of the studies reported three-dimensional coordinates for clusters or slice positions, rendering the precise comparison between studies impractical. Registration between rodent or NHP brains is, however, a computationally much easier challenge than between human brains due to the simpler and less idiosyncratic cortical folding (NHP) or lissencephalic cortex (rodents). The choice of atlases and the level of parcellations also have large implications for network analysis and graph theory metrics (see below).

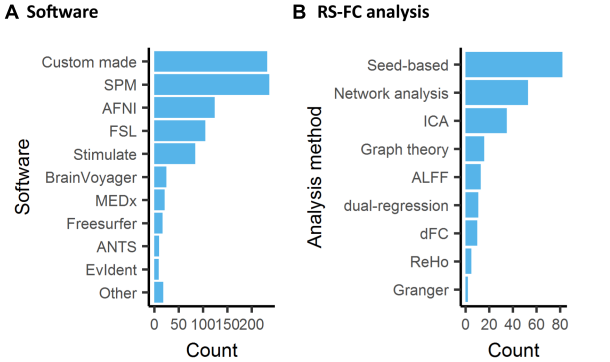

FIGURE 6 | Software used for data analysis of animal fMRI and functional connectivity analysis. **(A)** Custom made software or combination of existing software pipelines remained the most common approach to animal fMRI data processing, while SPM was the most used software package used. **(B)** Resting-state fMRI in animals is mainly analyzed with seed-based analysis.

Regional and Network Level Analysis of Resting-State fMRI

Stimulus-evoked, pharmacological, DBS, and opto-/chemogenetics fMRI studies are almost systematically analyzed with voxel-wise statistics where the time series at every voxel is assessed with an independent model, usually a model of the hemodynamic response to the stimulus/injection paradigms. This is often complemented with ROI analysis of the evoked response. In comparison, RS-FC is paradigm free, hence often relies on intrinsic models to infer connectivity or associated metrics. Consequently, there are several analysis methods that have been developed primarily in the human literature but which can easily be applied to animals as well (**Figure 6B**). Approaches range from hypothesis-driven (e.g., seed-based analysis) to data-driven (e.g., Independent Component Analysis, ICA) and can be applied at the level of networks or of particular ROI. Some metrics describe the relationship between areas; others are based on features of the low-frequency BOLD fluctuations from a single region. Here we provide a brief overview of some prominent methods and reflect on their interpretations.

Seed-Based Correlation

Seed-based correlation is the most intuitive of the analytical methods and the most commonly used in animals (**Figure 6B**). A seed region can be defined based on function or anatomy and range in size from a few voxels to a parcel from a brain atlas. The time courses from each voxel in the seed are averaged together, and then the correlation is calculated between the averaged seed time course and the time course from every other voxel in the brain. The resulting correlation values can be displayed at the location of each voxel, producing a correlation

map (Pawela et al., 2008; Williams et al., 2010; Kalthoff et al., 2011; Liang et al., 2013; Sforazzini et al., 2014; Zerbi et al., 2015; Paasonen et al., 2018). Average values can then be measured for ROIs. Alternatively, the signal from the desired target area can be measured and correlated with the seed time course to directly examine the connection from a particular pair of areas. Seed-based correlation is a low-level metric and thus relatively easy to interpret and to assess for quality. Reference maps for several seeds in the mouse brain are provided in Grandjean et al. (2019a). As with any measurement, it can be affected by the relative levels of signal and noise. While correlation is robust to differences in amplitude in the two signals, a reduction in BOLD amplitude can go hand in hand with an increase in non-neural noise, which does affect correlation values (Keilholz et al., 2016).

Independent Component Analysis

Independent Component Analysis is a data-driven way to identify networks within the brain. It is widely used in the human neuroimaging community and does not rely on the definition of a seed. Instead, it identifies a number of statistically independent networks that can be mapped spatially to the brain (Hutchison et al., 2010; Lu et al., 2012; Jonckers et al., 2014; Sforazzini et al., 2014). One of the challenges of the technique is that it is not immediately apparent how many components should be used. As more components are included, the resulting networks fragment into separate areas, and it may sometimes be necessary to combine components to recompose the full network structure. Accordingly, distributed networks of the rodent brain that are robustly identified using seed-based mapping, such as the DMN (Sforazzini et al., 2014), are only detectable with low-dimensional ICA, and are typically segregated into functional sub-portions when a more canonical number of components is selected. As such, the choice of component number is one of the sources of variability across experiments, but it is at least somewhat mitigated by the observation that the same networks can typically be detected in most studies, despite the occasional fragmentation. Other choices that contribute to variability across studies include whether ICA is performed on the entire group of animals at once, or on subgroups (e.g., mutant vs. wild type mice). If performed on the whole group, a single set of components is obtained and its strength can be examined in each group. One risk of this approach is that the component structure might be driven by one of the subgroups. If ICA is performed on subgroups, multiple sets of components are obtained with different spatial extents and strengths, making comparisons more difficult. ICA provides spatial maps of components and can be considered a mid-level parameter. Additional analysis is needed to examine the strength of the connectivity within or between networks obtained from ICA and is often calculated using correlation. Strict criterion for the identification should be encouraged, such as those proposed in Zerbi et al. (2015), to promote comparable classifications between studies.

Amplitude of Low Frequency Fluctuations

The amplitude of low-frequency fluctuations (ALFF; Zang et al., 2007) and fractional ALFF (Zou et al., 2008) represent the amplitude of the BOLD fluctuations within specific frequency bands, e.g., the 0.01–0.08 Hz range. For fALFF, the amplitude of the fluctuations in the range of interest is normalized by the amplitude of the full frequency range. Both of these measures give an estimate of the strength of the BOLD fluctuations used to map RS-FC, and may include both neural contributions and vascular effects like cerebrovascular reactivity (Golestani et al., 2016). ALFF and fALFF are low-level parameters. In rodents, they are most commonly used to compare across experimental groups (Yao et al., 2012; Chang et al., 2018; Wen et al., 2018).

Regional Homogeneity

Regional Homogeneity (ReHo) is a measure of the local correlation between adjacent voxels (Zang et al., 2004). Similarly to ALFF, and contrary to the majority of the other methods described here, ReHo is a measure that informs on the local signal coherence strength, but not of distal connectivity. The method has been effectively applied in rodents (Wu et al., 2017; Li et al., 2018) and NHP (Rao et al., 2017), such as to describe anesthesia effects on the mouse brain (Wu et al., 2017). ReHo is also a low-level parameter and is relatively simple to interpret.

Whole Brain Analysis

When pursuing a whole brain analysis of RS-FC data, the first question to be answered is that of parcelation. In theory, an analysis could also be performed using each voxel as an independent region, but the signal is noisy and spatially redundant. It is generally agreed upon to group voxels in some way to reduce the dimensionality of the ensuing analysis. The choice of the atlas is often dictated by the level of detail achieved. Parcelation by atlas is an anatomical approach, even though the atlas may be derived from functional information. Another possibility is to perform a functional parcelation, either by clustering or by using a dimensionality reduction algorithm like ICA (Jonckers et al., 2014; Medda et al., 2016). These approaches incorporate information carried by the resting BOLD signal instead of relying on spatial alignment. Following parcelation, other analysis methods are typically applied. One common approach is to calculate the correlation between the average time courses of every possible pairs of ROI. This is similar to seed-based correlation except that the regions of the atlas are used as seeds and targets. Partial volume effects can, therefore, distort the results. The correlation values for the whole brain are often displayed as matrices, where each line shows the correlation for a given ROI with all other possible ROIs. It is then possible to test correlation matrices for differences across groups (although correction for multiple comparisons is essential) or to calculate additional summary metrics using graph theory approaches, described in the next section.

Graph Theory

The brain can be viewed as a network, with ROI serving as nodes that are connected by edges whose weight is determined by a measure of RS-FC, usually correlation. From this perspective, an entire arsenal of graph-theoretical metrics can be used to describe the network of the brain. These range from mid-level metrics such as degree (the number of edges that connect to a node) to high-level metrics such as modularity that describe the

community structure of the brain. For an overview, see Bullmore and Sporns (2009). High-level metrics provide a convenient summary of the large-scale functional architecture of the rodent functional connectome, amenable to cross-species translation (Stafford et al., 2014; Liska et al., 2015; Bertero et al., 2018). They, however, can be influenced by low-level parameters, such as global correlations, and arbitrary parameters such as matrix sparsity whose effects cascade through the analysis and complicate interpretation.

Non-stationary Analysis

In recent years, interest has grown in examining fMRI data beyond the stationary assumptions made by several of the methods described above, also referred to as dynamic functional connectivity. The simplest approach is to use a windowed version of the image time series to calculate the metrics described above (e.g., correlation) (Keilholz et al., 2013). The window is moved along the time series and the calculation is repeated at different time points. A number of studies have examined the effects of window size, shape, and step size, but the ideal parameters remain difficult to pin down (Hindriks et al., 2015; Leonardi and Van De Ville, 2015; Shakil et al., 2016, 2018; Grandjean et al., 2017a). Windows can be applied to the time courses from a particular ROI or from the whole brain, where they are often summarized as a series of matrices (Allen et al., 2014). Other methods can be used to look at the co-occurrence of the individual events that drive RS-FC (Petridou et al., 2013; Liu et al., 2018) or at large-scale repeated patterns of activity (Majeed et al., 2011; Grandjean et al., 2017a; Belloy et al., 2018), offering the possibility of mapping RS-FC non-correlative terms. There are major methodological considerations to such analysis (Laumann et al., 2017; Liégeois et al., 2017). Yet, some of the crucial confounds, specifically head motion, are less applicable to animal studies in anesthetized or paralyzed animals. It emerges that non-stationary patterns are reproducible in both human and rodent datasets (Abrol et al., 2017; Grandjean et al., 2017a; Gutierrez-Barragan et al., 2018). These represent promising emerging methods to investigate the RS-FC signal beyond the stationary hypothesis which characterizes the methods discussed above.

Functional Connectivity Metrics and Interpretation

Choices of anesthesia and pre-processing pipeline have the greatest effect on the ability to compare results from different studies (Pan et al., 2015). However, the wide variety of analysis methods available also plays a role in our interpretation of the results. While the choice of analysis is ultimately dictated by the question of interest, there are steps that can be taken to promote standardization across studies. For example, reporting baseline metrics like correlation along with higher-level metrics like modularity would assist with interpretation and comparison to other studies. In human neuroimaging, a test–retest examination of varying RS-FC methods has highlighted reliable methods (Zuo and Xing, 2014), including dual-regression (Filippini et al., 2009). There are a few explicit examinations of test–retest reproducibility in rodents that undergo the same experimental protocols, providing insight into the level of reproducibility that might be expected. Zerbi et al. (2015) found an R^2 value of ~ 0.7 for optimally processed data from mice under medetomidine/isoflurane combination (Zerbi et al., 2015). Kalthoff et al. (2013) showed that the spatial localization of ICA components shares a common core, particularly under medetomidine sedation. Converging ICA and seed-based maps derived from multiple-datasets are available in the mouse as quality assurance references (Grandjean et al., 2019a). Nevertheless, substantial variability in the correlation coefficients from different studies is present, depending on pre-processing steps, ROI definition, and other factors.

Statistics and Resource Sharing

The statistical analysis carried out by the neuroimaging community has been under increasing scrutiny following reports of inflated false-positive rates in the parametric statistical models traditionally used (Eklund et al., 2016). To assess the emergence of non-parametric voxel-wise statistics, we recorded the occurrence of non-parametric statistics. We found only 12 mentions of such tests out of 868 studies. This low incidence is indicative of comparable trends in the corresponding human neuroimaging field. Differences between studies are accentuated as voxel-wise statistics in animal studies have been corrected with varying degrees of stringency, such as correcting by arbitrary *ad hoc* cluster size or *p*-value threshold. These render the comparison between studies opaque. To overcome these limitations and to permit meta-analysis, NeuroVault (Gorgolewski et al., 2015) offers a resource to publish statistical maps prior to statistical thresholds, leaving the users to explore, reinterpret, and repurpose these results. Unfortunately, such resources are not yet available to animal neuroimaging studies. The advent of RS-FC and network analysis is another source of dissension in the statistical analysis. With fine-grain ROI sets, the number of edges increases dramatically, hence the number of univariate tests and the need to correct for multiple comparisons. There, no consensus currently exists to effectively account for multiple comparisons and the heightened level of false positives ensuing.

The growth of the human neuroimaging community has been fueled by large datasets made publicly available in online repositories (Nichols et al., 2017). Making raw data available is becoming a requirement by the funding bodies, academic center, and the journals. In spite of these requirements, we only found 15 mentions of data availability, among 868 studies, seven of which upon reasonable request to the senior author. Publication of datasets on established repositories ensures lasting availability of the dataset and unbiased distribution. Databases such as XNAT[2] (Herrick et al., 2016) and Openneuro[3] (Poldrack et al., 2013) are becoming increasingly user-friendly, including standardized formats that allow for the easy organization and retrieval of functional and anatomical data (Gorgolewski et al., 2016). Importantly, potential reticence in human neuroimaging to share material to protect subject privacy do not apply in animal research. Importantly, shared material allows for in-depth

[2]https://central.xnat.org/
[3]https://openneuro.org/

scrutiny of published results and hence strengthen the trust in the published results and facilitate meta-analysis.

CONCLUSION AND OUTLOOK

With this study, we describe the general trends in animal functional neuroimaging and reflect on emerging collective efforts driving toward larger multi-center studies and a desire for the adoption of standards and good practices in the field. Several issues highlighted above are specific to the animal imaging field, such as those related to opto-/chemo-fMRI study designs, anesthesia, and data preprocessing. Others are shared with the human neuroimaging field, including acquisition sequences and data analysis methods, but still contain specific considerations for the animal imaging community. A general consensus on several acquisition procedures within the community is unlikely to be reached, especially on contentious topics such as anesthesia and animal preparation. Nonetheless, we report general trends which indicate some degrees of consensus. For instance, isoflurane and medetomidine and/or their combination represent an increasing proportion of the studies performed in anesthetized rodents, supported with increasing evidence from the literature. Sequences and contrasts are also reaching consensus, as the overwhelming majority of the studies were acquired using GE-EPI and BOLD contrast, predominantly at high fields such as 7T and 9.4T. Importantly, a number of aspects emerge which are currently lacking within our community and which could easily be implemented to greatly ameliorate how results are interpreted. While modest, these first steps will be necessary for the adoption of standards, replication studies, and meta-analysis.

Firstly, the systematic sharing of raw datasets upon publication is the easiest milestone to be achieved within our community. It is often requested by both funding agencies and publishers alike. Yet, less than 1% of the studies were published with its raw data. This represents a severe loss to our community as it prevents the repurposing of material and the critical re-assessment of past results. Arguably, a number of debates regarding methodological aspects of fMRI acquisitions would find a rapid resolution if the material were accessible by the community for in-depth scrutiny. Moreover, a number of variations in data processing highlighted above would be rendered moot as the material could be re-analyzed with other pipelines to confirm or compare results.

The second aspect within acceptable reach in the animal neuroimaging community is the adoption of common references spaces and the reporting of accurate coordinates in both figures and tables, as is common practice in human studies. Despite several templates being available for mice, rats, and NHP (Bakker et al., 2015), no consensus has yet emerged. The reliance on *ad hoc* templates further hinders the adoption of standard templates. While Paxinos and Franklin mice (Paxinos and Franklin, 2012) and Paxinos and Watson rats atlases (Paxinos and Watson, 1982) are systematically referred to, activation clusters have not been reported with respect to their three-dimensional coordinates reported in these atlases. Hence, the adoption of exact three-dimensional coordinate systems, together with tools to convert from one system to another would greatly ameliorate how results in animal neuroimaging studies are reported, and would also among other enable meta-analyses. This should also be accompanied with easily accessible, fully validated open-source data processing toolboxes tailored for animal fMRI data, similarly to what is available in human neuroimaging (Esteban et al., 2019).

Finally, contentious areas, specifically anesthesia and animal preparations, should be approached jointly by multiple laboratories to ensure that the manipulations lead to reproducible results between centers, and to generate a nucleus around which a consensus can emerge. Such efforts will be necessary for the emergence of animal population imaging studies centered on brain function. Such efforts, likewise to human neuroimaging is expected to dramatically accelerate our understanding of the mammalian brain, its evolution, and the pathological mechanisms which affects its function.

AUTHOR CONTRIBUTIONS

JG designed the study and collected and processed the data. All authors contributed to the manuscript preparation.

FUNDING

FM was supported by the University of Manchester and A*STAR Research Attachment Programme (ARAP), which was co-funded through the University of Manchester, Faculty of Biology, Medicine and Health, Doctoral Academy, and Singapore Bioimaging Consortium (SBIC), A*STAR, Singapore. JG wishes to acknowledge the SBIC core funds. AG was supported by the European Research Council (ERC, DISCONN, GA 802371), the Simons Foundation (SFARI 400101), the Brain and Behavior Foundation (NARSAD, Independent Investigator Grant 25861), and the NIH (1R21MH116473-01A1). MS and RD were supported by the Netherlands Organization for Scientific Research (NWO-VICI 016.130.662). GT was supported by the National Institute of Mental Health of the National Institutes of Health under award number R01MH111417.

SUPPLEMENTARY MATERIAL

The Supplementary Material for this article can be found online at: https://www.frontiersin.org/articles/10.3389/fninf.2019.00078/full#supplementary-material

REFERENCES

Abe, Y., Sekino, M., Terazono, Y., Ohsaki, H., Fukazawa, Y., Sakai, S., et al. (2012). Opto-fMRI analysis for exploring the neuronal connectivity of the hippocampal formation in rats. *Neurosci. Res.* 74, 248–255. doi: 10.1016/j.neures.2012.08.007

Abe, Y., Tsurugizawa, T., and Le Bihan, D. (2017). Water diffusion closely reveals neural activity status in rat brain loci affected by anesthesia. *PLoS Biol.* 15:e2001494. doi: 10.1371/journal.pbio.2001494

Abrol, A., Damaraju, E., Miller, R. L., Stephen, J. M., Claus, E. D., Mayer, A. R., et al. (2017). Replicability of time-varying connectivity patterns in large resting

state fMRI samples. *Neuroimage* 163, 160–176. doi: 10.1016/j.neuroimage.2017.09.020

Acker, L., Pino, E. N., Boyden, E. S., and Desimone, R. (2016). FEF inactivation with improved optogenetic methods. *Proc. Natl. Acad. Sci. U.S.A.* 113, E7297–E7306. doi: 10.1073/pnas.1610784113

Aguirre, G. K., Detre, J. A., Zarahn, E., and Alsop, D. C. (2002). Experimental design and the relative sensitivity of BOLD and perfusion fMRI. *Neuroimage* 15, 488–500. doi: 10.1006/nimg.2001.0990

Albaugh, D. L., Salzwedel, A., Van Den Berge, N., Gao, W., Stuber, G. D., and Shih, Y.-Y. I. (2016). Functional magnetic resonance imaging of electrical and optogenetic deep brain stimulation at the rat nucleus accumbens. *Sci. Rep.* 6:31613. doi: 10.1038/srep31613

Albers, F., Schmid, F., Wachsmuth, L., and Faber, C. (2018). Line scanning fMRI reveals earlier onset of optogenetically evoked BOLD response in rat somatosensory cortex as compared to sensory stimulation. *Neuroimage* 164, 144–154. doi: 10.1016/j.neuroimage.2016.12.059

Aldrin-Kirk, P., Heuer, A., Rylander Ottosson, D., Davidsson, M., Mattsson, B., and Björklund, T. (2018). Chemogenetic modulation of cholinergic interneurons reveals their regulating role on the direct and indirect output pathways from the striatum. *Neurobiol. Dis.* 109, 148–162. doi: 10.1016/j.nbd.2017.10.010

Alexander, G. M., Rogan, S. C., Abbas, A. I., Armbruster, B. N., Pei, Y., Allen, J. A., et al. (2009). Remote control of neuronal activity in transgenic mice expressing evolved G protein-coupled receptors. *Neuron* 63, 27–39. doi: 10.1016/j.neuron.2009.06.014

Allen, B. D., Singer, A. C., and Boyden, E. S. (2015). Principles of designing interpretable optogenetic behavior experiments. *Learn. Mem.* 22, 232–238. doi: 10.1101/lm.038026.114

Allen, E. A., Damaraju, E., Plis, S. M., Erhardt, E. B., Eichele, T., and Calhoun, V. D. (2014). Tracking whole-brain connectivity dynamics in the resting state. *Cerebral. Cortex* 24, 663–676. doi: 10.1093/cercor/bhs352

Amaro, E. Jr., and Barker, G. J. (2006). Study design in fMRI: basic principles. *Brain Cogn.* 60, 220–232. doi: 10.1016/j.bandc.2005.11.009

Aravanis, A. M., Wang, L.-P., Zhang, F., Meltzer, L. A., Mogri, M. Z., Schneider, M. B., et al. (2007). An optical neural interface: in vivo control of rodent motor cortex with integrated fiberoptic and optogenetic technology. *J. Neural Eng.* 4, S143–S156. doi: 10.1088/1741-2560/4/3/S02

Arey, B. J. (2014). "An historical introduction to biased signaling," in *Biased Signaling in Physiology, Pharmacology and Therapeutics*, ed. B. J. Arey, (Amsterdam: Elsevier), 1–39. doi: 10.1016/b978-0-12-411460-9.00001-x

Armbruster, B. N., Li, X., Pausch, M. H., Herlitze, S., and Roth, B. L. (2007). Evolving the lock to fit the key to create a family of G protein-coupled receptors potently activated by an inert ligand. *Proc. Natl. Acad. Sci. U.S.A.* 104, 5163–5168. doi: 10.1073/pnas.0700293104

Ashby, C. R. Jr., and Wang, R. Y. (1996). Pharmacological actions of the atypical antipsychotic drug clozapine: a review. *Synapse* 24, 349–394. doi: 10.1002/(sici)1098-2396(199612)24:4<349::aid-syn5>3.0.co;2-d

Atasoy, D., Aponte, Y., Su, H. H., and Sternson, S. M. (2008). A FLEX switch targets Channelrhodopsin-2 to multiple cell types for imaging and long-range circuit mapping. *J. Neurosci.* 28, 7025–7030. doi: 10.1523/JNEUROSCI.1954-08.2008

Báez-Yánez, M. G., Ehses, P., Mirkes, C., Tsai, P. S., Kleinfeld, D., and Scheffler, K. (2017). The impact of vessel size, orientation and intravascular contribution on the neurovascular fingerprint of BOLD bSSFP fMRI. *Neuroimage* 163, 13–23. doi: 10.1016/j.neuroimage.2017.09.015

Bakker, R., Tiesinga, P., and Kötter, R. (2015). The scalable brain Atlas: instant web-based access to public brain atlases and related content. *Neuroinformatics* 13, 353–366. doi: 10.1007/s12021-014-9258-x

Baltes, C., Bosshard, S., Mueggler, T., Ratering, D., and Rudin, M. (2011). Increased blood oxygen level-dependent (BOLD) sensitivity in the mouse somatosensory cortex during electrical forepaw stimulation using a cryogenic radiofrequency probe. *NMR Biomed.* 24, 439–446. doi: 10.1002/nbm.1613

Barttfeld, P., Uhrig, L., Sitt, J. D., Sigman, M., Jarraya, B., and Dehaene, S. (2015). Signature of consciousness in the dynamics of resting-state brain activity. *Proc. Natl. Acad. Sci. U.S.A.* 112, 887–892. doi: 10.1073/pnas.1418031112

Beery, A. K., and Zucker, I. (2011). Sex bias in neuroscience and biomedical research. *Neurosci. Biobehav. Rev.* 35, 565–572. doi: 10.1016/j.neubiorev.2010.07.002

Belcher, A. M., Yen, C. C., Stepp, H., Gu, H., Lu, H., Yang, Y., et al. (2013). Large-scale brain networks in the awake, truly resting marmoset monkey. *J. Neurosci.* 33, 16796–16804. doi: 10.1523/JNEUROSCI.3146-13.2013

Belloy, M. E., Shah, D., Abbas, A., Kashyap, A., Roßner, S., Van der Linden, A., et al. (2018). Quasi-periodic patterns of neural activity improve classification of Alzheimer's disease in mice. *Sci. Rep.* 8:10024. doi: 10.1038/s41598-018-28237-9

Berg, K. A., and Clarke, W. P. (2018). Making sense of pharmacology: inverse agonism and functional selectivity. *Int. J. Neuropsychopharmacol.* 21, 962–977. doi: 10.1093/ijnp/pyy071

Berndt, A., Lee, S. Y., Ramakrishnan, C., and Deisseroth, K. (2014). Structure-guided transformation of channelrhodopsin into a light-activated chloride channel. *Science* 344, 420–424. doi: 10.1126/science.1252367

Berndt, A., Yizhar, O., Gunaydin, L. A., Hegemann, P., and Deisseroth, K. (2009). Bi-stable neural state switches. *Nat. Neurosci.* 12, 229–234. doi: 10.1038/nn.2247

Bernstein, J. G., and Boyden, E. S. (2011). Optogenetic tools for analyzing the neural circuits of behavior. *Trends Cogn. Sci.* 15, 592–600. doi: 10.1016/j.tics.2011.10.003

Bertero, A., Liska, A., Pagani, M., Parolisi, R., Masferrer, M. E., Gritti, M., et al. (2018). Autism-associated 16p11.2 microdeletion impairs prefrontal functional connectivity in mouse and human. *Brain* 141, 2055–2065. doi: 10.1093/brain/awy111

Bifone, A., and Gozzi, A. (2012). Neuromapping techniques in drug discovery: pharmacological MRI for the assessment of novel antipsychotics. *Expert Opin. Drug Discov.* 7, 1071–1082. doi: 10.1517/17460441.2012.724057

Biswal, B., Hudetz, A. G., Zerrin Yetkin, F., Haughton, V. M., and Hyde, J. S. (1997). Hypercapnia reversibly suppresses low-frequency fluctuations in the human motor cortex during rest using echo–planar MRI. *J. Cereb. Blood Flow Metab.* 17, 301–308. doi: 10.1097/00004647-199703000-00007

Biswal, B., Yetkin, F. Z., Haughton, V. M., and Hyde, J. S. (1995). Functional connectivity in the motor cortex of resting human brain using echo-planar MRI. *Magn. Reson. Med.* 34, 537–541. doi: 10.1002/mrm.1910340409

Biswal, B. B., Mennes, M., Zuo, X.-N., Gohel, S., Kelly, C., Smith, S. M., et al. (2010). Toward discovery science of human brain function. *Proc. Natl. Acad. Sci. U.S.A.* 107, 4734–4739. doi: 10.1073/pnas.0911855107

Bonhomme, V., Boveroux, P., Brichant, J. F., Laureys, S., and Boly, M. (2012). Neural correlates of consciousness during general anesthesia using functional magnetic resonance imaging (fMRI). *Arch. Ital. Biol.* 150, 155–163. doi: 10.4449/aib.v150i2.1242

Borogovac, A., and Asllani, I. (2012). Arterial Spin Labeling (ASL) fMRI: advantages, theoretical constrains, and experimental challenges in neurosciences. *Int. J. Biomed. Imaging* 2012, 818456. doi: 10.1155/2012/818456

Bosshard, S. C., Baltes, C., Wyss, M. T., Mueggler, T., Weber, B., and Rudin, M. (2010). Assessment of brain responses to innocuous and noxious electrical forepaw stimulation in mice using BOLD fMRI. *Pain* 151, 655–663. doi: 10.1016/j.pain.2010.08.025

Boyden, E. S. (2015). Erratum: optogenetics and the future of neuroscience. *Nat. Neurosci.* 18:1862. doi: 10.1038/nn1215-1862b

Boyden, E. S., Zhang, F., Bamberg, E., Nagel, G., and Deisseroth, K. (2005). Millisecond-timescale, genetically targeted optical control of neural activity. *Nat. Neurosci.* 8, 1263–1268. doi: 10.1038/nn1525

Brevard, M. E., Duong, T. Q., King, J. A., and Ferris, C. F. (2003). Changes in MRI signal intensity during hypercapnic challenge under conscious and anesthetized conditions. *Magn. Reson. Imaging* 21, 995–1001. doi: 10.1016/s0730-725x(03)00204-2

Brocka, M., Helbing, C., Vincenz, D., Scherf, T., Montag, D., Goldschmidt, J., et al. (2018). Contributions of dopaminergic and non-dopaminergic neurons to VTA-stimulation induced neurovascular responses in brain reward circuits. *Neuroimage* 177, 88–97. doi: 10.1016/j.neuroimage.2018.04.059

Bruinsma, T. J., Sarma, V. V., Oh, Y., Jang, D. P., Chang, S.-Y., Worrell, G. A., et al. (2018). The relationship between dopamine neurotransmitter dynamics and the Blood-Oxygen-Level-Dependent (BOLD) signal: a review of pharmacological functional magnetic resonance imaging. *Front. Neurosci.* 12:238. doi: 10.3389/fnins.2018.00238

Buckner, R. L., and DiNicola, L. M. (2019). The brain's default network: updated anatomy, physiology and evolving insights. *Nat. Rev. Neurosci.* 20, 593–608. doi: 10.1038/s41583-019-0212-7

Buckner, R. L., Sepulcre, J., Talukdar, T., Krienen, F. M., Liu, H., Hedden, T., et al. (2009). Cortical hubs revealed by intrinsic functional connectivity: mapping, assessment of stability, and relation to Alzheimer's disease. *J. Neurosci.* 29, 1860–1873. doi: 10.1523/JNEUROSCI.5062-08.2009

Bukhari, Q., Schroeter, A., Cole, D. M., and Rudin, M. (2017). Resting State fMRI in mice reveals anesthesia specific signatures of brain functional networks and their interactions. *Front. Neural Circuits* 11:5. doi: 10.3389/fncir.2017.00005

Bukhari, Q., Schroeter, A., and Rudin, M. (2018). Increasing isoflurane dose reduces homotopic correlation and functional segregation of brain networks in mice as revealed by resting-state fMRI. *Sci. Rep.* 8:10591. doi: 10.1038/s41598-018-28766-3

Bullmore, E., and Sporns, O. (2009). Complex brain networks: graph theoretical analysis of structural and functional systems. *Nat. Rev. Neurosci.* 10, 186–198. doi: 10.1038/nrn2575

Button, K. S., Ioannidis, J. P. A., Mokrysz, C., Nosek, B. A., Flint, J., Robinson, E. S. J., et al. (2013). Power failure: why small sample size undermines the reliability of neuroscience. *Nat. Rev. Neurosci.* 14, 365–376. doi: 10.1038/nrn3475

Canese, R., Marco, E. M., De Pasquale, F., Podo, F., Laviola, G., and Adriani, W. (2011). Differential response to specific 5-Ht(7) versus whole-serotonergic drugs in rat forebrains: a phMRI study. *Neuroimage* 58, 885–894. doi: 10.1016/j.neuroimage.2011.06.089

Cardin, J. A., Carlén, M., Meletis, K., Knoblich, U., Zhang, F., Deisseroth, K., et al. (2010). Targeted optogenetic stimulation and recording of neurons in vivo using cell-type-specific expression of Channelrhodopsin-2. *Nat. Protoc.* 5, 247–254. doi: 10.1038/nprot.2009.228

Carp, J. (2012). The secret lives of experiments: methods reporting in the fMRI literature. *Neuroimage* 63, 289–300. doi: 10.1016/j.neuroimage.2012.07.004

Chai, Y., Bi, G., Wang, L., Xu, F., Wu, R., Zhou, X., et al. (2016). Direct detection of optogenetically evoked oscillatory neuronal electrical activity in rats using SLOE sequence. *Neuroimage* 125, 533–543. doi: 10.1016/j.neuroimage.2015.10.058

Chan, R. W., Leong, A. T. L., Ho, L. C., Gao, P. P., Wong, E. C., Dong, C. M., et al. (2017). Low-frequency hippocampal–cortical activity drives brain-wide resting-state functional MRI connectivity. *Proc. Natl. Acad. Sci. U.S.A.* 114, E6972–E6981. doi: 10.1073/pnas.1703309114

Chang, W.-T., Puspitasari, F., Garcia-Miralles, M., Yeow, L. Y., Tay, H.-C., Koh, K. B., et al. (2018). Connectomic imaging reveals Huntington-related pathological and pharmaceutical effects in a mouse model. *NMR Biomed.* 31:e4007. doi: 10.1002/nbm.4007

Chen, Y. C., Mandeville, J. B., Nguyen, T. V., Talele, A., Cavagna, F., and Jenkins, B. G. (2001). Improved mapping of pharmacologically induced neuronal activation using the IRON technique with superparamagnetic blood pool agents. *J. Magn. Reson. Imaging* 14, 517–524. doi: 10.1002/jmri.1215

Chen, Y. I., Brownell, A. L., Galpern, W., Isacson, O., Bogdanov, M., Beal, M. F., et al. (1999). Detection of dopaminergic cell loss and neural transplantation using pharmacological MRI. PET and behavioral assessment. *Neuroreport* 10, 2881–2886. doi: 10.1097/00001756-199909290-00001

Chen, Y.-W., Das, M., Oyarzabal, E. A., Cheng, Q., Plummer, N. W., Smith, K. G., et al. (2018). Genetic identification of a population of noradrenergic neurons implicated in attenuation of stress-related responses. *Mol. Psychiatry* 24, 710–725. doi: 10.1038/s41380-018-0245-8

Choe, K. Y., Sanchez, C. F., Harris, N. G., Otis, T. S., and Mathews, P. J. (2018). Optogenetic fMRI and electrophysiological identification of region-specific connectivity between the cerebellar cortex and forebrain. *Neuroimage* 173, 370–383. doi: 10.1016/j.neuroimage.2018.02.047

Christie, I. N., Wells, J. A., Southern, P., Marina, N., Kasparov, S., Gourine, A. V., et al. (2013). fMRI response to blue light delivery in the naïve brain: implications for combined optogenetic fMRI studies. *Neuroimage* 66, 634–641. doi: 10.1016/j.neuroimage.2012.10.074

Chuong, A. S., Miri, M. L., Busskamp, V., Matthews, G. A. C., Acker, L. C., Sørensen, A. T., et al. (2014). Noninvasive optical inhibition with a red-shifted microbial rhodopsin. *Nat. Neurosci.* 17, 1123–1129. doi: 10.1038/nn.3752

Ciobanu, L., Reynaud, O., Uhrig, L., Jarraya, B., and Le Bihan, D. (2012). Effects of anesthetic agents on brain blood oxygenation level revealed with ultra-high field MRI. *PLoS One* 7:e32645. doi: 10.1371/journal.pone.0032645

Cogan, S. F., Ludwig, K. A., Welle, C. G., and Takmakov, P. (2016). Tissue damage thresholds during therapeutic electrical stimulation. *J. Neural Eng.* 13:021001. doi: 10.1088/1741-2560/13/2/021001

Dai, W., Garcia, D., de Bazelaire, C., and Alsop, D. C. (2008). Continuous flow-driven inversion for arterial spin labeling using pulsed radio frequency and gradient fields. *Magn. Reson. Med.* 60, 1488–1497. doi: 10.1002/mrm.21790

Damoiseaux, J. S., and Greicius, M. D. (2009). Greater than the sum of its parts: a review of studies combining structural connectivity and resting-state functional connectivity. *Brain Struct. Funct.* 213, 525–533. doi: 10.1007/s00429-009-0208-6

Decot, H. K., Namboodiri, V. M. K., Gao, W., McHenry, J. A., Jennings, J. H., Lee, S.-H., et al. (2017). Coordination of brain-wide activity dynamics by dopaminergic neurons. *Neuropsychopharmacology* 42, 615–627. doi: 10.1038/npp.2016.151

Deisseroth, K. (2015). Optogenetics: 10 years of microbial opsins in neuroscience. *Nat. Neurosci.* 18, 1213–1225. doi: 10.1038/nn.4091

Desai, M., Kahn, I., Knoblich, U., Bernstein, J., Atallah, H., Yang, A., et al. (2011). Mapping brain networks in awake mice using combined optical neural control and fMRI. *J. Neurophysiol.* 105, 1393–1405. doi: 10.1152/jn.00828.2010

Detre, J. A., and Wang, J. (2002). Technical aspects and utility of fMRI using BOLD and ASL. *Clin. Neurophysiol.* 113, 621–634. doi: 10.1016/s1388-2457(02)00038-x

Di Martino, A., Yan, C.-G., Li, Q., Denio, E., Castellanos, F. X., Alaerts, K., et al. (2014). The autism brain imaging data exchange: towards a large-scale evaluation of the intrinsic brain architecture in autism. *Mol. Psychiatry* 19, 659–667. doi: 10.1038/mp.2013.78

Dorr, A. E., Lerch, J. P., Spring, S., Kabani, N., and Henkelman, R. M. (2008). High resolution three-dimensional brain atlas using an average magnetic resonance image of 40 adult C57Bl/6J mice. *Neuroimage* 42, 60–69. doi: 10.1016/j.neuroimage.2008.03.037

Eklund, A., Nichols, T. E., and Knutsson, H. (2016). Cluster failure: why fMRI inferences for spatial extent have inflated false-positive rates. *Proc. Natl. Acad. Sci. U.S.A.* 113, 7900–7905. doi: 10.1073/pnas.1602413113

Elias, Z., Powers, S. K., Atstupenas, E., and Tony Brown, J. (1987). Hyperthermia from interstitial laser irradiation in normal rat brain. *Lasers Surg. Med.* 7, 370–375. doi: 10.1002/lsm.1900070413

English, J. G., and Roth, B. L. (2015). Chemogenetics-a transformational and translational platform. *JAMA Neurol.* 72, 1361–1366. doi: 10.1001/jamaneurol.2015.1921

Esteban, O., Markiewicz, C. J., Blair, R. W., Moodie, C. A., Isik, A. I., Erramuzpe, A., et al. (2019). fMRIPrep: a robust preprocessing pipeline for functional MRI. *Nat. Methods* 16, 111–116. doi: 10.1038/s41592-018-0235-4

Farrell, M. S., Pei, Y., Wan, Y., Yadav, P. N., Daigle, T. L., Urban, D. J., et al. (2013). A Gαs DREADD mouse for selective modulation of cAMP production in striatopallidal neurons. *Neuropsychopharmacology* 38, 854–862. doi: 10.1038/npp.2012.251

Fenno, L., Yizhar, O., and Deisseroth, K. (2011). The development and application of optogenetics. *Annu. Rev. Neurosci.* 34, 389–412. doi: 10.1146/annurev-neuro-061010-113817

Ferenczi, E. A., Zalocusky, K. A., Liston, C., Grosenick, L., Warden, M. R., Amatya, D., et al. (2016). Prefrontal cortical regulation of brainwide circuit dynamics and reward-related behavior. *Science* 351:aac9698. doi: 10.1126/science.aac9698

Ferrari, L., Turrini, G., Crestan, V., Bertani, S., Cristofori, P., Bifone, A., et al. (2012). A robust experimental protocol for pharmacological fMRI in rats and mice. *J. Neurosci. Methods* 204, 9–18. doi: 10.1016/j.jneumeth.2011.10.020

Ferris, C. F., Febo, M., Luo, F., Schmidt, K., Brevard, M., Harder, J. A., et al. (2006). Functional magnetic resonance imaging in conscious animals: a new tool in behavioural neuroscience research. *J. Neuroendocrinol.* 18, 307–318. doi: 10.1111/j.1365-2826.2006.01424.x

Ferrari, M., Kruzliak, P., and Spiliopoulos, K. (2015). An insight into short- and long-term mechanical circulatory support systems. *Clin. Res. Cardiol.* 104, 95–111. doi: 10.1007/s00392-014-0771-6

Filippini, N., MacIntosh, B. J., Hough, M. G., Goodwin, G. M., Frisoni, G. B., Smith, S. M., et al. (2009). Distinct patterns of brain activity in young carriers of the APOE-epsilon4 allele. *Proc. Natl. Acad. Sci. U.S.A.* 106, 7209–7214. doi: 10.1073/pnas.0811879106

Franks, N. P. (2008). General anaesthesia: from molecular targets to neuronal pathways of sleep and arousal. *Nat. Rev. Neurosci.* 9, 370–386. doi: 10.1038/nrn2372

Garcia, P., Kolesky, S., and Jenkins, A. (2010). General anesthetic actions on GABAA receptors. *Curr. Neuropharmacol.* 8, 2–9. doi: 10.2174/157015910790909502

Garin, C. M., Nadkarni, N. A., Landeau, B., Chételat, G., Picq, J.-L., Bougacha, S., et al. (2019). Resting state cerebral networks in mouse lemur primates:

from multilevel validation to comparison with humans. *bioRxiv* [Preprint]. doi: 10.1101/599423

Garrett, K. M., and Gan, J. (1998). Enhancement of gamma-aminobutyric acidA receptor activity by alpha-chloralose. *J. Pharmacol. Exp. Ther.* 285, 680–686.

Giorgi, A., Migliarini, S., Galbusera, A., Maddaloni, G., Mereu, M., Margiani, G., et al. (2017). Brain-wide mapping of endogenous serotonergic transmission via chemogenetic fMRI. *Cell Rep.* 21, 910–918. doi: 10.1016/j.celrep.2017.09.087

Goense, J. B. M., and Logothetis, N. K. (2006). Laminar specificity in monkey V1 using high-resolution SE-fMRI. *Magn. Reson. Imaging* 24, 381–392. doi: 10.1016/j.mri.2005.12.032

Golestani, A. M., Wei, L. L., and Chen, J. J. (2016). Quantitative mapping of cerebrovascular reactivity using resting-state BOLD fMRI: validation in healthy adults. *Neuroimage* 138, 147–163. doi: 10.1016/j.neuroimage.2016.05.025

Gomez, J. L., Bonaventura, J., Lesniak, W., Mathews, W. B., Sysa-Shah, P., Rodriguez, L. A., et al. (2017). Chemogenetics revealed: DREADD occupancy and activation via converted clozapine. *Science* 357, 503–507. doi: 10.1126/science.aan2475

Gompf, H. S., Budygin, E. A., Fuller, P. M., and Bass, C. E. (2015). Targeted genetic manipulations of neuronal subtypes using promoter-specific combinatorial AAVs in wild-type animals. *Front. Behav. Neurosci.* 9:152. doi: 10.3389/fnbeh.2015.00152

Gorgolewski, K. J., Auer, T., Calhoun, V. D., Craddock, R. C., Das, S., Duff, E. P., et al. (2016). The brain imaging data structure, a format for organizing and describing outputs of neuroimaging experiments. *Sci. Data* 3:160044. doi: 10.1038/sdata.2016.44

Gorgolewski, K. J., Varoquaux, G., Rivera, G., Schwarz, Y., Ghosh, S. S., Maumet, C., et al. (2015). NeuroVault.org: a web-based repository for collecting and sharing unthresholded statistical maps of the human brain. *Front. Neuroinform.* 9:8. doi: 10.3389/fninf.2015.00008

Gozzi, A., Ceolin, L., Schwarz, A., Reese, T., Bertani, S., Crestan, V., et al. (2007). A multimodality investigation of cerebral hemodynamics and autoregulation in pharmacological MRI. *Magn. Reson. Imaging* 25, 826–833. doi: 10.1016/j.mri.2007.03.003

Gozzi, A., Jain, A., Giovannelli, A., Bertollini, C., Crestan, V., Schwarz, A. J., et al. (2012). A neural switch for active and passive fear. *Neuron* 73:854. doi: 10.1016/j.neuron.2012.02.007

Gozzi, A., Large, C. H., Schwarz, A., Bertani, S., Crestan, V., and Bifone, A. (2008). Differential Effects of Antipsychotic and Glutamatergic Agents on the phMRI Response to Phencyclidine. *Neuropsychopharmacology* 33, 1690–1703. doi: 10.1038/sj.npp.1301547

Gozzi, A., and Schwarz, A. J. (2016). Large-scale functional connectivity networks in the rodent brain. *Neuroimage* 127, 496–509. doi: 10.1016/j.neuroimage.2015.12.017

Grandjean, J., Canella, C., Anckaerts, C., Ayranci, G., Bougacha, S., Bienert, T., et al. (2019a). Common functional networks in the mouse brain revealed by multi-centre resting-state fMRI analysis. *bioRxiv* [Preprint]. doi: 10.1101/393389

Grandjean, J., Corcoba, A., Kahn, M. C., Upton, A. L., Deneris, E. S., Seifritz, E., et al. (2019b). A brain-wide functional map of the serotonergic responses to acute stress and fluoxetine. *Nat. Commun.* 10:350. doi: 10.1038/s41467-018-08256-w

Grandjean, J., Preti, M. G., Bolton, T. A. W., Buerge, M., Seifritz, E., Pryce, C. R., et al. (2017a). Dynamic reorganization of intrinsic functional networks in the mouse brain. *Neuroimage* 152, 497–508. doi: 10.1016/j.neuroimage.2017.03.026

Grandjean, J., Zerbi, V., Balsters, J. H., Wenderoth, N., and Rudin, M. (2017b). Structural basis of large-scale functional connectivity in the mouse. *J. Neurosci.* 37, 8092–8101. doi: 10.1523/JNEUROSCI.0438-17.2017

Grandjean, J., Schroeter, A., Batata, I., and Rudin, M. (2014). Optimization of anesthesia protocol for resting-state fMRI in mice based on differential effects of anesthetics on functional connectivity patterns. *Neuroimage* 102(Pt 2), 838–847. doi: 10.1016/j.neuroimage.2014.08.043

Grayson, D. S., Bliss-Moreau, E., Machado, C. J., Bennett, J., Shen, K., Grant, K. A., et al. (2016). The Rhesus monkey connectome predicts disrupted functional networks resulting from pharmacogenetic inactivation of the amygdala. *Neuron* 91, 453–466. doi: 10.1016/j.neuron.2016.06.005

Griessner, J., Pasieka, M., Böhm, V., Grössl, F., Kaczanowska, J., Pliota, P., et al. (2018). Central amygdala circuit dynamics underlying the benzodiazepine anxiolytic effect. *Mol. Psychiatry* doi: 10.1038/s41380-018-0310-3 [Epub ahead of print].

Guadagno, A., Kang, M. S., Devenyi, G. A., Mathieu, A. P., Rosa-Neto, P., Chakravarty, M., et al. (2018). Reduced resting-state functional connectivity of the basolateral amygdala to the medial prefrontal cortex in preweaning rats exposed to chronic early-life stress. *Brain Struct. Funct.* 223, 3711–3729. doi: 10.1007/s00429-018-1720-3

Gunaydin, L. A., Yizhar, O., Berndt, A., Sohal, V. S., Deisseroth, K., and Hegemann, P. (2010). Ultrafast optogenetic control. *Nat. Neurosci.* 13, 387–392. doi: 10.1038/nn.2495

Guru, A., Post, R. J., Ho, Y.-Y., and Warden, M. R. (2015). Making sense of optogenetics. *Int. J. Neuropsychopharmacol.* 18:yv079. doi: 10.1093/ijnp/pyv079

Gutierrez-Barragan, D., Albert Basson, M., Panzeri, S., and Gozzi, A. (2018). Oscillatory brain states govern spontaneous fMRI network dynamics. *bioRxiv* [Preprint]. doi: 10.1101/541060

Hagberg, G. E., Indovina, I., Sanes, J. N., and Posse, S. (2002). Real-time quantification of T(2)(*) changes using multiecho planar imaging and numerical methods. *Magn. Reson. Med.* 48, 877–882. doi: 10.1002/mrm.10283

Han, S., Son, J. P., Cho, H., Park, J., and Kim, S. (2019). Gradient-echo and spin-echo blood oxygenation level–dependent functional MRI at ultrahigh fields of 9.4 and 15.2 Tesla. *Magn. Reson. Med.* 81, 1237–1246. doi: 10.1002/mrm.27457

HD-200 Consortium, (2012). The ADHD-200 consortium: a model to advance the translational potential of neuroimaging in clinical neuroscience. *Front. Syst. Neurosci.* 6:62. doi: 10.3389/fnsys.2012.00062

Herrick, R., Horton, W., Olsen, T., McKay, M., Archie, K. A., and Marcus, D. S. (2016). XNAT Central: open sourcing imaging research data. *Neuroimage* 124, 1093–1096. doi: 10.1016/j.neuroimage.2015.06.076

Hess, A., Sergejeva, M., Budinsky, L., Zeilhofer, H. U., and Brune, K. (2007). Imaging of hyperalgesia in rats by functional MRI. *Eur. J. Pain* 11, 109–109. doi: 10.1016/j.ejpain.2006.01.005

Hight, A. E., Kozin, E. D., Darrow, K., Lehmann, A., Boyden, E., Brown, M. C., et al. (2015). Superior temporal resolution of Chronos versus channelrhodopsin-2 in an optogenetic model of the auditory brainstem implant. *Hear. Res.* 322, 235–241. doi: 10.1016/j.heares.2015.01.004

Hindriks, R., Woolrich, M., Luckhoo, H., Joensson, M., Mohseni, H., Kringelbach, M. L., et al. (2015). Role of white-matter pathways in coordinating alpha oscillations in resting visual cortex. *Neuroimage* 106, 328–339. doi: 10.1016/j.neuroimage.2014.10.057

Hinz, R., Peeters, L., Li, C., Van Der Linden, A., and Keliris, G. (2017). A comparison of BOLD response between optogenetic and visual stimulation of the lateral Geniculate Nucleus. *Front. Neurosci.* 11:59. doi: 10.3389/conf.fnins.2017.94.00059

Huber, D., Petreanu, L., Ghitani, N., Ranade, S., Hromádka, T., Mainen, Z., et al. (2008). Sparse optical microstimulation in barrel cortex drives learned behaviour in freely moving mice. *Nature* 451, 61–64. doi: 10.1038/nature06445

Hutchison, R. M., and Everling, S. (2012). Monkey in the middle: why non-human primates are needed to bridge the gap in resting-state investigations. *Front. Neuroanat.* 6:29. doi: 10.3389/fnana.2012.00029

Hutchison, R. M., Hutchison, M., Manning, K. Y., Menon, R. S., and Everling, S. (2014). Isoflurane induces dose-dependent alterations in the cortical connectivity profiles and dynamic properties of the brain's functional architecture. *Hum. Brain Mapp.* 35, 5754–5775. doi: 10.1002/hbm.22583

Hutchison, R. M., Mirsattari, S. M., Jones, C. K., Gati, J. S., and Leung, L. S. (2010). Functional networks in the anesthetized rat brain revealed by independent component analysis of resting-state FMRI. *J. Neurophysiol.* 103, 3398–3406. doi: 10.1152/jn.00141.2010

Hutchison, R. M., Womelsdorf, T., Allen, E. A., Bandettini, P. A., Calhoun, V. D., Corbetta, M., et al. (2013a). Dynamic functional connectivity: promise, issues, and interpretations. *Neuroimage* 80, 360–378. doi: 10.1016/j.neuroimage.2013.05.079

Hutchison, R. M., Womelsdorf, T., Gati, J. S., Everling, S., and Menon, R. S. (2013b). Resting-state networks show dynamic functional connectivity in awake humans and anesthetized macaques. *Hum. Brain Mapp.* 34, 2154–2177. doi: 10.1002/hbm.22058

Iordanova, B., Vazquez, A. L., Poplawsky, A. J., Fukuda, M., and Kim, S.-G. (2015). Neural and hemodynamic responses to optogenetic and sensory stimulation

in the rat somatosensory cortex. *J. Cereb. Blood Flow Metab.* 35, 922–932. doi: 10.1038/jcbfm.2015.10

Janke, A. L., and Ullmann, J. F. P. (2015). Robust methods to create ex vivo minimum deformation atlases for brain mapping. *Methods* 73, 18–26. doi: 10.1016/j.ymeth.2015.01.005

Jenkins, B. G. (2012). Pharmacologic magnetic resonance imaging (phMRI): imaging drug action in the brain. *Neuroimage* 62, 1072–1085. doi: 10.1016/j.neuroimage.2012.03.075

Johnson, G. A., Badea, A., Brandenburg, J., Cofer, G., Fubara, B., Liu, S., et al. (2010). Waxholm space: an image-based reference for coordinating mouse brain research. *Neuroimage* 53, 365–372. doi: 10.1016/j.neuroimage.2010.06.067

Jonckers, E., Delgado y Palacios, R., Shah, D., Guglielmetti, C., Verhoye, M., and Van der Linden, A. (2014). Different anesthesia regimes modulate the functional connectivity outcome in mice. *Magn. Reson. Med.* 72, 1103–1112. doi: 10.1002/mrm.24990

Jonckers, E., Shah, D., Hamaide, J., Verhoye, M., and Van der Linden, A. (2015). The power of using functional fMRI on small rodents to study brain pharmacology and disease. *Front. Pharmacol.* 6:231. doi: 10.3389/fphar.2015.00231

Jonckers, E., Van Audekerke, J., De Visscher, G., Van der Linden, A., and Verhoye, M. (2011). Functional connectivity fMRI of the rodent brain: comparison of functional connectivity networks in rat and mouse. *PLoS One* 6:e18876. doi: 10.1371/journal.pone.0018876

Jung, W. B., Shim, H.-J., and Kim, S.-G. (2019). Mouse BOLD fMRI at ultrahigh field detects somatosensory networks including thalamic nuclei. *Neuroimage* 195, 203–214. doi: 10.1016/j.neuroimage.2019.03.063

Kahn, I., Desai, M., Knoblich, U., Bernstein, J., Henninger, M., Graybiel, A. M., et al. (2011). Characterization of the functional MRI response temporal linearity via optical control of neocortical pyramidal neurons. *J. Neurosci.* 31, 15086–15091. doi: 10.1523/jneurosci.0007-11.2011

Kahn, I., Knoblich, U., Desai, M., Bernstein, J., Graybiel, A. M., Boyden, E. S., et al. (2013). Optogenetic drive of neocortical pyramidal neurons generates fMRI signals that are correlated with spiking activity. *Brain Res.* 1511, 33–45. doi: 10.1016/j.brainres.2013.03.011

Kalisch, R., Elbel, G. K., Gössl, C., Czisch, M., and Auer, D. P. (2001). Blood pressure changes induced by arterial blood withdrawal influence bold signal in anesthesized rats at 7 Tesla: implications for pharmacologic mri. *Neuroimage* 14, 891–898. doi: 10.1006/nimg.2001.0890

Kalthoff, D., Po, C., Wiedermann, D., and Hoehn, M. (2013). Reliability and spatial specificity of rat brain sensorimotor functional connectivity networks are superior under sedation compared with general anesthesia. *NMR Biomed.* 26, 638–650. doi: 10.1002/nbm.2908

Kalthoff, D., Seehafer, J. U., Po, C., Wiedermann, D., and Hoehn, M. (2011). Functional connectivity in the rat at 11.7T: impact of physiological noise in resting state fMRI. *Neuroimage* 54, 2828–2839. doi: 10.1016/j.neuroimage.2010.10.053

Keilholz, S. D., Billings, J. C. W., Kai, W., Abbas, A., Hafeneger, C., Wen-Ju Pan, et al. (2016). Multiscale network activity in resting state fMRI. *Conf. Proc. IEEE Eng. Med. Biol. Soc.* 2016, 61–64. doi: 10.1109/EMBC.2016.7590640

Keilholz, S. D., Magnuson, M. E., Pan, W.-J., Willis, M., and Thompson, G. J. (2013). Dynamic properties of functional connectivity in the rodent. *Brain Connect.* 3, 31–40. doi: 10.1089/brain.2012.0115

Keilholz, S. D., Silva, A. C., Raman, M., Merkle, H., and Koretsky, A. P. (2006). BOLD and CBV-weighted functional magnetic resonance imaging of the rat somatosensory system. *Magn. Reson. Med.* 55, 316–324. doi: 10.1002/mrm.20744

Kim, S.-G., and Ogawa, S. (2012). Biophysical and physiological origins of blood oxygenation level-dependent fMRI signals. *J. Cereb. Blood Flow Metab.* 32, 1188–1206. doi: 10.1038/jcbfm.2012.23

Kim, T., Masamoto, K., Fukuda, M., Vazquez, A., and Kim, S.-G. (2010). Frequency-dependent neural activity, CBF, and BOLD fMRI to somatosensory stimuli in isoflurane-anesthetized rats. *Neuroimage* 52, 224–233. doi: 10.1016/j.neuroimage.2010.03.064

Kiyatkin, E. A. (2007). Physiological and pathological brain hyperthermia. *Prog. Brain Res.* 162, 219–243. doi: 10.1016/S0079-6123(06)62012-8

Klapoetke, N. C., Murata, Y., Kim, S. S., Pulver, S. R., Birdsey-Benson, A., Cho, Y. K., et al. (2014). Addendum: independent optical excitation of distinct neural populations. *Nat. Methods* 11:972. doi: 10.1038/nmeth0914-972

Klein, A., Andersson, J., Ardekani, B. A., Ashburner, J., Avants, B., Chiang, M.-C., et al. (2009). Evaluation of 14 nonlinear deformation algorithms applied to human brain MRI registration. *Neuroimage* 46, 786–802. doi: 10.1016/j.neuroimage.2008.12.037

Klein, R. L., Dayton, R. D., Leidenheimer, N. J., Jansen, K., Golde, T. E., and Zweig, R. M. (2006). Efficient neuronal gene transfer with AAV8 leads to neurotoxic levels of Tau or green fluorescent proteins. *Mol. Ther.* 13, 517–527. doi: 10.1016/j.ymthe.2005.10.008

Klomp, A., Tremoleda, J. L., Schrantee, A., Gsell, W., and Reneman, L. (2012). The use of pharmacological-challenge fMRI in pre-clinical research: application to the 5-HT system. *J. Vis. Exp.* 62:3956. doi: 10.3791/3956

Knabl, J., Witschi, R., Hösl, K., Reinold, H., Zeilhofer, U. B., Ahmadi, S., et al. (2008). Reversal of pathological pain through specific spinal GABAA receptor subtypes. *Nature* 451, 330–334. doi: 10.1038/nature06493

Kundu, P., Inati, S. J., Evans, J. W., Luh, W.-M., and Bandettini, P. A. (2012). Differentiating BOLD and non-BOLD signals in fMRI time series using multi-echo EPI. *Neuroimage* 60, 1759–1770. doi: 10.1016/j.neuroimage.2011.12.028

Kundu, P., Santin, M. D., Bandettini, P. A., Bullmore, E. T., and Petiet, A. (2014). Differentiating BOLD and non-BOLD signals in fMRI time series from anesthetized rats using multi-echo EPI at 11.7 T. *Neuroimage* 102(Pt 2), 861–874. doi: 10.1016/j.neuroimage.2014.07.025

Kyathanahally, S. P., Jia, H., Pustovyy, O. M., Waggoner, P., Beyers, R., Schumacher, J., et al. (2015). Anterior-posterior dissociation of the default mode network in dogs. *Brain Struct. Funct.* 220, 1063–1076. doi: 10.1007/s00429-013-0700-x

Lahti, K. M., Ferris, C. F., Li, F., Sotak, C. H., and King, J. A. (1999). Comparison of evoked cortical activity in conscious and propofol-anesthetized rats using functional MRI. *Magn. Reson. Med.* 41, 412–416. doi: 10.1002/(sici)1522-2594(199902)41:2<412::aid-mrm28>3.3.co;2-v

Lai, H.-Y., Albaugh, D. L., Kao, Y.-C. J., Younce, J. R., and Shih, Y.-Y. I. (2015). Robust deep brain stimulation functional MRI procedures in rats and mice using an MR-compatible tungsten microwire electrode. *Magn. Reson. Med.* 73, 1246–1251. doi: 10.1002/mrm.25239

Långsjö, J. W., Kaisti, K. K., Aalto, S., Hinkka, S., Aantaa, R., Oikonen, V., et al. (2003). Effects of subanesthetic doses of ketamine on regional cerebral blood flow, oxygen consumption, and blood volume in humans. *Anesthesiology* 99, 614–623. doi: 10.1097/00000542-200309000-00016

Larkin, J. R., Simard, M. A., Khrapitchev, A. A., Meakin, J. A., Okell, T. W., Craig, M., et al. (2018). Quantitative blood flow measurement in rat brain with multiphase arterial spin labelling magnetic resonance imaging. *J. Cereb. Blood Flow Metab.* 39, 1557–1569. doi: 10.1177/0271678X18756218

Laumann, T. O., Snyder, A. Z., Mitra, A., Gordon, E. M., Gratton, C., Adeyemo, B., et al. (2017). On the stability of BOLD fMRI correlations. *Cereb. Cortex* 27, 4719–4732. doi: 10.1093/cercor/bhw265

Lee, H.-M., Giguere, P. M., and Roth, B. L. (2014). DREADDs: novel tools for drug discovery and development. *Drug Discov. Today* 19, 469–473. doi: 10.1016/j.drudis.2013.10.018

Lein, E. S., Hawrylycz, M. J., Ao, N., Ayres, M., Bensinger, A., Bernard, A., et al. (2007). Genome-wide atlas of gene expression in the adult mouse brain. *Nature* 445, 168–176. doi: 10.1038/nature05453

Lemieux, L., Whittingstall, K., and Uludağ, K. (2015). "Combining fMRI with other modalities: multimodal neuroimaging," in *fMRI: From Nuclear Spins to Brain Functions Biological Magnetic Resonance*, eds K. Uludag, K. Ugurbil, and L. Berliner, (Boston, MA: Springer US), 739–768. doi: 10.1007/978-1-4899-7591-1_25

Lenz, C., Rebel, A., van Ackern, K., Kuschinsky, W., and Waschke, K. F. (1998). Local cerebral blood flow, local cerebral Glucose utilization, and flow-metabolism coupling during Sevoflurane versus isoflurane Anesthesia in rats. *Anesthesiology* 89, 1480–1488. doi: 10.1097/00000542-199812000-00026

Leonardi, N., and Van De Ville, D. (2015). On spurious and real fluctuations of dynamic functional connectivity during rest. *Neuroimage* 104, 430–436. doi: 10.1016/j.neuroimage.2014.09.007

Leong, A. T. L., Dong, C. M., Gao, P. P., Chan, R. W., To, A., Sanes, D. H., et al. (2018). Optogenetic auditory fMRI reveals the effects of visual cortical inputs on auditory midbrain response. *Sci. Rep.* 8:8736. doi: 10.1038/s41598-018-26568-1

Leslie, R. A., and James, M. F. (2000). Pharmacological magnetic resonance imaging: a new application for functional MRI. *Trends Pharmacol. Sci.* 21, 314–318. doi: 10.1016/s0165-6147(00)01507-8

Li, G., Shih, Y.-Y. I., Kiel, J. W., De La Garza, B. H., Du, F., and Duong, T. Q. (2013). MRI study of cerebral, retinal and choroidal blood flow responses to acute hypertension. *Exp. Eye Res.* 112, 118–124. doi: 10.1016/j.exer.2013.04.003

Li, J., Yang, R., Xia, K., Wang, T., Nie, B., Gao, K., et al. (2018). Effects of stress on behavior and resting-state fMRI in rats and evaluation of Telmisartan therapy in a stress-induced depression model. *BMC Psychiatry* 18:337. doi: 10.1186/s12888-018-1880-y

Li, C.-X., and Zhang, X. (2018). Evaluation of prolonged administration of isoflurane on cerebral blood flow and default mode network in macaque monkeys anesthetized with different maintenance doses. *Neurosci. Lett.* 662, 402–408. doi: 10.1016/j.neulet.2017.10.034

Liang, Z., King, J., and Zhang, N. (2011). Uncovering intrinsic connectional architecture of functional networks in awake rat brain. *J. Neurosci.* 31, 3776–3783. doi: 10.1523/JNEUROSCI.4557-10.2011

Liang, Z., Li, T., King, J., and Zhang, N. (2013). Mapping thalamocortical networks in rat brain using resting-state functional connectivity. *Neuroimage* 83, 237–244. doi: 10.1016/j.neuroimage.2013.06.029

Liang, Z., Liu, X., and Zhang, N. (2015a). Dynamic resting state functional connectivity in awake and anesthetized rodents. *Neuroimage* 104, 89–99. doi: 10.1016/j.neuroimage.2014.10.013

Liang, Z., Watson, G. D. R., Alloway, K. D., Lee, G., Neuberger, T., and Zhang, N. (2015b). Mapping the functional network of medial prefrontal cortex by combining optogenetics and fMRI in awake rats. *Neuroimage* 117, 114–123. doi: 10.1016/j.neuroimage.2015.05.036

Liégeois, R., Laumann, T. O., Snyder, A. Z., Zhou, J., and Yeo, B. T. T. (2017). Interpreting temporal fluctuations in resting-state functional connectivity MRI. *Neuroimage* 163, 437–455. doi: 10.1016/j.neuroimage.2017.09.012

Lin, J. Y. (2011). A user's guide to channelrhodopsin variants: features, limitations and future developments. *Exp. Physiol.* 96, 19–25. doi: 10.1113/expphysiol.2009.051961

Lin, J. Y., Knutsen, P. M., Muller, A., Kleinfeld, D., and Tsien, R. Y. (2013). ReaChR: a red-shifted variant of channelrhodopsin enables deep transcranial optogenetic excitation. *Nat. Neurosci.* 16, 1499–1508. doi: 10.1038/nn.3502

Lin, J. Y., Lin, M. Z., Steinbach, P., and Tsien, R. Y. (2009). Characterization of engineered channelrhodopsin variants with improved properties and kinetics. *Biophys. J.* 96, 1803–1814. doi: 10.1016/j.bpj.2008.11.034

Lin, P., Fang, Z., Liu, J., and Lee, J. H. (2016). Optogenetic Functional MRI. *J. Vis. Exp.* 110:53346. doi: 10.3791/53346

Lin, Y. J., and Koretsky, A. P. (1997). Manganese ion enhances T1-weighted MRI during brain activation: an approach to direct imaging of brain function. *Magn. Reson. Med.* 38, 378–388. doi: 10.1002/mrm.1910380305

Liska, A., Bertero, A., Gomolka, R., Sabbioni, M., Galbusera, A., Barsotti, N., et al. (2018). Homozygous loss of autism-risk gene CNTNAP2 results in reduced local and long-range prefrontal functional connectivity. *Cereb. Cortex* 28, 1141–1153. doi: 10.1093/cercor/bhx022

Liska, A., Galbusera, A., Schwarz, A. J., and Gozzi, A. (2015). Functional connectivity hubs of the mouse brain. *Neuroimage* 115, 281–291. doi: 10.1016/j.neuroimage.2015.04.033

Liu, H.-S., Jan, M.-S., Chou, C.-K., Chen, P.-H., and Ke, N.-J. (1999). Is green fluorescent protein toxic to the living cells? *Biochem. Biophys. Res. Commun.* 260, 712–717. doi: 10.1006/bbrc.1999.0954

Liu, X., and Duyn, J. H. (2013). Time-varying functional network information extracted from brief instances of spontaneous brain activity. *Proc. Natl. Acad. Sci. U.S.A.* 110, 4392–4397. doi: 10.1073/pnas.1216856110

Liu, X., Zhu, X.-H., Zhang, Y., and Chen, W. (2013). The change of functional connectivity specificity in rats under various Anesthesia levels and its neural origin. *Brain Topogr.* 26, 363–377. doi: 10.1007/s10548-012-0267-5

Liu, X., Zhang, N., Chang, C., and Duyn, J. H. (2018). Co-activation patterns in resting-state fMRI signals. *Neuroimage* 180, 485–494. doi: 10.1016/j.neuroimage.2018.01.041

Liu, X.-H., Zhu, X., Zhang, Y., and Chen, W. (2011). Neural origin of Spontaneous Hemodynamic fluctuations in rats under burst-suppression Anesthesia condition. *Cereb. Cortex* 21, 374–384. doi: 10.1093/cercor/bhq105

Lohani, S., Poplawsky, A. J., Kim, S.-G., and Moghaddam, B. (2017). Unexpected global impact of VTA dopamine neuron activation as measured by opto-fMRI. *Mol. Psychiatry* 22, 585–594. doi: 10.1038/mp.2016.102

Lowe, M. J., Dzemidzic, M., Lurito, J. T., Mathews, V. P., and Phillips, M. D. (2000). Correlations in low-frequency BOLD fluctuations reflect cortico-cortical connections. *Neuroimage* 12, 582–587. doi: 10.1006/nimg.2000.0654

Lu, H., Donahue, M. J., and van Zijl, P. C. M. (2006). Detrimental effects of BOLD signal in arterial spin labeling fMRI at high field strength. *Magn. Reson. Med.* 56, 546–552. doi: 10.1002/mrm.20976

Lu, H., Golay, X., Pekar, J. J., and van Zijl, P. C. M. (2003). Functional magnetic resonance imaging based on changes in vascular space occupancy. *Magn. Reson. Med.* 50, 263–274. doi: 10.1002/mrm.10519

Lu, H., and Stein, E. A. (2014). Resting state functional connectivity: its physiological basis and application in neuropharmacology. *Neuropharmacology* 84, 79–89. doi: 10.1016/j.neuropharm.2013.08.023

Lu, H., Zou, Q., Gu, H., Raichle, M. E., Stein, E. A., and Yang, Y. (2012). Rat brains also have a default mode network. *Proc. Natl. Acad. Sci. U.S.A.* 109, 3979–3984. doi: 10.1073/pnas.1200506109

Lu, H., Zuo, Y., Gu, H., Waltz, J. A., Zhan, W., Scholl, C. A., et al. (2007). Synchronized delta oscillations correlate with the resting-state functional MRI signal. *Proc. Natl. Acad. Sci. U.S.A.* 104, 18265–18269. doi: 10.1073/pnas.0705791104

Luo, F., Wu, G., Li, Z., and Li, S.-J. (2003). Characterization of effects of mean arterial blood pressure induced by cocaine and cocaine methiodide on BOLD signals in rat brain. *Magn. Reson. Med.* 49, 264–270. doi: 10.1002/mrm.10366

MacLaren, D. A. A., Browne, R. W., Shaw, J. K., Krishnan Radhakrishnan, S., Khare, P., España, R. A., et al. (2016). Clozapine N-Oxide administration produces behavioral effects in long-evans rats: implications for designing DREADD experiments. *eNeuro* 3:ENEURO.0219-16.2016. doi: 10.1523/ENEURO.0219-16.2016

Madisen, L., Mao, T., Koch, H., Zhuo, J.-M., Berenyi, A., Fujisawa, S., et al. (2012). A toolbox of Cre-dependent optogenetic transgenic mice for light-induced activation and silencing. *Nat. Neurosci.* 15, 793–802. doi: 10.1038/nn.3078

Magnuson, M. E., Thompson, G. J., Pan, W.-J., and Keilholz, S. D. (2014). Time-dependent effects of isoflurane and dexmedetomidine on functional connectivity, spectral characteristics, and spatial distribution of spontaneous BOLD fluctuations. *NMR Biomed.* 27, 291–303. doi: 10.1002/nbm.3062

Mahler, S. V., and Aston-Jones, G. (2018). CNO Evil? Considerations for the use of DREADDs in behavioral neuroscience. *Neuropsychopharmacology* 43, 934–936. doi: 10.1038/npp.2017.299

Majeed, W., Magnuson, M., Hasenkamp, W., Schwarb, H., Schumacher, E. H., Barsalou, L., et al. (2011). Spatiotemporal dynamics of low frequency BOLD fluctuations in rats and humans. *Neuroimage* 54, 1140–1150. doi: 10.1016/j.neuroimage.2010.08.030

Mandeville, J. B. (2012). IRON fMRI measurements of CBV and implications for BOLD signal. *Neuroimage* 62, 1000–1008. doi: 10.1016/j.neuroimage.2012.01.070

Mandeville, J. B., Jenkins, B. G., Chen, Y.-C. I., Choi, J.-K., Kim, Y. R., Belen, D., et al. (2004). Exogenous contrast agent improves sensitivity of gradient-echo functional magnetic resonance imaging at 9.4 T. *Magn. Reson. Med.* 52, 1272–1281. doi: 10.1002/mrm.20278

Mandeville, J. B., Leite, F. P., and Marota, J. J. A. (2007). Spin-echo MRI underestimates functional changes in microvascular cerebral blood plasma volume using exogenous contrast agent. *Magn. Reson. Med.* 58, 769–776. doi: 10.1002/mrm.21380

Mandeville, J. B., and Marota, J. J. (1999). Vascular filters of functional MRI: spatial localization using BOLD and CBV contrast. *Magn. Reson. Med.* 42, 591–598.

Mandeville, J. B., Marota, J. J., Kosofsky, B. E., Keltner, J. R., Weissleder, R., Rosen, B. R., et al. (1998). Dynamic functional imaging of relative cerebral blood volume during rat forepaw stimulation. *Magn. Reson. Med.* 39, 615–624. doi: 10.1002/mrm.1910390415

Mandeville, J. B., Sander, C. Y. M., Jenkins, B. G., Hooker, J. M., Catana, C., Vanduffel, W., et al. (2013). A receptor-based model for dopamine-induced fMRI signal. *Neuroimage* 75, 46–57. doi: 10.1016/j.neuroimage.2013.02.036

Mantini, D., Gerits, A., Nelissen, K., Durand, J.-B., Joly, O., Simone, L., et al. (2011). Default mode of brain function in monkeys. *J. Neurosci.* 31, 12954–12962. doi: 10.1523/JNEUROSCI.2318-11.2011

Manvich, D. F., Webster, K. A., Foster, S. L., Farrell, M. S., Ritchie, J. C., Porter, J. H., et al. (2018). The DREADD agonist clozapine N-oxide (CNO) is reverse-metabolized to clozapine and produces clozapine-like interoceptive stimulus effects in rats and mice. *Sci. Rep.* 8:3840. doi: 10.1038/s41598-018-22116-z

Markicevic, M., Fulcher, B. D., Lewis, C., Helmchen, F., Rudin, M., Zerbi, V., et al. (2018). Cortical excitation:inhibition imbalance causes network specific functional hypoconnectivity: a DREADD-fMRI study. *bioRxiv* [Preprint]. doi: 10.1101/492108

Marota, J. J., Mandeville, J. B., Weisskoff, R. M., Moskowitz, M. A., Rosen, B. R., and Kosofsky, B. E. (2000). Cocaine activation discriminates dopaminergic projections by temporal response: an fMRI study in Rat. *Neuroimage* 11, 13–23. doi: 10.1006/nimg.1999.0520

Martin, C., and Sibson, N. R. (2008). Pharmacological MRI in animal models: a useful tool for 5-HT research? *Neuropharmacology* 55, 1038–1047. doi: 10.1016/j.neuropharm.2008.08.014

Maus, B., and van Breukelen, G. J. P. (2013). Optimal design for functional magnetic resonance imaging experiments. *Zeitschrift für Psychologie* 221, 174–189. doi: 10.1027/2151-2604/a000145

Mazziotta, J., Toga, A., Evans, A., Fox, P., Lancaster, J., Zilles, K., et al. (2001). A probabilistic atlas and reference system for the human brain: International Consortium for Brain Mapping (ICBM). *Philos. Trans. R. Soc. Lond. B Biol. Sci.* 356, 1293–1322. doi: 10.1098/rstb.2001.0915

McLaren, D. G., Kosmatka, K. J., Oakes, T. R., Kroenke, C. D., Kohama, S. G., Matochik, J. A., et al. (2009). A population-average MRI-based atlas collection of the rhesus macaque. *Neuroimage* 45, 52–59. doi: 10.1016/j.neuroimage.2008.10.058

Mechling, A. E., Hübner, N. S., Lee, H.-L., Hennig, J., von Elverfeldt, D., and Harsan, L.-A. (2014). Fine-grained mapping of mouse brain functional connectivity with resting-state fMRI. *Neuroimage* 96, 203–215. doi: 10.1016/j.neuroimage.2014.03.078

Medda, A., Hoffmann, L., Magnuson, M., Thompson, G., Pan, W.-J., and Keilholz, S. (2016). Wavelet-based clustering of resting state MRI data in the rat. *Magn. Reson. Imaging* 34, 35–43. doi: 10.1016/j.mri.2015.10.005

Medhi, B., Misra, S., Avti, P. K., Kumar, P., Kumar, H., and Singh, B. (2014). Role of neuroimaging in drug development. *Rev. Neurosci.* 25, 663–673. doi: 10.1515/revneuro-2014-0031

Milham, M. P., Ai, L., Koo, B., Xu, T., Amiez, C., Balezeau, F., et al. (2018). An open resource for non-human primate imaging. *Neuron* 100:61-74.e2. doi: 10.1016/j.neuron.2018.08.039

Miller, K. L. (2012). FMRI using balanced steady-state free precession (SSFP). *Neuroimage* 62, 713–719. doi: 10.1016/j.neuroimage.2011.10.040

Miller, K. L., Alfaro-Almagro, F., Bangerter, N. K., Thomas, D. L., Yacoub, E., Xu, J., et al. (2016). Multimodal population brain imaging in the UK Biobank prospective epidemiological study. *Nat. Neurosci.* 19, 1523–1536. doi: 10.1038/nn.4393

Miller, K. L., and Jezzard, P. (2008). Modeling SSFP functional MRI contrast in the brain. *Magn. Reson. Med.* 60, 661–673. doi: 10.1002/mrm.21690

Miller, K. L., Smith, S. M., Jezzard, P., and Pauly, J. M. (2006). High-resolution FMRI at 1.5T using balanced SSFP. *Magn. Reson. Med.* 55, 161–170. doi: 10.1002/mrm.20753

Miller, K. L., Smith, S. M., Jezzard, P., Wiggins, G. C., and Wiggins, C. J. (2007). Signal and noise characteristics of SSFP FMRI: a comparison with GRE at multiple field strengths. *Neuroimage* 37, 1227–1236. doi: 10.1016/j.neuroimage.2007.06.024

Minzenberg, M. J. (2012). Pharmacological MRI approaches to understanding mechanisms of drug action. *Curr. Top. Behav. Neurosci.* 11, 365–388. doi: 10.1007/7854_2011_177

Miranda-Dominguez, O., Mills, B. D., Grayson, D., Woodall, A., Grant, K. A., Kroenke, C. D., et al. (2014). Bridging the gap between the human and macaque connectome: a quantitative comparison of global interspecies structure-function relationships and network topology. *J. Neurosci.* 34, 5552–5563. doi: 10.1523/JNEUROSCI.4229-13.2014

Miyashita, T., Shao, Y. R., Chung, J., Pourzia, O., and Feldman, D. E. (2013). Long-term channelrhodopsin-2 (ChR2) expression can induce abnormal axonal morphology and targeting in cerebral cortex. *Front. Neural Circuits* 7:8. doi: 10.3389/fncir.2013.00008

Morgan, V. L., Dawant, B. M., Li, Y., and Pickens, D. R. (2007). Comparison of fMRI statistical software packages and strategies for analysis of images containing random and stimulus-correlated motion. *Comput. Med. Imaging Graph.* 31, 436–446. doi: 10.1016/j.compmedimag.2007.04.002

Mueggler, T., Baumann, D., Rausch, M., and Rudin, M. (2001). Bicuculline-induced brain activation in mice detected by functional magnetic resonance imaging. *Magn. Reson. Med.* 46, 292–298. doi: 10.1002/mrm.1190

Murphy, K., Birn, R. M., and Bandettini, P. A. (2013). Resting-state fMRI confounds and cleanup. *Neuroimage* 80, 349–359. doi: 10.1016/j.neuroimage.2013.04.001

Nadkarni, N. A., Bougacha, S., Garin, C., Dhenain, M., and Picq, J.-L. (2018). Digital templates and brain atlas dataset for the mouse lemur primate. *Data Brief* 21, 1178–1185. doi: 10.1016/j.dib.2018.10.067

Nagel, G., Szellas, T., Huhn, W., Kateriya, S., Adeishvili, N., Berthold, P., et al. (2003). Channelrhodopsin-2, a directly light-gated cation-selective membrane channel. *Proc. Natl. Acad. Sci. U.S.A.* 100, 13940–13945. doi: 10.1073/pnas.1936192100

Nichols, T. E., Das, S., Eickhoff, S. B., Evans, A. C., Glatard, T., Hanke, M., et al. (2017). Best practices in data analysis and sharing in neuroimaging using MRI. *Nat. Neurosci.* 20, 299–303. doi: 10.1038/nn.4500

Nie, B., Chen, K., Zhao, S., Liu, J., Gu, X., Yao, Q., et al. (2013). A rat brain MRI template with digital stereotaxic atlas of fine anatomical delineations in paxinos space and its automated application in voxel-wise analysis. *Hum. Brain Mapp.* 34, 1306–1318. doi: 10.1002/hbm.21511

Norris, D. G. (2006). Principles of magnetic resonance assessment of brain function. *J. Magn. Reson. Imaging* 23, 794–807. doi: 10.1002/jmri.20587

Norris, D. G. (2012). Spin-echo fMRI: the poor relation? *Neuroimage* 62, 1109–1115. doi: 10.1016/j.neuroimage.2012.01.003

Nunes, D., Ianus, A., and Shemesh, N. (2019). Layer-specific connectivity revealed by diffusion-weighted functional MRI in the rat thalamocortical pathway. *Neuroimage* 184, 646–657. doi: 10.1016/j.neuroimage.2018.09.050

Ogawa, S., Lee, T. M., Kay, A. R., and Tank, D. W. (1990). Brain magnetic resonance imaging with contrast dependent on blood oxygenation. *Proc. Natl. Acad. Sci. U.S.A.* 87, 9868–9872.

Ortiz, J. J., Portillo, W., Paredes, R. G., Young, L. J., and Alcauter, S. (2018). Resting state brain networks in the prairie vole. *Sci. Rep.* 8:1231. doi: 10.1038/s41598-017-17610-9

Paasonen, J., Stenroos, P., Salo, R. A., Kiviniemi, V., and Gröhn, O. (2018). Functional connectivity under six anesthesia protocols and the awake condition in rat brain. *Neuroimage* 172, 9–20. doi: 10.1016/j.neuroimage.2018.01.014

Pagani, M., Bertero, A., Liska, A., Galbusera, A., Sabbioni, M., Barsotti, N., et al. (2019). Deletion of autism risk gene Shank3 disrupts prefrontal connectivity. *J. Neurosci.* 39, 5299–5310. doi: 10.1523/JNEUROSCI.2529-18.2019

Pan, W.-J., Billings, J. C. W., Grooms, J. K., Shakil, S., and Keilholz, S. D. (2015). Considerations for resting state functional MRI and functional connectivity studies in rodents. *Front. Neurosci.* 9:269. doi: 10.3389/fnins.2015.00269

Patel, A. J., Honoré, E., Lesage, F., Fink, M., Romey, G., and Lazdunski, M. (1999). Inhalational anesthetics activate two-pore-domain background K+ channels. *Nat. Neurosci.* 2, 422–426. doi: 10.1038/8084

Pawela, C. P., Biswal, B. B., Cho, Y. R., Kao, D. S., Li, R., Jones, S. R., et al. (2008). Resting-state functional connectivity of the rat brain. *Magn. Reson. Med.* 59, 1021–1029. doi: 10.1002/mrm.21524

Paxinos, G., and Franklin, K. B. J. (2012). *Paxinos and Franklin's the Mouse Brain in Stereotaxic Coordinates*. Cambridge, MA: Academic Press.

Paxinos, G., and Watson, C. (1982). *The Rat Brain in Stereotaxic Coordinates*. Amsterdam: Elsevier, doi: 10.1016/c2009-0-63235-9

Peters, A. M., Brookes, M. J., Hoogenraad, F. G., Gowland, P. A., Francis, S. T., Morris, P. G., et al. (2007). T2* measurements in human brain at 1.5, 3 and 7 T. *Magn. Reson. Imaging* 25, 748–753. doi: 10.1016/j.mri.2007.02.014

Petersen, R. C., Aisen, P. S., Beckett, L. A., Donohue, M. C., Gamst, A. C., Harvey, D. J., et al. (2010). Alzheimer's Disease Neuroimaging Initiative (ADNI): clinical characterization. *Neurology* 74, 201–209. doi: 10.1212/WNL.0b013e3181cb3e25

Petridou, N., Gaudes, C. C., Dryden, I. L., Francis, S. T., and Gowland, P. A. (2013). Periods of rest in fMRI contain individual spontaneous events which are related

to slowly fluctuating spontaneous activity. *Hum. Brain Mapp.* 34, 1319–1329. doi: 10.1002/hbm.21513

Poldrack, R. A., Barch, D. M., Mitchell, J. P., Wager, T. D., Wagner, A. D., Devlin, J. T., et al. (2013). Toward open sharing of task-based fMRI data: the OpenfMRI project. *Front. Neuroinform.* 7:12. doi: 10.3389/fninf.2013.00012

Poldrack, R. A., Fletcher, P. C., Henson, R. N., Worsley, K. J., Brett, M., and Nichols, T. E. (2008). Guidelines for reporting an fMRI study. *Neuroimage* 40, 409–414. doi: 10.1016/j.neuroimage.2007.11.048

Poser, B. A., Versluis, M. J., Hoogduin, J. M., and Norris, D. G. (2006). BOLD contrast sensitivity enhancement and artifact reduction with multiecho EPI: parallel-acquired inhomogeneity-desensitized fMRI. *Magn. Reson. Med.* 55, 1227–1235. doi: 10.1002/mrm.20900

Posse, S., Wiese, S., Gembris, D., Mathiak, K., Kessler, C., Grosse-Ruyken, M. L., et al. (1999). Enhancement of BOLD-contrast sensitivity by single-shot multi-echo functional MR imaging. *Magn. Reson. Med.* 42, 87–97. doi: 10.1002/(sici)1522-2594(199907)42:1<87::aid-mrm13>3.0.co;2-o

Power, J. D., Mitra, A., Laumann, T. O., Snyder, A. Z., Schlaggar, B. L., and Petersen, S. E. (2014). Methods to detect, characterize, and remove motion artifact in resting state fMRI. *Neuroimage* 84, 320–341. doi: 10.1016/j.neuroimage.2013.08.048

Raichle, M. E. (2015). The brain's default mode network. *Annu. Rev. Neurosci.* 38, 433–447. doi: 10.1146/annurev-neuro-071013-014030

Raichle, M. E., MacLeod, A. M., Snyder, A. Z., Powers, W. J., Gusnard, D. A., and Shulman, G. L. (2001). A default mode of brain function. *Proc. Natl. Acad. Sci. U.S.A.* 98, 676–682. doi: 10.1073/pnas.98.2.676

Ramos-Cabrer, P., Weber, R., Wiedermann, D., and Hoehn, M. (2005). Continuous noninvasive monitoring of transcutaneous blood gases for a stable and persistent BOLD contrast in fMRI studies in the rat. *NMR Biomed.* 18, 440–446. doi: 10.1002/nbm.978

Rao, J.-S., Liu, Z., Zhao, C., Wei, R.-H., Zhao, W., Tian, P.-Y., et al. (2017). Ketamine changes the local resting-state functional properties of anesthetized-monkey brain. *Magn. Reson. Imaging* 43, 144–150. doi: 10.1016/j.mri.2017.07.025

Rauch, A., Rainer, G., Augath, M., Oeltermann, A., and Logothetis, N. K. (2008). Pharmacological MRI combined with electrophysiology in non-human primates: effects of Lidocaine on primary visual cortex. *Neuroimage* 40, 590–600. doi: 10.1016/j.neuroimage.2007.12.009

Ray, R. S., Corcoran, A. E., Brust, R. D., Kim, J. C., Richerson, G. B., Nattie, E., et al. (2011). Impaired respiratory and body temperature control upon acute serotonergic neuron inhibition. *Science* 333, 637–642. doi: 10.1126/science.1205295

Razoux, F., Baltes, C., Mueggler, T., Seuwen, A., Russig, H., Mansuy, I., et al. (2013). Functional MRI to assess alterations of functional networks in response to pharmacological or genetic manipulations of the serotonergic system in mice. *Neuroimage* 74, 326–336. doi: 10.1016/j.neuroimage.2013.02.031

Reimann, C., Brangsch, J., Kaufmann, J. O., Adams, L. C., Onthank, D. C., Robinson, S. P., et al. (2018). Contrast-enhanced magnetic resonance angiography using a novel elastin-specific molecular probe in an experimental animal model. *Contrast Media Mol. Imaging* 2018:9217456. doi: 10.1155/2018/9217456

Reimann, H. M., Todiras, M., Hodge, R., Huelnhagen, T., Millward, J. M., Turner, R., et al. (2018). Somatosensory BOLD fMRI reveals close link between salient blood pressure changes and the murine neuromatrix. *Neuroimage* 172, 562–574. doi: 10.1016/j.neuroimage.2018.02.002

Roelofs, T. J. M., Verharen, J. P. H., van Tilborg, G. A. F., Boekhoudt, L., van der Toorn, A., de Jong, J. W., et al. (2017). A novel approach to map induced activation of neuronal networks using chemogenetics and functional neuroimaging in rats: a proof-of-concept study on the mesocorticolimbic system. *Neuroimage* 156, 109–118. doi: 10.1016/j.neuroimage.2017.05.021

Rohlfing, T., Kroenke, C. D., Sullivan, E. V., Dubach, M. F., Bowden, D. M., Grant, K. A., et al. (2012). The INIA19 template and NeuroMaps Atlas for primate brain image parcellation and spatial normalization. *Front. Neuroinform.* 6:27. doi: 10.3389/fninf.2012.00027

Roth, B. L. (2016). DREADDs for neuroscientists. *Neuron* 89, 683–694. doi: 10.1016/j.neuron.2016.01.040

Rudrapatna, U. S., van der Toorn, A., van Meer, M. P. A., and Dijkhuizen, R. M. (2012). Impact of hemodynamic effects on diffusion-weighted fMRI signals. *Neuroimage* 61, 106–114. doi: 10.1016/j.neuroimage.2012.02.050

Rungta, R. L., Osmanski, B.-F., Boido, D., Tanter, M., and Charpak, S. (2017). Light controls cerebral blood flow in naive animals. *Nat. Commun.* 8:14191. doi: 10.1038/ncomms14191

Ryali, S., Shih, Y.-Y. I., Chen, T., Kochalka, J., Albaugh, D., Fang, Z., et al. (2016). Combining optogenetic stimulation and fMRI to validate a multivariate dynamical systems model for estimating causal brain interactions. *Neuroimage* 132, 398–405. doi: 10.1016/j.neuroimage.2016.02.067

Saleem, K. S., and Logothetis, N. K. (2012). *A Combined MRI and Histology Atlas of the Rhesus Monkey Brain in Stereotaxic Coordinates*. Cambridge, MA: Academic Press.

Scheffler, K., and Ehses, P. (2016). High-resolution mapping of neuronal activation with balanced SSFP at 9.4 tesla. *Magn. Reson. Med.* 76, 163–171. doi: 10.1002/mrm.25890

Scheffler, K., Seifritz, E., Bilecen, D., Venkatesan, R., Hennig, J., Deimling, M., et al. (2001). Detection of BOLD changes by means of a frequency-sensitive trueFISP technique: preliminary results. *NMR Biomed.* 14, 490–496. doi: 10.1002/nbm.726

Schlegel, F., Schroeter, A., and Rudin, M. (2015). The hemodynamic response to somatosensory stimulation in mice depends on the anesthetic used: implications on analysis of mouse fMRI data. *Neuroimage* 116, 40–49. doi: 10.1016/j.neuroimage.2015.05.013

Schmid, F., Wachsmuth, L., Albers, F., Schwalm, M., Stroh, A., and Faber, C. (2017). True and apparent optogenetic BOLDfMRI signals. *Magn. Reson. Med.* 77, 126–136. doi: 10.1002/mrm.26095

Schmid, F., Wachsmuth, L., Schwalm, M., Prouvot, P.-H., Jubal, E. R., Fois, C., et al. (2016). Assessing sensory versus optogenetic network activation by combining (o)fMRI with optical Ca2 recordings. *J. Cereb. Blood Flow Metab.* 36, 1885–1900. doi: 10.1177/0271678x15619428

Schroeder, M. P., Weiss, C., Procissi, D., Disterhoft, J. F., and Wang, L. (2016). Intrinsic connectivity of neural networks in the awake rabbit. *Neuroimage* 129, 260–267. doi: 10.1016/j.neuroimage.2016.01.010

Schroeter, A., Schlegel, F., Seuwen, A., Grandjean, J., and Rudin, M. (2014). Specificity of stimulus-evoked fMRI responses in the mouse: the influence of systemic physiological changes associated with innocuous stimulation under four different anesthetics. *Neuroimage* 94, 372–384. doi: 10.1016/j.neuroimage.2014.01.046

Schwarz, A. J., Danckaert, A., Reese, T., Gozzi, A., Paxinos, G., Watson, C., et al. (2006). A stereotaxic MRI template set for the rat brain with tissue class distribution maps and co-registered anatomical atlas: application to pharmacological MRI. *Neuroimage* 32, 538–550. doi: 10.1016/j.neuroimage.2006.04.214

Schwarz, A. J., Gozzi, A., Reese, T., Heidbreder, C. A., and Bifone, A. (2007). Pharmacological modulation of functional connectivity: the correlation structure underlying the phMRI response to d-amphetamine modified by selective dopamine D3 receptor antagonist SB277011A. *Magn. Reson. Imaging* 25, 811–820. doi: 10.1016/j.mri.2007.02.017

Schweinhardt, P., Fransson, P., Olson, L., Spenger, C., and Andersson, J. L. R. (2003). A template for spatial normalisation of MR images of the rat brain. *J. Neurosci. Methods* 129, 105–113. doi: 10.1016/s0165-0270(03)00192-4

Sciolino, N. R., Plummer, N. W., Chen, Y.-W., Alexander, G. M., Robertson, S. D., Dudek, S. M., et al. (2016). Recombinase-dependent mouse lines for chemogenetic activation of genetically defined cell types. *Cell Rep.* 15, 2563–2573. doi: 10.1016/j.celrep.2016.05.034

Scott, N. A., and Murphy, T. H. (2012). Hemodynamic responses evoked by neuronal stimulation via Channelrhodopsin-2 can be independent of intracortical glutamatergic synaptic transmission. *PLoS One* 7:e29859. doi: 10.1371/journal.pone.0029859

Selent, J., López, L., Sanz, F., and Pastor, M. (2008). Multi-receptor binding profile of clozapine and olanzapine: a structural study based on the New β2Adrenergic receptor template. *ChemMedChem* 3, 1194–1198. doi: 10.1002/cmdc.200800074

Sforazzini, F., Schwarz, A. J., Galbusera, A., Bifone, A., and Gozzi, A. (2014). Distributed BOLD and CBV-weighted resting-state networks in the mouse brain. *Neuroimage* 87, 403–415. doi: 10.1016/j.neuroimage.2013.09.050

Shah, D., Blockx, I., Guns, P.-J., De Deyn, P. P., Van Dam, D., Jonckers, E., et al. (2015). Acute modulation of the cholinergic system in the mouse brain detected by pharmacological resting-state functional MRI. *Neuroimage* 109, 151–159. doi: 10.1016/j.neuroimage.2015.01.009

Shah, D., Blockx, I., Keliris, G. A., Kara, F., Jonckers, E., Verhoye, M., et al. (2016). Cholinergic and serotonergic modulations differentially affect large-scale functional networks in the mouse brain. *Brain Struct. Funct.* 221, 3067–3079. doi: 10.1007/s00429-015-1087-7

Shah, Y. B., Prior, M. J. W., Dixon, A. L., Morris, P. G., and Marsden, C. A. (2004). Detection of cannabinoid agonist evoked increase in BOLD contrast in rats using functional magnetic resonance imaging. *Neuropharmacology* 46, 379–387. doi: 10.1016/j.neuropharm.2003.09.023

Shakil, S., Billings, J. C., Keilholz, S. D., and Lee, C.-H. (2018). Parametric dependencies of sliding window correlation. *IEEE Trans. Biomed. Eng.* 65, 254–263. doi: 10.1109/TBME.2017.2762763

Shakil, S., Keilholz, S. D., and Chin-Hui, L. (2016). Adaptive change point detection of dynamic functional connectivity networks. *Conf. Proc. IEEE Eng. Med. Biol. Soc.* 2016, 1135–1138. doi: 10.1109/EMBC.2016.7590904

Shih, Y.-Y. I., Chiang, Y.-C., Shyu, B.-C., Jaw, F.-S., Duong, T. Q., and Chang, C. (2012a). Endogenous opioid-dopamine neurotransmission underlie negative CBV fMRI signals. *Exp. Neurol.* 234, 382–388. doi: 10.1016/j.expneurol.2011.12.042

Shih, Y.-Y. I., Li, G., Muir, E. R., De La Garza, B. H., Kiel, J. W., and Duong, T. Q. (2012b). Pharmacological MRI of the choroid and retina: blood flow and BOLD responses during nitroprusside infusion. *Magn. Reson. Med.* 68, 1273–1278. doi: 10.1002/mrm.24112

Shih, Y.-Y. I., Huang, S., Chen, Y.-Y., Lai, H.-Y., Kao, Y.-C. J., Du, F., et al. (2014). Imaging neurovascular function and functional recovery after stroke in the rat striatum using forepaw stimulation. *J. Cereb. Blood Flow Metab.* 34, 1483–1492. doi: 10.1038/jcbfm.2014.103

Shim, H.-J., Jung, W. B., Schlegel, F., Lee, J., Kim, S., Lee, J., et al. (2018). Mouse fMRI under ketamine and xylazine anesthesia: robust contralateral somatosensory cortex activation in response to forepaw stimulation. *Neuroimage* 177, 30–44. doi: 10.1016/j.neuroimage.2018.04.062

Sicard, K., Shen, Q., Brevard, M. E., Sullivan, R., Ferris, C. F., King, J. A., et al. (2003). Regional cerebral blood flow and BOLD responses in conscious and anesthetized rats under basal and hypercapnic conditions: implications for functional MRI studies. *J. Cereb. Blood Flow Metab.* 23, 472–481. doi: 10.1097/00004647-200304000-00011

Silva, A. C. (2012). Using manganese-enhanced MRI to understand BOLD. *Neuroimage* 62, 1009–1013. doi: 10.1016/j.neuroimage.2012.01.008

Silva, A. C., and Kim, S.-G. (1999). Pseudo-continuous arterial spin labeling technique for measuring CBF dynamics with high temporal resolution. *Magn. Reson. Med.* 42, 425–429. doi: 10.1002/(sici)1522-2594(199909)42:3<425::aid-mrm3>3.3.co;2-j

Silva, A. C., Lee, S. P., Yang, G., Iadecola, C., and Kim, S. G. (1999). Simultaneous blood oxygenation level-dependent and cerebral blood flow functional magnetic resonance imaging during forepaw stimulation in the rat. *J. Cereb. Blood Flow Metab.* 19, 871–879. doi: 10.1097/00004647-199908000-00006

Sinclair, M. D. (2003). A review of the physiological effects of alpha2-agonists related to the clinical use of medetomidine in small animal practice. *Can. Vet. J.* 44, 885–897.

Smith, K. S., Bucci, D. J., Luikart, B. W., and Mahler, S. V. (2016). DREADDS: use and application in behavioral neuroscience. *Behav. Neurosci.* 130, 137–155. doi: 10.1037/bne0000135

Soares, J. M., Magalhães, R., Moreira, P. S., Sousa, A., Ganz, E., Sampaio, A., et al. (2016). A Hitchhiker's guide to functional magnetic resonance imaging. *Front. Neurosci.* 10:515. doi: 10.3389/fnins.2016.00515

Speck, O., and Hennig, J. (1998). Functional imaging by I0- and T2*-parameter mapping using multi-image EPI. *Magn. Reson. Med.* 40, 243–248. doi: 10.1002/mrm.1910400210

Sporns, O., and Betzel, R. F. (2016). Modular brain networks. *Annu. Rev. Psychol.* 67, 613–640. doi: 10.1146/annurev-psych-122414-033634

Squillace, M., Dodero, L., Federici, M., Migliarini, S., Errico, F., Napolitano, F., et al. (2014). Dysfunctional dopaminergic neurotransmission in asocial BTBR mice. *Transl. Psychiatry* 4, e427. doi: 10.1038/tp.2014.69

Stafford, J. M., Jarrett, B. R., Miranda-Dominguez, O., Mills, B. D., Cain, N., Mihalas, S., et al. (2014). Large-scale topology and the default mode network in the mouse connectome. *Proc. Natl. Acad. Sci. U.S.A.* 111, 18745–18750. doi: 10.1073/pnas.1404346111

Steward, C. A., Marsden, C. A., Prior, M. J. W., Morris, P. G., and Shah, Y. B. (2005). Methodological considerations in rat brain BOLD contrast pharmacological MRI. *Psychopharmacology* 180, 687–704. doi: 10.1007/s00213-005-2213-7

Straathof, M., Sinke, M. R., Dijkhuizen, R. M., and Otte, W. M. (2019). A systematic review on the quantitative relationship between structural and functional network connectivity strength in mammalian brains. *J. Cereb. Blood Flow Metab.* 39, 189–209. doi: 10.1177/0271678X18809547

Stujenske, J. M., Spellman, T., and Gordon, J. A. (2015). Modeling the spatiotemporal dynamics of light and heat propagation for in vivo optogenetics. *Cell Rep.* 12, 525–534. doi: 10.1016/j.celrep.2015.06.036

Takata, N., Yoshida, K., Komaki, Y., Xu, M., Sakai, Y., Hikishima, K., et al. (2015). Optogenetic activation of CA1 pyramidal neurons at the dorsal and ventral hippocampus evokes distinct brain-wide responses revealed by mouse fMRI. *PLoS One* 10:e0121417. doi: 10.1371/journal.pone.0121417

Tjandra, T., Brooks, J. C. W., Figueiredo, P., Wise, R., Matthews, P. M., and Tracey, I. (2005). Quantitative assessment of the reproducibility of functional activation measured with BOLD and MR perfusion imaging: implications for clinical trial design. *Neuroimage* 27, 393–401. doi: 10.1016/j.neuroimage.2005.04.021

Tsubota, T., Ohashi, Y., Tamura, K., and Miyashita, Y. (2012). Optogenetic inhibition of Purkinje cell activity reveals cerebellar control of blood pressure during postural alterations in anesthetized rats. *Neuroscience* 210, 137–144. doi: 10.1016/j.neuroscience.2012.03.014

Tsurugizawa, T., Ciobanu, L., and Le Bihan, D. (2013). Water diffusion in brain cortex closely tracks underlying neuronal activity. *Proc. Natl. Acad. Sci. U.S.A.* 110, 11636–11641. doi: 10.1073/pnas.1303178110

Tuor, U. I., McKenzie, E., and Tomanek, B. (2002). Functional magnetic resonance imaging of tonic pain and vasopressor effects in rats. *Magn. Reson. Imaging* 20, 707–712. doi: 10.1016/s0730-725x(02)00599-4

Uhrig, L., Ciobanu, L., Djemai, B., Le Bihan, D., and Jarraya, B. (2014). Sedation agents differentially modulate cortical and subcortical blood oxygenation: evidence from ultra-high field MRI at 17.2 T. *PLoS One* 9:e100323. doi: 10.1371/journal.pone.0100323

Uhrig, L., Sitt, J. D., Jacob, A., Tasserie, J., Barttfeld, P., Dupont, M., et al. (2018). Resting-state dynamics as a cortical signature of Anesthesia in monkeys. *Anesthesiology* 129, 942–958. doi: 10.1097/ALN.0000000000002336

Uludağ, K., Müller-Bierl, B., and Uğurbil, K. (2009). An integrative model for neuronal activity-induced signal changes for gradient and spin echo functional imaging. *Neuroimage* 48, 150–165. doi: 10.1016/j.neuroimage.2009.05.051

Valdés-Hernández, P. A., Sumiyoshi, A., Nonaka, H., Haga, R., Aubert-Vásquez, E., Ogawa, T., et al. (2011). An in vivo MRI template set for morphometry, tissue segmentation, and fMRI localization in rats. *Front. Neuroinform.* 5:26. doi: 10.3389/fninf.2011.00026

Van der Linden, A., Van Camp, N., Ramos-Cabrer, P., and Hoehn, M. (2007). Current status of functional MRI on small animals: application to physiology, pathophysiology, and cognition. *NMR Biomed.* 20, 522–545. doi: 10.1002/nbm.1131

van der Marel, K., Homberg, J. R., Otte, W. M., and Dijkhuizen, R. M. (2013). Functional and structural neural network characterization of serotonin transporter knockout rats. *PLoS One* 8:e57780. doi: 10.1371/journal.pone.0057780

Van Essen, D. C., Glasser, M. F., Dierker, D. L., and Harwell, J. (2012). Cortical parcellations of the macaque monkey analyzed on surface-based atlases. *Cereb. Cortex* 22, 2227–2240. doi: 10.1093/cercor/bhr290

Van Essen, D. C., Smith, S. M., Barch, D. M., Behrens, T. E. J., Yacoub, E., Ugurbil, K., et al. (2013). The WU-Minn Human Connectome Project: an overview. *Neuroimage* 80, 62–79. doi: 10.1016/j.neuroimage.2013.05.041

Van Essen, D. C., and Ugurbil, K. (2012). The future of the human connectome. *Neuroimage* 62, 1299–1310. doi: 10.1016/j.neuroimage.2012.01.032

van Meer, M. P. A., Otte, W. M., van der Marel, K., Nijboer, C. H., Kavelaars, A., van der Sprenkel, J. W. B., et al. (2012). Extent of Bilateral neuronal network reorganization and functional recovery in relation to stroke severity. *J. Neurosci.* 32, 4495–4507. doi: 10.1523/jneurosci.3662-11.2012

van Meer, M. P. A., van der Marel, K., Wang, K., Otte, W. M., El Bouazati, S., Roeling, T. A. P., et al. (2010). Recovery of sensorimotor function after experimental stroke correlates with restoration of resting-state interhemispheric functional connectivity. *J. Neurosci.* 30, 3964–3972. doi: 10.1523/JNEUROSCI.5709-09.2010

Vincent, J. L., Patel, G. H., Fox, M. D., Snyder, A. Z., Baker, J. T., Van Essen, D. C., et al. (2007). Intrinsic functional architecture in the anaesthetized monkey brain. *Nature* 447, 83–86. doi: 10.1038/nature05758

Vogt, B. A., and Paxinos, G. (2014). Cytoarchitecture of mouse and rat cingulate cortex with human homologies. *Brain Struct. Funct.* 219, 185–192. doi: 10.1007/s00429-012-0493-3

Vovenko, E. P., and Sokolova, I. B. (1998). [Oxygen tension in the brain cortex arterioles during spontaneous respiration with the hypoxic gas mixture in rats]. *Ross. Fiziol. Zh. Im. I M Sechenova* 84, 527–535.

Wang, J., Aguirre, G. K., Kimberg, D. Y., Roc, A. C., Li, L., and Detre, J. A. (2003). Arterial spin labeling perfusion fMRI with very low task frequency. *Magn. Reson. Med.* 49, 796–802. doi: 10.1002/mrm.10437

Wang, K., van Meer, M. P. A., van der Marel, K., van der Toorn, A., Xu, L., Liu, Y., et al. (2011). Temporal scaling properties and spatial synchronization of spontaneous blood oxygenation level-dependent (BOLD) signal fluctuations in rat sensorimotor network at different levels of isoflurane anesthesia. *NMR Biomed.* 24, 61–67. doi: 10.1002/nbm.1556

Wang, R., Foniok, T., Wamsteeker, J. I., Qiao, M., Tomanek, B., Vivanco, R. A., et al. (2006). Transient blood pressure changes affect the functional magnetic resonance imaging detection of cerebral activation. *Neuroimage* 31, 1–11. doi: 10.1016/j.neuroimage.2005.12.004

Weiner, M. W., Veitch, D. P., Aisen, P. S., Beckett, L. A., Cairns, N. J., Green, R. C., et al. (2012). The Alzheimer's disease neuroimaging initiative: a review of papers published since its inception. *Alzheimers. Dement.* 8, S1–S68. doi: 10.1016/j.jalz.2011.09.172

Weitz, A. J., Fang, Z., Lee, H. J., Fisher, R. S., Smith, W. C., Choy, M., et al. (2015). Optogenetic fMRI reveals distinct, frequency-dependent networks recruited by dorsal and intermediate hippocampus stimulations. *Neuroimage* 107, 229–241. doi: 10.1016/j.neuroimage.2014.10.039

Wen, J., Goyal, M. S., Astafiev, S. V., Raichle, M. E., and Yablonskiy, D. A. (2018). Genetically defined cellular correlates of the baseline brain MRI signal. *Proc. Natl. Acad. Sci. U.S.A.* 115, E9727–E9736. doi: 10.1073/pnas.1808121115

Williams, D. S., Detre, J. A., Leigh, J. S., and Koretsky, A. P. (1992). Magnetic resonance imaging of perfusion using spin inversion of arterial water. *Proc. Natl. Acad. Sci. U.S.A.* 89, 212–216. doi: 10.1073/pnas.89.1.212

Williams, K. A., Magnuson, M., Majeed, W., LaConte, S. M., Peltier, S. J., Hu, X., et al. (2010). Comparison of α-chloralose, medetomidine and isoflurane anesthesia for functional connectivity mapping in the rat. *Magn. Reson. Imaging* 28, 995–1003. doi: 10.1016/j.mri.2010.03.007

Witten, I. B., Steinberg, E. E., Lee, S. Y., Davidson, T. J., Zalocusky, K. A., Brodsky, M., et al. (2011). Recombinase-driver rat lines: tools, techniques, and optogenetic application to dopamine-mediated reinforcement. *Neuron* 72, 721–733. doi: 10.1016/j.neuron.2011.10.028

Wu, T., Grandjean, J., Bosshard, S. C., Rudin, M., Reutens, D., and Jiang, T. (2017). Altered regional connectivity reflecting effects of different anaesthesia protocols in the mouse brain. *Neuroimage* 149, 190–199. doi: 10.1016/j.neuroimage.2017.01.074

Wu, W.-C., Fernández-Seara, M., Detre, J. A., Wehrli, F. W., and Wang, J. (2007). A theoretical and experimental investigation of the tagging efficiency of pseudocontinuous arterial spin labeling. *Magn. Reson. Med.* 58, 1020–1027. doi: 10.1002/mrm.21403

Xu, F., Uh, J., Brier, M. R., Hart, J. Jr., Yezhuvath, U. S., Gu, H., et al. (2011). The influence of carbon dioxide on brain activity and metabolism in conscious humans. *J. Cereb. Blood Flow Metab.* 31, 58–67. doi: 10.1038/jcbfm.2010.153

Yacoub, E., Duong, T. Q., Van De Moortele, P.-F., Lindquist, M., Adriany, G., Kim, S.-G., et al. (2003). Spin-echo fMRI in humans using high spatial resolutions and high magnetic fields. *Magn. Reson. Med.* 49, 655–664. doi: 10.1002/mrm.10433

Yao, Q.-L., Zhang, H.-Y., Nie, B.-B., Fang, F., Jiao, Y., and Teng, G.-J. (2012). MRI assessment of amplitude of low-frequency fluctuation in rat brains with acute cerebral ischemic stroke. *Neurosci. Lett.* 509, 22–26. doi: 10.1016/j.neulet.2011.12.036

Yizhar, O., Fenno, L. E., Davidson, T. J., Mogri, M., and Deisseroth, K. (2011). Optogenetics in neural systems. *Neuron* 71, 9–34. doi: 10.1016/j.neuron.2011.06.004

Yoshida, K., Mimura, Y., Ishihara, R., Nishida, H., Komaki, Y., Minakuchi, T., et al. (2016). Physiological effects of a habituation procedure for functional MRI in awake mice using a cryogenic radiofrequency probe. *J. Neurosci. Methods* 274, 38–48. doi: 10.1016/j.jneumeth.2016.09.013

Yu, G., Onodera, H., Aono, Y., Kawano, F., Ueda, Y., Furuya, A., et al. (2016). Optical manipulation of the alpha subunits of heterotrimeric G proteins using photoswitchable dimerization systems. *Sci. Rep.* 6:35777. doi: 10.1038/srep35777

Zang, Y., Jiang, T., Lu, Y., He, Y., and Tian, L. (2004). Regional homogeneity approach to fMRI data analysis. *Neuroimage* 22, 394–400. doi: 10.1016/j.neuroimage.2003.12.030

Zang, Y.-F., He, Y., Zhu, C.-Z., Cao, Q.-J., Sui, M.-Q., Liang, M., et al. (2007). Altered baseline brain activity in children with ADHD revealed by resting-state functional MRI. *Brain Dev.* 29, 83–91. doi: 10.1016/j.braindev.2006.07.002

Zeng, H., and Madisen, L. (2012). Mouse transgenic approaches in optogenetics. *Prog. Brain Res.* 196, 193–213. doi: 10.1016/b978-0-444-59426-6.00010-0

Zerbi, V., Grandjean, J., Rudin, M., and Wenderoth, N. (2015). Mapping the mouse brain with rs-fMRI: an optimized pipeline for functional network identification. *Neuroimage* 123, 11–21. doi: 10.1016/j.neuroimage.2015.07.090

Zeuthen, T. (1978). Potentials and small-signal impedances of platinum microelectrodes in vivo and in vitro. *Med. Biol. Eng. Comput.* 16, 489–499. doi: 10.1007/bf02457798

Zhang, F., Gradinaru, V., Adamantidis, A. R., Durand, R., Airan, R. D., de Lecea, L., et al. (2010). Optogenetic interrogation of neural circuits: technology for probing mammalian brain structures. *Nat. Protoc.* 5, 439–456. doi: 10.1038/nprot.2009.226

Zhang, F., Prigge, M., Beyrière, F., Tsunoda, S. P., Mattis, J., Yizhar, O., et al. (2008). Red-shifted optogenetic excitation: a tool for fast neural control derived from Volvox carteri. *Nat. Neurosci.* 11, 631–633. doi: 10.1038/nn.2120

Zhang, F., Wang, L.-P., Boyden, E. S., and Deisseroth, K. (2006). Channelrhodopsin-2 and optical control of excitable cells. *Nat. Methods* 3, 785–792. doi: 10.1038/nmeth936

Zhang, F., Wang, L.-P., Brauner, M., Liewald, J. F., Kay, K., Watzke, N., et al. (2007). Multimodal fast optical interrogation of neural circuitry. *Nature* 446, 633–639. doi: 10.1038/nature05744

Zhao, F., Zhao, T., Zhou, L., Wu, Q., and Hu, X. (2008). BOLD study of stimulation-induced neural activity and resting-state connectivity in medetomidine-sedated rat. *Neuroimage* 39, 248–260. doi: 10.1016/j.neuroimage.2007.07.063

Zhong, K., Leupold, J., Hennig, J., and Speck, O. (2007). Systematic investigation of balanced steady-state free precession for functional MRI in the human visual cortex at 3 Tesla. *Magn. Reson. Med.* 57, 67–73. doi: 10.1002/mrm.21103

Zhou, Z. C., Salzwedel, A. P., Radtke-Schuller, S., Li, Y., Sellers, K. K., Gilmore, J. H., et al. (2016). Resting state network topology of the ferret brain. *Neuroimage* 143, 70–81. doi: 10.1016/j.neuroimage.2016.09.003

Zhu, H., Aryal, D. K., Olsen, R. H. J., Urban, D. J., Swearingen, A., Forbes, S., et al. (2016). Cre-dependent DREADD (Designer Receptors Exclusively Activated by Designer Drugs) mice. *Genesis* 54, 439–446. doi: 10.1002/dvg.22949

Zimmermann, D., Zhou, A., Kiesel, M., Feldbauer, K., Terpitz, U., Haase, W., et al. (2008). Effects on capacitance by overexpression of membrane proteins. *Biochem. Biophys. Res. Commun.* 369, 1022–1026. doi: 10.1016/j.bbrc.2008.02.153

Zou, Q.-H., Zhu, C.-Z., Yang, Y., Zuo, X.-N., Long, X.-Y., Cao, Q.-J., et al. (2008). An improved approach to detection of amplitude of low-frequency fluctuation (ALFF) for resting-state fMRI: fractional ALFF. *J. Neurosci. Methods* 172, 137–141. doi: 10.1016/j.jneumeth.2008.04.012

Zuo, X.-N., and Xing, X.-X. (2014). Test-retest reliabilities of resting-state FMRI measurements in human brain functional connectomics: a systems neuroscience perspective. *Neurosci. Biobehav. Rev.* 45, 100–118. doi: 10.1016/j.neubiorev.2014.05.009

Conflict of Interest: The authors declare that the research was conducted in the absence of any commercial or financial relationships that could be construed as a potential conflict of interest.

frontiers in Neuroinformatics

TECHNOLOGY AND CODE
published: 11 February 2020
doi: 10.3389/fninf.2020.00005

An Automated Open-Source Workflow for Standards-Compliant Integration of Small Animal Magnetic Resonance Imaging Data

Horea-Ioan Ioanas[1]*, *Markus Marks*[2], *Clément M. Garin*[3], *Marc Dhenain*[3], *Mehmet Fatih Yanik*[2] *and Markus Rudin*[1]

[1] *Institute for Biomedical Engineering, ETH and University of Zurich, Zurich, Switzerland,* [2] *Institute of Neuroinformatics, ETH and University of Zurich, Zurich, Switzerland,* [3] *Centre National de la Recherche Scientifique (CNRS), Université Paris-Sud, Paris, France*

Large-scale research integration is contingent on seamless access to data in standardized formats. Standards enable researchers to understand external experiment structures, pool results, and apply homogeneous preprocessing and analysis workflows. Particularly, they facilitate these features without the need for numerous potentially confounding compatibility add-ons. In small animal magnetic resonance imaging, an overwhelming proportion of data is acquired via the ParaVision software of the Bruker Corporation. The original data structure is predominantly transparent, but fundamentally incompatible with modern pipelines. Additionally, it sources metadata from free-field operator input, which diverges strongly between laboratories and researchers. In this article we present an open-source workflow which automatically converts and reposits data from the ParaVision structure into the widely supported and openly documented Brain Imaging Data Structure (BIDS). Complementing this workflow we also present operator guidelines for appropriate ParaVision data input, and a programmatic walk-through detailing how preexisting scans with uninterpretable metadata records can easily be made compliant after the acquisition.

Keywords: MRI/fMRI, small animal imaging, repositing, FOSS, Bruker, ParaVision, Python

OPEN ACCESS

Edited by:
Jan G. Bjaalie,
University of Oslo, Norway

Reviewed by:
Reza M. Salek,
International Agency For Research On Cancer (IARC), France
Jason Lerch,
Toronto Centre for Phenogenomics, Canada
Remi Gau,
Catholic University of Louvain, Belgium

***Correspondence:**
Horea-Ioan Ioanas
ioanas@biomed.ee.ethz.ch;
chr@chymera.eu

Received: *31 May 2019*
Accepted: *16 January 2020*
Published: *11 February 2020*

Citation:
Ioanas H-I, Marks M, Garin CM, Dhenain M, Yanik MF and Rudin M (2020) An Automated Open-Source Workflow for Standards-Compliant Integration of Small Animal Magnetic Resonance Imaging Data. Front. Neuroinform. 14:5. doi: 10.3389/fninf.2020.00005

1. INTRODUCTION

Magnetic resonance imaging (MRI), and functional MRI (fMRI) are highly popular methods in the field of neuroscience. Their high tissue penetration makes them eminently suited for reporting features at the whole-brain level *in vivo*. High assay coverage is particularly relevant for an organ as holistic in its function as the brain, as it facilitates the interrogation of not only sensitivity but also regional specificity. However, MRI methods generate signal via nuclear spin polarization—which is commonly very weak—and characteristically posses low intrinsic sensitivity. Additionally, fMRI methods rely on highly indirect measures of neuronal activity, and are consequently susceptible to numerous confounding factors.

In animal fMRI in particular, subject preparation, and more specifically cerebrovascular parameters (Schroeter et al., 2016) and anesthesia (Schlegel et al., 2015; Bukhari et al., 2018) are widely known drivers of result variability. In order to integrate data which may be thus strongly

confounded—as well as in order to clarify the confounds themselves (Grandjean et al., 2019)—it is vital that data is shared in a raw state, i.e., having undergone no or as little processing as possible. Raw data sharing increases transparency and reproducibility, as data can be assumed to be free from undocumented "fixes." Such attempts at *ex post facto* data improvement may not just include data matrix manipulations, but also outlier (subject or session) filtering. While valid rationales for both outlier filtering and data editing exist, these processes are best performed in a transparent and well-documented fashion, leaving the raw data untouched as an ultimate recourse.

As published data is intended for reuse, it is reasonable to assume that it may be employed to explore hypotheses other than those under the constraints of which it was originally acquired. In such cases, it is vital that the shared entry and feature pool be as inclusive as possible. It is likely, above all in the effort of methodological comparison and improvement, that what is an artifact or outlier for the interrogation of a narrow hypothesis, may constitute a strong driver of the effect of another hypothesis. Therefore, it is the best choice for small animal MRI researchers to publish data in as raw a form as possible.

The documentation of directed information processing is known as data provenance, and in the effort of establishing a point of recourse it is helpful to map out data traces to the earliest record or earliest record in digital form. In **Figure 1**, a simplified summary of data provenance is showcased, based on the most common features of small animal MRI. While the rawest data is in theoretical terms the best possible recourse, the extent of this overview illustrates that the choice of a raw data origin point is also constrained by the scope of a researcher's work. Particularly the first step, reconstructing volumetric information from the time domain k-space record, is commonly not covered by modern MRI pipelines, and instead left to the original acquisition software.

Whether directly from the k-space file or from the reconstructed image, the data needs to be converted into a standard, vendor-independent form. Standards are a cornerstone of scientific collaboration, as they concomitantly enable result comparability and data integration. They can, however, also be potentially restrictive, since a standard may impose artificial limitations on features or artificial requirements not pertinent to a particular study. Such limitations may materialize in negative restrictions on software tools (e.g., proprietary standards may preclude data processing with non-proprietary tools), restrictions on hypotheses (e.g., data organized by one hierarchical principle may lead to loss or obfuscation of certain category correspondence relationships), or positive restrictions of technologies (e.g., data available in highly specific formats might require usage of and familiarity with highly specialized tools)—with the latter restriction being particularly relevant in database standards.

In order to access the benefits and mitigate the pitfalls of standards compliance, data should be migrated to a form which is openly and thoroughly documented, and easily accessible for user manipulation. In the field of small animal MRI, the vast majority acquisition devices (∼80 %) are produced by the Bruker Corporation, and thus the largest segment of data is initially formatted according to the ParaVision standard. This standard is largely transparent, with most metadata stored in plain-text files. The data, however, are stored in a binary format, which strongly diverges from the *de facto* standard of NIfTI (Cox et al., 2004), and for which extensive documentation is not openly available. Conversion tools from the ParaVision standard to NIfTI exist (Ferraris et al., 2017; Rorden and Naveaum, 2018), and have more recently also been made available from the manufacturer (presently only in closed-source form and only in ParaVision 360, without backward compatibility). Contingent on the scope limitations of the NIfTI format itself, these tools can however not repackage the majority of metadata represented in ParaVision standard plain-text files. This situation exemplifies how the utility of standards is not only contingent on their suitability for use as a common origin format, but also on their flexibility to accommodate all relevant information.

The Brain Imaging Data Structure (BIDS) standard (Gorgolewski et al., 2016), is a prominent candidate for repositing small animal magnetic resonance imaging data. It is thoroughly tested and well-adopted in the field of human MRI, and its extensible and permissive nature makes it easily adaptable to small animal data—as well as generally accommodating for broad swathes of eclectic use cases. The standard builds upon the NIfTI format (Cox et al., 2004), one of the most widely used formats for high-level neuroimaging analysis, which is compact, as it offers on-the-fly lossless compression, and general-purpose, as its header only contains the minimal amount of metadata required for spatiotemporal image representation. In addition, BIDS offers an extendable specification for metadata, stored in sidecar text files. This separation of minimal and full metadata

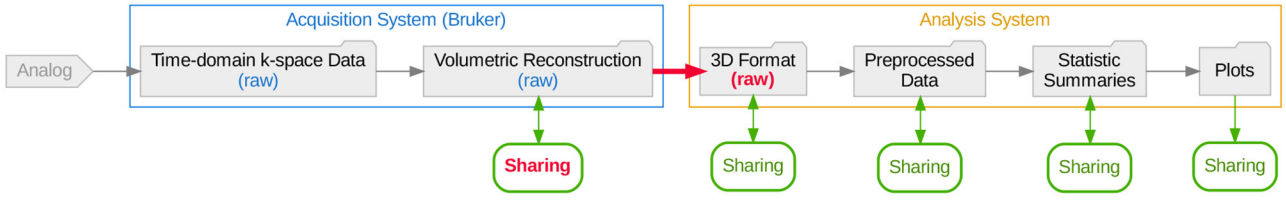

FIGURE 1 | Data provenance flowchart, with the leftmost data being the rawest. Folder nodes represent data states on disk, with nodes suitable as raw data recourse highlighted with the word raw in parentheses. The introduction of a standardized conversion process (red arrow edge) would permit the creation of a 3D format representation usable as raw data recourse, as well as the sharing of Bruker acquisition system volumetric reconstruction data (also highlighted in red).

space makes BIDS easily and incrementally accessible for new users and portable to further modalities, as the core requirements can rapidly be met and further relevant metadata fields can be processed and added as they become required for analysis. The standard's usage of plain-text metadata files also makes them accessible to ubiquitous, minimal, and Free and Open Source (FOSS) tools, e.g., the Standard GNU Utilities, or equivalent core utility implementations. Particularly, the representation of metadata as text allows data set versions with increments in metadata availability to be compared via `diff`-type commands (Hunt and MacIlroy, 1976), which is less feasible for binary data. The format is organized around a simple directory hierarchy, with key metadata fields captured in the file and path names. This makes BIDS data intuitive to access from both a console and a graphical user interface.

Given varying specifications, it is common for standards to not map fully onto each other (e.g., one metadata field may not have a clear correspondence relationship in both standards). As data conversion is always based only on the most recent parent format, this means that the risk of data (or more specifically, metadata) loss or obfuscation grows with each transition to a new standard. Thus, in the example of **Figure 1**, collaborative potential is best served if both the "3D Format" representation is infused with sufficient and sufficiently accessible metadata, *and* the original "Volumetric Reconstruction" is rendered shareable.

Both these goals can be attained by the introduction of an automated open-source workflow which can perform the standard transition. As such, all metadata fields which are identified as equivalent between the ParaVision and BIDS standards can be made accessible in the final form. Conversely, if ParaVision standard data is automatically interpretable as input for a concatenation of processing workflows, this original form can also serve as a shareable raw data recourse.

2. THE WORKFLOW

The workflow, entitled `bru2bids` (Bruker ParaVision to BIDS), is distributed as part of SAMRI (Ioanas et al., 2019b), a free and open source workflow package of the ETH and University of Zurich Institute for Biomedical Engineering. This repositing workflow can be used stand-alone, but also serves as a gateway to all the further workflows included in the SAMRI package (encompassing dedicated solutions for all analysis steps showcased in **Figure 1**). As such, the ParaVision-to-BIDS workflow not only permits users to convert data into a format which is more widely supported and flexible, but also easily links to reference implementations for BIDS-based small animal processing functionalities (e.g., registration; Ioanas et al., 2019c).

The workflow reposits data and metadata from the ParaVision standard into a BIDS-compliant form, notifying the user of BIDS validation possibilities upon completion. The repositing process automatically handles the conversion of data from ParaVision volumetric reconstruction files (`2dseq`) to NIfTI files. Additionally, it assigns metadata from the specific ParaVision text files to either the NIfTI header, the BIDS metadata files, or the BIDS directory hierarchy, as applicable. A simplified overview of this process is presented in **Figure 2A**. A more extensive break-down of metadata sourcing—showing the actual input and output files, and highlighting metadata fields represented in the data paths—is laid out in **Figure 2B**.

The repositing functionality described herein can be accessed from both Bash and Python, via `SAMRI bru2bids` or `samri.pipelines.reposit.bru2bids()`, respectively. Invocation variants are illustrated in **Figure 3**, and link to the same code implementation. The `bru2bids` function is highly parameterized, with the same parameter set available in either Bash or Python. A full list of parameters can be obtained by executing the `SAMRI bru2bids -help` command from the console. The current parameter listing for Bash is presented under **Figure S1**.

Notable parameters include the functional, diffusion-weighted, and structural scan specification. These three selectors each use an input dictionary (pairs of one *key*, which is a BIDS metadata string, and a list of accepted *values*), to identify which scans are to be reposited. Examples of such dictionaries are given in **Figure 3**, where scans with an "EPI" acquisition field are categorized as functional, and files with a "TurboRARE" acquisition field are categorized as structural. The repositing pipeline is run sequentially for all scan categories, as separate processes are required for each scan type (examples of the internal processing nodes are shown in **Figure 6**). Further parameters not included in the workflow to date, such as magnetic resonance spectroscopy (MRS) data selection, can easily be implemented, given the availability and familiarity with enough example data, by copying and editing the process instructions from present parameters inside the `samri.pipelines.reposit.bru2bids()` function.

2.1. Operator Guidelines

The process of scan categorization and metadata sourcing for BIDS conversion is contingent on the presence of operator input records interpretable by the workflow. As the ParaVision metadata files contain free-field input, adherence to a minimal set of guidelines is necessary to ensure unambiguous error-free conversion.

The acquisition of data in the Bruker ParaVision graphical user interface is commenced by creating a new study in the "Study Registration" window (**Figure S2**). In this window the operator should fill in the "Animal ID" entry corresponding to the intended BIDS subject identifier (i.e., the `sub` field in the resulting path and file names), and the "Study Name" entry corresponding to the intended BIDS session identifier (i.e., the `ses` field in the resulting path and file names). Notably, the values for both of these fields should be BIDS-compliant—meaning that they should contain only alphanumeric characters, necessarily excluding underscores and hyphens, which are used in the BIDS standard as field separators.

Once the study is created, scans should be renamed in the graphical user interface (before or after acquisition) to contain the additional relevant metadata information according to the BIDS standard. Thus, a resting-state scan acquired with an EPI sequence resolving BOLD contrast should contain the following string in the "Instruction Name" column of the

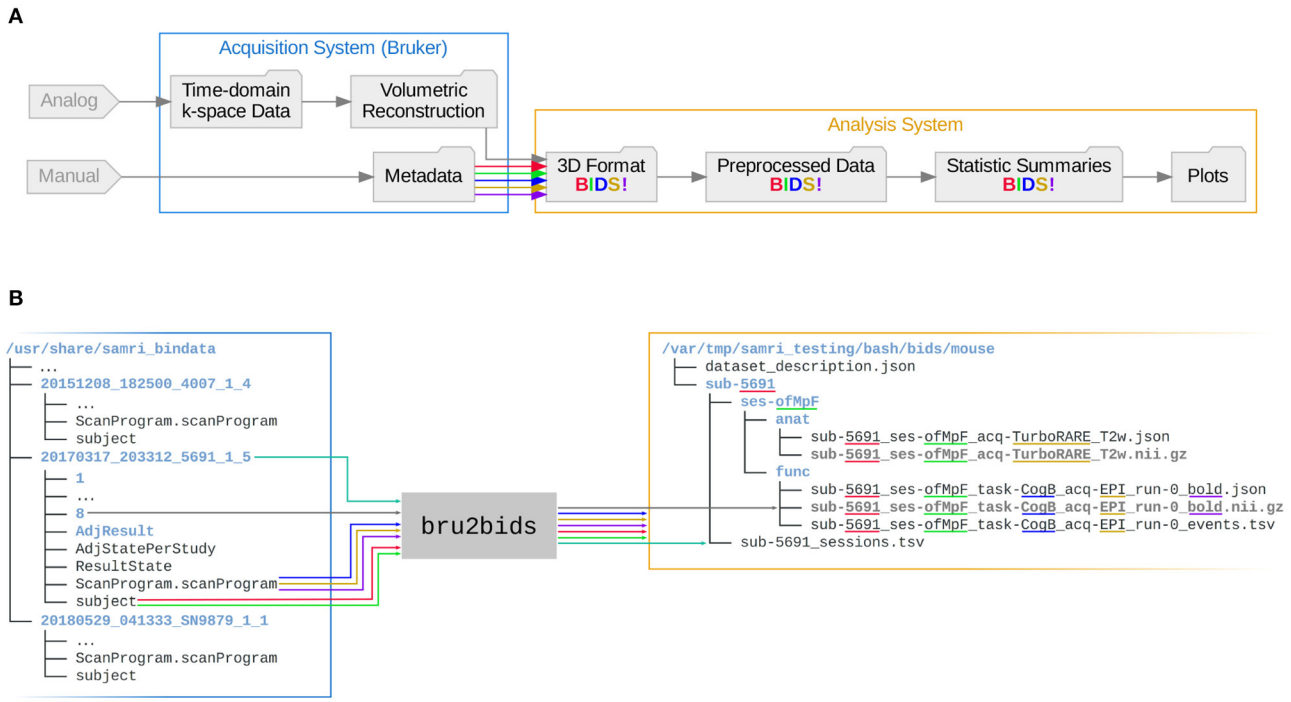

FIGURE 2 | The Paravision-to-BIDS repositing process automatically interprets the source data structure and determines corresponding variables in the BIDS standard. Depicted are color-coded overviews of data and metadata streams during the SAMRI `bru2bids` repositing process, with the data matrix content coded in gray, the subject field in red, the session field in green, the task field in blue, the acquisition field in ochre, and the modality suffix in purple. **(A)** Processing flowchart, breaking down the Bruker to BIDS repositing step (highlighted in **Figure 1**) to depict data-metadata integration, and downstream metadata encoding in the BIDS directory hierarchy and corresponding metadata files. **(B)** Directory tree overview of Bruker to BIDS repositing. Depicted are source and result directories, with arrows indicating which files the most relevant BIDS variable fields are sourced from. Date information is coded in cyan, and is sourced directly from the ParaVision scan directory name. The conversion presented herein shows the mouse data form the test data collection, and is performed given the instructions in **Figure 3A**: note that no BIDS entries from the 4007 and SN9879 subject directories were processed (as well as from any of the other species). This is happening by design and because no entries in any of the other scans match the selection criteria.

A

```
user@host ~ $ SAMRI bru2bids\
        -o /var/tmp/samri_testing/bash\
        -f '{"acquisition":["EPI"]}'\
        -s '{"acquisition":["TurboRARE"]}'\
        /usr/share/samri_bindata
```

B

```
from samri.pipelines.reposit import bru2bids
bru2bids('/usr/share/samri_bindata/',
        inflated_size=False,
        functional_match={'acquisition':['EPI']},
        structural_match={'acquisition':['TurboRARE']},
        out_base='/var/tmp/samri_testing/pytest/',
        )
```

FIGURE 3 | Both Bash and Python can be used to access the repositing functionality. As the Bash binding is auto-generated from the Python function, features become available synchronously, and inspection can be coherently performed regardless of the invocation language. Both code snippets specify the exact same instructions regarding the data source: they indicate that ParaVision standard data from `/usr/share/samri_bindata/` is to be reposited into a BIDS standard form, categorizing scans with an "EPI" acquisition string as functional, and files with a "TurboRARE" acquisition string as structural. Both of the above invocations are included in the package test suite. **(A)** Bash invocation, repositing data into a BIDS directory located under `/var/tmp/samri_testing/bash`. **(B)** Python invocation, repositing data into a BIDS directory located under `/var/tmp/samri_testing/pytest`.

ParaVision interface: `acq-seEPI_task-rest_bold`. The format is composed out of the BIDS short identifier (e.g., `acq` for acquisition), followed by a hyphen and the desired metadata field value (e.g., `seEPI` for spin-echo echo-planar imaging). The level of detail in these fields is at the discretion of the operator, as per the flexible nature of the standard. If recognizing the EPI variant at-a-glance is deemed irrelevant for the data at hand, this field may simply be assigned a value of `EPI`, or could conversely be expanded to include an arbitrary amount of additional detail. Pairs of BIDS short identifiers and desired values should be separated by underscores, with the modality suffix appended at the end after a final underscore separator.

Additional BIDS fields such as the run ordinal number (e.g., `run-0`, as seen in **Figure 2B**), are automatically determined by

the bru2bids workflow. The modality suffix, if not explicitly specified by the operator, can also be automatically assigned in a small number of cases where it is unambiguous (e.g., a scan with a FLASH acquisition but with no operator defined modality will be assigned a T1w modality suffix, and similarly, one with a TruboRARE acquisition will be assigned a T2w suffix).

Entering metadata in this fashion during scanner operation creates records which can directly serve as input for analysis workflows, and are thus immediately ready for sharing or analysis. Examples for such interpretable metadata scans are available in the SAMRI ParaVision testing data archive, and the example strings specified in this section are sourced from the rat data identified in the archive by the 20171106_184345_21_1_1 directory name.

2.2. Preexisting Data Compliance

Preexisting data sets—acquired with operator metadata input divergent from the recommended guidelines—can also be redressed, via a small number of plain text editing operations. Performing such edits is highly recommended, as it is still easier than manually repositing data in the BIDS standard, and also permits direct ParaVision data sharing, as shown in **Figure 1**.

The relevant parts of a ParaVision scan directory which need to be edited are single lines in the subject and Scanprogram.scanProgram files. Editing the subject identifier in the ParaVision directory name is also advisable, though only for ease of overview—since the subject field is not read from the directory name by the repositing workflow.

Before editing, value names for all available metadata fields must be chosen, such as respect the constraints of the BIDS standard. This means that subject, session, task, and all other desired identifiers need to contain only alphanumeric characters (digits 0 through 9, and lower and uppercase letters). Once all identifiers are properly chosen, they can be replaced or retroactively entered into the ParaVision metadata fields.

The subject file defines both the subject and the session of the scan. To enter the subject identifier, the line *below* the line containing the string ##$SUBJECT_id= must be edited. This following line should contain the subject identifier between greater than and less than characters, e.g., for a subject identified as Mc365A, the line should read <Mc365A>. Analogously, to enter the session identifier, the line *below* the line containing the string ##$SUBJECT_study_name= needs to be edited to read e.g., <R02> for a session identified as R02 within the study, as shown in **Figure 4B**.

The Scanprogram.scanprogram file is used to define other BIDS metadata fields. Within this file, individual lines containing the string ␣(E (with the open box character representing a space) are used both to record the ParaVision "Instruction Name" and to establish correspondence with the respective numbered ParaVision scan directory. On such lines, after the open <displayName> tag, and up to the space character before the open parenthesis, an arbitrary sequence of BIDS short identifiers and value pairs, separated by underscores, can be inserted—as shown in **Figure 4A**.

Examples for manually redressed data are included in the SAMRI ParaVision testing data archive, and are in their end form indistinguishable from data acquired along the lines of the operator recommendations. In **Figure 5**, we show the changes which were required to render mouse lemur testing data compliant with the repositing workflow.

2.3. Package Management

The workflow becomes available upon installation of the SAMRI software package. The dependency list of the package is documented inside the SAMRI repository and version archive (Ioanas et al., 2019b) in accordance with the Package Manager Specification (Bennett et al., 2017). Automatic installation of the entire dependency stack has been made available for package managers conforming to this specification (Ioanas et al., 2017), including the standard package manager of Gentoo Linux and its derivatives (Ioanas et al., 2017). The package design is based on the widely-adopted Python setuptools functionality, and is thus easily accessible to maintainers using further distributions.

3. RESULTS

To demonstrate the capabilities of the workflow, we have compiled a versioned reference archive of multi-species small animal MRI data. The resulting package, samri_bindata

A

```
@@ -3225 +3225 @@
-<displayName>MSME_200um (E6)</displayName>
+<displayName>acq-MSME200um_T2w (E6)</displayName>
@@ -4218 +4218 @@
-<displayName>GE_EPI_sat_mat96_1mm (E7)</displayName>
+<displayName>acq-geEPI_task-rest_bold (E7)</displayName>
```

B

```
@@ -10,2 +10,2 @@
 ##$SUBJECT_id=( 60 )
-<MD1704-Mc285AB-P02>
+<Mc285AB>
@@ -28,2 +28,2 @@
 ##$SUBJECT_study_name=( 64 )
-<MD1704_RsLemurs_Rs02>
+<R02>
```

FIGURE 4 | Editing operations on only up to four lines are required to render preexisting data compatible with repositing via the workflow at hand. Depicted are file differences for the 20171024_165248_MD1704_Mc285AB_P02_1_1 testing dataset scan, in a patch syntax. The line numbers identifying the position of the text segment (before and after editing) are highlighted between arobase characters and in cyan. Deleted and added lines are highlighted in red or green, and prefixed with a minus or plus, respectively. Conserved lines are printed in black. **(A)** A total of two lines need to be edited in the ScanProgram.scanProgram file in order to render acquisition, task, and contrast automatically interpretable. **(B)** A total of two lines need to be edited in the subject file in order to make session and subject information automatically interpretable.

```
/usr/share/samri_bidsdata
├── 20151208_182500_4007_1_4
│   ├── 10
│   ├── 2
│   ├── 3
│   ├── 4
│   ├── 5
│   ├── 7
│   ├── 8
│   ├── 9
│   ├── AdjResult
│   ├── AdjStatePerStudy
│   ├── ResultState
│   ├── ScanProgram.scanProgram
│   └── subject
├── 20170317_203312_5691_1_5
│   ├── 1
│   ├── 2
│   ├── 3
│   ├── 4
│   ├── 5
│   ├── 6
│   ├── 7
│   ├── 8
│   ├── AdjResult
│   ├── AdjStatePerStudy
│   ├── ResultState
│   ├── ScanProgram.scanProgram
│   └── subject
├── 20171024_165248_MD1704_Mc285AB_P02_1_1
│   ├── 5
│   ├── 6
│   ├── 7
│   ├── AdjResult
│   ├── AdjStatePerStudy
│   ├── ResultState
│   ├── ScanProgram.scanProgram
│   └── subject
├── 20171106_184345_21_1_1
│   ├── 1
│   ├── 12
│   ├── 13
│   ├── 16
│   ├── 17
│   ├── 18
│   ├── 22
│   ├── 3
│   ├── 4
│   ├── 6
│   ├── 9
│   ├── AdjResult
│   ├── AdjStatePerStudy
│   ├── ResultState
│   ├── ScanProgram.scanProgram
│   └── subject
└── 20180529_041333_SN9879_1_1
    ├── 1
    ├── 2
    ├── 4
    ├── 5
    ├── 6
    ├── 8
    ├── AdjResult
    ├── AdjStatePerStudy
    ├── ResultState
    ├── ScanProgram.scanProgram
    └── subject
```

```
user@host ~ $ SAMRI bru2bids\
        -o /var/tmp/samri_testing/bash/mouse\
        -f '{"acquisition":["EPI"]}'\
        -s '{"acquisition":["TurboRARE"]}'\
        /usr/share/samri_bindata
```

```
/var/tmp/samri_testing/bash/mouse
└── bids
    ├── dataset_description.json
    └── sub-5691
        ├── ses-ofMpF
        │   ├── anat
        │   │   ├── sub-5691_ses-ofMpF_acq-TurboRARE_T2w.json
        │   │   └── sub-5691_ses-ofMpF_acq-TurboRARE_T2w.nii.gz
        │   └── func
        │       ├── sub-5691_ses-ofMpF_task-CogB_acq-EPI_run-0_bold.json
        │       ├── sub-5691_ses-ofMpF_task-CogB_acq-EPI_run-0_bold.nii.gz
        │       └── sub-5691_ses-ofMpF_task-CogB_acq-EPI_run-0_events.tsv
        └── sub-5691_sessions.tsv
```

```
user@host ~ $ SAMRI bru2bids\
        -o /var/tmp/samri_testing/bash/rat\
        -f '{"acquisition":["seEPI"]}'\
        /usr/share/samri_bindata
```

```
/var/tmp/samri_testing/bash/rat/
└── bids
    ├── dataset_description.json
    └── sub-21
        ├── ses-noFUSr0
        │   └── func
        │       ├── sub-21_ses-noFUSr0_task-MhBu_acq-seEPI_run-1_bold.json
        │       ├── sub-21_ses-noFUSr0_task-MhBu_acq-seEPI_run-1_bold.nii.gz
        │       ├── sub-21_ses-noFUSr0_task-MhBu_acq-seEPI_run-1_events.tsv
        │       ├── sub-21_ses-noFUSr0_task-rest_acq-seEPI_run-0_bold.json
        │       ├── sub-21_ses-noFUSr0_task-rest_acq-seEPI_run-0_bold.nii.gz
        │       └── sub-21_ses-noFUSr0_task-rest_acq-seEPI_run-0_events.tsv
        └── sub-21_sessions.tsv
```

```
user@host ~ $ SAMRI bru2bids\
        -o /var/tmp/samri_testing/bash/lemur\
        -f '{"acquisition":["geEPI"]}'\
        -s '{"acquisition":["MSME200um"]}'\
        /usr/share/samri_bindata
```

```
/var/tmp/samri_testing/bash/lemur/
└── bids
    ├── dataset_description.json
    └── sub-Mc285AB
        ├── ses-R02
        │   ├── anat
        │   │   ├── sub-Mc285AB_ses-R02_acq-MSME200um_T2w.json
        │   │   └── sub-Mc285AB_ses-R02_acq-MSME200um_T2w.nii.gz
        │   └── func
        │       ├── sub-Mc285AB_ses-R02_task-rest_acq-geEPI_run-0_bold.json
        │       ├── sub-Mc285AB_ses-R02_task-rest_acq-geEPI_run-0_bold.nii.gz
        │       └── sub-Mc285AB_ses-R02_task-rest_acq-geEPI_run-0_events.tsv
        └── sub-Mc285AB_sessions.tsv
```

FIGURE 5 | The workflow can automatically select, convert, and reposit ParaVision data from a general collection directory into dedicated shareable data sets, formatted for the BIDS standard. The left column shows the contents of the source directory, analogous to a collection directory on a server or scanner, and packaged by us as `samri_bindata`. The right column contains the Bash commands needed to produce dedicated mouse, rat, and lemur data sets (in that order). Below each Bash command shell, the resulting BIDS directory contents are shown. Directories are highlighted in blue. As ParaVision provides no way of integrating stimulatioin information, the workflow creates empty events files (`*_events.tsv`), which the user can fill with the appropriate stimulation content, delete, or simply ignore (if empty the files carry no meaning in BIDS).

(Ioanas et al., 2019a), includes multi-center ParaVision standard scans from mice, rats, and mouse lemurs, and serves as testing data for the SAMRI package, including the repositing workflow. The data in this archive is based on scans acquired with originally compliant operator input, as well as on preexisting scans rendered compliant *ex post facto*, as detailed in this article.

In **Figure 5**, we test the capability of the workflow to correctly and automatically source specified datasets from a diverse collection, and reposit them in the BIDS standard. The resulting three separate and shareable BIDS data sets pass the BIDS validator with no errors. The commands listed in this section are included in the SAMRI test suite, and monitored for continued quality assurance.

4. METHODS FOR IMPLEMENTATION

The data of our reference ParaVision testing archive, `samri_bindata` (Ioanas et al., 2019a), were acquired at three separate centers, using three different scanner types, and in two rodent species (mouse and rat) and one primate species (mouse lemur)—with ParaVision `6.0.1`. Mouse data were acquired at the Animal Imaging Center of the ETH and University of Zurich, using a Bruker Biospec 70/16 system, or a Bruker Biospec 94/30 system. Rat data were acquired at the Neurotechnology Group of the University of Zurich Neuroinformatics Institute, using a Bruker PharmaScan 70/16 system. Mouse lemur data were acquired at the Molecular Imaging Research Center (MIRCen) of the Commissariat à l'Énergie Atomique et aux Énergies Alternatives (CEA), using a 11.7 Tesla Bruker BioSpec system.

The workflow is implemented as a function in the Python programming language, and uses the Nipype package (Gorgolewski et al., 2011) for workflow execution, overview generation, parallelization, and access to non-Python tools. Bash bindings are auto-generated based on the Python function definition and documentation string by the Argh package.

Data conversion from the ParaVision `2dseq` format to NIfTI is performed by the `Bru2` function from the Bru2Nii package (Rorden and Naveaum, 2018). Preliminary to workflow execution, ParaVision metadata parsing and BIDS metadata assignment is performed by Python utility functions implemented in the SAMRI package. These functions iterate through the lines of the relevant metadata files: `subject` and `ScanProgram.scanProgram`, falling back to `<scan_number>/acqp` if the scan program file is corrupted. Metadata detection is performed via regular expressions, to afford a maximum of flexibility, and avoid dependency on more convoluted higher-level tools.

The processed metadata is recorded in a Pandas Dataframe (McKinney, 2010), which is both used internally and written to disk in the "work directory" to permit debugging. This record is then divided along the lines of the supported scan categories (structural, functional, and diffusion-weighted), and the resulting selections are used to initiate the respective workflow iterations, as seen in **Figure 6**. Following successful

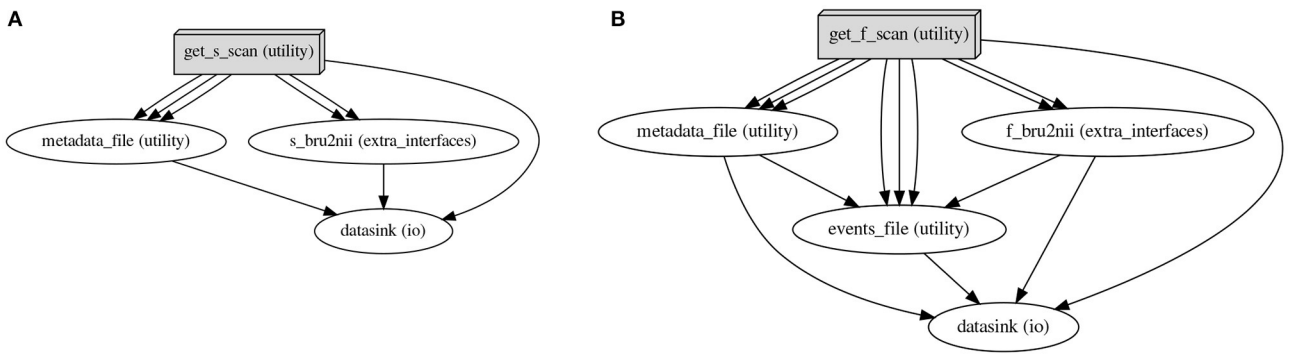

FIGURE 6 | Dedicated workflows are set up for each scan category. Depicted are directed acyclic graphs, as produced by the workflow engine, Nipype. The `bru2bids` function iteratively executes e.g., structural **(A)** and functional **(B)** repositing workflows, contingent on data availability. Node names specify the source code identifiers, with the text in parentheses indicating, which modules they are implemented in: `utility` and `extra_interfaces` are modules of the SAMRI package, and `io` is a module of the Nipype package. **(A)** Structural scan category repositing graph. The `get_s_scan` node queries the base Pandas Dataframe for scan entries selected as structural, and computes data descriptors, which are further piped in the following fashion: (1) the `metadata_file` node, responsible for creating a JSON BIDS metadata file is supplied with (i) a bundled subject and session identifier, (ii) the exact ParaVision scan path including the numbered subdirectory, and (iii) the computed BIDS output metadata file name; (2) the `s_bru2nii` node, responsible for creating a BIDS-named NIfTI data file is supplied with (i) the exact scan path including the numbered subdirectory and (ii) the computed BIDS output file name; (3) the `datasink` node, responsible for creating a BIDS-style directory hierarchy is supplied with a bundled subject and session identifier. **(B)** Functional scan category repositing graph. The `get_f_scan` node queries the base Pandas Dataframe for scan entries selected as functional, and computes data descriptors, which are further piped in the following fashion: (1) the `metadata_file` node, responsible for creating a JSON BIDS metadata file is supplied with (i) a bundled subject and session identifier, (ii) the exact ParaVision scan path including the numbered subdirectory, and (iii) the computed BIDS output metadata file name; (2) the `f_bru2nii` node, responsible for creating a BIDS-named NIfTI data file is supplied with (i) the exact scan path, and (ii) the BIDS output file name; (3) the `events_file` node, responsible for creating a BIDS-style events file is supplied with (i) the exact scan path, (ii) the task identifier, (iii) the BIDS output event file name, (iv) the metadata file (to query delay entries), and (v) the functional file path (to determine the repetition time necessary to perform eventfile adjustments in light of the metadata); (4) the `datasink` node, responsible for creating a BIDS-style directory hierarchy is supplied with a bundled subject and session identifier.

workflow execution, the BIDS standard `*_sessions.tsv` file is separately generated, recording the onset acquisition times for each session.

The guidelines regarding operator input and preexisting data compliance presented in this document are based on the ParaVison `6.x` release series. The parsing functionality of the workflow in the current SAMRI version (`0.4.1`) is based on the ParaVison `6.x` release series and the BIDS `1.x` specification.

5. DISCUSSION

The `bru2bids` workflow presented herein is a significant first step in rendering data in the Bruker ParaVision standard automatically interpretable for high-level analysis pipelines. This is done by repositing the ParaVision data according to the BIDS standard, which offers superior legibility, as well as integration with community analysis tools, specifically with tools adapted from human fMRI. The BIDS reposited data form can serve as a mere intermediary, facilitating data usage with standardized workflows, but can also be used in and of itself as raw data recourse—if data management expediency is prioritized over the larger pool of accessible information in the full ParaVision standard.

To demonstrate and persistently track compliance, we release a versioned archive of Bruker ParaVision testing data, diverse in terms of both animal species and acquisition protocols. We test the performance of the workflow on the dataset, and report compliance with the target standard. These demonstrated capabilities of the workflow are rendered accessible to the community by procedural instructions addressed to Bruker MRI scanner operators. Additional accessibility is conferred by a detailed walk-through, which allows custodians of Bruker ParaVision data to render preexisting records compatible as a workflow input. Further, we describe the general principles of the software implementation, which in conjunction with the documentation internal to the software enable collaborators to inspect, debug, augment, or create derivations based on our work.

The demonstrated performance of this workflow, its position at the transition from the most popular small animal MRI acquisition format into the most popular MRI data sharing format, as well as its transparent free and open source nature, make the SAMRI's `bru2bids` a strong foundation for the rapid and collaborative improvement of fMRI data analysis methodology.

DATA AVAILABILITY STATEMENT

All datasets generated for this study are included in the article/**Supplementary Material**.

ETHICS STATEMENT

Ethical review and approval was not required for the animal study because this study concerns an ex post facto technological method, for which only preexisting animal data was used.

AUTHOR CONTRIBUTIONS

The final submitted form of this document was edited by H-II. The document was drafted by H-II and MM. The text review process encompassed all authors. The software was authored by H-II and MM. Data was acquired by H-II, MM, and CG. Technology access and institutional backing was provided by MR, MY, and MD. Material support, supervision, and computational resources, as required during pipeline development, were offered by MR and MY.

FUNDING

The workflow development work was supported by Swiss National Science Foundation (SNF) (Grant Nos. 310030-160310 and 310030-179257) granted to MR.

SUPPLEMENTARY MATERIAL

The Supplementary Material for this article can be found online at: https://www.frontiersin.org/articles/10.3389/fninf.2020.00005/full#supplementary-material

REFERENCES

Bennett, S. P., Faulhammer, C., McCreesh, C., Müller, U., and Gentoo Linux. (2017). *Package Manager Specification*. Available online at: https://projects.gentoo.org/pms/6/pms.html

Bukhari, Q., Schroeter, A., and Rudin, M. (2018). Increasing isoflurane dose reduces homotopic correlation and functional segregation of brain networks in mice as revealed by resting-state fMRI. *Sci. Rep*. 8:10591. doi: 10.1038/s41598-018-28766-3

Cox, R. W., Ashburner, J., Breman, H., Fissell, K., Haselgrove, C., Holmes, C. J., et al. (2004). "A (sort of) new image data format Standard: NIfTI-1," in *OHBM* (Budapest, HU).

Ferraris, S., Shakir, D. I., Merwe, J. V. D., Gsell, W., Deprest, J., and Vercauteren, T. (2017). Bruker2nifti: Magnetic Resonance Images converter from Bruker ParaVision to NIfTI format. *J. Open Source Softw*. 2:354. doi: 10.21105/joss.00354

Gorgolewski, K., Burns, C. D., Madison, A., Clark, D., Halchenko, Y. O., Waskom, M. L., et al. (2011). Nipype: a flexible, lightweight and extensible neuroimaging data processing framework in Python. *Front. Neuroinform*. 5. Available from: http://dx.doi.org/10.3389/fninf.2011.00013

Gorgolewski, K. J., Auer, T., Calhoun, V. D., Craddock, R. C., Das, S., Duff. E. P., et al. (2016). The brain imaging data structure, a format for organizing and describing outputs of neuroimaging experiments. *Sci. Data* 3:160044. doi: 10.1038/sdata.2016.44

Grandjean, J., Canella, C., Anckaerts, C., Ayrancı, G., Bougacha, S., Bienert, T., et al. (2019). *Common Functional Networks in the Mouse Brain Revealed by Multi-Centre Resting-State fMRI Analysis*. Available online at: https://doi.org/10.1101/541060

Hunt, J. W., and MacIlroy, M. D. (1976). *An Algorithm for Differential File Comparison*. Available online at: http://www.cs.dartmouth.edu/~doug/diff.pdf

Ioanas, H. I., Marks, M., Garin, C. M., Dhenain, M., Yanik, M. F., and Rudin, M. (2019a). *ParaVision Mouse, Rat, and Lemur Testing Data for SAMRI*. Available online at: https://doi.org/10.5281/zenodo.3234924

Ioanas, H. I., Marks, M., Segessemann, T., Schmidt, D., Aymanns, F., and Rudin, M. (2019b). *SAMRI—Small Animal Magnetic Resonance Imaging*. Available online at: https://doi.org/10.5281/zenodo.3566868

Ioanas, H. I., Marks, M., Yanik, M. F., and Rudin, M. (2019c). An optimized registration workflow and standard geometric space for small animal brain imaging. *bioRxiv*.

Ioanas, H. I., Saab, B., and Rudin, M. (2017). Gentoo Linux for Neuroscience — a replicable, flexible, scalable, rolling-release environment that provides direct access to development software. *Res. Ideas Outcomes.* 3:e12095. doi: 10.3897/rio.3.e12095

McKinney, W. (2010) "Data structures for statistical computing in Python," in *Proceedings of the 9th Python in Science Conference*, eds S. van der Walt and J. Millman (Austin, TX), 51–56.

Rorden, C., and Naveaum M. (2018). *Bruker ParaVision to NIfTI Conversion*. Available online at: https://web.archive.org/web/20180611113306; https://github.com/neurolabusc/Bru2Nii

Schlegel, F., Schroeter, A., and Rudin, M. (2015). The hemodynamic response to somatosensory stimulation in mice depends on the anesthetic used: implications on analysis of mouse fMRI data. *Neuroimage* 116, 40–49. doi: 10.1016/j.neuroimage.2015.05.013

Schroeter, A., Grandjean, J., Schlegel, F., Saab, B. J., and Rudin, M. (2016). Contributions of structural connectivity and cerebrovascular parameters to functional magnetic resonance imaging signals in mice at rest and during sensory paw stimulation. *J. Cereb. Blood Flow Metab*. 37, 2368–2382. doi: 10.1177/0271678x16666292

Conflict of Interest: The authors declare that the research was conducted in the absence of any commercial or financial relationships that could be construed as a potential conflict of interest.

frontiers in Neuroinformatics

ORIGINAL RESEARCH
published: 19 May 2020
doi: 10.3389/fninf.2020.00022

A Multicenter Preclinical MRI Study: Definition of Rat Brain Relaxometry Reference Maps

*Tristan Deruelle[1], Frank Kober[2], Adriana Perles-Barbacaru[2], Thierry Delzescaux[3], Vincent Noblet[4], Emmanuel L. Barbier[1] and Michel Dojat[1]**

[1] INSERM, U1216, Grenoble Institut des Neurosciences, Université Grenoble Alpes, Grenoble, France, [2] CNRS, CRMBM, Aix-Marseille Université, Marseille, France, [3] UMR-9199, CNRS, CEA-MIRCen, Paris Saclay, Fontenay-aux-Roses, France, [4] CNRS, ICube – IMAGeS, Strasbourg University, Strasbourg, France

Similarly to human population imaging, there are several well-founded motivations for animal population imaging, the most notable being the improvement of the validity of statistical results by pooling a sufficient number of animal data provided by different imaging centers. In this paper, we demonstrate the feasibility of such a multicenter animal study, sharing raw data from forty rats and processing pipelines between four imaging centers. As specific use case, we focused on T1 and T2 mapping of the healthy rat brain at 7T. We quantitatively report about the variability observed across two MR data providers and evaluate the influence of image processing steps on the final maps, using three fitting algorithms from three centers. Finally, to derive relaxation times from different brain areas, two multi-atlas segmentation pipelines from different centers were performed on two different platforms. Differences between the two data providers were 2.21% for T1 and 9.52% for T2. Differences between processing pipelines were 1.04% for T1 and 3.33% for T2. These maps, obtained in healthy conditions, may be used in the future as reference when exploring alterations in animal models of pathology.

Keywords: MRI, brain imaging, rat, quantitative imaging, digital atlas

OPEN ACCESS

Edited by:
David A. Gutman, Emory University, United States

Reviewed by:
Frithjof Kruggel, University of California, Irvine, United States
Benjamin Marty, Sorbonne Université, France

****Correspondence:***
Michel Dojat
Michel.Dojat@inserm.fr

Received: *29 May 2019*
Accepted: *21 April 2020*
Published: *19 May 2020*

Citation:
Deruelle T, Kober F, Perles-Barbacaru A, Delzescaux T, Noblet V, Barbier EL and Dojat M (2020) A Multicenter Preclinical MRI Study: Definition of Rat Brain Relaxometry Reference Maps. Front. Neuroinform. 14:22. doi: 10.3389/fninf.2020.00022

INTRODUCTION

In the clinical domain, multicenter studies are common. Their main objective is to gather data from a sufficient number of patients in a reasonable period of time to improve the statistical power and consequently the robustness of the reported results. Multicenter studies also set the basis for developing and validating quantitative and reproducible imaging biomarkers. Similarly, there are several well-founded motivations for animal population imaging: optimization of costs, reduction of experimentation duration, and improvement of quality of science, notably by the use of sufficiently large animal cohorts for ensuring the validity of statistical results [see the special Lab Animal focus on reproducibility in animal research (Prescott and Lidster, 2017)]. This domain is still in its infancy, and we may expect it to develop in the near future. Consequently, only few tools are available to facilitate preclinical data pooling. Moreover, there is a clear lack of large actions for standardization of image acquisition conditions and post-processing techniques. Finally, there are no reliable commonly adopted preclinical imaging biomarkers for differentiating normal vs. pathological conditions. The aim of the present work was to assess the feasibility of multicenter

preclinical studies in order to define robust biomarkers. We thus considered a specific use case: quantitative T1 and T2 mapping of the healthy rat brain at 7T.

The T1 and T2 relaxation times are tissue- and region-dependent. As they may reflect micro-anatomical alterations, they are biomarkers for various pathologies (Deoni, 2010). To map these relaxation times, series of weighted images are acquired with varying acquisition parameters such as echo time (TE), inversion time (TI) or flip angle. Voxel-per-voxel fitting of a model equation (with generally two or three parameters) to these series is then used to calculate relaxation time maps (Guilfoyle et al., 2003; de Graaf et al., 2006; Wright et al., 2008). Alternatively, newer fingerprinting methods based on the use of dictionaries currently emerge (Gao et al., 2015). A large number of monocentric studies measured T1 and T2 in rodents, at different magnetic fields and using different acquisition protocols. They show that T1 relaxation time increases with magnetic field while T2 relaxation time decreases (de Graaf et al., 2006; van de Ven et al., 2007; Wright et al., 2008). Some studies also reported regional values (Cremillieux et al., 1998; Barbier et al., 2005; Del Bigio et al., 2011; Gigliucci et al., 2014; Suleymanova et al., 2014; Koundal et al., 2015; Liachenko and Ramu, 2017; Behroozi et al., 2018), but no consensus has been reached yet about values of reference for specific rat brain regions. To define such reference maps, a large number of brain structures or regions should be considered and a sufficient number of animals should be included to reflect inter-individual variability. In this context, a multicenter study is relevant.

For Human studies, to facilitate data storage, data sharing and data processing with specific pipelines, several infrastructures have been proposed such as COINS (Landis et al., 2016), LORIS + BRAIN (Das et al., 2016) or LONI (Rex et al., 2003) for Neuroimaging multicenter studies [see recent works in this field (Dojat et al., 2017)]. These infrastructures support the "Open Science" approach, an international action to improve the use of resources, to ease study replication, and to strengthen the validity of scientific results (NAP, 2018). This promotes studies on very large cohorts (e.g., Adhikari et al., 2019), the development of reference databases [see for Alzheimer disease (Li et al., 2017), Parkinson disease (Chahine et al., 2018) or Human connectome project (Hodge et al., 2016)] and fair and robust comparison of image processing solutions (Commowick et al., 2018). Here, we propose to use an extension of the SHAring NeurOImaging Resources environment (Barillot et al., 2016) for storing preclinical imaging data (Small Animal Shanoir, SAS)[1] in conjunction with the VIP[2] architecture, a platform dedicated to the execution of image processing pipelines (Glatard et al., 2013). We quantitatively report about the variability observed across two data provider centers and evaluate different image processing pipelines. We finally discuss the feasibility of small animal population studies. To promote data sharing in the preclinical domain, raw and processed datasets as well as processing pipelines have been made available (see section "Discussion").

MATERIALS AND METHODS

Distribution of Tasks Between Centers

Two centers, GIN (C1) and CRMBM (C2) hosted the animals and performed brain MRI acquisitions. Three centers C2, MIRCen (C3) and ICube (C4) provided processing pipelines.

Animals

Twenty Sprague Dawley rats (male, Janvier Labs, Paris France, mean weight 279 ± 40 g [(min: 249.5 g, max: 314 g), details in **Supplementary Table S1**] were scanned in two imaging centers (C1 and C2). Animals were anesthetized with isoflurane [2% in air at C2 and 2% in a mixture of Air and O_2 (7:3) at C1] that was delivered via a nose cone during the experiment. Animals were positioned in prone position on an animal bed (Bruker Biospin, Ettlingen, Germany). Breath rate was monitored using a pneumatic pillow sensor placed under the abdomen. Body temperature was measured with a rectal probe and maintained in the normal range at 36.2 ± 1.4°C using a heated blanket. To control acquisition reproducibility, three rats were scanned twice, one rat (Subject 32, S32) at C2 at a 2-day interval and two rats (Subject 21, S21 and Subject 22, S22) at C1 at a 3-day interval. All experiments were approved by the local ethics committee of each center and were in full compliance with the guidelines of the European Union (EUVD 86/609/EEC) for the care and use of the laboratory animals. Experiments were performed under permits from the French Ministry of Agriculture (n° 380945 and A3851610008 for experimental and animal care facilities for C1 and G130555 for C2).

MRI Protocol

Acquisitions were performed on 7T horizontal Bruker scanners using the same MR sequences and parameters at data provider centers C1 and C2 (aC1 and aC2, respectively, see details in **Table 1**). Preliminary *in vitro* experiments were performed at C1 and C2 in order to select the best sequences to use, with the objective to minimize acquisition time and geometric artifacts, and to maximize spatial resolution. A 3D MDEFT sequence (with Inversion Preparation as MPRAGE) was chosen for T1 mapping (REF)[3]. Multi-Slice Multi-Echo (MSME) was chosen for T2 mapping. For T1 mapping, the MPRAGE sequence was run seven times with incremental inversion times (TI) and for T2 mapping, a 3D MSME sequence with 28 echo times (TE) was used (DiFrancesco et al., 2008; Liu et al., 2011). Main sequence parameters are shown in **Table 1**. Total experiment duration per animal was about 2 h.

Data Processing and Analysis

Figure 1 illustrates the complete image processing workflow. Several preprocessing steps were performed using SPM12[4] and MATLAB R2015a. Briefly, Bruker files were first converted into NIFTI images using home-made software. All anatomical images were rigidly realigned on a study-specific rat template.

[1] https://shanoir-ng-dev.irisa.fr/

[2] https://www.creatis.insa-lyon.fr/vip/

[3] https://www.ncbi.nlm.nih.gov/pmc/articles/PMC3085577/

[4] http://www.fil.ion.ucl.ac.uk/spm

TABLE 1 | Equipment characteristics, Fitting and Segmentation methods. In the model equations, A, B, T1 and T2 are the parameters to be estimated.

Acquisition	**GIN (aC1)**	**CRMBM (aC2)**
Scanner model	Bruker BioSpin MRI GmbH – Biospec 70/20 7.0T	Bruker BioSpin MRI GmbH – Pharmascan B-C 70/16US 7.0T
Transmitting coil	Linear Volumetric Coil 72 mm	Quadrature Resonator 72 mm
Receiving coil	Rat Head Coil (Surface) 1 channel	GIN coil
Gradient system	BGA12S2 (110 mm, max 660 mT/m, slew rate 4570 T/m/s)	BGA 9SHP (90 mm, max 750 mT/m, slew rate 6840 T/m/s)
T1 mapping	MPRAGE sequence; TI = 247, 408, 674, 1112, 1838, 3030, and 5000 ms; TR = 6500 ms	
T2 mapping	3D MSME; TE = (8:224 ms); TR = 600 ms	
	FOV: 2.7 cm × 2.7 cm × 2.8 cm, matrix size: 128 × 128 × 66, spatial resolution: 211 μm × 211 μm × 424 μm	

Fitting	**GIN (fC1)**	**CRMBM (fC2)**	**MIRCen (fC3)**
Software	MATLAB R2015a	ImageJ v1.51	BrainVISA/Python
Equation T1	$y = \left\lvert A.\left(1 - 2B.\exp\left(-\frac{TI}{T1}\right)\right)\right\rvert$	$y = \left\lvert A.\left(1 - 2B.\exp\left(-\frac{TI}{T1}\right)\right)\right\rvert$	$y = \left\lvert A.\left(1 - 2B.\exp\left(-\frac{TI}{T1}\right)\right)\right\rvert$
Equation T2	$y = \left\lvert A.\exp\left(-\frac{TE}{T2}\right)\right\rvert$	$y = \left\lvert A.\exp\left(-\frac{TE}{T2}\right)\right\rvert$	$y = \left\lvert A.\exp\left(-\frac{TE}{T2}\right)\right\rvert$

Segmentation	**ICube (sC4)**	**MIRCEN (sC3)**
Brain masking	Matlab/spm12	
Bias field correction	N4	
Registration	Non-rigid [ANTS (Avants et al., 2010)]	Rigid + Block-Matching affine (Lebenberg et al., 2010)
Number of atlases	11	12
Probability rule	Majority voting	

See text for details.

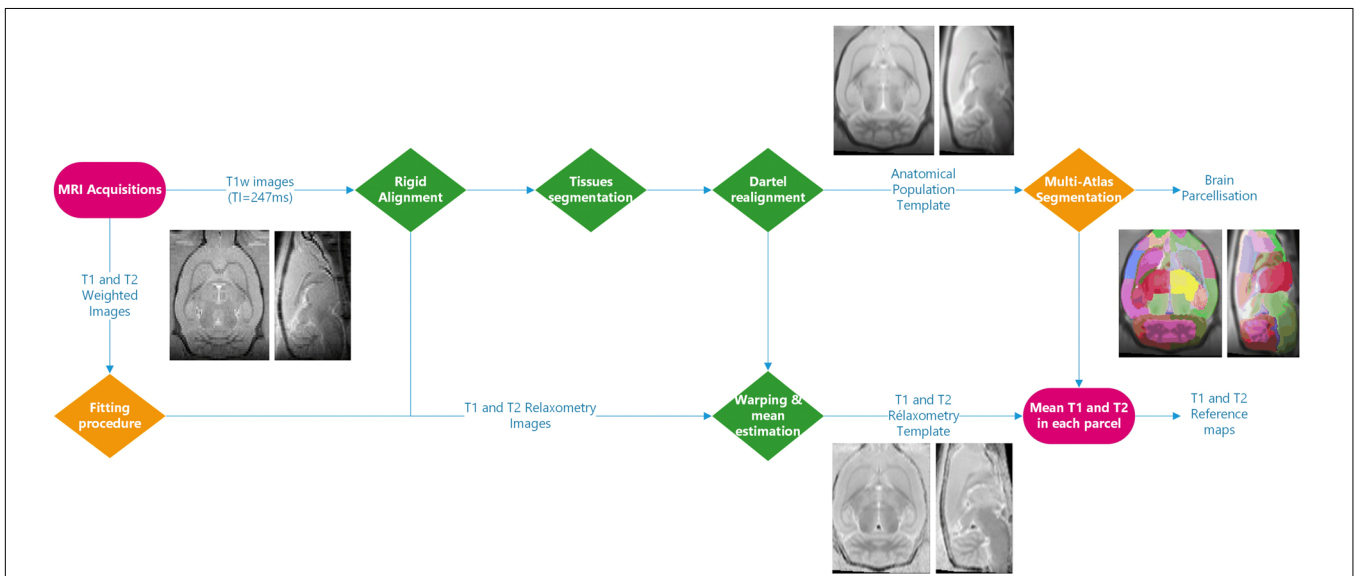

FIGURE 1 | Processing workflow: the processing steps performed using SPM12 are shown in green. Three different fitting procedures and two implementations of the multi-atlas segmentation method were introduced. The inserted MR images are representative of the imaging processing outputs.

Tissue segmentation was performed for each animal (Ashburner and Friston, 2005) based on our study-specific, tissue prior, template. Using the Dartel registration algorithm (Ashburner, 2007) adapted to rat images, these tissue images were non-rigidly registered.

The individual deformation field was then applied to the corresponding individual anatomical and relaxometry images, and all these images were averaged to compute anatomical and relaxometry mean templates. Additionally, T1 and T2 weighted raw images were separately processed using three different fitting pipelines. The differences between these pipelines developed at C1, C2, and C3 (fC1, fC2 and fC3, respectively), are summarized in **Table 1**. All algorithms performed non-linear pixel-per-pixel fitting for each voxel independently. Negative values and values greater than 3000 ms for T1 and 300 ms for T2 were discarded. The optimization algorithm was Levenberg-Marquardt for fC1

and fC3 and the Simplex algorithm provided with ImageJ for fC2 (Nelder and Mead, 1965). The three T2 estimation procedures rely on the same model equations.

Rat brain parcelation was performed using two multi-atlas approaches similar to the one proposed by Lancelot et al. (2014), for a precise and reproducible delineation of brain structures in preclinical *in vivo* imaging. A maximum probability automatic delineation was obtained by the fusion of several manually delineated images placed in a common space and constituting the multi-atlas dataset. This dataset was registered to the native space of the MR image to segment. At each voxel, the most likely label in the dataset was selected by a maximum probability rule. Two versions of this approach were implemented and executed, one at C3 (sC3) using BrainVISA[5] and one at C4 (sC4) using VIP (Glatard et al., 2013), which differ in some aspects as detailed in **Table 1**. Twenty-nine brain regions were defined (see **Figure 2**). MR data initially stored in the SAS database were automatically sent to the VIP processing platform and processed results were seamlessly stored [see more details and the Figure 8 in Commowick et al. (2018) for database and computing platform integration with Shanoir].

The twelve pipelines combining data acquisition (aC1 and aC2), fitting (fC1, fC2, and fC3) and segmentation (sC3 and sC4) were compared. The processing pipelines and data are available on request (see section "Discussion"). Statistical analysis was performed with MS Excel 2010 and Real Statistics[6]. Because most of the samples did not present a normal distribution (Shapiro–Wilk test), non-parametric tests were performed.

RESULTS

Inter-Subject Data Variability

For each individually segmented rat brain, we computed the mean T1 and T2 values for the 29 regions (13 in each hemisphere and 3 non-lateralized regions). **Figure 2** shows these values for each region of the left hemisphere and for each rat, computed using the fC1 fitting pipeline and the sC4 multi-atlas segmentation.

We note that for both T1 and T2 values, the largest dispersion is for the ventricles (lateral, 3rd and 4th ventricles). On average, the differences between the minimum and maximum values of each region are 170 ms for T1 and 11 ms for T2 (left hemisphere regions, excluding ventricles). We obtained similar results for the right hemisphere (169 and 9.3 ms, respectively) and with the other pipelines (e.g., **Supplementary Figure S1** for an example using the fC2 fitting pipeline and the sC3 multi-atlas).

Inter-Center Acquisition Reproducibility

We studied the differences between T1 and T2 values computed from data acquired at aC1 and aC2 using the same pipelines. Between the two centers, the differences (see **Supplementary Figure S2**) were significant for T2 (Mann–Whitney test $p < 2\ 10^{-4}$, with 9% mean error), but not for T1 (Mann–Whitney test $p = 0.02$, with 2% mean error).

Control of Intra-Center Acquisition Reproducibility

We studied the scan-rescan differences for each subject (see **Supplementary Figure S3**). The differences were less than two standard deviations in all ROIs of all subjects, except in the left lateral ventricle (S32), the right olfactory bulb (S21) and the 3rd and 4th ventricles (S22). For T2, large differences were found in the left lateral ventricle (S32), and in the 3rd and 4th ventricles (S21 and S22). A Wilcoxon statistical test was run to compare the results between the first and second MR acquisition for T1 and T2, for each rat, and for different pipeline combinations. Differences were not statistically significant. The parameters of the linear regression between the results from the scan-rescan experiment for each subject were close to the identity curve with a R2 coefficient for T1 equal to (0.89, 0.89, and 0,94) and for T2 (0.88, 0.97, and 0.99) for rats S32, S32, and S22, respectively.

Fitting Pipeline Comparison

To compare results obtained with the three fitting pipelines, regressions were computed and indicated good consistency (see **Figure 3**, Top). The linear regression parameters were $y = 0.99x + 5.11$ ($R^2 = 0.99$) for T1 (C2f) vs. T1 (C1f), $y = 0.92x + 111.9$ ($R^2 = 0.98$) for T1 (C3f) vs. T1 (C1f), and $y = 0.93x + 101.94$ ($R^2 = 0.99$) for T1 (C3f) vs. T1 (C2f).

Similar results were obtained for T2 (see **Supplementary Figure S4**) and using two different segmentation pipelines (see **Supplementary Figure S4**). A Wilcoxon statistical test was run for each pair of pipelines. Differences were not statistically significant (mean error to identity for T2: 3.33%, for T1 1.04%).

Segmentation Pipeline Comparison

To compare results obtained using the two segmentation pipelines, regressions were computed. As for the fitting pipelines, **Figure 3** (bottom) shows a good concordance between the methods. The linear regression parameters were $y = 1.012x\text{-}16.92$ ($R^2 = 0.99$) for T1 (C3s) vs. T1 (C4s) and $y = 1.0583x\text{-}2.9489$ ($R^2 = 0.99$) for T2 (C3s) vs. T2 (C4s).

P-values obtained with a Wilcoxon test were 0.823 and 0.994 for T1 and T2, respectively. These values were obtained via the two implementations of the same multi-atlas segmentation method (mean error to identity of 0.24% for T1 and 0.81% for T2). Similar results were obtained when using the two other fitting methods (e.g., **Supplementary Figure S4** for fC2).

Comparison With Literature

Figure 4 shows the T1 and T2 values obtained in this study and those reported in literature. When literature only reported one cortical ROI, that value was replicated for all cortical ROIs of this study.

[5]http://brainvisa.info/

[6]Real Statistics Resource Pack software (Release 5.4). Copyright (2013 – 2018) Charles Zaiontz. www.real-statistics.com

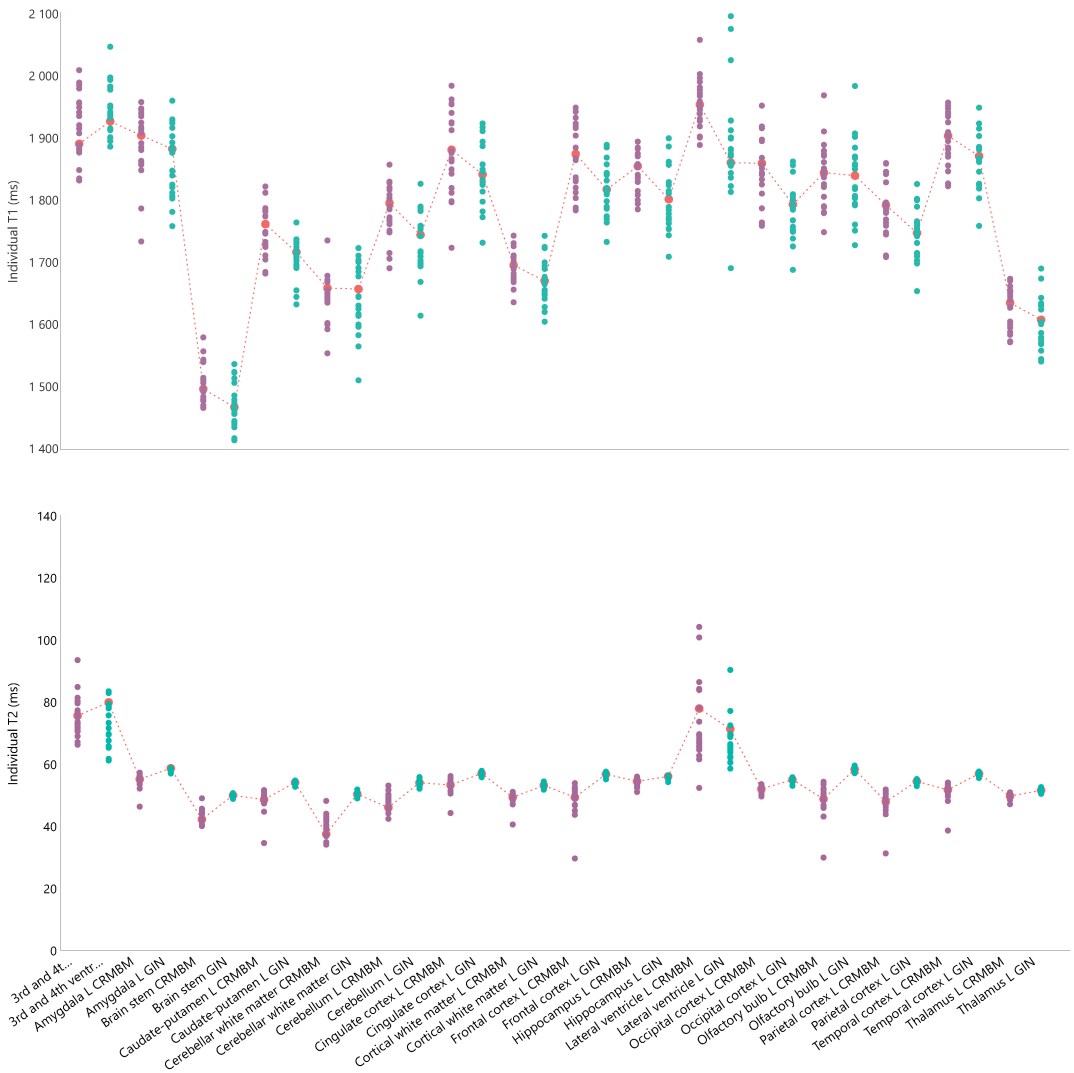

FIGURE 2 | Individual relaxation times for 16 regions of interest for the left hemisphere including 3 regions overlappping the two hemispheres. **Top:** Individual T1 values. **Bottom:** Individual T2 values. Green circles for aC1 values; purple circles for aC2 values and corresponding mean values indicated with a red mark and dash-line. The fC1 fitting pipeline and the sC4 multi-atlas segmentation were used.

DISCUSSION

In this study, we report a multicenter T1 and T2 mapping of the rat brain at 7 Tesla. Four centers were involved: two contributed to data acquisition, and two centers provided two multi-atlas segmentation pipelines to derive relaxation times per brain region. To facilitate the pooling of the preclinical MR datasets, we used the SHAring NeurOImaging Resources (Shanoir) environment, initially developed for the web-oriented management of collaborative neuroimaging projects in Humans, and recently extended for preclinical studies (Small Animal Shanoir, SAS).

Data Pooling

We successfully combined MR data acquired on forty rats in two different centers. We took advantage of the fact that the fleet of MR scanners for preclinical studies tends to be more uniform across labs than Human imaging systems. Indeed, the MR scanners in both centers were from the same manufacturer (Bruker Biospin) and, as indicated in **Table 1**, there were very few differences between the two systems. The acquisition sequence parameters could thus be set identical in both centers. Consequently, **Figure 3** shows a small dispersion of individual T1 and T2 values in brain regions, except for the ventricles (lateral and 3rd and 4th ventricles). Moreover, we noted a good intra-center reproducibility for T1 and T2 values obtained on three rats. There was no significant difference in the scan-rescan experiment of each rat. Good reproducibility was also obtained when using different processing solutions (**Supplementary Figure S3**). The observed differences for ventricles could be a consequence of the small number of voxels of these structures compared to other regions (3500 and around 11000 voxels for lateral and 3rd and

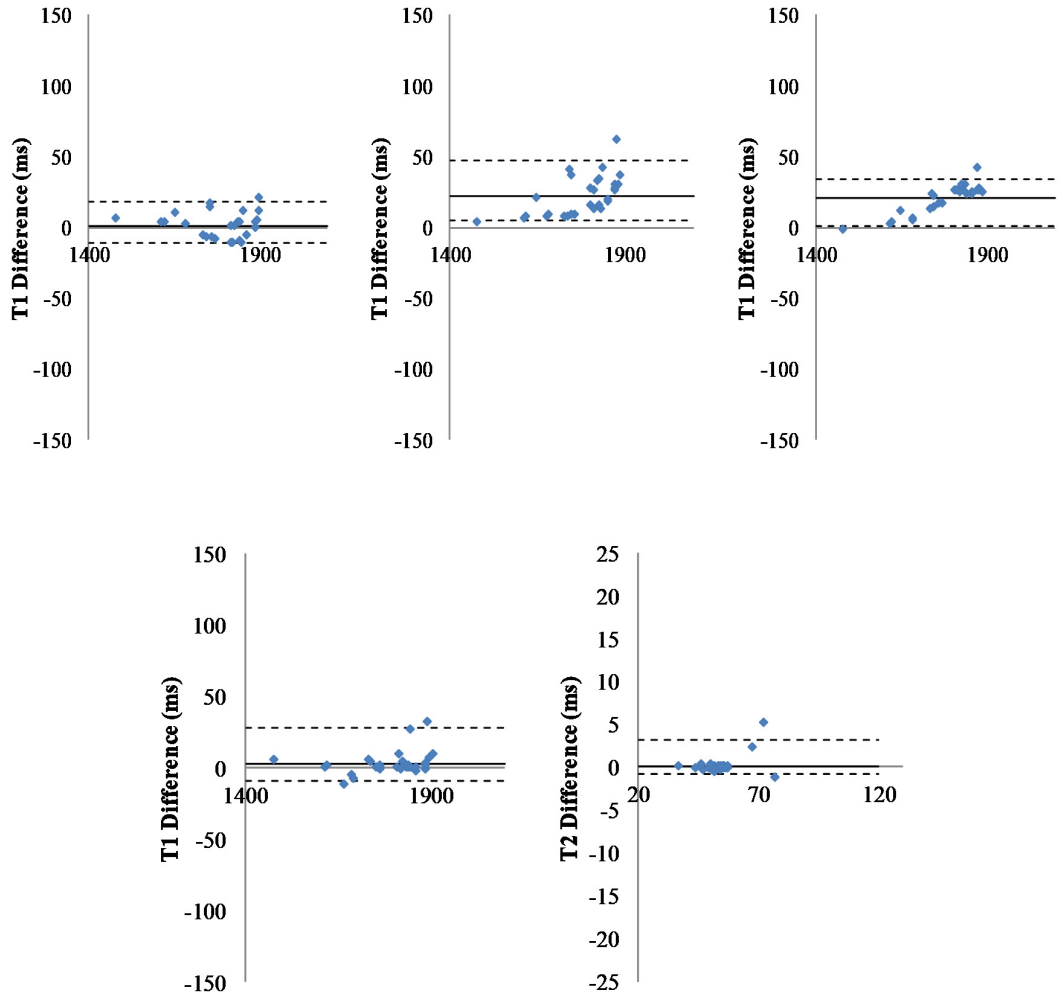

FIGURE 3 | Comparison of pipelines. **Top:** Fitting pipelines. Bland-Altman representation of difference between T1 relaxation times for all regions of interest (n = 29), averaged across all animals (n = 40) and obtained with three different fitting pipelines. Left: T1 differences for fC1 minus fC2; Middle: T1 differences for fC1 minus fC3; Right: T1 differences for fC2 minus fC3. The sC4 was used for segmentation. Solid line: Mean difference. Dash-lines: ± two standard deviations. **Bottom:** Segmentation pipelines: Bland-Altman graph of the T1 (left) and T2 (right) differences measured for all regions of interest (n = 29), averaged all animals (n = 40) and obtained with two different segmentation pipelines (one point per region of interest). The fC1 fitting pipeline was used. Solid line: mean difference. Dash-lines: ± two standard deviations.

4th ventricles, respectively, versus 33000 voxels on average for the other structures) and to the large differences in relaxation times between brain tissue and cerebrospinal fluid. Moreover, in T1-weighted images, the contrast between ventricles and tissue was low. This made the registration process more prone to errors. Also, small movements of the cerebrospinal fluid in the ventricles during acquisition may lead to a biased estimation of relaxation times in these regions, especially for T2, which exhibits the largest difference between tissue and ventricles. Moreover, for some rats (n = 3), ventricles were found dilated. Such dilation may impact the global results. T1 values computed from data acquired at C1 or C2 using different fitting and segmentation pipelines were not different (see **Supplementary Figure S4**), except for fC3 fitting algorithm ($p < 0.01$). T2 differences were significantly different for all conditions. We cannot rule out a potential effect of the anesthesia conditions, since the gas mixture was slightly different between the two centers (2% in air at C2 vs. 2% in a mixture of Air and O_2 (7:3). However, no T2 differences were found in an additional experiment in which the effect of breathing air or 100% O_2 as carrier gas was tested. Another potential source of T2 difference between C1 and C2 may be that despite standard spoiling settings in the sequence, the T2 measurements may be affected by the presence of residual stimulated echo signal. Given the different transmit coils (single-channel for C1 and quadrature for C2), these signals may differ between C1 and C2 and account for differences found in T2 values.

Finally, we note that, in literature, T2 values generally seem more variable between centers than T1 values (see **Figure 4**). After examining multicenter data quality, we searched for possible differences when processing data with software developed in different centers.

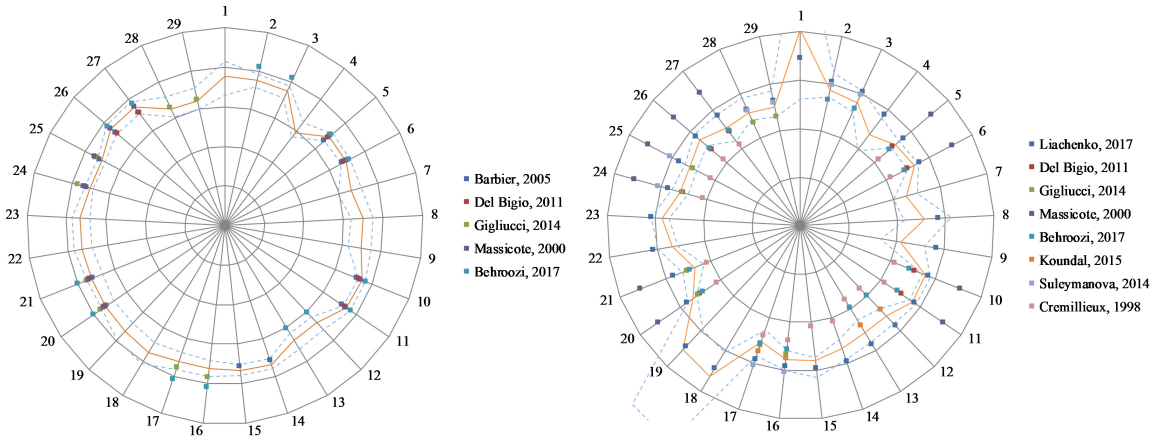

FIGURE 4 | Relaxation values for this study and five published studies (see References list for details) in 29 regions of interest. **Left:** T1 relaxation values. Scale: 500 ms/division. **Right:** T2 relaxation. Scale: 15 ms/division. The orange line indicates results from this study. Dash lines indicate ± one standard deviation from our results. 1: 3rd and 4th ventricles, 2: Amygdala L, 3: Amygdala R, 4: Brain stem, 5: Caudate-putamen L, 6: Caudate-putamen R, 7: Cerebellar white matter, 8: Cerebellum L, 9: Cerebellum R, 10: Cingulate cortex L, 11: Cingulate cortex R, 12: Cortical white matter L, 13: Cortical white matter R, 14: Frontal cortex L, 15: Frontal cortex R, 16: Hippocampus L, 17: Hippocampus R, 18: Lateral ventricle L, 19: Lateral ventricle R, 20: Occipital cortex L, 21: Occipital cortex R, 22: Olfactory bulb L, 23: Olfactory bulb R, 24: Parietal cortex L, 25: Parietal cortex R, 26: Temporal cortex L, 27: Temporal cortex R, 28: Thalamus L, 29: Thalamus R.

Image Processing Pipeline Comparison

The goal of this comparison was to explore whether data processing could be distributed to different centers using the solution locally developed rather than benchmarking them for selecting the best one. For relaxometry mapping, two main steps are required: fitting the raw data to extract relaxation times and segmenting the brain to compute mean values per brain area. Fitting data is clearly a simple mathematical operation. No consensus currently exists for this operation, and, as indicated in **Table 1**, differences exist in available solutions hosted in our three centers. Advantageously, the differences in fitting equation and in optimization methods did not impact the final results, neither for T1 nor for T2. Note that differences generated by the use of different fitting parameters were lower than those between the data acquisition centers and even those between data acquired at the same center.

For brain segmentation, we adopted a multi-atlas procedure. Multi-atlas techniques outperform single atlas approaches in accounting for individual structural variability (Wang et al., 2014). Here, we considered two implementations on two different platforms, BrainVISA and VIP, of the multi-atlas approach proposed in Lancelot et al. (2014) for rats. As mentioned in **Table 1**, some preprocessing steps differ: the registration [ANTS (Avants et al., 2010) vs. block-matching combined to Free Form Deformation (Lebenberg et al., 2010)] and the number of atlases used (11 vs. 12). Comparison of the parcelations obtained using the two methods revealed no differences in terms of parcel volume and DICE score. DICE were higher than 0.8 but for ventricles (see **Supplementary Figure S5**), suggesting and excellent overlap between parcelations. Differences were not significant when comparing T1 and T2 values obtained with the two multi-atlas segmentation procedures.

Reference Maps

Publicly available quantitative reference maps for longitudinal (T1) and transverse (T2) relaxation times are valuable for investigating and monitoring deviations from normality in animal models of pathologies. Both T1 and T2 values have been reported in literature based on a limited number of animals. We extended these works by using a larger number of animals (n = 40) and by providing values in additional regions. **Figure 4** shows the T1 and T2 values obtained in this study together with literature values. There is a good agreement between all T1 values. This is consistent with the low dispersion found between the two data providers (2%). The dispersion of literature values is larger for T2, especially when older studies are included. Similarly, we found a larger 9.5% dispersion between T2 values from our two data providers. Altogether, the values reported in this study are in good agreement with several recent publications (Del Bigio et al., 2011; Gigliucci et al., 2014; Suleymanova et al., 2014; Koundal et al., 2015; Liachenko and Ramu, 2017).

Limitations

Data came from only two providers running similar MR systems from the same manufacturer. This is, however, very common in the preclinical imaging community. Data were acquired in only one animal strain (Sprague Dawley) and at one age (young adult). These two factors may indeed modify relaxation times (Knight et al., 2016; Liu et al., 2018). Additional changes in values may also occur in case of physiological changes (perfusion, oxygenation, temperature). In addition, our reference maps could be refined by including even more individuals and data could be reanalyzed to further limit the impact of stimulated echoes in T2 estimates, a potential source of bias. However, data acquired and processed with the same methods as those used in the study would remain comparable to the reference maps available from this study.

DATA AVAILABILITY STATEMENT

Raw data and reference T1 and T2 relaxometry maps, as well as processing pipelines are freely available on request from the corresponding author MD. Please refer to the present paper in case of the reuse of these datasets and pipelines.

ETHICS STATEMENT

The animal study was reviewed and approved by the French Ministry of Agriculture (nos. 380945 and A3851610008 for experimental and animal care facilities for C1 and G130555 for C2).

AUTHOR CONTRIBUTIONS

TrD, FK, ThD, VN, EB, and MD contributed to the conception and design of the study and performed the data analysis. TrD, FK, EB, and MD acquired the data. TrD organized the database and pipelines. TrD and MD wrote the first draft of the manuscript. All authors contributed to the manuscript revision, read, and approved the submitted version.

FUNDING

This work and IRMaGe MR facility are partly funded by the French program "Investissement d'Avenir" run by the Agence Nationale de la Recherche (ANR-11-INBS-0006).

ACKNOWLEDGMENTS

The authors thank the technical staff of VIP (https://www.creatis.insa-lyon.fr/vip/), for their support for the multi-atlas segmentation algorithm portage, and the FLI-IAM team (https://portal.fli-iam.irisa.fr/preclinical_imaging_studies) for data management support.

SUPPLEMENTARY MATERIAL

The Supplementary Material for this article can be found online at: https://www.frontiersin.org/articles/10.3389/fninf.2020.00022/full#supplementary-material

REFERENCES

Adhikari, B. M., Jahanshad, N., Shukla, D., Turner, J., Grotegerd, D., Dannlowski, U., et al. (2019). A resting state fMRI analysis pipeline for pooling inference across diverse cohorts: an ENIGMA rs-fMRI protocol. *Brain Imaging Behav.* 13, 1453–1467. doi: 10.1007/s11682-018-9941-x

Ashburner, J. (2007). A fast diffeomorphic image registration algorithm. *Neuroimage* 38, 95–113. doi: 10.1016/j.neuroimage.2007.07.007

Ashburner, J., and Friston, K. J. (2005). Unified segmentation. *Neuroimage* 26, 839–851. doi: 10.1016/j.neuroimage.2005.02.018

Avants, B. B., Yushkevich, P., Pluta, J., Minkoff, D., Korczykowski, M., Detre, J., et al. (2010). The optimal template effect in hippocampus studies of diseased populations. *Neuroimage* 49, 2457–2466. doi: 10.1016/j.neuroimage.2009.09.062

Barbier, E. L., Liu, L., Grillon, E., Payen, J. F., Lebas, J. F., Segebarth, C., et al. (2005). Focal brain ischemia in rat: acute changes in brain tissue T1 reflect acute increase in brain tissue water content. *NMR Biomed.* 18, 499–506. doi: 10.1002/nbm.979

Barillot, C., Bannier, E., Commowick, O., Corouge, I., Baire, A., Fakhfakh, I., et al. (2016). Shanoir: applying the software as a service distribution model to manage brain imaging research repositories. *Front. ICT* 3:25. doi: 10.3389/fict.2016.00025

Behroozi, M., Chwiesko, C., Strockens, F., Sauvage, M., Helluy, X., Peterburs, J., et al. (2018). In vivo measurement of T1 and T2 relaxation times in awake pigeon and rat brains at 7T. *Magn. Reson. Med.* 79, 1090–1100. doi: 10.1002/mrm.26722

Chahine, L. M., Urbe, L., Caspell-Garcia, C., Aarsland, D., Alcalay, R., Barone, P., et al. (2018). Cognition among individuals along a spectrum of increased risk for Parkinson's disease. *PLoS One* 13:e0201964. doi: 10.1371/journal.pone.0201964

Commowick, O., Istace, A., Kain, M., Laurent, B., Leray, F., Simon, M., et al. (2018). Objective evaluation of multiple sclerosis lesion segmentation using a data management and processing infrastructure. *Sci. Rep.* 8:13650.

Cremillieux, Y., Ding, S., and Dunn, J. F. (1998). High-resolution *in vivo* measurements of transverse relaxation times in rats at 7 Tesla. *Magn. Reson. Med.* 39, 285–290. doi: 10.1002/mrm.1910390216

Das, S., Glatard, T., Rogers, C., Saigle, J., Paiva, S., MacIntyre, L., et al. (2016). Cyberinfrastructure for open science at the montreal neurological institute. *Front. Neuroinform.* 10:53. doi: 10.3389/fninf.2016.00053

de Graaf, R. A., Brown, P. B., McIntyre, S., Nixon, T. W., Behar, K. L., and Rothman, D. L. (2006). High magnetic field water and metabolite proton T1 and T2 relaxation in rat brain in vivo. *Magn. Reson. Med.* 56, 386–394. doi: 10.1002/mrm.20946

Del Bigio, M. R., Slobodian, I., Schellenberg, A. E., Buist, R. J., and Kemp-Buors, T. L. (2011). Magnetic resonance imaging indicators of blood-brain barrier and brain water changes in young rats with kaolin-induced hydrocephalus. *Fluids Barriers CNS* 8:22.

Deoni, S. (2010). Quantitative relaxometry of the brain. *Top. Magn. Reson. Imaging?* 21, 101–113. doi: 10.1097/rmr.0b013e31821e56d8

DiFrancesco, M. W., Rasmussen, J. M., Yuan, W., Pratt, R., Dunn, S., Dardzinski, B. J., et al. (2008). Comparison of SNR and CNR for in vivo mouse brain imaging at 3 and 7 T using well matched scanner configurations. *Med. Phys.* 35, 3972–3978. doi: 10.1118/1.2968092

Dojat, M., Kennedy, D., and Niessen, W. (2017). MAPPING: management and processing of images for population ImagiNG. *Front. ICT* 4:18. doi: 10.3389/fict.2017.00018

Gao, Y., Chen, Y., Ma, D., Jiang, Y., Herrmann, K. A., Vincent, J. A., et al. (2015). Preclinical MR fingerprinting (MRF) at 7 T: effective quantitative imaging for rodent disease models. *NMR Biomed.* 28, 384–394. doi: 10.1002/nbm.3262

Gigliucci, V., Gormley, S., Gibney, S., Rouine, J., Kerskens, C., Connor, T. J., et al. (2014). Characterisation of the antidepressant properties of nitric oxide synthase inhibitors in the olfactory bulbectomised rat model of depression. *Eur. Neuropsychopharmacol.* 24, 1349–1361. doi: 10.1016/j.euroneuro.2014.05.003

Glatard, T., Lartizien, C., Gibaud, B., da Silva, R. F., Forestier, G., Cervenansky, F., et al. (2013). A virtual imaging platform for multi-modality medical image simulation. *IEEE Trans. Med. Imaging* 32, 110–118. doi: 10.1109/tmi.2012.2220154

Guilfoyle, D. N., Dyakin, V. V., O'Shea, J., Pell, G. S., and Helpern, J. A. (2003). Quantitative measurements of proton spin-lattice (T1) and spin-spin (T2) relaxation times in the mouse brain at 7.0 T. *Magn. Reson. Med.* 49, 576–580. doi: 10.1002/mrm.10371

Hodge, M. R., Horton, W., Brown, T., Herrick, R., Olsen, T., Hileman, M. E., et al. (2016). ConnectomeDB–Sharing human brain connectivity data. *Neuroimage* 124(Pt B), 1102–1107. doi: 10.1016/j.neuroimage.2015.04.046

Knight, M. J., McCann, B., Tsivos, D., Couthard, E., and Kauppinen, R. A. (2016). Quantitative T1 and T2 MRI signal characteristics in the human brain: different patterns of MR contrasts in normal ageing. *Magma* 29, 833–842. doi: 10.1007/s10334-016-0573-0

Koundal, S., Gandhi, S., Kaur, T., Trivedi, R., and Khushu, S. (2015). Investigation of prolonged hypobaric hypoxia-induced change in rat brain using T2 relaxometry and diffusion tensor imaging at 7T. *Neuroscience* 289, 106–113. doi: 10.1016/j.neuroscience.2014.12.049

Lancelot, S., Roche, R., Slimen, A., Bouillot, C., Levigoureux, E., Langlois, J. B., et al. (2014). A multi-atlas based method for automated anatomical rat brain MRI segmentation and extraction of PET activity. *PLoS One* 9:e109113. doi: 10.1371/journal.pone.0109113

Landis, D., Courtney, W., Dieringer, C., Kelly, R., King, M., Miller, B., et al. (2016). COINS Data Exchange: an open platform for compiling, curating, and disseminating neuroimaging data. *Neuroimage* 124(Pt B), 1084–1088. doi: 10.1016/j.neuroimage.2015.05.049

Lebenberg, J., Herard, A. S., Dubois, A., Dauguet, J., Frouin, V., Dhenain, M., et al. (2010). Validation of MRI-based 3D digital atlas registration with histological and autoradiographic volumes: an anatomofunctional transgenic mouse brain imaging study. *Neuroimage* 51, 1037–1046. doi: 10.1016/j.neuroimage.2010.03.014

Li, J., Zhang, Q., Chen, F., Meng, X., Liu, W., Chen, D., et al. (2017). Genome-wide association and interaction studies of CSF T-tau/Abeta42 ratio in ADNI cohort. *Neurobiol. Aging* 57, 241–247.

Liachenko, S., and Ramu, J. (2017). Quantification and reproducibility assessment of the regional brain T2 relaxation in naive rats at 7T. *J. Magn. Reson. Imaging* 45, 700–709. doi: 10.1002/jmri.25378

Liu, C., Jin, C., Jian, Z., Wang, M., Li, X., Liu, H., et al. (2018). Assessment of myelination progression in subcortical white matter of children aged 6-48 months using T2-weighted imaging. *Neuroradiology* 60, 1343–1351. doi: 10.1007/s00234-018-2108-z

Liu, J. V., Bock, N. A., and Silva, A. C. (2011). Rapid high-resolution three-dimensional mapping of T1 and age-dependent variations in the non-human primate brain using magnetization-prepared rapid gradient-echo (MPRAGE) sequence. *Neuroimage* 56, 1154–1163. doi: 10.1016/j.neuroimage.2011.02.075

NAP (2018). *In: Open Science by Design: Realizing a Vision for 21st Century Research*. Washington, DC: National Academy of Sciences.

Nelder, J., and Mead, R. (1965). A simplex method for function minimization. *Comput. J.* 7, 308–313. doi: 10.1093/comjnl/7.4.308

Prescott, M. J., and Lidster, K. (2017). Improving quality of science through better animal welfare: the NC3Rs strategy. *Lab. Anim.* 46, 152–156. doi: 10.1038/laban.1217

Rex, D. E., Ma, J. Q., and Toga, A. W. (2003). The LONI pipeline processing environment. *Neuroimage* 19, 1033–1048. doi: 10.1016/s1053-8119(03)00185-x

Suleymanova, E., Gulyaev, M., and Chepurnova, N. (2014). Ginseng extract attenuates early MRI changes after status epilepticus and decreases subsequent reduction of hippocampal volume in the rat brain. *Epilepsy Res.* 108, 223–231. doi: 10.1016/j.eplepsyres.2013.11.018

van de Ven, R. C., Hogers, B., van den Maagdenberg, A. M., de Groot, H. J., Ferrari, M. D., Frants, R. R., et al. (2007). T(1) relaxation in in vivo mouse brain at ultra-high field. *Magn. Reson. Med.* 58, 390–395. doi: 10.1002/mrm.21313

Wang, J., Vachet, C., Rumple, A., Gouttard, S., Ouziel, C., Perrot, E., et al. (2014). Multi-atlas segmentation of subcortical brain structures via the AutoSeg software pipeline. *Front. Neuroinform.* 8:7. doi: 10.3389/fninf.2014.00007

Wright, P. J., Mougin, O. E., Totman, J. J., Peters, A. M., Brookes, M. J., Coxon, R., et al. (2008). Water proton T1 measurements in brain tissue at 7, 3, and 1.5 T using IR-EPI, IR-TSE, and MPRAGE: results and optimization. *Magma* 21, 121–130. doi: 10.1007/s10334-008-0104-8

Conflict of Interest: The authors declare that the research was conducted in the absence of any commercial or financial relationships that could be construed as a potential conflict of interest.

frontiers in Neuroinformatics

TECHNOLOGY AND CODE
published: 19 May 2020
doi: 10.3389/fninf.2020.00020

Small Animal Shanoir (SAS) A Cloud-Based Solution for Managing Preclinical MR Brain Imaging Studies

Michael Kain[1], Marjolaine Bodin[2], Simon Loury[2], Yao Chi[1], Julien Louis[1], Mathieu Simon[1], Julien Lamy[3], Christian Barillot[1] and Michel Dojat[2]**

[1] INRIA U1228, INSERM, Université de Rennes, Rennes, France, [2] INSERM U1216, Grenoble Institut des Neurosciences, Université Grenoble Alpes, CHU Grenoble Alpes, Grenoble, France, [3] ICube, University of Strasbourg-CNRS, Strasbourg, France

Clinical multicenter imaging studies are frequent and rely on a wide range of existing tools for sharing data and processing pipelines. This is not the case for preclinical (small animal) studies. Animal population imaging is still in infancy, especially because a complete standardization and control of initial conditions in animal models across labs is still difficult and few studies aim at standardization of acquisition and post-processing techniques. Clearly, there is a need of appropriate tools for the management and sharing of data, post-processing and analysis methods dedicated to small animal imaging. Solutions developed for Human imaging studies cannot be directly applied to this specific domain. In this paper, we present the Small Animal Shanoir (SAS) solution for supporting animal population imaging using tools compatible with open data. The integration of automated workflow tools ensures accessibility and reproducibility of research outputs. By sharing data and imaging processing tools, hosted by SAS, we promote data preparation and tools for reproducibility and reuse, and participation in multicenter or replication "*open science*" studies contributing to the improvement of quality science in preclinical domain. SAS is a first step for promoting open science for small animal imaging and a contribution to the valorization of data and pipelines of reference.

Keywords: MRI, data sharing, open science, population imaging, image processing

OPEN ACCESS

Edited by:
David A. Gutman, Emory University, United States

Reviewed by:
Graham J. Galloway, University of Queensland, Australia
Christian Haselgrove, University of Massachusetts Medical School, United States

****Correspondence:***
Michael Kain
michael.kain@inria.fr
Michel Dojat
michel.dojat@inserm.fr

Received: *14 June 2019*
Accepted: *16 April 2020*
Published: *19 May 2020*

Citation:
Kain M, Bodin M, Loury S, Chi Y, Louis J, Simon M, Lamy J, Barillot C and Dojat M (2020) Small Animal Shanoir (SAS) A Cloud-Based Solution for Managing Preclinical MR Brain Imaging Studies. Front. Neuroinform. 14:20. doi: 10.3389/fninf.2020.00020

INTRODUCTION

Recently, the validity of the published results in life sciences has been questioned (Button et al., 2013; Ingre, 2013). The poor replication of research findings is directly linked to an endemic low statistical power of the majority of biological studies. It is now well recognized that data sharing should be promoted to improve the robustness and the replicability of the scientific results (Poldrack et al., 2017). Technical solutions should be proposed to support a more "*open science*" approach, making data discoverable, accessible, interpretable, and reusable, as captured in the FAIR Guiding Principles (Findability, Accessibility, Interoperability, and Reusability)

(Wilkinson et al., 2016). For human population imaging, large data repositories exist, such as ADNI for Alzheimer disease, PPMI for Parkinson disease, centerTBI for brain trauma, United Kingdom Biobank for various diseases or ConnectomeDB for the Human Connectome Project, extensively used by researchers all over the world and leading to new findings. Additionally, data analysis plays an important role. For such large datasets, image processing pipelines should be constructed based on the best algorithms available and their performance should be objectively compared to diffuse the more relevant solutions. Also, provenance of processed data should be secured (Mackenzie-Graham et al., 2008). Specific architectures (e.g., COINS, LONI) are now available mainly for human population imaging [see (Kennedy et al., 2019) and other recent works here].

Similarly, to human population imaging, there are several well-founded motivations for *animal population imaging*: optimization of costs and subject participation, improvement of quality of science (use of sufficiently large animal cohorts for ensuring statistical result validity, e.g., drug development process) and enhancement of research discovery [see the special Lab Animal focus on reproducibility in animal research (Prescott and Lidster, 2017)]. However, at the difference of Human imaging, where the issues with large cohorts are well-known and solutions have been proposed, sharing small animal imaging data and corresponding image processing pipelines is a recent preoccupation. Some efforts are performed especially toward the construction of animal atlases (Sunkin et al., 2013; Bjerke et al., 2018; Wang et al., 2018). Despite of some attempts (Lee et al., 2010), there is a clear miss of appropriate infrastructure for facilitating sharing data and processing tools for animal population imaging. Indeed, solutions developed for Human studies can only be reused in part and should be adapted and extended to take into account the specificities of animal studies: for instance, with the introduction, in the data model, of new concepts for strain and anesthetic, or of a specific converter for raw data (e.g., mainly Bruker files). Moreover, population imaging infrastructures for clinical or preclinical purposes, have to handle, presently or in a close future, very large datasets while providing a fast and robust data access via an efficient web interface. Today the proposed solutions do not really address this issue because internal mechanisms for scalability are missing. Presently, as an example, we currently handle clinical studies with up to 3000 subjects with around 4Tb of data and we are now just at the emergence of the population imaging studies, recently boosted by the introduction in life science domain of efficient machine learning approaches, avid of large mass of data.

In this paper, we present the Small Animal Shanoir (SAS) solution. SAS is an extension of the Shanoir data management system for Human brain imaging repositories (Barillot et al., 2016) with the integration of dedicated microservices for small animal imaging studies. SAS was developed under the hospices of the national infrastructure project France Life Imaging, with the goal of coordinating research activities in France in *in vivo* imaging and combining the skills to push the current technological barriers. The specific action "Information Analysis and Management" (FLI-IAM) was devoted to the development of a federated infrastructure for the management of *in vivo* imaging data and processing tools. FLI-IAM is partner of OpenAIRE-connect, an H2020 European project promoting Open Science.[1] The paper is organized as follows: firstly, the global architecture of FLI-IAM is presented, then SAS and the notion of micro-service are introduced, illustrated by the description of a selection of representative micro-services; then current applications are briefly presented followed by the discussion section.

ARCHITECTURE OVERVIEW

The goal of the architecture is to federate different systems that have their specific data model which does not necessary fulfill the XNAT reference scheme. For this purpose, we chose to use the core ontology OntoNeurolog, accessible via BioPortal.[2] This ontology is based at the upper level on the DOLCE foundational ontology and described in details in Temal et al. (2008); Gibaud et al. (2011); Batrancourt et al. (2015). All specific data models including XNAT are mapped to this core ontology. The technical architecture of FLI-IAM is shown in **Figure 1**. The FLI-IAM architecture is web-oriented and constructed on three main functionalities: (1) query and retrieval of data and image processing pipelines (via the web portal), (2) storage of data and associated metadata (via the image archive module), and (3) the execution of the selected pipelines on the selected data (via the computing platforms module).

The data transfer module (DTM) is used to exchange data between the image archive and the computing platforms. The architecture was successfully used for hosting two MICCAI Human imaging challenges on Multiple Sclerosis (Commowick et al., 2018) and PET tumor segmentation (Hatt et al., 2018).

FLI-IAM Web Portal

The web portal of FLI-IAM[3] guides the user to the resource or service adapted to his/her needs. Therefore, an overview of all resources and services available is proposed. After registration and authentication, the candidate accesses to the set of components: the image archive via the common catalog graphical interface, the computing platforms via the CARMIN client (see below) and the DTM via the DTM client. Technically the FLI-IAM web portal is based on Liferay Portal Server v6.2, Community Edition, a Java Enterprise application server that provides a full content management system and a market place with multiple extensions. For the MICCAI challenges the portal was used to inform about the challenge rules, register as candidate, with a process specifically integrated for this purpose, and give access to the data.

FLI-IAM Authentication Process

Security is a sensitive aspect for all web-oriented data management systems. OpenID Connect (OIDC) is the

[1]OpenAire aims at developing a technical infrastructure for an interoperable European network of research repositories through the establishment of common guidelines and shared metadata standards.

[2]https://bioportal.bioontology.org/ontologies/ONL-DP

[3]https://portal.fli-iam.irisa.fr/home

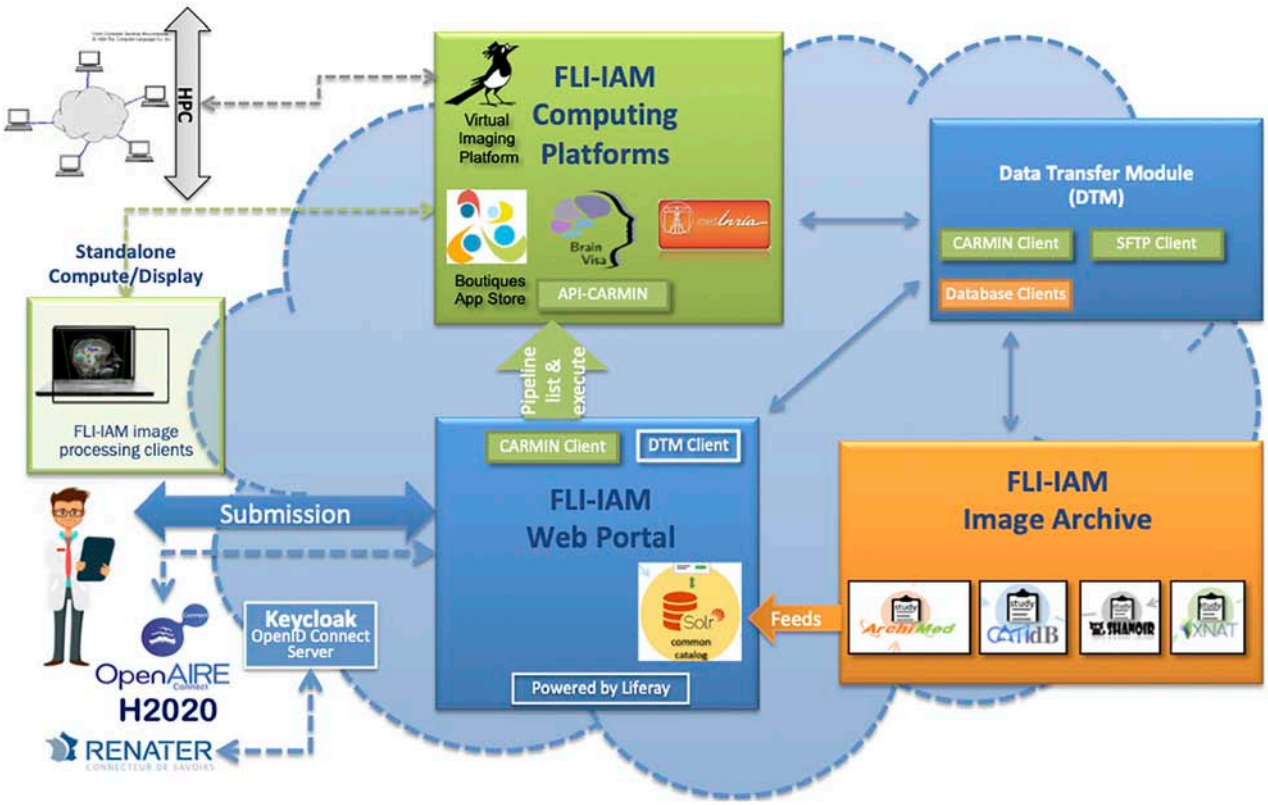

FIGURE 1 | The FLI-IAM architecture. Three major blocks compose the core of this distributed web architecture: the web portal (in blue), the image archive (in orange) and the computing platforms (in green). The data transfer module (in blue) ensures data exchange between these three modules. The API-CARMIN allows the seamless connection of data and pipelines. The user submits a query via the web portal (e.g., selecting images following criteria and choosing the execution of an imaging processing pipeline). The user's identification can be done via a Renater account or realized via OpenID connect implemented using Keycloak. Presently, four databases and four computing platforms are federated by the infrastructure. The integration of a new database is realized by the introduction of a connector that maps its data model to the common catalog. Each database manages autonomously multicenter imaging studies. Several instances of each database can be managed be the infrastructure. Pipelines can be executed on high performance computing cluster (HPC) or on a local machine. This DTM module ensures the transfer of data between a database (dedicated clients in orange) and the corresponding computing resource via the API-CARMIN. A local file system and database are used for a temporarily storage. Each platform (database or computing resource) can be configured with its web address and each transfer can be started and monitored. For each transfer between two platforms, a communication channel (protocol) can be chosen. A scheduler assures long-time data transfers. The architecture is part of the H2020 European OpenAire project for open science promotion.

authentication protocol used by the FLI-IAM infrastructure, implemented in Keycloak, to verify the identity of a user based on the authentication performed by an authorization server, as well as to obtain basic profile information about the user in an interoperable and REST-like manner (see **Figure 1**). All components in FLI-IAM delegate the authentication to Keycloak that allows single sign-on with identity and access management to applications and services. In line with GDPR, all user passwords are exclusively stored in Keycloak and only the current user has knowledge of his/her password. For academic researchers who have a Renater account, a connection between FLI-IAM Keycloak with Renater is always possible with the SAML authentication provider.

Common Catalog

FLI-IAM portal users can execute cross-database searches to find published datasets and studies in the different databases using the common catalog. A free search-field and a search result display page are provided within the graphical user interface of the portal (see **Figure 2**) thanks to the search engine Apache Solr.

A specific workflow for the combination of metadata has been developed for the whole interrogation of the set of databases. Imaging studies, associated meta-data and corresponding images are hosted within each instance of the federated databases. Each database manages independently its users, access rights and roles for the hosted studies. The Principal Investigator (PI) of a study has the responsibility to place metadata into the common catalog of the FLI-IAM infrastructure for sharing the study publicly or with specific user groups, using access control lists. Users of the portal can then identify the origin of the datasets and ask the corresponding PI for data access. Technically a common search index has been defined and four mapping plugins have been developed, used for the connection to the common catalog of the corresponding database instance. Once a PI has allowed data sharing of a study, a nightly job updates the common catalog. When he/she decides the

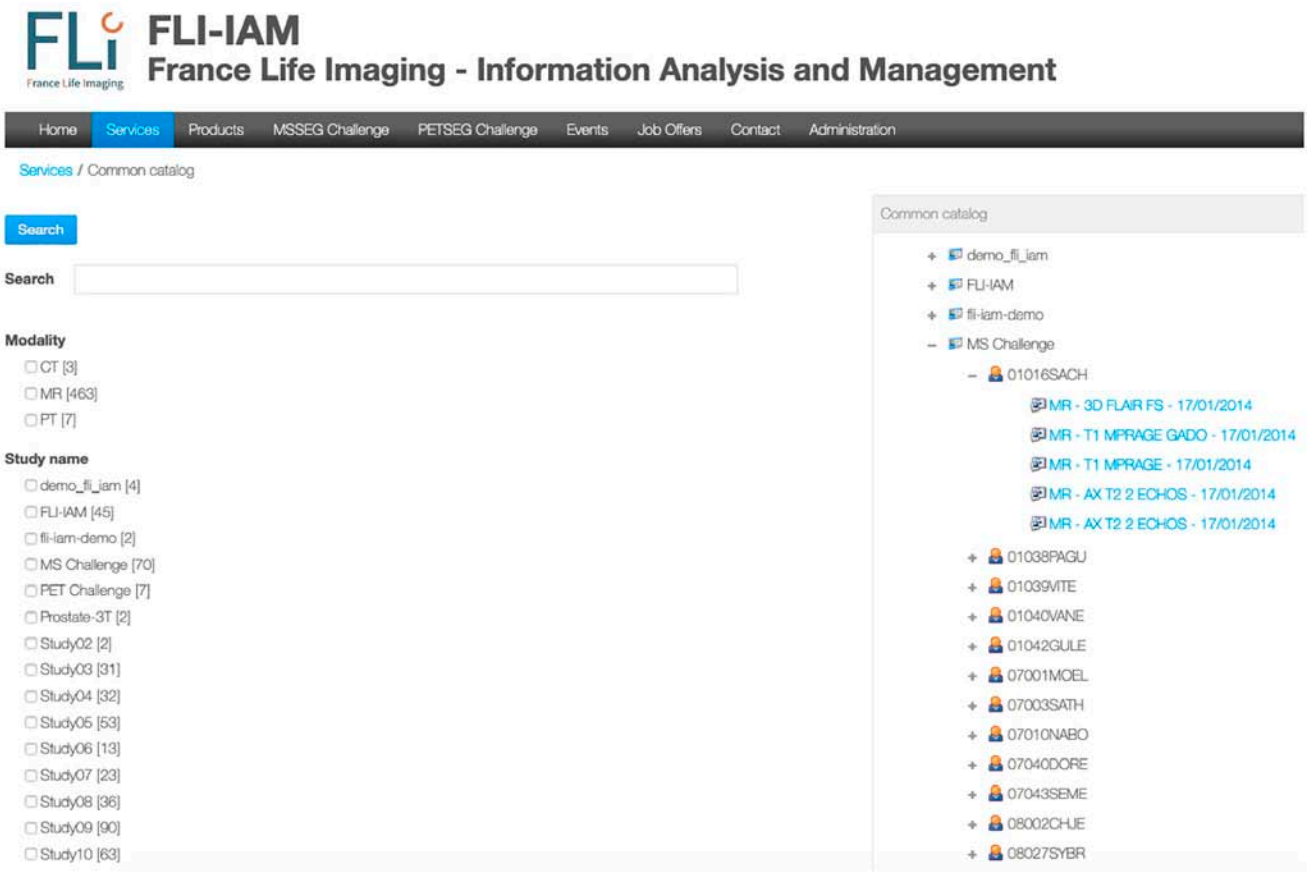

FIGURE 2 | User's interface for either a specific search query or to display all images available for one user. In this example, no specific query is addressed and the interface shows all the available studies. An expanded view on T1-weighted images for the MICCAI MS challenge is displayed.

sharing ending, the corresponding datasets are deleted from the search index.

FLI-IAM Image Archive

The FLI-IAM infrastructure federates currently four imaging databases. Their main features are described in **Table 1**. CATI-DB and Shanoir manage various large mono- or multicenter brain studies, while ArchiMed (Micard et al., 2016) collects imaging data from various clinical research projects. Presently, each database is hosted on an independent hardware infrastructure and could be hosted in a future central FLI-IAM hardware infrastructure. Each database has its independent workflow to import images. The federative architecture is constructed for a seamless integration of new databases.

For a common interrogation of the federated databases, an excerpt of the common catalog is presented in **Table 2**.

Computing Platforms

As shown in **Figure 1**, beside databases, FLI-IAM integrates four computing platforms: BrainVisa, medInria, Virtual Imaging Platform (Glatard et al., 2013) and Boutiques (Glatard et al., 2018). The former, BrainVisa is a neuroimaging software platform for mass data analysis, providing image processing tools such as Morphologist for brain segmentation and sulcal morphometry, and an interactive 3D neuroimaging data visualizer (Anatomist). medInria is a multi-platform medical image processing and visualization software. Through a graphical user interface, medInria offers processing tools for medical images, such as 2D/3D/4D image visualization, image registration, diffusion MR processing and fiber tracking. VIP is a web portal for the execution of medical image processing pipelines for massive data analysis and simulation. It leverages resources available in the biomed virtual organization of the European Grid Infrastructure to offer an open service to academic researchers worldwide. Boutiques represents the app store of FLI-IAM. Boutiques allows automatic publication, integration and execution of applications across computational platforms. Boutiques applications are described in a JSON file and enable the simulation, validation, evaluation, and application-specific monitoring of command-line tools. Providers can integrate their application into a Docker or Singularity container, describe it and share it via Boutiques. Each computing platform can be used and installed independently. Note that Boutiques is integrated into VIP.

FLI-IAM provides an integration layer with two features: (1) an authentication using OpenID Connect and (2) a unified

TABLE 1 | Main characteristics of the four databases currently hosted by FLI-IAM.

Database	Who	Key concepts	Modalities	Browser	Add. Info	Open source
ArchiMed	CIC-IT, Nancy, Inserm, Fr	Centralized server, Model close to DICOM/PACS, Desktop client, PAAS	MRI, CT	No	Link	Not yet
CATI-DB	CATI, Paris, CEA, Fr	Centralized file-system (NFS) with meta-data server, Model oriented on processing, Perfectly adapted into CATI-infrastructure, SAAS (turn-key)	MRI, PET/SPECT	No	Link	Yes, access registration
Shanoir	Empenn, Rennes, Inria, Fr	Centralized server, Ontology based, Model remains fix, Web client, PAAS	MRI, PET, CT, EEG	Yes	Link	Yes, on GitHub
XNAT	NRG Lab, Washington, University School of Medicine, US	Centralized server, Schema based, Default model to customize, Web client, PAAS	MRI, PET, CT	Yes	Link	Yes, on Bitbucket

PAAS, Platform As A Service; SAAS, Software As A Service. MRI, Magnetic Resonance Imaging; CT, Computed Tomography, PET, Position Emission Tomography: SPECT, Single-Photon Emission Computed Tomography; EEG, Electro-Encephalography.

TABLE 2 | Common catalog. A common catalog is required for querying the different databases accessible via the federated platform.

Common catalog	ArchiMed	CATI-DB	Shanoir	XNAT
study_name	study_code	Study.name	Study_Name	projectData.name
center_name	institution_name	Center.name	Center_Id	experimentData.acquisitionSite
manufacturer	manufacturer + manufacturer_model	unknown	Manufacturer_Name + Manufacturer_Model	imageSessionData.scanner
principal_investigator	study_investigator	Study.main_investigator	Investigator_Id	experimentData.investigator
subject_identifier	unknown in db, examCode used	Subject.code_in_study	Subject_Name	subjectData.ID
series_modality	file_type_acronym	Fileset.attribute.modality	Dataset_Ref_Dataset _Modality_Type_Id	imageScanData.modality
series_protocol	serie_desc	Fileset.attribute.sequence	Dataset_Name	imageScanData.series_description
series_creation_date	serie_date_time	Assessment.date	Dataset_Creation_Date	imageSessionData.date

The table above describes the structure of the common index and the mapping of each database into the common catalog.

remote access via the REST-API, CARMIN. Using such an environment, the same client can remotely use each platform implementing the interface. For example, this allows the FLI-IAM web portal, via the CARMIN client (JavaScript library), to access to a list of pipelines provided by VIP, send data and execute a pipeline. Moreover, the same CARMIN client can be integrated into each of the database instances present in the FLI-IAM image archive for its connection to any computing platform. Note that CARMIN is also implemented in CBrain, a Canadian infrastructure used for managing very large imaging medical projects. Thus, the users of the FLI-IAM web portal have potentially access to CBrain and *vice versa*.

Data Transfer Module

The DTM connects the image archive with the computing platforms. It transfers primarily images from one database (source) to one computing platform (destination), but can as well transfer images between databases or between computing platforms. Additionally, DTM can call a computing platform, e.g., VIP, to start processing pipelines with a given pipeline identifier, check for computation results and import the processed images back into one of the databases (see **Figure 1**). Therefore, it integrates four client libraries (one for each database), a SFTP client and a CARMIN client. The DTM is completely configurable on using its web interface and has been used for the MICCAI 2016 challenges. A MySQL database is used to maintain state and all transferred data are temporarily stored in a local file system.

SMALL ANIMAL SHANOIR

Small Animal Shanoir is built on the top of a recent version of Shanoir, called Shanoir-NG, which relies on recent web technologies, such as Single-Page-Applications (SPAs) and micro-services, with the double objective of reinforcing the flexibility and scalability of the architecture.

Single-Page Application

Shanoir-NG has been developed as SPA for two major reasons: first to give the user the feeling of interacting with a desktop application rather than with a web application; second to support as many browsers as possible, even mobile browsers. This is based on the assumption, that modern modular SPAs could be more easily adapted to reduced screen sizes and other requirements of mobile applications. Technically SPAs rewrite parts of a page rather than loading the entire page and the application code is completely loaded when the application starts. Appropriate resources are dynamically loaded and added to the page as necessary, usually in response to actions of the user. Angular five

has been chosen as front-end technology after an evaluation of different frameworks available yet.

Micro-Service Architecture

Inspired by the multi-agent architecture (Minsky, 1986), the micro-service architecture[4] considers the application as a suite of independent services; each service running with its own process and communicating with lightweight mechanisms, often an HTTP resource API. The main advantage of adopting a micro-architecture is the scalability in case of evolving computational load or availability of hardware resources. Moreover, the strong independency of services allows for their development and deployment separately from the others ensuring a continuous service delivery. Each micro-service can be developed using the more efficient language for its functionality with its own memory management, as long as the common external interface policy is respected.

The strong independency of services requires the improvement of the control at the global level of the architecture. Some control concerns are particularly important for our applications: for instance, how does react a micro-service when another depending service is no more available? Or how each micro-service is informed about changes in its environment or security policy? Some inconsistencies have to be tolerated for a short period of time and handled afterward, when a micro-service, stopped for a while, is back to function. Specific errors or activity tracing mechanisms have to be introduced to trace the service states, user actions and other events.

As a Cloud-native application, each micro-service is integrated in a Docker container. For instance, the DTM micro-service described above runs its own Docker container, provides a REST-API and an Angular five front-end to configure available platforms, connection settings (channels) or initiate/monitor transfers. The entire Shanoir-NG architecture is deployed using a Docker Compose script that initiates and runs each Docker container encapsulating a micro-service.

Based on the application specifications, we have to define how to distribute the different functionalities into a reasonable collection of micro-services, while preserving a good integration. **Figure 1** in **Supplementary Material** shows the current architecture. Six key services have been identified so far Users, Studies, Import, Datasets, Preclinical and Dicomifier. The two-latter specific for small animal applications are detailed below.

Preclinical Micro-Services

For preclinical applications, the initial OntoNeurolog ontology was extended by the preclinical working group of FLI-IAM (SAIN) to introduce several concepts related to animal study for facilitating their sharing (see **Figure 3**). Thus, concepts have been added to describe the subject (specie, strain, provider, type [transgenic or not], and stabling), the model of pathology under study and the administered therapy. The experimental conditions are also described (type of anesthetic, physiological measurements: e.g., blood gas, temperature, SaO2, heart rate, ...). The ontology is represented in OWL using Protégé (Musen, 2015).

The ontological preclinical model has been translated into a relational database model and integrated into the preclinical microservice. It manages its own graphical user interface (GUI) and database and was added to Shanoir-NG. **Figures 4**, **5** show the corresponding dedicated interface.

Dicomifier Micro-Service

Dicomifier is a generic and open-source converter designed to process both preclinical and clinical imaging data and to be easily extensible to account for the wealth of meta-data associated with medical images. This micro-service converts the current imaging data formats, Bruker and DICOM files. The former is largely used in preclinical imaging centers because the same manufacturer (Bruker Biospin) designs the preclinical MR scanners. The converter is modular: one part handles the conversion from the Bruker format to the DICOM format and another part handles the conversion from the DICOM format (either native or converted from the Bruker format) to NIfTI. This design allows future extensions, e.g., conversion from NIfTI to DICOM to store segmentation results in a PACS. Similar concepts guiding the hierarchy of data exist in both Bruker and DICOM formats: patient (or subject), study (i.e., a set of exams performed for a single goal) and series (single or multiple 2D or 3D images from one acquisition). However, implementation of those concepts in both formats differs, and, in addition to the file-format difference, data alignment is an integral part of the conversion. The Bruker-DICOM alignment is a mapping process in which a pre-defined, modality-specific, set of DICOM elements is extracted from the Bruker-format exam. The mapping may be a direct one, i.e., mapping a single Bruker element to a single DICOM element without additional transforms, or a more complex one, using data from multiple Bruker fields, transforming them, and storing them in disjoint DICOM fields.

Regarding the NIfTI conversion, we leverage the multi-dimensional capabilities of NIfTI to store images per-series, following the dimensions given by the DICOM files. For instance, a diffusion MRI acquisition with multiple b-values would appear as a five-dimensional dataset. The fixed-size header of the NIfTI format cannot accommodate the wide range of meta-data stored in the DICOM format, although this data may nevertheless be required for further processing, e.g., in parametric MRI. We chose to store the metadata in the widespread JSON format, for its seamless handling by many software libraries while remaining human-readable. For native DICOM files, i.e., not converted from Bruker, a normalization step is also applied to parse the data from vendor-specific fields, when the syntax of those fields is known.

Current SAS Applications

In vivo T1 and T2 relaxation times extracted from MR imaging data are tissue dependent and their modifications may be characteristic of specific anatomical regions and pathological situations. Recently, we used the SAS infrastructure to produce quantitative 3D T1 and T2 maps for the healthy rat brain at 7T. Such maps were defined based on data acquired at two different

[4]https://martinfowler.com/microservices/

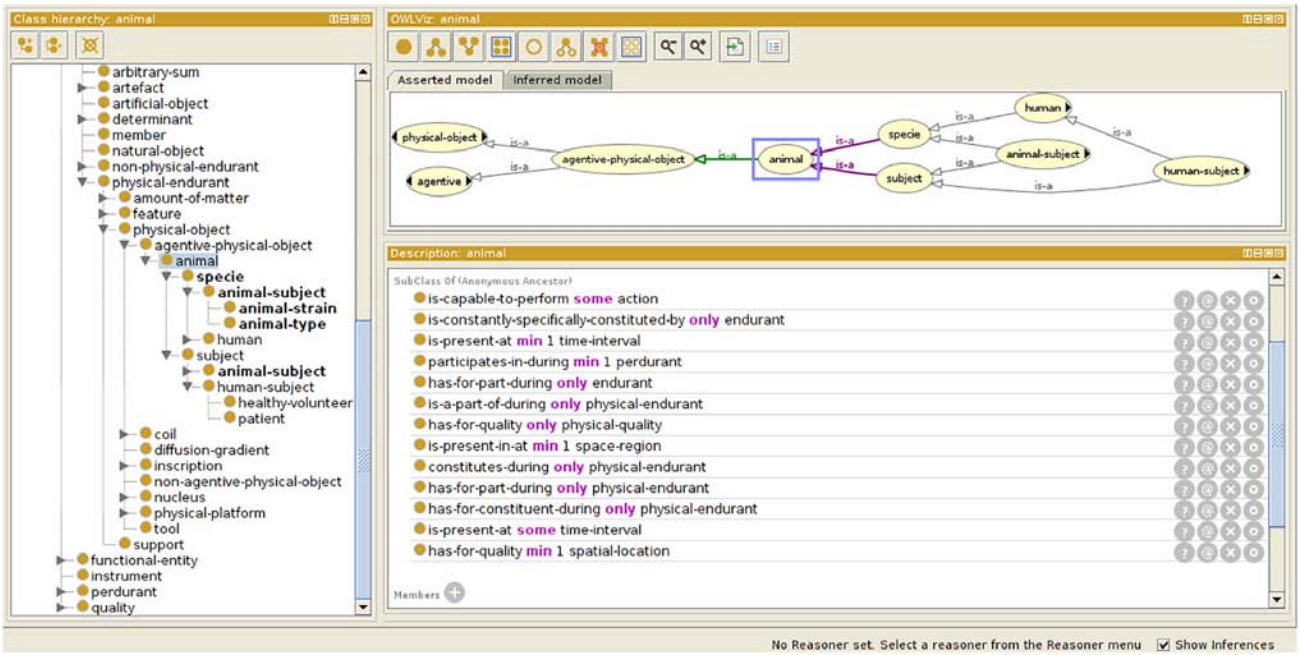

FIGURE 3 | Ontology extension for preclinical study. Specific concepts are introduced extending the OntoNeurolog ontology expressed in OWL and represented using Protégé (https://protege.stanford.edu/about.php).

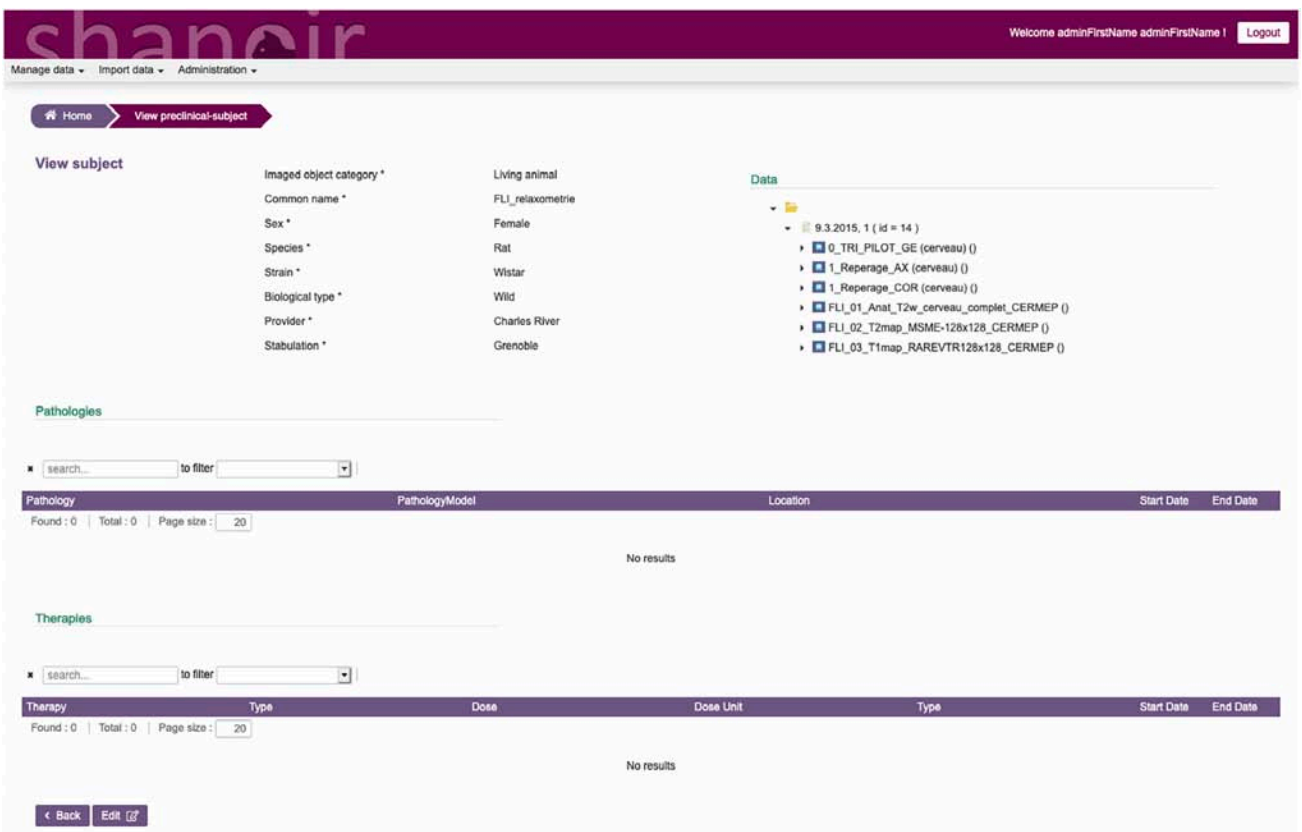

FIGURE 4 | SAS, GUI for animal studies, information about the subject. Pathologies and therapies can be added and managed.

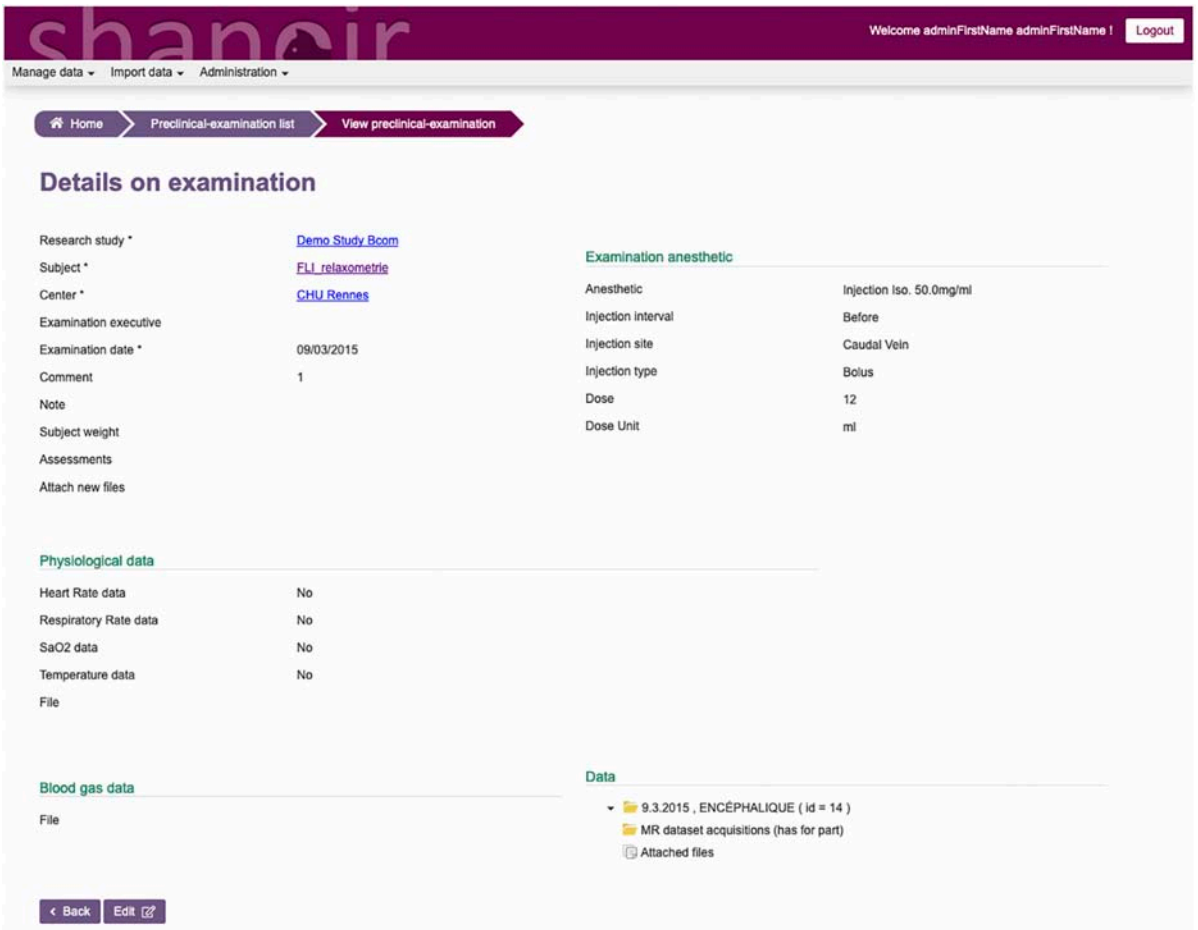

FIGURE 5 | SAS, GUI for animal studies, details about the experimental conditions. Anesthetic, physiological, and blood gas data can be added and managed.

centers on twenty Sprague-Dawley rats at GIN (Grenoble, Fr) and twenty Sprague-Dawley rats at CRMBM (Marseille, Fr). We used three different fitting algorithms from three difference centers (CRMBM, MRICen (Fontenay-aux-roses, Fr) and Icube (Strasbourg, Fr) to compute the T1 and T2 values in each voxel and to evaluate the influence of image processing steps on the final maps. To derive relaxation time values per brain area, two multi-atlas segmentation pipelines from MIRCen and Icube were executed. All data were stored on SAS and image processing pipelines were embedded into Docker containers and executed on the VIP processing platform. With the DTM, processed data were stored in SAS for each individual.

This work investigated the influence of data acquisition centers (n = 2) and image processing pipelines (n = 3) on the production of T1 and T2 brain maps. **Figure 6** shows the reproducibility of the T1 and T2 relaxometry values computed from two MR acquisitions for each rat in each center (intra-reproducibility) and the coherency between the values obtained between the centers (inter-reproducibility).

It showed the coherence of the final computed maps when the acquisition sequence parameters are optimized and harmonized between centers (Deruelle et al., 2020). Using SAS, the study demonstrates the feasibility of pooling animal data from different centers. The use of a distributed computing architecture for image storage and for processing pipeline execution paves the way for future multi-center preclinical studies. The quantitative reference maps produced for longitudinal (T1) and transverse (T2) relaxation times obtained on 40 rats (to our knowledge the largest number to date) are valuable to investigate and monitor deviations from normality in animal model of pathologies. A similar study at different magnetic field on mice is undergoing with the same infrastructure involving more data providers (12 centers).

DISCUSSION

Similarly to human research, sharing (data and tools) requirements will necessarily grow up in the next future for preclinical (animal) studies. The design of SAS was motivated by the needs of the preclinical research community. The problem of replication and reproducibility in preclinical studies is now well documented (Sena et al., 2010; Begley and Ellis, 2012; Tsilidis et al., 2013) and can negatively impacted the

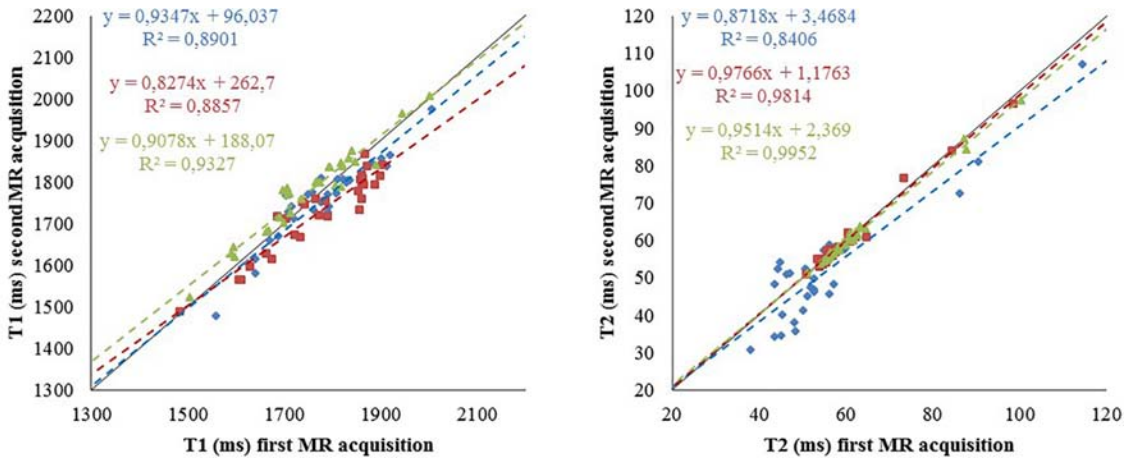

FIGURE 6 | Reproducibility of the relaxometry maps. T1 **(left)** and T2 **(right)** values for the 29 regions of interest from data acquired at CRMBM (in blue) for one rat (S32) and at GIN for two rats (S21 and S22) in red and green, respectively. The pipelines were provided by CRMBM (fitting) and Icube (segmentation). Dashed line: linear regression, corresponding equation are indicated with the same color code as values, R^2: correlation coefficient. Bold line identity curve.

translation to human studies, leading to waste of resources, unnecessary risks for volunteers and slowing down new therapies development. The first cause of non-reproducibility is the weakness of experimental design including low power (Begley and Ioannidis, 2015).

With SAS, we show that animal population imaging is feasible and that research in this field can be conducted using tools compatible with open sharing and use of automated workflow tools to ensure accessibility and reproducibility of research outputs. Our first preliminary experiments (see §3.5) demonstrate the strong interest of the community to promote the federation of multiple sources of information, processing tools and diffusion of knowledge distributed in various centers for preclinical studies. We will promote data preparation and tools for reproducibility and reuse and participation in multicenter or replication studies. Thanks to the FLI-IAM architecture used, we will diffuse our results beyond the national community. Indeed, a recent external survey (30 interviews) indicated that the primary application domain for such an infrastructure was preclinical imaging where solution is missing. Note that developing such a platform requires some efforts: from 2016, up to 15 computer engineers were employed for Shanoir-NG and SAS developments.

Moreover, FLI-IAM is partner of OpenAIRE-connect, for connection with European large scale open science projects. Additionally, SAS will contribute to the promotion of this platform and in return will be internationally visible: data and tools will be interoperable and queryable via international platforms. In using SAS, users strongly advocate for the diffusion of acquired and processed data and dissemination of imaging processing pipelines. They promote *Open Science by Design* (Committee on Toward an Open Science Enterprise et al., 2017), meaning that research conducted openly and transparently leads to better science. SAS is a first step for promoting Open science for small animal imaging and a contribution to the valorization of data and pipelines of reference. SAS will also be a good starting point for launching specific working group for animal MR studies at the European (RDA) or International (INCF, ISMRM) levels creating a culture that actively supports Open science by Design.

Extensions and Future Plans

As a cloud platform, multiple extensions are already defined in the roadmap of Shanoir-NG. From the operational point of view the following extensions will have to be addressed: continuous delivery, automatic service discovery, data replication, backup and constant monitoring. The usage of smaller, in terms of memory usage, Docker container base images should be evaluated to optimize the memory footprint of the entire application. With the extension of the number of micro-services, the use of new container management platforms such as Apache Mesos or Kubernetes should be envisaged. From the functional point of view, we plan extensions for massive data import and download and management of BIDS format.

Finally, our next step is to connect SAS, a tool dedicated for small animal imaging, to other complementary environments dedicated to genetics or biology. The idea is to seamlessly integrate SAS with the open science community and to provide researchers a tool for easy sharing in a controlled way.

Shanoir-NG and its extension SAS are open-source software, published under the GNU General Public License (GPL), version 3. The source code is freely available on GitHub under[5]. The current implementation of SAS is available at[6]. Developer documentation is centralized in the GitHub Wiki[7] with code[8] and general user information can be found under http://shanoir.org. The development of Shanoir-NG is driven by a roadmap that is defined by the members of the consortium Shanoir within InriaSoft. Contributions are integrated in form of pull requests. The source code of Dicomifier is available at[9].

[5]https://github.com/fli-iam/shanoir-ng

[6]https://shanoir-ng-dev.irisa.fr

[7]https://github.com/fli-iam/shanoir-ng/wiki

[8]https://github.com/fli-iam/shanoir-ng/tree/appning

[9]https://github.com/lamyj/dicomifier

OpenID Connect (OIDC) is an authentication layer on the top of the authorization framework OAuth 2.0, a standardized protocol controlled by the OpenID Foundation. This protocol is implemented in Keycloak, an open source software product that implements the OpenID Connect protocol and then is used as the central authorization server.

Renater is a highly fast and secured academic European network for internet access and associated services.

SAML (Security Assertion Markup Language) defines a protocol for security information exchange. It is based on XML and proposes a unique (single sign-on) identifier.

Apache Solr is a search and navigation platform built on the open-source HTTP server, Apache.

Docker allows to define containers in a standardized way that encapsulate code and the associated dependencies for an execution on different computing environments.

Singularity is an alternative solution to Docker.

CARMIN (Common API for Research Medical Imaging Network) defines a REST-API for exchanging data and remotely calling pipelines provided by computing platforms. The REST-API is specified using the OpenAPI initiative (OAI) available on SwaggerHub.

DATA AVAILABILITY STATEMENT

The datasets generated for this study are available on request to the corresponding author.

AUTHOR CONTRIBUTIONS

MK, CB, and MD contributed conception and design of the study. MK, MB, SL, YC, JL, and MS implement the different micro services; MK, JL, and MD wrote the first draft of the manuscript. All authors contributed to manuscript revision, read and approved the submitted version.

FUNDING

This work is partly funded by the French program "Investissement d'Avenir" run by the Agence Nationale pour la Recherche (ANR-11-INBS-0006).

ACKNOWLEDGMENTS

The authors thank the technical staff of VIP (https://www.creatis.insa-lyon.fr/vip/), for their support and all the members of the FLI-IAM project for inspiring discussions and fruitful collaborations.

SUPPLEMENTARY MATERIAL

The Supplementary Material for this article can be found online at: https://www.frontiersin.org/articles/10.3389/fninf.2020.00020/full#supplementary-material

REFERENCES

Barillot, C., Bannier, E., Commowick, O., Corouge, I., Baire, A., Fakhfakh, I., et al. (2016). Shanoir: applying the software as a service distribution model to manage brain imaging research repositories. *Front. ICT* 3:25. doi: 10.3389/fict.2016.00025

Batrancourt, B., Dojat, M., Gibaud, B., and Kassel, G. (2015). A multilayer ontology of instruments for neurological, behavioral and cognitive assessments. *Neuroinformatics* 13, 93–110. doi: 10.1007/s12021-014-9244-3

Begley, C. G., and Ellis, L. M. (2012). Drug development: raise standards for preclinical cancer research. *Nature* 483, 531–533. doi: 10.1038/483531a

Begley, C. G., and Ioannidis, J. P. (2015). Reproducibility in science: improving the standard for basic and preclinical research. *Circ. Res.* 116, 116–126. doi: 10.1161/CIRCRESAHA.114.303819

Bjerke, I. E., Øvsthus, M., Papp, E. A., Yates, S. C., Silvestri, L., Fiorilli, J., et al. (2018). Data integration through brain atlasing: human brain project tools and strategies. *Eur. Psychiatry* 50, 70–76. doi: 10.1016/j.eurpsy.2018.02.004

Button, K. S., Ioannidis, J. P., Mokrysz, C., Nosek, B. A., Flint, J., Robinson, E. S., et al. (2013). Power failure: why small sample size undermines the reliability of neuroscience. *Nat. Rev. Neurosci.* 14, 365–376. doi: 10.1038/nrn3475

Committee on Toward an Open Science Enterprise, Board on Research Data, and Information and Affairs PaG, (2017). *Open Science by Design: Realizing a Vision for 21st Century Research*. Washinghton, DC: The National Academies Press.

Commowick, O., Istace, A., Kain, M., Laurent, B., Leray, F., Simon, M., et al. (2018). Objective evaluation of multiple sclerosis lesion segmentation using a data management and processing infrastructure. *Sci. Rep.* 8:13650. doi: 10.1038/s41598-018-31911-7

Deruelle, T., Perles-Barbacaru, A., Kober, F., Noblet, V., Delzescaux, T., Barbier, E., et al. (2020). A Multicenter preclinical MRI study: definition of rat brain relaxometry referecne maps. *Front. ICT Sect. Comput. Image Anal. Rev.* doi: 10.1101/2020.02.06.928549

Gibaud, B., Kassel, G., Dojat, M., Batrancourt, B., Michel, F., Gaignard, A., et al. (2011). NeuroLOG: sharing neuroimaging data using an ontology-based federated approach. *AMIA Annu. Symp. Proc.* 2011, 472–480.

Glatard, T., Kiar, G., Aumentado-Armstrong, T., Beck, N., Bellec, P., Bernard, R., et al. (2018). Boutiques: a flexible framework to integrate command-line applications in computing platforms. *Gigascience* 7:giy016. doi: 10.1093/gigascience/giy016

Glatard, T., Lartizien, C., Gibaud, B., da Silva, R. F., Forestier, G., Cervenansky, F., et al. (2013). A virtual imaging platform for multi-modality medical image simulation. *IEEE Trans. Med. Imag.* 32, 110–118. doi: 10.1109/TMI.2012.2220154

Hatt, M., Laurent, B., Ouahabi, A., Fayad, H., Tan, S., Li, L., et al. (2018). The first MICCAI challenge on PET tumor segmentation. *Med. Image Anal.* 44, 177–195. doi: 10.1016/j.media.2017.12.007

Ingre, M. (2013). Why small low-powered studies are worse than large high-powered studies and how to protect against "trivial" findings in research: comment on Friston (2012). *Neuroimage* 81, 496–498. doi: 10.1016/j.neuroimage.2013.03.030

Kennedy, D. N., Abraham, S. A., Bates, J. F., Crowley, A., Ghosh, S., Gillespie, T., et al. (2019). Everything matters: the repronim perspective on reproducible neuroimaging. *Front. Neuroinform.* 13:1. doi: 10.3389/fninf.2019.00001

Lartizien, C., Gibaud, B., da Silva, R. F., Forestier, G., Cervenansky, F., et al. (2013). A virtual imaging platform for multi-modality medical image simulation. *IEEE Trans. Med. Imaging* 32, 110–118. doi: 10.1109/TMI.2012.2220154

Lee, D., Ruffins, S., Ng, Q., Sane, N., Anderson, S., and Toga, A. (2010). MBAT: a scalable informatics system for unifying digital atlasing workflows. *BMC Bioinformatics* 11:608. doi: 10.1186/1471-2105-11-608

Mackenzie-Graham, A. J., Van Horn, J. D., Woods, R. P., Crawford, K. L., and Toga, A. W. (2008). Provenance in neuroimaging. *Neuroimage* 42, 178–195. doi: 10.1016/j.neuroimage.2008.04.186

Micard, E., Husson, D., CIC-IT Team, and Felblinger, J. (2016). ArchiMed: a data management system for clinical research in imaging. *Front ICT Sect. Comput. Image Anal.* doi: 10.3389/fict.2016.00031

Minsky, M. (1986). *The Society of Mind*. New York: Simon & Schuter.

Musen, M. (2015). The Protégé project: a look back and a look forward. *AI Matters* 1, 4–12.

Poldrack, R. A., Baker, C. I., Durnez, J., Gorgolewski, K. J., Matthews, P. M., Munafo, M. R., et al. (2017). Scanning the horizon: towards transparent and reproducible neuroimaging research. *Nat. Rev. Neurosci.* 18, 115–126. doi: 10.1038/nrn.2016.167

Prescott, M. J., and Lidster, K. (2017). Improving quality of science through better animal welfare: the NC3Rs strategy. *Lab. Anim.* 46, 152–156. doi: 10.1038/laban.1217

Sena, E. S., van der Worp, H. B., Bath, P. M., Howells, D. W., and Macleod, M. R. (2010). Publication bias in reports of animal stroke studies leads to major overstatement of efficacy. *PLoS Biol.* 8:e1000344. doi: 10.1371/journal.pbio.1000344

Sunkin, S. M., Ng, L., Lau, C., Dolbeare, T., Gilbert, T. L., Thompson, C. L., et al. (2013). Allen Brain Atlas: an integrated spatio-temporal portal for exploring the central nervous system. *Nucleic Acids Res.* 41, D996–D1008. doi: 10.1093/nar/gks1042

Temal, L., Dojat, M., Kassel, G., and Gibaud, B. (2008). Towards an ontology for sharing medical images and regions of interest in neuroimaging. *J. Biomed. Inform.* 41, 766–778. doi: 10.1016/j.jbi.2008.03.002

Tsilidis, K. K., Panagiotou, O. A., Sena, E. S., Aretouli, E., Evangelou, E., Howells, D. W., et al. (2013). Evaluation of excess significance bias in animal studies of neurological diseases. *PLoS Biol.* 11:e1001609. doi: 10.1371/journal.pbio.1001609

Wang, N., Anderson, R., Badea, A., Cofer, G., Dibb, R., Qi, Y., et al. (2018). Whole mouse brain structural connectomics using magnetic resonance histology. *Brain Struct. Funct.* 223, 4323–4335. doi: 10.1007/s00429-018-1750-x

Wilkinson, M. D., Dumontier, M., Aalbersberg, I. J., Appleton, G., Axton, M., and Baak, A. (2016). The FAIR guiding principles for scientific data management and stewardship. *Sci Data* 3:160018. doi: 10.1038/s41597-019-0009-6

Conflict of Interest: The authors declare that the research was conducted in the absence of any commercial or financial relationships that could be construed as a potential conflict of interest.

frontiers in Neuroinformatics

TECHNOLOGY AND CODE
published: 28 May 2020
doi: 10.3389/fninf.2020.00024

Sammba-MRI: A Library for Processing SmAll-MaMmal BrAin MRI Data in Python

Marina Celestine [1,2†], Nachiket A. Nadkarni [1,2†], Clément M. Garin [1,2], Salma Bougacha [1,2,3,4†] and Marc Dhenain [1,2]*

[1] UMR9199 Laboratory of Neurodegenerative Diseases, Centre National de la Recherche Scientifique (CNRS), Fontenay-aux-Roses, France, [2] MIRCen, Institut de Biologie François Jacob, Commissariat à l'Energie Atomique et aux Energies Alternatives (CEA), Fontenay-aux-Roses, France, [3] UMR-S U1237 Physiopathologie et imagerie des troubles Neurologiques (PhIND), INSERM, Université de Caen-Normandie, GIP Cyceron, Caen, France, [4] Normandie Université, UNICAEN, PSL Research University, EPHE, Inserm, U1077, CHU de Caen, Neuropsychologie et Imagerie de la Mémoire Humaine, Caen, France

Small-mammal neuroimaging offers incredible opportunities to investigate structural and functional aspects of the brain. Many tools have been developed in the last decade to analyse small animal data, but current softwares are less mature than the available tools that process human brain data. The Python package Sammba-MRI (SmAll-MaMmal BrAin MRI in Python; http://sammba-mri.github.io) allows flexible and efficient use of existing methods and enables fluent scriptable analysis workflows, from raw data conversion to multimodal processing.

Keywords: processing pipeline, MRI, registration, small animal neuroimaging, Python

OPEN ACCESS

Edited by:
Jan G. Bjaalie, University of Oslo, Norway

Reviewed by:
Luz Maria Alonso-Valerdi, Monterrey Institute of Technology and Higher Education (ITESM), Mexico
Eszter Agnes Papp, University of Oslo, Norway

***Correspondence:**
Marc Dhenain
marc.dhenain@cea.fr

† These authors have contributed equally to this work

Received: *31 May 2019*
Accepted: *23 April 2020*
Published: *28 May 2020*

Citation:
Celestine M, Nadkarni NA, Garin CM, Bougacha S and Dhenain M (2020) Sammba-MRI: A Library for Processing SmAll-MaMmal BrAin MRI Data in Python. Front. Neuroinform. 14:24. doi: 10.3389/fninf.2020.00024

1. INTRODUCTION

The use of magnetic resonance imaging (MRI) methods in animals provides considerable benefits for improving our understanding of brain structure and function in health and diseases. The greatest advantages of preclinical MRI include group homogeneity and the opportunity to acquire a high amount of information repeated as needed. This added value, together with practical and ethical considerations, resulted in an increase of the use of small-mammal MRI in research. In human brain imaging, a large variety of high level software solutions is available for MRI preprocessing and analysis (e.g., SPM[1], FSL[2], or AFNI[3]). Less Free and Open Source Software (FOSS) are already available to analyse animal MRI. Atlas-based Imaging Data Analysis of structural and functional mouse brain MRI (AIDAmri) (Pallast et al., 2019) package allows registration of functional and diffusion mouse brain MRI with the Allen Mouse Brain Atlas (Allen Institute for Brain Science, 2004; Lein et al., 2007). The SAMRI (Small Animal Magnetic Resonance Imaging) package provides fMRI preprocessing, metadata parsing, and data analysis functions optimized for mouse brains (Ioanas et al., 2020). Today, there is still a need for other efficient and collaborative tools that would facilitate the adoption and dissemination of standardized pre-processing strategies for small animal MRI. Sammba-MRI was designed to process MR images, including anatomical, functional, and perfusion images. It allows to preprocess image dataset (conversion to NIfTI, bias correction), register images to templates or atlases, and perform perfusion measures.

[1] https://www.fil.ion.ucl.ac.uk/spm/software/
[2] http://freesurfer.net/
[3] https://afni.nimh.nih.gov/

2. WORKFLOW

2.1. Tools: Python Ecosystem and Neuroimaging Software Packages

With its FOSS dependency stack and its growing neuroimaging community Python has been naturally the language of choice for our package. The scientific Python libraries used inSammba-MRI are NumPy (Oliphant, 2006), SciPy (Millman and Aivazis, 2011), the neuroimaging data analysis tools nibabel[4], Nilearn (Abraham et al., 2014) and Nipype (Gorgolewski et al., 2011). Visualization functionality depends on Matplotlib (Hunter, 2007) or Graphviz (Gansner and North, 2000), but neither is required to perform MRI data processing.

Via Nipype, we utilize basic MRI preprocessing functions from AFNI (Cox, 1996), FSL (Jenkinson et al., 2012) and ANTs (Avants et al., 2009) packages. The dependency on the efficient but non open-source brain segmentation RATs tool (Oguz et al., 2014) is optional.

More specifically, Sammba-MRI and the examples provided in its manual depends on the following libraries: Nipype $\geq$ 1.0.4; Nilearn $\geq$ 0.4.0; Numpy $\geq$ 1.14; SciPy $\geq$ 0.19; Nibabel $\geq$ 2.0.2; Sklearn $\geq$ 0.19; matplotlib $\geq$ 1.5.1; nose $\geq$ 1.2.1; doctest-ignore-unicode; DICOM ToolKit package as well as FSL (version 5.0), AFNI, ANTs, and RATS.

2.2. Code Design

Sammba-MRI is developed within GitHub development platform[5]. Coding guidelines follow the model of Nilearn and other successfully adopted packages (e.g., Scikit-learn Pedregosa et al., 2011) to make the codebase understandable and easily maintainable[6]. Objects are used with parsimony: the different registration classes share all the same interface, and the brain extraction classes comply to the Nipype `BaseInterface`.

Effort is made to keep the code uniformly formatted and to use consistent naming for the functions and parameters following the coding conventions of Nilearn. Preprocessing building blocks and pipelines are automatically tested on light MRI data samples to ensure code quality. Finally, the user is guided through Sammba-MRI with extensive documentation including installation instructions, application programming interface (API) reference, pipeline graphs, and practical examples based on publicly available small animal neuroimaging datasets.

An overview of the modules used to manipulate images is presented in **Figure 1**. These modules are implemented either as "stand-alone" (i.e., `bias_correction`) or as ready-to-use pipelines (i.e., `TemplateRegistrator`).

2.3. DICOM to NIfTI Conversion

Sammba-MRI allows to convert Bruker DICOM (digital imaging and communications in medicine) files to the standard Neuroimaging Informatics Technology Initiative format (NIfTI-1) and extracts extensive information using DCMTK package (Eichelberg et al., 2004). Bruker files conversion is an active development field, with various available tools handling DICOM (e.g., dicomifier[7]) or not (e.g., bru2nii[8], Bruker2nifti[9], bruker2nifti[10]). Finally, ParaVision 360 with the latest patch 1.1 can export the NIFTI format since February 2019. Our implementation is meant to be a light helper function, allowing to handle the conversion on the fly. It has been tested only for Paravision 6 and a limited number of imaging sequences.

2.4. Bias Field Correction

Intensity non-uniformity modeling is essential in preclinical studies because the intensity gradient corrupting MR images becomes particularly pronounced at high field strengths (Boyes et al., 2008). Sammba-MRI relies on AFNI's `3dUnifize` to correct for intensity bias in anatomical images, and on `N4BiasFieldCorrection` function of the ANTs package (Tustison et al., 2010) for the other modalities. `3dUnifize` is also used to aid brain extraction, as detailed in the following paragraph.

2.5. Skull-Stripping

Skull-stripping is a critical early step in processing MR images from small animals. Various automatic rodent-specific softwares (Chou et al., 2011; Oguz et al., 2014) or adaptations of human algorithms (Wood et al., 2013; AFNI's 3dskullstrip -rat) are freely available for research purposes. We choose to rely on the LOGISMOS-based graph segmentation (Yin et al., 2010) based on grayscale mathematical morphology RATS software (Oguz et al., 2014) because of its good performance across a wide range of datasets (Sargolzaei et al., 2018). An alternative to the free but non-open source RATS tool is also available, based on an adaptation of the human histogram-based brain extraction method of Nilearn. This method can be used in any pipeline by setting the parameter `use_rats_tool` to `False`. Because intensity inhomogeneity can hamper the performance of automatic skull-stripping, prior bias field correction is usually recommended (Sled et al., 1998) and is performed by default with `3dUnifize`. The helper function `brain_segmentation_report` from Sammba-MRI `segmentation` module allows to efficiently tune the initial intensity threshold used in bias correction by producing for a given set of thresholds 5 informative measures characterizing the extracted mask to bypass time consuming repetitive visual checks. The returned features consist of the total volume of the extracted mask, its anteroposterior length, its right-left width, and its inferior-superior height as well as the sample Pearson's product-moment correlation coefficient between the brain mask image and its reflection with respect to the estimated mid-sagittal plane (Powell et al., 2016).

2.6. Registrations

Several registration algorithms are implemented within Sammba-MRI. First, rigid-body registration can be performed to roughly align individual images from the same modality or from different modalities. It minimizes normalized mutual information between brain extracted images. This registration

[4]https://nipy.org/nibabel/

[5]https://github.com/sammba-mri/sammba-mri

[6]http://gael-varoquaux.info/programming/software-design-for-maintainability.html

[7]https://github.com/lamyj/dicomifier

[8]https://github.com/neurolabusc/Bru2Nii

[9]https://github.com/CristinaChavarrias/Bruker2nifti

[10]https://github.com/SebastianoF/bruker2nifti

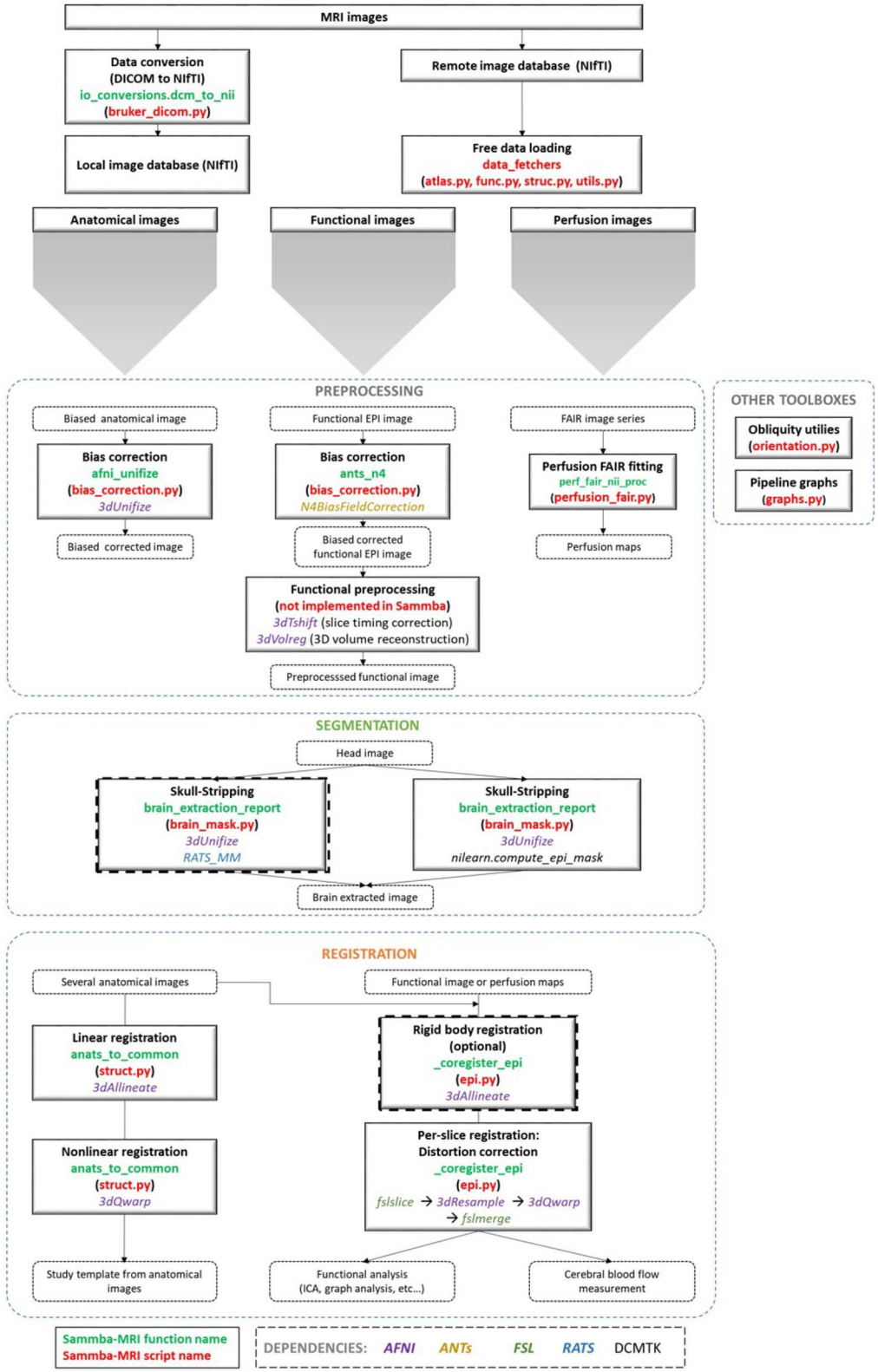

FIGURE 1 | Sammba-MRI workflow. Anatomical, functional, or perfusion images are imported from MRI local scanners or databases. They are analyzed using different preprocessing, segmentation and registration modules. Each function (green) and python-scripts (red) of Sammba-MRI are presented. Library dependencies are specified with color codes.

is finally estimated and applied to the whole head images. Second, linear registration estimates linear transforms between a source image and a reference image. It relies on AFNI's 3dAllineate function. Linear registration is more efficient when performed on brain-extracted rather than on whole head images. Third, non-linear registration (piecewise polynomial C^1 diffeomorphism) between a source image and a reference image can also performed. It relies on AFNI's 3dQwarp and iterations toward patch size reduction until a maximum refinement "level" is reached. Unlike linear registration, it is more efficient when computed using whole head images.

2.6.1. Group-Wise Registration and Study-Template

Group-wise registration aims to align all images from different animals within a common space, resulting in an average brain (study template) that represents the commonalities among individual brain anatomies of a particular population. Using a study template eliminates possible bias toward external features and improves subsequent analyses (De Feo and Giove, 2019). Sammba-MRI implements the multi-level, iterative scheme proposed by Kovačević et al. (2005) to create a fine anatomical template from individual anatomical MRI scans. A first rough template is obtained by averaging bias corrected head images centered on their respective brain mask centroids. Then the individual images are registered to this template. This process of successive averaging/registration is iterated while increasing the number of degrees of freedom of the estimated transform and updating the target template (see Nadkarni et al., 2019 for a detailed description of the pipeline).

2.6.2. Inter-Modality Registration

Several multimodal images can be recorded from a single animal, including structural imaging with different contrasts, blood-oxygenation-level-dependent (BOLD) and arterial spin labeling (ASL) MRI. BOLD imaging is largely used to investigate brain function in response to specific tasks or in the absence of explicit tasks (i.e., in resting state conditions) (Glover, 2011). ASL is an attractive method to image the vascular system by directly measuring blood flow (Kober et al., 2008).

In addition to the inherent difficulties in intermodality registration (Ashburner and Friston, 1997), severe image artifacts can corrupt BOLD or ASL scans resulting in a low signal-to-noise ratio (SNR). For instance, the echo planar imaging (EPI) technique widely used in functional and perfusion imaging suffers from non-linear geometric and intensity distortions caused by static magnetic field inhomogeneity that worsen at higher field strengths (Hong et al., 2015).

Thus a specific module called `_coregister_epi` was developed to register anatomical and EPI scans from individual animals. Anatomical images are first reoriented to match EPI images. Next, the reoriented anatomical images and the EPI scans are split into 2D slices along the z-direction (according to the slice geometry of EPI). Each EPI slice then undergoes a non-linear registration to match the corresponding anatomical slice. This per-slice registration corrects for EPI distortion while being more conservative than a global 3D non-linear registration.

3. PIPELINES

Sammba-MRI proposes two ready-to-use pipelines to perform spatial registrations to a population or standard reference template as well as inter-modalities registration between anatomical, functional, or perfusion images. These pipelines have been tested throughout the different stages of their development process on various datasets from mice, rats and mouse lemurs and used in several publications from our lab (Garin et al., 2018, 2019; Nadkarni et al., 2019). The two pipelines are called `Coregistrator` and `TemplateRegistrator`.

All pipelines start with bias field correction for the individual images, involve skull-stripping and specific registration algorithms depending on image modality.

3.1. Registration Between Anatomical Images and Another Modality:`Coregistrator`

Intra-subject registration between an anatomical scan and another modality (BOLD or ASL) is handled in the individual space through the `Coregistrator` class from the `registration` module (**Figure 2**).

```
from sammba.registration import
    Coregistrator
coregistrator = Coregistrator(
brain volume=400)
```

Multimodal processing slightly differs between modality. Thus, user can choose modality of interest and the critical parameters that lead to the best registration.

BOLD scans are preprocessed using the same usual steps for human data with optional slice timing correction, bias field correction, realignment to the first volume and computation of the temporal mean of all the volumes. The corresponding structural scan is then registered to the average BOLD scan. Since this is a critical step, the user can choose either to pursue with human-like pipeline by estimating a rigid body functional-to-structural transform and applying its inverse to the structural image, or to assume that the head motion between the two scans is negligible. In all cases, it is better to only reorient the anatomical image to match the modality of interest. Finally, per-slice-based registration is performed as described in *section 2.6.2*.

```
coregistrator.fit_anat(
    'mouse01_t1.nii.gz')
coregistrator.fit_modality(
    'mouse01_t2.nii.gz',
    'func',
    slice_timing=True,
    reorient_only=True)
```

Sammba-MRI was also designed to analyse ASL scans to perform perfusion measures. This analysis relies on Bruker-FAIR (Flow-sensitive Alternating Inversion Recovery) EPI sequences. Quantitative CBF maps are first estimated using `perf_fair_nii_proc` function from the `modality_processor` module. Then Sammba-MRI allows to preprocess functional ASL scans with the equilibrium magnetization maps (M0) used as the representative volume for

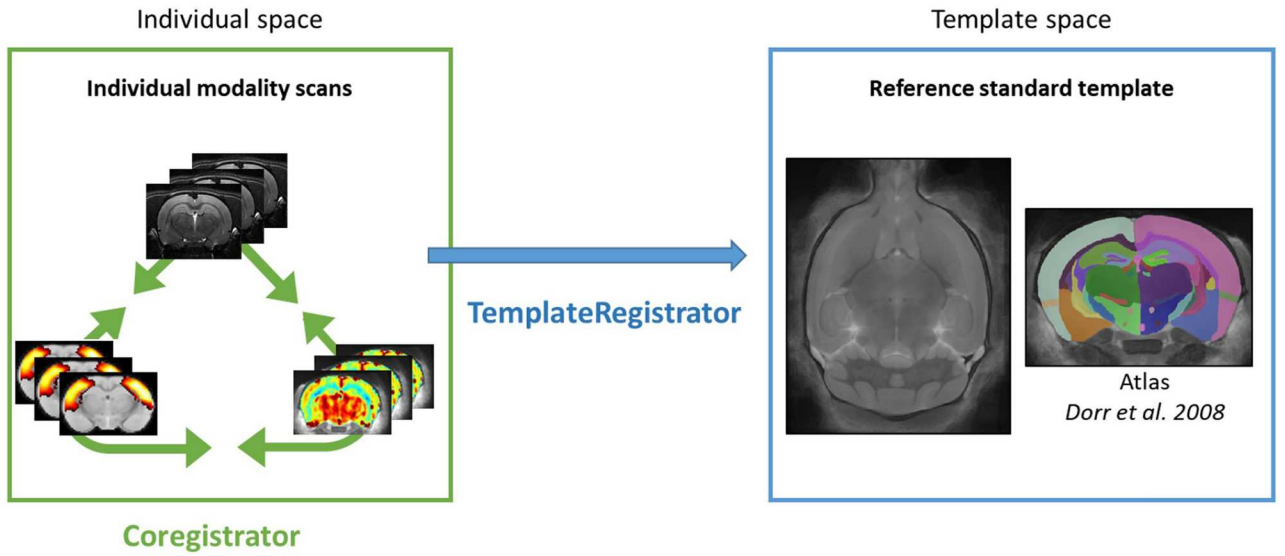

FIGURE 2 | Sammba-MRI pipelines. Color box represents spaces in which individual images are registered. Registration between individual modalities is performed by Coregistrator class (green arrow). Registration of individual modality images to a reference standard template space is performed by TemplateRegistrator class (blue arrow).

registration. The M0 volume is aligned to the anatomical, first with a rigid body registration and then on a per-slice basis.

```
coregistrator.fit_anat(
    'mouse01_t1.nii.gz')
coregistrator.fit_modality(
    'mouse01_t2.nii.gz',
    'perf',
    reorient_only=True)
```

3.2. Template-Based Multi-Modal Processing: `TemplateRegistrator`

Multimodal images (anatomical, functional, or perfusion MRI) can be handled in the template space through the `TemplateRegistrator` class. This pipeline matches individual images to a reference template, a necessary step for group studies (**Figure 2**).

3.2.1. Template Matching

Sammba-MRI proposes to download reference templates both for mouse and rat brains. The user needs to specify the path to the template of his choice to the `TemplateRegistrator` class from the `registration` module.

```
from sammba.registration import
TemplateRegistrator
registrator=TemplateRegistrator(
'dorr_t2.nii.gz',
brain_volume=400)
registrator.fit('mouse01_t1.nii.gz')
```

3.2.2. BOLD and ASL Preprocessing

BOLD and ASL preprocessing can also be performed in template space with `TemplateRegistrator`. The structural-to-template warp, the functional-to-structural rigid body transform and the perslice functional-to-structural warps are combined and applied in a one-big-step transformation to the functional data to minimize interpolation errors. The `TemplateRegistrator` class encompasses an `inverse_transform_towards_modality` method to bring an image from the reference space to the individual's space.

4. RESULTS

Sammba-MRI is available through the GitHub platform[11] and was tested using different image datasets.

4.1. Group-Wise Registration, Registration of Anatomical Images to a Common Space, and Template Creation

First, we evaluated group-wise registration and template creation using a dataset of *in vivo* T2-weighted images of 10 Sprague-Dawley rat brains (Lancelot et al., 2014). The scans were acquired using a 7.0 T Bruker scanner at 100 × 100 × 500 μm resolution using 30 different slices. We used `anats_to_common` to register images from the different animals and create a group average template (**Figure 3**).

For comparison purposes, the registration between images from each animal was also performed using algorithms from SPM8[12] with the SPMMouse toolbox[13] (Sawiak et al., 2009), a reference method for image-registrations. The brain images were segmented into gray (GM) and white matter (WM) tissue

[11] https://sammba-mri.github.io/introduction.html#installation
[12] www.fil.ion.ucl.ac.uk/spm
[13] http://spmmouse.org

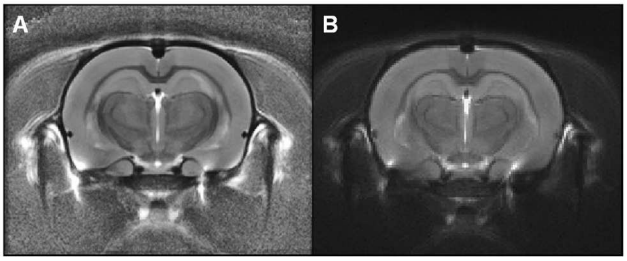

FIGURE 3 | Rat templates issued from Sammba-MRI **(A)** or SPM-based **(B)** registrations. These templates were calculated from anatomical images of 10 animals. Visual observation suggests similar quality of the two templates.

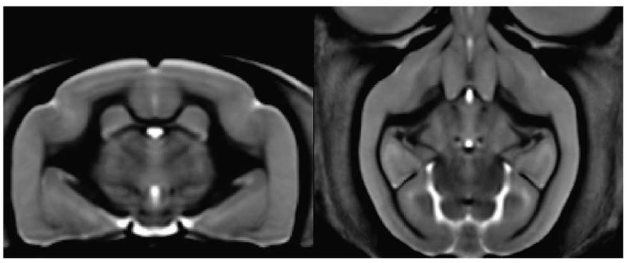

FIGURE 4 | Mouse lemur template from 34 animals. Coronal section of the mouse lemur MRI template (level of hippocampus).

probability maps using locally developed priors, then spatially transformed to a standard space. Priors were based on 100 × 100 × 100 μm resolution images and 134 slices. Affine regularization was set for an average-sized template, with a bias non-uniformity FWHM cut off of 10mm, a 5mm basis-function cut off and sampling distance of 0.3 mm. The resulting GM and WM portions were output in rigid template space, and DARTEL (Ashburner, 2007) was used to create non-linearly registered maps for each animal and common templates for the cohort of animals. The deformation fields were applied to the MR images of each animal and the resulting images were averaged to create a template. **Figure 3** shows the template obtained with SPM/Dartel. No obvious difference could be identified between the two templates.

Sammba-MRI adapts to different small animal species. **Figure 4** shows a template of mouse lemurs as another example (Nadkarni et al., 2018).

4.2. Validation of Template Matching

The Sprague-Dawley dataset is associated to brain segmentations into 28 regions for each animal (Lancelot et al., 2014). It also includes a study-template and an atlas based on segmentation of this template into 28 regions. Each image of the 12 individual animal was registered to the template using Sammba-MRI and the deformation fields were applied to the segmented images of each animal. We then measured the regional overlap between each region of the transformed atlases of each animal and the template-segmentation using Dice similarity coefficient ($2\frac{|A \cap B|}{|A|+|B|}$).

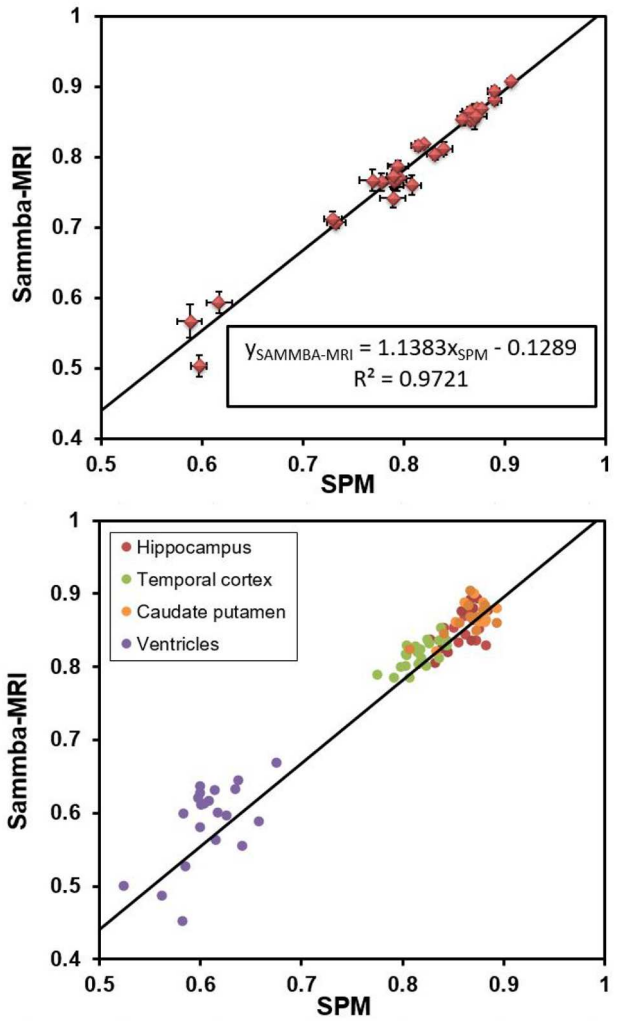

FIGURE 5 | Dice coefficients obtained after registering individual images to a rat brain templates with Sammba-MRI and SPM/Dartel. **(Top)** Comparisons showing 27 brains regions. Bars represents standard error of the mean. **(Bottom)** Individual measures for four different brain regions.

The deformation fields calculated with SPM were also applied to the MR and segmented images of each animal. We also measured the regional overlap between each region of the SPM-transformed segmentations of each animal and the template-segmentation also using Dice similarity coefficient.

Figure 5 shows that Dice coefficients obtained with Sammba-MRI were highly correlated with those obtained using SPM mouse and outperformed those of SPM in several cases (points above the line). Regions with lower Dice values correspond to ventricles.

4.3. fMRI and Perfusion Modalities

Resting state fMRI allows to study temporally synchronized BOLD oscillations reflecting functionally connected brain

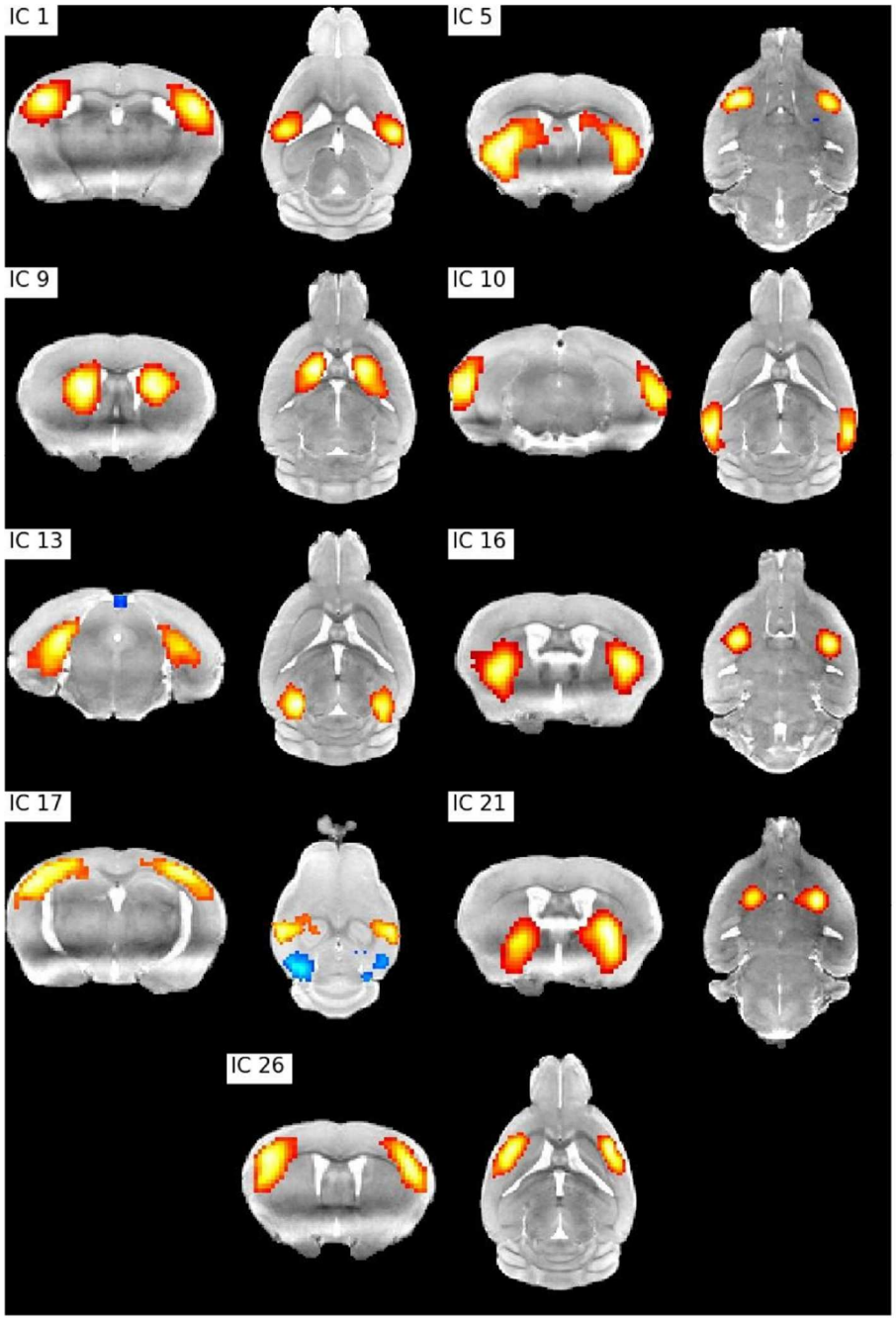

FIGURE 6 | ICA bilateral components. IC 1: Barrel field (i) cortex, IC 5: Lateral striatum, IC 9: Dorsal striatum (i), IC 10: Visual cortex, IC1 3: Hippocampus, IC 16: Dorsal striatum (ii), IC 17: Barrel field (ii) cortex, IC 21: Ventral striatum, IC 26: Supplementary cortex.

networks. As in human resting state fMRI, spatial networks can be extracted using Independent Components Analysis (ICA) (Zerbi et al., 2015; Grandjean et al., 2020). We preprocessed the publicly shared functional data from 15 mice (2–3 months old) from (Zerbi et al., 2015) paper with Sammba-MRI and performed a group ICA (Varoquaux et al., 2010) with 30 components. Relevant bilateral regions related to somatosensory, hippocampal, visual, basal ganglia, and sensorimotor networks were obtained without additional data post-processing (**Figure 6**).

To illustrate the perfusion processing pipeline, we used perfusion FAIR images from 30 C57BL/6J mice (6–8 months) to quantify CBF. **Figure 7** shows regional absolute CBF values. Perfusion values of 152±22 and 143±26 ml/100g/min in the hippocampus and temporal cortex, respectively. These values are lower than those reported by Kober et al. (208±20 and

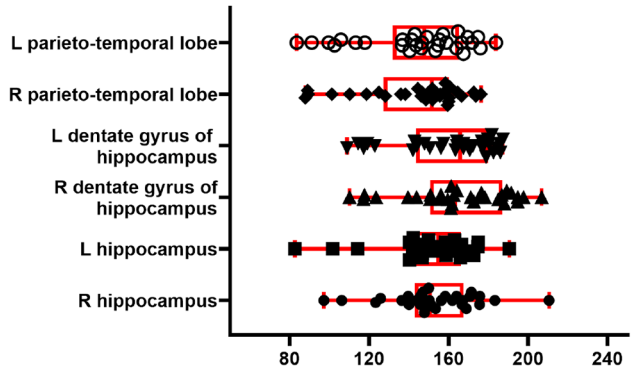

FIGURE 7 | CBF from 30 C57BL/6J mice. Boxplot shows median, interquartile range, upper and lower adjacent values for six brain region. Each dot represents regional CBF in ml/100g/min from one animal.

243±35 ml/100g/min in the hippocampus and cortex) with FAIR method (Kober et al., 2008). They are higher than those (118±6 ml/100g/min in the cortex) reported with the same method by (Zheng et al., 2010).

5. BIG DATA, REPRODUCIBILITY, COLLABORATION

The package design facilitates big data exploration: the user is able to run an entire analysis in a single Python script. Rerunning pipelines are optimized through Nipype caching mechanism and long lasting steps (non-linear warping, perfusion fitting) are executed in parallel. We believe that reproducibility in the neuroimaging field is not possible without making the acquired images and the preprocessing code available to the community. For this reason, Sammba-MRI promotes the sharing of MRI data by providing utility functions to download public small animal brain MRI datasets and relies on it for demonstrating the package capabilities. In order to encourage external contributions, our library source code is hosted on the open collaborative GitHub platform and distributed under the CeCILL v2.1 license, a FOSS license adapted to both international and French legal matters allowing anyone to make changes and redistribute it. Sammba-MRI supports GNU/Linux and Mac OS X operating systems (OS), used by over 70% of neuroimagers (Hanke and Halchenko, 2011). So far, Sammba-MRI is designed for advanced users but documentation is provided to help novices.

6. CONCLUSION

By efficiently combining different existing human and animal neuroimaging tools, Sammba-MRI allows to tackle common processing issues in a fully automated fashion. High quality spatial registration can be easily performed, including template matching, between modalities registration as well as the creation of cohort-specific templates. Sammba-MRI also implements functional and perfusion MRI preprocessing methods and cerebral blood flow estimation for FAIR perfusion images. Emphasis is put on code readability and ease of use to favor contributions from the community.

DATA AVAILABILITY STATEMENT

The mouse lemur dataset can be automatically loaded through Sammba-MRI or directly from https://nitrc.org/projects/mouselemuratlas for the template and https://openneuro.org/datasets/ds001945 for the original anatomical images. The perfusion dataset will be made publicly available following publication.

ETHICS STATEMENT

The animal study was reviewed and approved by local ethics committees CEtEA-CEA DSV IdF.

AUTHOR CONTRIBUTIONS

SB designed the Sammba-architecture and its implementation on Github. SB, NN, and MC contributed code to the project. NN, CG, and MD contributed to data acquisition. SB wrote the first version of the manuscript with input from CG and NN. MC and MD wrote the final version of the manuscript.

FUNDING

This work was funding by French Public Investment Bank's ROMANE program.

ACKNOWLEDGMENTS

We thank the France-Alzheimer Association, Plan Alzheimer Foundation, the Foundation Vaincre-Alzheimer, and the French Public Investment Bank's ROMANE program for funding this study.

REFERENCES

Abraham, A., Pedregosa, F., Eickenberg, M., Gervais, P., Mueller, A., Kossaifi, J., et al. (2014). Machine learning for neuroimaging with scikit-learn. *Front. Neuroinform.* 8:14. doi: 10.3389/fninf.2014.00014

Allen Institute for Brain Science (2004). *Allen Mouse Brain Atlas*. Available online at: http://mouse.brain-map.org

Ashburner, J. (2007). A fast diffeomorphic image registration algorithm. *Neuroimage* 38, 95–113. doi: 10.1016/j.neuroimage.2007.07.007

Ashburner, J., and Friston, K. (1997). Multimodal image coregistration and partitioning-a unified framework. *Neuroimage* 6, 209–217. doi: 10.1006/nimg.1997.0290

Avants, B. B., Tustison, N., and Song, G. (2009). Advanced normalization tools (ANTS). *Insight J.* 2, 1–35.

Boyes, R. G., Gunter, J. L., Frost, C., Janke, A. L., Yeatman, T., Hill, D. L., et al. (2008). Intensity non-uniformity correction using N3 on 3-T scanners with multichannel phased array coils. *Neuroimage* 39, 1752–1762. doi: 10.1016/j.neuroimage.2007.10.026

Chou, N., Wu, J., Bingren, J. B., Qiu, A., and Chuang, K.-H. (2011). Robust automatic rodent brain extraction using 3-D pulse-coupled neural networks (PCNN). *IEEE Trans. Image Process.* 20, 2554–2564. doi: 10.1109/TIP.2011.2126587

Cox, R. W. (1996). AFNI: software for analysis and visualization of functional magnetic resonance neuroimages. *Comput. Biomed. Res.* 29, 162–173. doi: 10.1006/cbmr.1996.0014

De Feo, R., and Giove, F. (2019). Towards an efficient segmentation of small rodents brain: a short critical review. *J. Neurosci. Methods* 323, 82–89. doi: 10.1016/j.jneumeth.2019.05.003

Eichelberg, M., Riesmeier, J., Wilkens, T., Hewett, A. J., Barth, A., and Jensch, P. (2004). "Ten years of medical imaging standardization and prototypical implementation: the DICOM standard and the OFFIS DICOM toolkit (DCMTK)," in *Medical Imaging 2004: PACS and Imaging Informatics*, Vol. 5371 (International Society for Optics and Photonics), 57–69. doi: 10.1117/12.534853

Gansner, E. R., and North, S. C. (2000). An open graph visualization system and its applications to software engineering. *Softw. Pract. Exp.* 30, 1203–1233. doi: 10.1002/1097-024X(200009)30:11<1203::AID-SPE338>3.0.CO;2-N

Garin, C. M., Nadkarni, N. A., Bougacha, S., Picq, J.-L., Pepin, J., Flament, J., et al. (2018). "Resting state, gluCEST and anatomical MRI approaches at 11.7T for brain aging studies in a non-human primate," in *Proceedings of the Joint Annual Meeting of the International Society for Magnetic Resonance in Medicine and European Society for Magnetic Resonance in Medicine and Biology* (Paris).

Garin, C. M., Nadkarni, N. A., Landeau, B., Chetelat, G., Picq, J.-L., Bougacha, S., et al. (2019). Resting state cerebral networks in mouse lemur primates: from multilevel validation to comparison with humans. *bioRixv*. doi: 10.1101/599423

Glover, G. H. (2011). Overview of functional magnetic resonance imaging. *Neurosurg. Clin. N. Am.* 22, 133–139. doi: 10.1016/j.nec.2010.11.001

Gorgolewski, K., Burns, C. D., Madison, C., Clark, D., Halchenko, Y. O., Waskom, M. L., et al. (2011). Nipype: a flexible, lightweight and extensible neuroimaging data processing framework in python. *Front. Neuroinform.* 5:13. doi: 10.3389/fninf.2011.00013

Grandjean, J., Canella, C., Anckaerts, C., Ayranci, G., Bougacha, S., Bienert, T., et al. (2020). Common functional networks in the mouse brain revealed by multi-centre resting-state fMRI analysis. *Neuroimage*, 205:116278. doi: 10.1016/j.neuroimage.2019.116278

Hanke, M., and Halchenko, Y. O. (2011). Neuroscience runs on GNU/Linux. *Front. Neuroinform.* 5:8. doi: 10.3389/fninf.2011.00008

Hong, X., To, X. V., Teh, I., Soh, J. R., and Chuang, K.-H. (2015). Evaluation of EPI distortion correction methods for quantitative MRI of the brain at high magnetic field. *Mag. Reson. Imaging* 33, 1098–1105. doi: 10.1016/j.mri.2015.06.010

Hunter, J. D. (2007). Matplotlib: A 2D graphics environment. *Comput. Sci. Eng.* 9:90. doi: 10.1109/MCSE.2007.55

Ioanas, H.-I., Marks, M., Garin, C., Dhenain, M., Yanik, M. F., and Rudin, M. (2020). An automated open-source workflow for standards-compliant integration of small animal magnetic resonance imaging data. *Front. Neuroinform.* 14:5. doi: 10.3389/fninf.2020.00005

Jenkinson, M., Beckmann, C. F., Behrens, T. E., Woolrich, M. W., and Smith, S. M. (2012). Fsl. *Neuroimage* 62, 782–790. doi: 10.1016/j.neuroimage.2011.09.015

Kober, F., Duhamel, G., and Cozzone, P. J. (2008). Experimental comparison of four FAIR arterial spin labeling techniques for quantification of mouse cerebral blood flow at 4.7 T. *NMR Biomed.* 21, 781–792. doi: 10.1002/nbm.1253

Kovačević, N., Henderson, J., Chan, E., Lifshitz, N., Bishop, J., Evans, A., et al. (2005). A three-dimensional MRI atlas of the mouse brain with estimates of the average and variability. *Cereb. Cortex* 15, 639–645. doi: 10.1093/cercor/bhh165

Lancelot, S., Roche, R., Slimen, A., Bouillot, C., Levigoureux, E., Langlois, J., et al. (2014). A multi-atlas based method for automated anatomical rat brain MRI segmentation and extraction of PET activity. *PLoS ONE* 9:e109113. doi: 10.1371/journal.pone.0109113

Lein, E. S., Hawrylycz, M. J., Ao, N., Ayres, M., Bensinger, A., Bernard, A., et al. (2007). Genome-wide atlas of gene expression in the adult mouse brain. *Nature* 445, 168–176. doi: 10.1038/nature05453

Millman, K. J., and Aivazis, M. (2011). Python for scientists and engineers. *Comput. Sci. Eng.* 13, 9–12. doi: 10.1109/MCSE.2011.36

Nadkarni, N. A., Bougacha, S., Garin, C., Dhenain, M., and Picq, J.-L. (2018). Digital templates and brain atlas dataset for the mouse lemur primate. *Data Brief* 21, 1178–1185. doi: 10.1016/j.dib.2018.10.067

Nadkarni, N. A., Bougacha, S., Garin, C., Dhenain, M., and Picq, J.-L. (2019). A 3D population-based brain atlas of the mouse lemur primate with examples of applications in aging studies and comparative anatomy. *Neuroimage* 185, 85–95. doi: 10.1016/j.neuroimage.2018.10.010

Oguz, I., Zhang, H., Rumple, A., and Sonka, M. (2014). RATS: rapid automatic tissue segmentation in rodent brain MRI. *J. Neurosci. Methods* 221, 175–182. doi: 10.1016/j.jneumeth.2013.09.021

Oliphant, T. E. (2006). *A Guide to NumPy*. Vol. 1. Trelgol Publishing.

Pallast, N., Diedenhofen, M., Blaschke, S., Wieters, F., Wiedermann, D., Hoehn, M., et al. (2019). Processing pipeline for atlas-based imaging data analysis of structural and functional mouse brain MRI (AIDAmri). *Front. Neuroinform.* 13:42. doi: 10.3389/fninf.2019.00042

Pedregosa, F., Varoquaux, G., Gramfort, A., Michel, V., Thirion, B., Grisel, O., et al. (2011). Scikit-learn: Machine learning in Python. *J. Mach. Learn. Res.* 12, 2825–2830.

Powell, N. M., Modat, M., Cardoso, M. J., Ma, D., Holmes, H. E., Yu, Y., et al. (2016). Fully-automated μMRI morphometric phenotyping of the Tc1 mouse model of Down syndrome. *PLoS ONE* 11:e0162974. doi: 10.1371/journal.pone.0162974

Sargolzaei, S., Cai, Y., Wolahan, S. M., Gaonkar, B., Sargolzaei, A., Giza, C. C., et al. (2018). "A comparative study of automatic approaches for preclinical MRI-based brain segmentation in the developing rat," in *2018 40th Annual International Conference of the IEEE Engineering in Medicine and Biology Society (EMBC)* (Honolulu, HI: IEEE), 652–655. doi: 10.1109/EMBC.2018.8512402

Sawiak, S., Wood, N., Williams, G., Morton, A., and Carpenter, T. (2009). Voxel-based morphometry in the R6/2 transgenic mouse reveals differences between genotypes not seen with manual 2D morphometry. *Neurobiol. Dis.* 33, 20–27. doi: 10.1016/j.nbd.2008.09.016

Sled, J. G., Zijdenbos, A. P., and Evans, A. C. (1998). A nonparametric method for automatic correction of intensity nonuniformity in MRI data. *IEEE Trans. Med. Imaging* 17, 87–97. doi: 10.1109/42.668698

Tustison, N. J., Avants, B. B., Cook, P. A., Zheng, Y., Egan, A., Yushkevich, P. A., et al. (2010). N4ITK: improved N3 bias correction. *IEEE Trans. Med. Imaging* 29:1310. doi: 10.1109/TMI.2010.2046908

Varoquaux, G., Sadaghiani, S., Pinel, P., Kleinschmidt, A., Poline, J.-B., and Thirion, B. (2010). A group model for stable multi-subject ICA on fMRI datasets. *Neuroimage* 51, 288–299. doi: 10.1016/j.neuroimage.2010.02.010

Wood, T. C., Lythgoe, D. J., and Williams, S. C. (2013). "rBET: making BET work for rodent brains," in *Proceedings of the 21th Meeting of the International Society for Magnetic Resonance in Medicine* (Salt Lake City, UT), Vol. 21, 2706.

Yin, Y., Zhang, X., Williams, R., Wu, X., Anderson, D. D., and Sonka, M. (2010). LOGISMOS - Layered Optimal Graph Image Segmentation of Multiple Objects and Surfaces: cartilage segmentation in the knee joint. *IEEE Trans. Med. Imaging* 29, 2023–2037. doi: 10.1109/TMI.2010.2058861

Zerbi, V., Grandjean, J., Rudin, M., and Wenderoth, N. (2015). Mapping the mouse brain with Rs-fMRI: an optimized pipeline for functional network identification. *Neuroimage* 123, 11–21. doi: 10.1016/j.neuroimage.2015.07.090

Zheng, B. W., Lee, P. T. H., and Golay, X. (2010). High-sensitivity cerebral perfusion mapping in mice by kbGRASE-fair at 9.4 t. *NMR Biomed.* 23, 1061–1070. doi: 10.1002/nbm.1533

Conflict of Interest: The authors declare that the research was conducted in the absence of any commercial or financial relationships that could be construed as a potential conflict of interest.

frontiers in Neuroinformatics

METHODS
published: 21 August 2020
doi: 10.3389/fninf.2020.00037

Nutil: A Pre- and Post-processing Toolbox for Histological Rodent Brain Section Images

Nicolaas E. Groeneboom, Sharon C. Yates, Maja A. Puchades and Jan G. Bjaalie**

Neural Systems Laboratory, Institute of Basic Medical Sciences, University of Oslo, Oslo, Norway

With recent technological advances in microscopy and image acquisition of tissue sections, further developments of tools are required for viewing, transforming, and analyzing the ever-increasing amounts of high-resolution data produced. In the field of neuroscience, histological images of whole rodent brain sections are commonly used for investigating brain connections as well as cellular and molecular organization in the normal and diseased brain, but present a problem for the typical neuroscientist with no or limited programming experience in terms of the pre- and post-processing steps needed for analysis. To meet this need we have designed *Nutil*, an open access and stand-alone executable software that enables automated transformations, post-processing, and analyses of 2D section images using multi-core processing (OpenMP). The software is written in C++ for efficiency, and provides the user with a clean and easy graphical user interface for specifying the input and output parameters. *Nutil* currently contains four separate tools: (1) A transformation toolchain named "Transform" that allows for rotation, mirroring and scaling, resizing, and renaming of very large tiled tiff images. (2) "TiffCreator" enables the generation of tiled TIFF images from other image formats such as PNG and JPEG. (3) A "Resize" tool completes the preprocessing toolset and allows downscaling of PNG and JPEG images with output in PNG format. (4) The fourth tool is a post-processing method called "Quantifier" that enables the quantification of segmented objects in the context of regions defined by brain atlas maps generated with the *QuickNII* software based on a 3D reference atlas (mouse or rat). The output consists of a set of report files, point cloud coordinate files for visualization in reference atlas space, and reference atlas images superimposed with color-coded objects. The *Nutil* software is made available by the Human Brain Project (https://www.humanbrainproject.eu) at https://www.nitrc.org/projects/nutil/.

Keywords: image processing, rodent atlas, brain, QuickNII, QUINT, workflow

OPEN ACCESS

Edited by:
David A. Gutman,
Emory University, United States

Reviewed by:
Sweyta Lohani,
Yale University, United States
Bennett Allan Landman,
Vanderbilt University, United States

****Correspondence:***
Maja A. Puchades
m.a.puchades@medisin.uio.no
Jan G. Bjaalie
j.g.bjaalie@medisin.uio.no

Received: *21 June 2019*
Accepted: *17 July 2020*
Published: *21 August 2020*

Citation:
Groeneboom NE, Yates SC, Puchades MA and Bjaalie JG (2020) Nutil: A Pre- and Post-processing Toolbox for Histological Rodent Brain Section Images. Front. Neuroinform. 14:37. doi: 10.3389/fninf.2020.00037

INTRODUCTION

The process of changing data from one "raw" format to another to make the data suitable for analysis – often referred to as data wrangling or data transformation – is generally required when employing standardized analytical pipelines. A common example is the pre-processing of magnetic resonance data, involving a set of operations to "clean" the raw images before they can

be analyzed and interpreted. In basic neuroscience, two-dimensional (2D) images depicting rodent histological brain sections are typical output of animal model studies designed to investigate brain structure, function, and disease. Large series of these images, generated with a broad repertoire of experimental techniques, serve as the starting point for quantification and mapping of features such as the distribution of molecules, presence of particular cell types, or connections between anatomical regions. The images commonly require transformation prior to analysis, but due to the sheer size and number of image files, transformations are difficult to execute and replicate for biological researchers with limited coding ability. Typically, researchers need access to technology packages such as *Adobe Photoshop*™, *GIMP*[1], or *NIH ImageJ* (Schneider et al., 2012), but these all have their own limitations such as file size restrictions or lack of parallel processing support. Some basic scripting ability and access to data analysis software such as *ImageMagick* (The ImageMagick Development Team, 2020), *R* (Chambers, 2008) or *Matlab* (MATLAB, 2010) are useful. However, even with these tools and skills, transformations can be time consuming when applied to hundreds of images for whole brain comparative studies.

With image pre-processing required for most analytic pipelines (Yates et al., 2019), there is a need for access to user-friendly tools that can perform the most commonly required transformations. Furthermore, for brain microscopy data, researchers typically endeavor to spatially analyze features in the images by sorting outputs according to anatomical brain region. In light of published 3D reference atlases for mouse and rat brains (Lein et al., 2007; Oh et al., 2014; Papp et al., 2014; Kjonigsen et al., 2015), and software for generating brain atlas maps that are customized to match the proportions and cutting plane of the sections (Puchades et al., 2019), we have created a pre- and post-processing toolbox for histological brain section images that aims to meet both these needs. An early beta version of the tool was an integral part of the QUINT workflow for quantification and spatial analysis of labeling in rodent brain sections (Yates et al., 2019), see https://www.youtube.com/watch?v=yPkAbSfla_c. Nutil has since been expanded and improved considerably with the present manuscript describing the full range of Nutil functionalities. Based on feedback from our users, we have implemented a proper graphical user interface (GUI) for entering analysis parameters and for selecting different options like i.e., object splitting or customized atlas regions. Nutil can also be used independently of the QUINT workflow to preprocess images in preparation for other downstream processes. It enables automated transformations such as rotation and scaling, cropping, resizing, and renaming; in addition to analytical post-processing of segmentations that are generated from the brain section images, based on input from customized reference atlas maps (**Figure 1**). *Nutil* is designed specifically for operations on very large images and is therefore optimized for speed, memory usage and parallelization. The toolbox is intended for use in combination with one of the open source image analysis tools that are currently available, e.g., *NIH ImageJ* (Schneider et al., 2012) or ilastik (Berg et al., 2019).

[1]www.gimp.org

OVERVIEW OF FUNCTIONALITY

Nutil aims to both simplify and streamline the mechanism of pre-and-post processing 2D brain image data. *Nutil* is developed as a stand-alone application for Windows with a GUI requiring little-to-no experience to execute. The user specifies the input and output parameters for the operations in a template in the GUI, which is saved as a text file (in.NUT format) prior to initiating the operation. Pre-processing operations include 2D transformations of extremely large tiled TIFF files (rotation, flipping, and scaling), in addition to renaming, copying, and downsizing (Transform). The tiled TIFF format was selected for the Transform operation as it allows for optimal memory usage, as well as being an output file type of microscope scanners. Some users may need to convert their images to tiled TIFF format to enable transformation with *Nutil* Transform, and so an image format converter (JPEG/PNG to tiled TIFF format) is included in the *Nutil* software (TiffCreator). To complete the set, *Nutil* also includes a resizing operation (Resize) that enables downscaling of PNG and JPEG images to PNG format. Post-processing with *Nutil* (Quantifier) is based on analysis of segmented images in the context of brain regions defined by a 3D reference atlas such as the Allen Adult Mouse brain reference atlas (Lein et al., 2007; Oh et al., 2014) or the Waxholm Space Atlas of the Sprague Dawley rat brain (Papp et al., 2014; Kjonigsen et al., 2015; Osen et al., 2019). All functions operate in batch mode, and operate in parallel on multiple CPUs.

Transform

The *Nutil* Transform function is seemingly straight-forward, since in reality it only applies a generic 2D TSR (Translation, Scaling, and Rotation) matrix to an image. However, due to the sheer size of the image files to be transformed, *Nutil* has been designed with several optimization methods to prevent memory problems and to increase execution speed. For example, a single image of size 70,000 × 50,000 pixels takes up almost 10 GB of memory, with a need for additional copies to be stored in memory during rotation. Even worse, if the user were to perform eight transformations on multiple cores, the amount of RAM required would exceed 160 GB.

In order to solve the memory problem, *Nutil* Transform (rotate, flipping, and renaming) operates on tiled TIFF files only, with a separate TiffCreator tool included for converting JPEG/PNG images to the required tiled TIFF format. Tiled TIFF files are effectively compressed (JPEG/LZW) folders of smaller-sized images (tiles) that collectively make up the entire image. By operating (loading/releasing) on these tiles instead of an entire image, memory consumption is greatly reduced; however, this comes at the expense of increased code complexity, with a requirement to keep track of/sort stacks of recently used tiles. To enhance execution speed, *Nutil* is written in C++, which is highly optimized for low-level execution of memory-intensive parallel code.

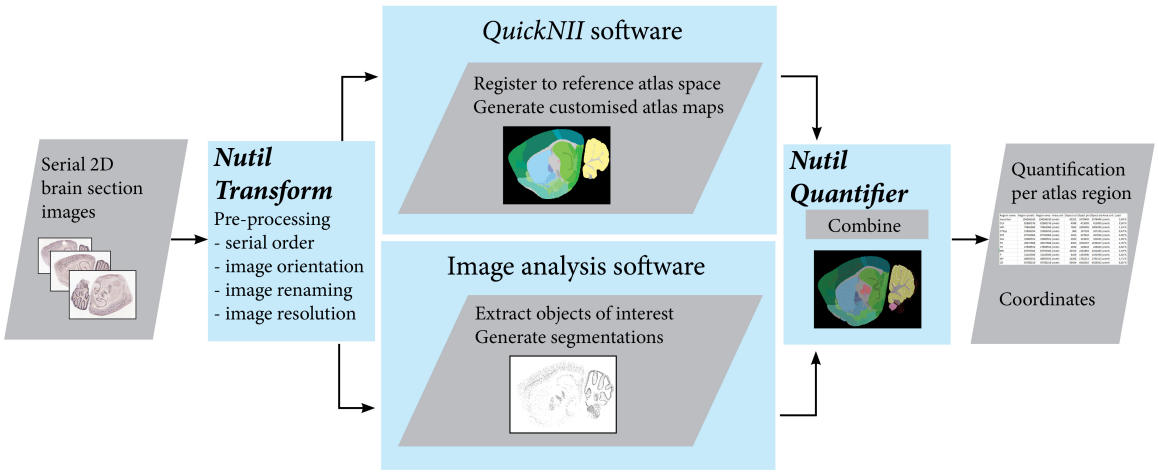

FIGURE 1 | The QUINT workflow utilizes three software tools to extract, quantify and spatially analyze labeled features in series of images of histological mouse or rat brain sections. Initially, the *Nutil* Transform operation is used to correct the orientation and serial order of the images, to rename the files, and to downscale the images. The images are then registered to a reference atlas with *QuickNII*, and segmented with an image analysis software such as *ilastik*. The atlas maps and segmentations are post-processed with *Nutil* Quantifier to extract quantifications per atlas region and coordinates for visualization in reference atlas space. Image Credit for 2D section images: Allen Institute.

Nutil performs two kinds of downsampling of TIFF images: original scanner images that are large (usually around 30,000 × 18,000 and up to 80,000 × 70,000 pixels) to about 1–25% of the original area, and original images to very small thumbnails. Nutil does not currently support any form of antialiasing when downsampling TIFF images, only pointwise sampling. In its most basic form, single pixels are selected as representative for the area. **Supplementary File 1** summarizes Nutil operating times for image transformations in batch mode on several platforms.

Pseudocode Block

1. Read input list of files with their corresponding 2D transform parameters.
2. For each input file, verify that parameters are correct and image files exist.
3. For each file (in separate threads) do:

    a. Open the input TIFF file, verify that it is indeed tiled.
    b. Calculate new file resolution and boundaries – rotating an image will alter the resolution.
    c. Perform 2D transformation on each separate tile, keep an optimized list of recently accessed tiles for speed improvements. Also, simultaneously calculate new bounding boxes for the rotated image (auto-cropping step).
    d. Save the rotated image to a temporary file, close file handle.
    e. Create a new file with auto-cropped boundaries calculated in (c) and start copying from the temporary file to the final image.
    f. If the thumbnails creation option is toggled, open the finished auto-cropped image and downsize it. Save as a.png (or.jpg) in a separate thumbnail folder. No anti-aliasing step is performed here.

TiffCreator

Even though the tiled TIFF format is useful, very few image services exist that are able to efficiently convert images to tiled TIFF format. Standard image software such as *GIMP* and *Adobe Photoshop* are certainly able to load tiled TIFFs (that are not too large), but are unable to save them. The conversion tool in *ImageMagick* can successfully create images, but require the knowledge of command line parameters in addition to being slow and non-parallelized. The *Nutil* TiffCreator function solves this problem by producing tiled TIFF files from JPEG or PNG images, and employs the support of multiple CPUs for efficient, parallelized operations. TiffCreator lets the user specify the input directory containing JPEG/PNG files and the output directory, in addition to some TIFF-specific parameters (size of sub-tiles, etc.).

Pseudocode Block

1. Read input directory and create a list of all image files.
2. For each file in the list

    a. Load the image
    b. Convert to a tiled TIFF format
    c. Save the tiled TIFF

Resize

The *Nutil* Resize operation is a helpful post processing operation that allows the user to downscale PNG and JPEG files in bulk. An input directory, output directory, compression type and resize factor are specified in the GUI, and the program automatically identifies and transforms all files from the source directory to the target directory. The resize factor can be either a fixed-width number or a percentage of the original size. Nutil does

not currently support enlargement of images as this serves no purpose in the context of histological image analysis. As with the other operations in *Nutil*, Resize operates in parallel and utilizes all (or as many as specified) cores on the system it is running.

Pseudocode Block

For each file in the list

1. Open the file
2. Resize the file (using either bilinear filtering or no filtering)
3. Save the file

Quantifier

Quantifier is a post processing operation for the extraction, quantification and spatial analysis of labeling in 2D rodent brain section images (for example, immunohistochemical labeling). Nutil contains all the necessary label files for analysis of features in the following atlases: Allen brain atlas Common Coordinate Framework v3, 2015 and 2017 versions (®2004 Allen Institute for Brain Science. Allen Mouse Brain Atlas. Available from: http://download.alleninstitute.org/informatics-archive/current-release/mouse_ccf/annotation/) (Lein et al., 2007; Oh et al., 2014) and the Waxholm Space Atlas of the Sprague Dawley rat brain v2 and v3 (Available from: https://www.nitrc.org/projects/whs-sd-atlas) (Papp et al., 2014; Kjonigsen et al., 2015; Osen et al., 2019). To run Quantifier, *Nutil* requires segmentations that are generated from the brain section images, with the labeling of interest displayed in a unique RGB color (Red Green Blue color model) and reference atlas maps customized to match the proportions and cutting plane of the sections (generated with the QuickNII software, available from: https://www.nitrc.org/projects/quicknii) (Puchades et al., 2019). Quantifications may be performed on the entire image or in regions defined by masks. *Nutil* quantifies labeling in each parcellated brain region, extracts spatial coordinates for visualization in 3D reference atlas space, and generates output including: reports (in CSV or HTML format), coordinates (in JSON format), and reference atlas map images superimposed with the extracted features that are color-coded according to their assigned anatomical location (Yates et al., 2019).

Quantifier starts by applying a breadth-first search (BFS) method to identify areas of interest in a series of images as specified by colors defined in the *Nutil* GUI. This method proceeds by separating foreground areas (of interest) from background areas, before calculating various statistical measures (area, centroid, shape). When this process is complete, Quantifier continues by anchoring each identified object to a specific brain region by looking up the individual pixel coordinates in the anchoring map provided by the *QuickNII* output data. If an area overlaps N regions of the brain, the area is either assigned to one of the regions at random (with object splitting switched OFF) or split into N distinct areas with IDs coupled to their respective regions (with object splitting switched ON). In addition, various filters can be applied such as minimum and maximum object size, which are useful for removing noise. Functionality tailored specifically for connectivity data has been implemented, with support for masks to enable differentiation of connections in the right and left hemispheres. The object splitting feature was also implemented for connectivity data as connections typically span multiple atlas regions. With object splitting switched ON each object pixel is registered to its respective atlas region. However, users will typically want to switch this feature OFF for small objects such as cells, to enable accurate counting. Object splitting invalidates the object counts as objects are split at region boundaries.

The output results are assembled based on information provided in the *Nutil* GUI, which includes the option to define customized regions (ensembles of reference brain region IDs) together with a name ("Cortex") and color ("red") (via an Excel template; see **Supplementary File 2**). This enables the user to constrain the output data to specific areas of the brain (e.g., "Amygdala,", "Hippocampus," "Primary Somatosensory Cortex"). Report outputs are written as a series of files in CSV or HTML format containing report information per section, and for all sections combined (global information), and are organized first by all the regions listed in the relevant reference atlas (e.g., Allen adult mouse brain reference atlas) and second by the optional user-defined custom regions. Moreover, *Nutil* generates 3D point clouds, colorized based on report specifications that may be visualized in the online *MeshView* atlas viewer[2]. The point clouds are exported in a simple JSON-formatted text file that is compatible with Python, containing a raw list of 3D coordinates collected together with color-coding based on the input report. Support for specifying the required point cloud density has been implemented to enable the extraction of coordinates for datasets with very large objects (such as those typical of connectivity data, where a user may, for example, request extraction of one coordinate per 5th object pixel).

Pseudocode Block

1. For each input file, verify that parameters are correct and that the files in the file list exist.
2. Create output directories.
3. For each slice (in separate threads) do:
4. Open segmented image.
5. Apply masks, calculate some statistics.
6. Perform a breadth-first algorithm that counts the number of areas, and place them into an object list.
7. Open the corresponding atlas slice and assign each area to a unique atlas ID.
8. Calculate various area statistics.
9. Create a visual.png file by merging the segmented image file with the atlas image file, and add label text and colors to the identified areas.
10. When all threads have completed, combine areas into one object and calculate both individual slice and global statistics.
11. Write reports:
12. Individual slice reports.
13. Combined area reports.
14. Write 3D data (perform an inverse matrix operation to get back to atlas space).
15. Clean up memory and temporary files.

[2]https://www.nitrc.org/projects/meshview

TECHNICAL SPECIFICATIONS

Nutil is written in C++ using standard Qt[3] libraries, and is optimized for parallel operations on multiple CPUs. *Nutil* is downloaded as a zip archive file and can be extracted and run anywhere on the computer. No installation executable is necessary, and the directory can be moved around the file system as required. Settings data are stored in the local program folder. Nutil does not currently utilize any GPU extensions. The external libraries that are used in *Nutil* are:

1. Libtiff for fast and efficient TIFF file handling[4]
2. LibXLNT for Excel file I/O[5]

Hosting and Updates

Nutil is available from two locations:

1. Windows binaries (no installer required): https://www.nitrc.org/projects/nutil/
2. Source code: https://github.com/leuat/nutil/

Hardware Requirements

Nutil is a stand-alone program that can be executed on either a server, desktop or laptop computer. *Nutil* will employ all the cores that are available to your current system. While there are no specific hardware limitations, the processing time is dependent on the system's compute power. The more cores and memory you have available, the faster the operations will be performed. However, running *Nutil* on a single-core laptop is also possible. This way, we allow the user to not be constrained by any hardware restrictions, as Nutil should be able to run on almost any computer.

USE CASES

Use Case Material

Three mouse brain image series were exported from the Allen Brain Atlas Data Portal with a Python script. The images were exported in JPEG format, and served as the test series for the TiffCreator, Transform, and Quantifier functions. The first series (use case A) included 20 sagittal mouse brain sections from the left hemisphere labeled for parvalbumin by *in situ* hybridization, and may be viewed here: http://mouse.brain-map.org/experiment/show/75457579 (Specimen 06-0419, Probe RP_060523_03_E07; ®2004 Allen Institute for Brain Science). The second *in situ* hybridization series (use case B) include 57 coronal sections labeled for parvalbumin[6] (Specimen 335-1125, Probe 071204_01_E06; ®2004 Allen Institute for Brain Science. Allen Mouse Brain Atlas. Available from: mouse.brain-map.org) (Lein et al., 2007; Oh et al., 2014). The third series (use case C) was a connectivity dataset displaying projections from the primary somatosensory mouth area. Nine images were selected for the use case and can be viewed here: https://connectivity.brain-map.org/projection/experiment/112936582 (Mouse strain: C57BL/6J, Tracer type: EGFP; ®2011 Allen Institute for Brain Science. Allen Mouse Brain Connectivity Atlas).

TiffCreator and Transform

TiffCreator enables batch conversion of JPEG/PNG images to the tiled TIFF format that is compatible with the Transform function. Transform then allows the user to perform a variety of image pre-processing steps such as scaling, rotation, and renaming, which are prerequisites for analysis by the method described in the other use cases (illustrated in **Figure 2**), but also for analysis by other means. For both TiffCreator and Transform, all the input and output parameters were entered in the *Nutil* GUI, and the desired operation run in batch mode. As *Nutil* Transform operates on tiled TIFF images only, the first operation for all the use cases was to convert the JPEG images to tiled TIFF using TiffCreator. Next, Transform was used to rename the files – to make them compatible with *QuickNII* and *Nutil* Quantifier – and to create the thumbnails required for registration to reference atlas space. As the images were well-organized and small in size, conversion from tiled TIFF to PNG was the only additional step required before segmentation with *ilastik* (Berg et al., 2019).

Note that all *Nutil* Transform operations – such as rotation, scaling and thumbnail creation – may be implemented in one process or separately. The thumbnail feature is particularly useful for visualizing the result of a transformation without having to open large images, as it allows the application of a resize factor with image export in PNG format, in addition to export of the original size transformed images. For rotation, the user may choose any angle and define the background color (i.e., black or white) in the new image. The rotation feature includes an auto-cropping function, which ensures the removal of redundant pixels. The *Nutil* GUI has an inbuilt user manual, accessible via help buttons. A user manual is also part of the *Nutil* software package and will be updated with new releases.

Quantifier: *In situ* Hybridization Dataset (Use Cases A and B)

Quantifier allows the quantification and spatial analysis of labeling in series of mouse or rat brain section images based on input from segmentations and customized atlas maps, both generated from the section images (**Figure 3**). Quantifier was used to extract, quantify and assign anatomical location to parvalbumin positive cells that were extracted from the image series that is described in section "Use Case Material". The images were pre-processed with *Nutil* TiffCreator and Transform as described above. For the sagittal parvalbumin example, derived input files (customized atlas maps and segmentations) and output files (Csv reports, point cloud, and atlas map images with superimposed features) are available for download

[3]https://www.qt.io/

[4]http://www.libtiff.org/

[5]https://github.com/tfussell/xlnt/

[6]http://mouse.brain-map.org/experiment/show/79556738

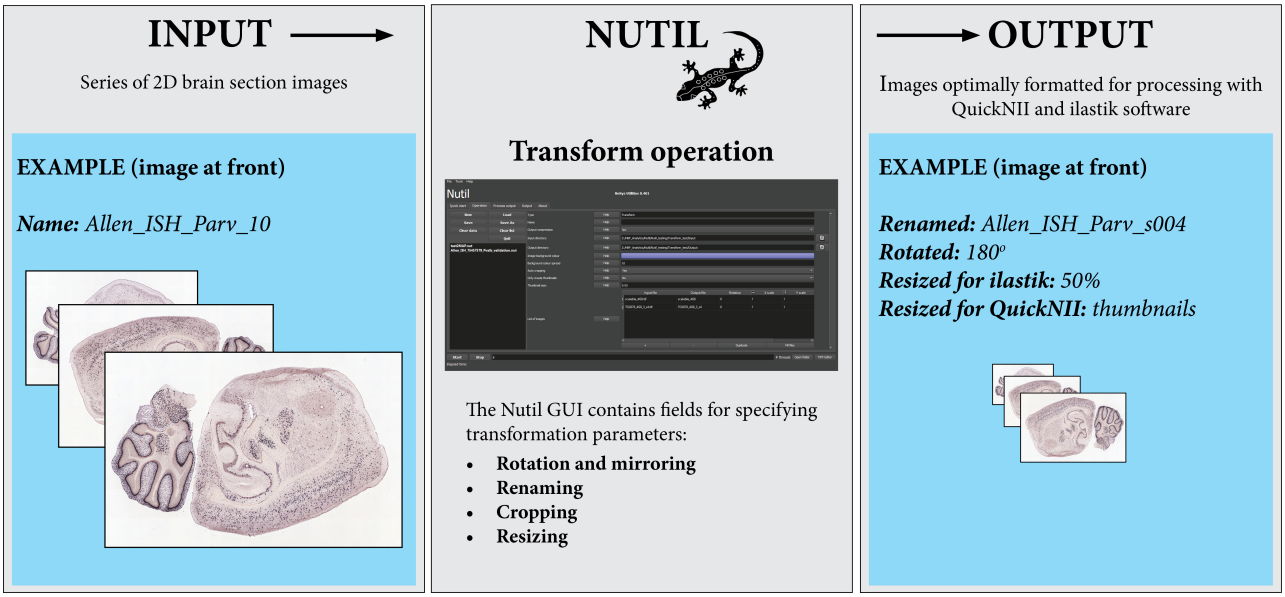

FIGURE 2 | The Nutil Transform operation takes series of images as input, and outputs copies of the images that have been formatted based on parameters defined by the user in the *Nutil* GUI. Nutil Transform includes the option to rotate and mirror, rename, crop, resize, and convert file type. Image Credit for 2D section images: Allen Institute.

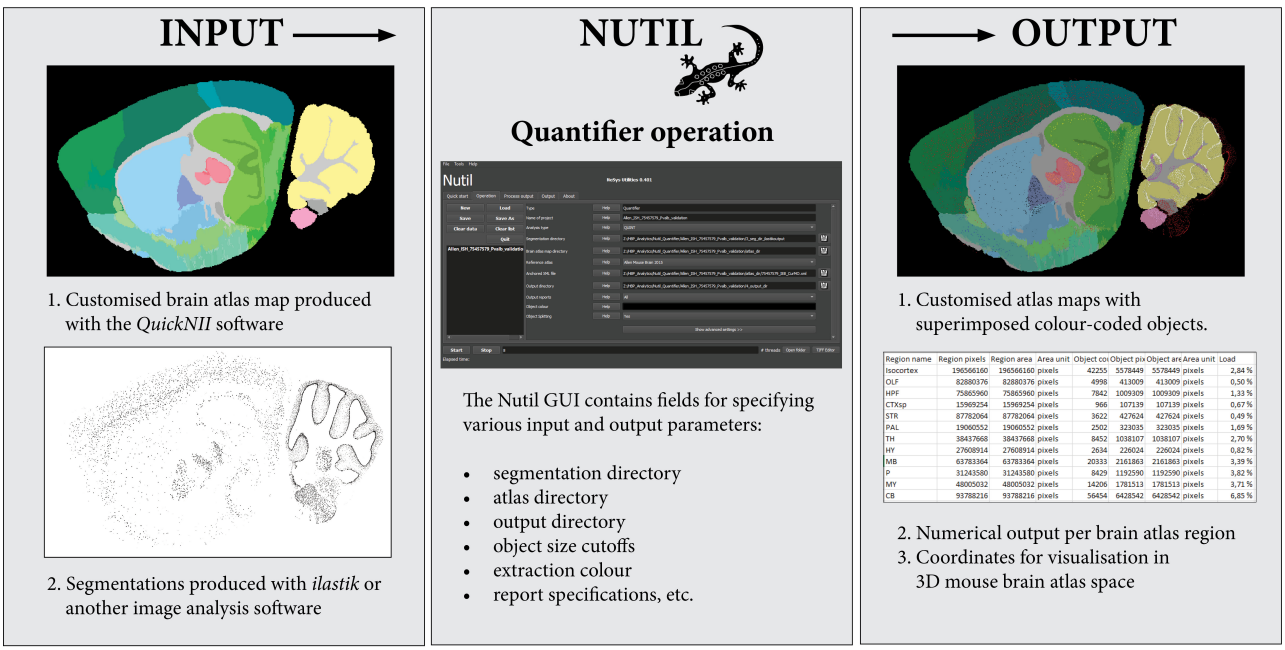

Region name	Region pixels	Region area	Area unit	Object coi	Object pix	Object are	Area unit	Load
Isocortex	196566160	196566160	pixels	42255	5578449	5578449	pixels	2,84 %
OLF	82880376	82880376	pixels	4998	413009	413009	pixels	0,50 %
HPF	75865960	75865960	pixels	7842	1005309	1005309	pixels	1,33 %
CTXsp	15969254	15969254	pixels	966	107139	107139	pixels	0,67 %
STR	87782064	87782064	pixels	3622	427624	427624	pixels	0,49 %
PAL	19060552	19060552	pixels	2502	323035	323035	pixels	1,69 %
TH	38437668	38437668	pixels	8452	1038107	1038107	pixels	2,70 %
HY	27608914	27608914	pixels	2634	226024	226024	pixels	0,82 %
MB	63783364	63783364	pixels	20333	2161863	2161863	pixels	3,39 %
P	31243580	31243580	pixels	8429	1192590	1192590	pixels	3,82 %
MY	48005032	48005032	pixels	14206	1781513	1781513	pixels	3,71 %
CB	93788216	93788216	pixels	56454	6428542	6428542	pixels	6,85 %

FIGURE 3 | The *Nutil* Quantifier operation takes atlas maps and segmentations as input, and outputs reports with quantifications per atlas region, atlas maps with superimposed color-coded objects and point clouds for visualization in reference atlas space. The *Nutil* GUI supports specification of parameters such as color for extraction, minimum and maximum object size, and coordinate file requirements. The GUI includes an in build user manual accessible via help buttons.

from the EBRAINS KnowledgeGraph database (DOI: 10.25493/6DYS-M3W)[7].

To generate the atlas maps, the mouse brain section images were registered to Allen Adult Mouse Brain Reference Atlas space (Common Coordinate Framework version 3, 2015) with the *QuickNII* software version 2.1 (Available from: https://www.nitrc.org/projects/quicknii) (**Figure 3**, Input 1). In a parallel

[7]https://kg.ebrains.eu/search/instances/Dataset/8e8ac473-08fc-4510-bf81-e6d94c9c15d6

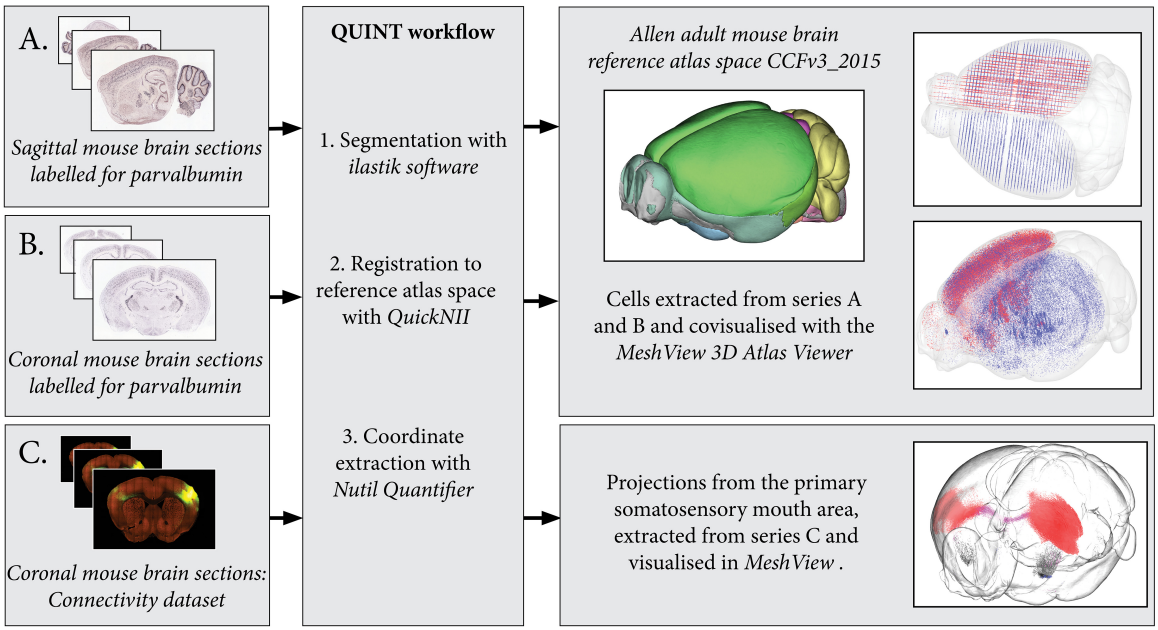

FIGURE 4 | By processing several image series with the QUINT workflow, point clouds representing labeled features can be covisualized in reference atlas space allowing comparisons of expression patterns. Here, parvalbumin positive cells are extracted from two mouse brain section series: one cut in the sagittal plane **(A)** and the other in the coronal plane **(B)**. The cells are covisualized in Allen Adult Mouse Brain Reference atlas space with the *MeshView* atlas viewer. Likewise, the connectivity use case **(C)** displays projections from the primary somatosensory mouth area, labeling in all brain areas is quantified and visualized in 3D with differential color coding dependent on the brain region (neocortex, red; corpus callosum, pink; striatum, black). Image Credit for 2D section images: Allen Institute. Series: http://mouse.brain-map.org/experiment/show/75457579, http://mouse.brain-map.org/experiment/show/79556738, https://connectivity.brain-map.org/projection/experiment/112936582.

procedure, the section images were classified with the Pixel Classification workflow in the *ilastik* software to identify the parvalbumin positive cells (version 1.3.2rc1; available from: https://www.ilastik.org). Segmentations were generated in PNG format, with RGB color value (0, 0, 0) (black) applied to the class representing the positive cells (**Figure 3**, Input 2). The Quantifier template in the *Nutil* GUI was populated with the input and output directories, as well as parameters such as minimum and maximum object size and coordinate file requirements. Object splitting was switched OFF. Quantifier was subsequently applied to all the images in batch mode. The point cloud was visualized with the *MeshView* Atlas Viewer (AMBA version 3 2015, available from: https://www.nitrc.org/projects/meshview). The same procedure was repeated for use case B, and the datasets were co-visualized in 3D (**Figure 4**). The processing of the dataset with Nutil Quantifier on a standard laptop with 2 to 4 cores and 16 GB of memory took less than 10 min, including selection of the files and analysis parameters in the GUI interface.

Quantifier: Connectivity Dataset (Use Case C)

The connectivity dataset was preprocessed with Nutil Transform, segmented with *ilastik* and registered to Allen Adult Mouse Brain Reference Atlas space (Common Coordinate Framework version 3, 2015) with *QuickNII* in the same way as described for the *in situ* hybridization datasets. The dataset was processed with Nutil Quantifier with object splitting switched ON, with masks to differentiate connections in the right and left hemisphere and with a reduced point cloud density to enable visualization in 3D (**Figure 4**).

Quantifier Validation

To validate the use case output, we compared the results obtained with *Nutil* Quantifier for the *in situ* hybridization dataset with the raw expression values provided by the Allen Brain Institute for the same dataset and brain regions. Despite considerable differences in quantification methods (Bohland et al., 2010) and minor differences in the atlas registration, the outputs were comparable as demonstrated in **Supplementary File 3**.

A proper validation of *Nutil* Quantifier was done with a synthetic dataset of two sections, each with a set number of objects of known size (in pixels) and anatomical location. This dataset confirms that the quantification data delivered by *Nutil* Quantifier are correct (**Supplementary File 4**). Further validation is provided in Yates et al. (2019).

DISCUSSION

With the development of microscopes and scanners for whole section imaging and volumetric data acquisition, scientists are able to collect high-resolution images of different organs including the brain. The sheer size of these images has

necessitated the development of new software tools for viewing, transforming and analyzing imaging data; but are typically only available commercially, and often with restrictions in terms of functionality that do not promote optimal analysis. For human brains, methods for 2D image reconstruction from multiple blocks have allowed researchers to conduct multimodal imaging studies (Hashimoto et al., 2016). There are also some open-access tools such as "HistoStitcher" (Chappelow et al., 2011) that enable specific pre-processing operations like reassembly of tissue fragments. Most pre-processing steps may be done with scripts, many available online; however, for a neuroscientist with limited programming experience, pre-processing can be a slow and painful process. There is a need for open-access tools that operate without the need for coding expertise with functionality tailored specifically for series of histological brain section images.

With *Nutil*, neuroscientists will find a user-friendly and convenient tool, specifically designed with serial rodent brain sections in mind. It enables image transformations in an automated batch operation, making downstream image analysis accessible to the wider community. In a separate post-processing operation, *Nutil* allows the quantification and spatial analysis of labeling in 2D image series of rodent brain sections, when used in combination with *QuickNII* (Puchades et al., 2019) – an open-access software for registering section images to reference atlases – in addition to an image segmentation tool such as *NIH ImageJ* (Schneider et al., 2012) or *ilastik* (Berg et al., 2019). Several groups have developed custom codes and workflows along the same lines, for the analysis of whole brain volumes by registration to reference atlases. In a recent study, Kim et al. (2017) used the 3D Allen mouse reference atlas (Lein et al., 2007; Oh et al., 2014) for quantification of several interneuronal types in serial two-photon tomography data. By registering all datasets to the same reference space, they were able to discover sex differences in specific atlas sub-regions. Other studies rely on block-face photography (Vandenberghe et al., 2016) or 3D reconstruction (Majka et al., 2012). Likewise, *Nutil* has the potential to contribute to discoveries based on histological experimental data without the need for 3D volumes or 3D reconstruction. Several other groups have proposed tools for analysis of 2D mouse brain section images, without the need for 3D reconstruction (Furth et al., 2018; Xiong et al., 2018); however, the requirement for coding knowledge restricts the accessibility of these methods. The AIDAhisto tool enable atlas based quantifications but lack multi-angle adjustment (Pallast et al., 2019).

In contrast to the cited studies, *Nutil* Quantifier may be applied to both mouse and rat brain data, as both mouse and rat brain reference atlases are inbuilt in the *Nutil* software, with *QuickNII* versions available for both species. *Nutil* Quantifier supports quantification of both small objects such as cells, typical of immunohistochemistry and *in situ* hybridization data, and the exploration of large objects that span multiple atlas regions, such as those typical of connectivity data. There is also a feature for combining masks with the atlas maps, to allow comparative analysis of right and left hemisphere expression. As the TiffCreator, Transform, Resize, and Quantifier operations run independently, TiffCreator, Transform, and Resize may be used to process any type of image, and can be incorporated into workflows that do not include the Quantifier operation. However, the pre-processing package is ideally suited for use with Quantifier; with all operations running on multiple CPUs, which drastically increases processing speed, making them ideal for batch processing of section images. By combining information from segmented images with corresponding atlas maps produced with *QuickNII* (Puchades et al., 2019; Yates et al., 2019), several datasets may be analyzed and then compared (**Figure 4**), offering new analytical possibilities as discussed in depth in Bjerke et al. (2018). The present developments are part of a larger European effort to establish tools and services for neuroscience research (Amunts et al., 2019).

DATA AVAILABILITY STATEMENT

Publicly available datasets were analyzed in this study. This data can be found here: http://mouse.brain-map.org/experiment/show/75457579, doi: 10.25493/6DYS-M3W.

AUTHOR CONTRIBUTIONS

NG created the *Nutil* software, contributed to the writing of the technical parts of the manuscript, and to the design of the validation studies. SY performed *Nutil* analyses, performed the validation studies, contributed to the development of the *Nutil* software, and contributed to writing the manuscript. MP conceived the study, supervised the analysis and the development of *Nutil,* and wrote the manuscript. JB conceived the study, supervised development of software tools, contributed with infrastructure, and contributed to writing of the manuscript. All authors contributed to the article and approved the submitted version.

FUNDING

This research was supported by the EBRAINS research infrastructure, funded from the European Union's Horizon 2020 Framework Programme for Research and Innovation under the Specific Grant Agreement No. 785907 (Human Brain Project SGA2) and Specific Grant Agreement No. 945539 (Human Brain Project SGA3).

ACKNOWLEDGMENTS

We thank Gergely Csucs and Dmitri Darine for discussions and expert technical assistance.

SUPPLEMENTARY MATERIAL

The Supplementary Material for this article can be found online at: https://www.frontiersin.org/articles/10.3389/fninf.2020.00037/full#supplementary-material

REFERENCES

Amunts, K., Knoll, A. C., Lippert, T., Pennartz, C. M. A., Ryvlin, P., Destexhe, A., et al. (2019). The Human Brain Project-Synergy between neuroscience, computing, informatics, and brain-inspired technologies. *PLoS Biol.* 17:e3000344. doi: 10.1371/journal.pbio.3000344

Berg, S., Kutra, D., Kroeger, T., Straehle, C. N., Kausler, B. X., Haubold, C., et al. (2019). ilastik: interactive machine learning for (bio)image analysis. *Nat. Methods* 16, 1226–1232. doi: 10.1038/s41592-019-0582-9

Bjerke, I. E., Ovsthus, M., Papp, E. A., Yates, S. C., Silvestri, L., Fiorilli, J., et al. (2018). Data integration through brain atlasing: human brain project tools and strategies. *Eur. Psychiatry* 50, 70–76. doi: 10.1016/j.eurpsy.2018.02.004

Bohland, J. W., Bokil, H., Pathak, S. D., Lee, C. K., Ng, L., Lau, C., et al. (2010). Clustering of spatial gene expression patterns in the mouse brain and comparison with classical neuroanatomy. *Methods* 50, 105–112. doi: 10.1016/j.ymeth.2009.09.001

Chambers, J. M. (2008). *Software for Data Analysis: Programming with R*. New York: Springer.

Chappelow, J., Tomaszewski, J. E., Feldman, M., Shih, N., and Madabhushi, A. (2011). HistoStitcher((c)): an interactive program for accurate and rapid reconstruction of digitized whole histological sections from tissue fragments. *Comput. Med. Imaging Graph* 35, 557–567. doi: 10.1016/j.compmedimag.2011.01.010

Furth, D., Vaissiere, T., Tzortzi, O., Xuan, Y., Martin, A., Lazaridis, I., et al. (2018). An interactive framework for whole-brain maps at cellular resolution. *Nat. Neurosci.* 21, 139–149. doi: 10.1038/s41593-017-0027-7

Hashimoto, N., Bautista, P. A., Haneishi, H., Snuderl, M., and Yagi, Y. (2016). Development of a 2D image reconstruction and viewing system for histological images from multiple tissue blocks: towards high-resolution whole-organ 3D histological images. *Pathobiology* 83, 127–139. doi: 10.1159/000443278

Kim, Y., Yang, G. R., Pradhan, K., Venkataraju, K. U., Bota, M., Garcia Del, et al. (2017). Brain-wide maps reveal stereotyped cell-type-based cortical architecture and subcortical sexual dimorphism. *Cell* 171, 456–469.e22. doi: 10.1016/j.cell.2017.09.020

Kjonigsen, L. J., Lillehaug, S., Bjaalie, J. G., Witter, M. P., and Leergaard, T. B. (2015). Waxholm Space atlas of the rat brain hippocampal region: three-dimensional delineations based on magnetic resonance and diffusion tensor imaging. *Neuroimage* 108, 441–449. doi: 10.1016/j.neuroimage.2014.12.080

Lein, E. S., Hawrylycz, M. J., Ao, N., Ayres, M., Bensinger, A., Bernard, A., et al. (2007). Genome-wide atlas of gene expression in the adult mouse brain. *Nature* 445, 168–176. doi: 10.1038/nature05453

Majka, P., Kublik, E., Furga, G., and Wojcik, D. K. (2012). Common atlas format and 3D brain atlas reconstructor: infrastructure for constructing 3D brain atlases. *Neuroinformatics* 10, 181–197. doi: 10.1007/s12021-011-9138-6

MATLAB (2010). *Version 7.10.0 (R2010a)*. Natick, Massachusetts: The MathWorks Inc.

Oh, S. W., Harris, J. A., Ng, L., Winslow, B., Cain, N., Mihalas, S., et al. (2014). A mesoscale connectome of the mouse brain. *Nature* 508, 207–214. doi: 10.1038/nature13186

Osen, K. K., Imad, J., Wennberg, A. E., Papp, E. A., and Leergaard, T. B. (2019). Waxholm Space atlas of the rat brain auditory system: three-dimensional delineations based on structural and diffusion tensor magnetic resonance imaging. *Neuroimage* 199, 38–56. doi: 10.1016/j.neuroimage.2019.05.016

Pallast, N., Wieters, F., Fink, G. R., and Aswendt, M. (2019). Atlas-based imaging data analysis tool for quantitative mouse brain histology (AIDAhisto). *J. Neurosci. Methods* 326:108394. doi: 10.1016/j.jneumeth.2019.108394

Papp, E. A., Leergaard, T. B., Calabrese, E., Johnson, G. A., and Bjaalie, J. G. (2014). Waxholm Space atlas of the Sprague Dawley rat brain. *Neuroimage* 97, 374–386. doi: 10.1016/j.neuroimage.2014.04.001

Puchades, M. A., Csucs, G., Ledergerber, D., Leergaard, T. B., and Bjaalie, J. G. (2019). Spatial registration of serial microscopic brain images to three-dimensional reference atlases with the QuickNII tool. *PLoS One* 14:e0216796. doi: 10.1371/journal.pone.0216796

Schneider, C. A., Rasband, W. S., and Eliceiri, K. W. (2012). NIH image to ImageJ: 25 years of image analysis. *Nat. Methods* 9, 671–675. doi: 10.1038/nmeth.2089

The ImageMagick Development Team (2020). *ImageMagick. Version 7.0.10*. Available online at: https://imagemagick.org (accessed June 12, 2020).

Vandenberghe, M. E., Herard, A. S., Souedet, N., Sadouni, E., Santin, M. D., Briet, D., et al. (2016). High-throughput 3D whole-brain quantitative histopathology in rodents. *Sci. Rep.* 6:20958. doi: 10.1038/srep20958

Xiong, J., Ren, J., Luo, L., and Horowitz, M. (2018). Mapping histological slice sequences to the allen mouse brain atlas without 3D reconstruction. *Front. Neuroinform.* 12:93. doi: 10.3389/fninf.2018.00093

Yates, S. C., Groeneboom, N. E., Coello, C., Lichtenthaler, S. F., Kuhn, P. H., Demuth, H. U., et al. (2019). QUINT: workflow for quantification and spatial analysis of features in histological images from rodent brain. *Front. Neuroinform.* 13:75. doi: 10.3389/fninf.2019.00075

Conflict of Interest: The authors declare that the research was conducted in the absence of any commercial or financial relationships that could be construed as a potential conflict of interest.

Advantages of publishing in Frontiers

OPEN ACCESS
Articles are free to read for greatest visibility and readership

FAST PUBLICATION
Around 90 days from submission to decision

HIGH QUALITY PEER-REVIEW
Rigorous, collaborative, and constructive peer-review

TRANSPARENT PEER-REVIEW
Editors and reviewers acknowledged by name on published articles

Frontiers
Avenue du Tribunal-Fédéral 34
1005 Lausanne | Switzerland

Visit us: www.frontiersin.org
Contact us: frontiersin.org/about/contact

REPRODUCIBILITY OF RESEARCH
Support open data and methods to enhance research reproducibility

DIGITAL PUBLISHING
Articles designed for optimal readership across devices

FOLLOW US
@frontiersin

IMPACT METRICS
Advanced article metrics track visibility across digital media

EXTENSIVE PROMOTION
Marketing and promotion of impactful research

LOOP RESEARCH NETWORK
Our network increases your article's readership